Department of Meteorology

School of Mathematical, Physical and Computational Sciences

Ocean heat transport and the latitude of the sea ice edge

by

Jake Robert Aylmer

Thesis submitted for the degree of Doctor of Philosophy

PhD in Atmosphere, oceans and climate

August 2021

University of Reading

This page intentionally left blank.

Declaration of original authorship

I confirm that this is my own work and the use of all material from other sources has been properly and fully acknowledged.

Signed:

JAKE ROBERT AYLMER

This page intentionally left blank.

Abstract

Ocean heat transport (OHT) has been proposed as a major driver of sea ice extent on multidecadal timescales. This thesis brings new insight into the mechanisms behind this relationship, with implications for uncertainties arising in simulations of present and future climate with coupled general circulation models (GCMs).

Using a novel implementation of a zonally-averaged energy-balance model (EBM), it is shown that sea ice is intrinsically more sensitive to ocean that atmospheric heat transport (AHT). The ratio of sensitivities to the two heat transports mainly depends on large-scale atmospheric radiation parameters. A simple equation is derived relating changes in sea ice, OHT, and surface temperature, revealing how the sea ice sensitivity to OHT arises from emergent constraints on the top-of-atmosphere radiation balance.

Simulations by GCMs exhibit strong anticorrelation between poleward OHT and sea ice extent in both hemispheres, applying to both internal and forced (future) multidecadal variability. These relationships are captured and explained by the aforementioned EBM equation. Different qualitative processes are exhibited in each hemisphere, robust across 20 GCMs and with analogues in the EBM. In the Arctic, OHT converges along the Atlantic sea ice edge, efficiently eroding the ice edge and enhancing AHT to higher latitudes. Poleward OHT into the Southern Ocean is released relatively uniformly under the Antarctic sea ice pack.

Under rising greenhouse-gas emissions, GCMs simulate a wide range of pro-

jected sea ice losses in both hemispheres. This is strongly related to biases in the mean-state and future change of poleward OHT. These results motivate the need for improved ocean representation in GCMs to better constrain future sea ice projections.

Acknowledgements

Firstly, I thank my supervisors, David Ferreira and Danny Feltham, for their unwavering support and enthusiasm for this research project over the years. Our regular meetings have always been productive yet light-hearted, and overall it has been a pleasure to work with you both.

I am also grateful to Jonathan Gregory and Bill Collins, who formed my monitoring committee. They made sure the project was on track, and brought potential issues to my attention that may otherwise have been overlooked, ultimately strengthening this thesis.

I thank Jonathan Gregory (again), my internal examiner, and Dirk Notz, external examiner, for their enthusiastic discussion and constructive feedback during the viva examination. Their suggestions have helped improve the quality of the thesis and (it is hoped) future publications arising from this work.

This research was funded by NERC via the SCENARIO Doctoral Training Partnership (DTP). As part of this, various training courses—particularly in software engineering—greatly facilitated the technical aspects of the project. The DTP also supported my attendance at several national and major international scientific conferences, contributing to my professional development and enabling discussion of this work with other researchers.

Finally, a great deal of the efforts generating this thesis are owed to my family, whom I thank for their overwhelming personal support.

This page intentionally left blank.

Table of contents

This page intentionally left blank.

List of abbreviations

Page cross references are to the first use or definition of each abbreviation:

AHT	Atmospheric heat transport . . . p. 11
AHTC	Atmospheric heat transport convergence . . . p. 15
AMOC	Atlantic meridional overturning circulation . . . p. 4
BC	Bjerknes compensation . . . p. 13
CMIP	Coupled Model Intercomparison Project . . . p. 1
EBM	Energy balance model . . . p. 16
ECS	Equilibrium climate sensitivity . . . p. 58
GCM	General circulation model . . . p. 1
LHS	Left-hand side . . . p. 17
MHT	Meridional heat transport . . . p. 13
NH	Northern hemisphere . . . p. 87
OHT	Ocean heat transport . . . p. 1
OHTC	Ocean heat transport convergence . . . p. 14
OLR	Outgoing longwave radiation . . . p. 16
OLS	Ordinary least squares . . . p. 22
PI	Pre-industrial . . . p. 8
RHS	Right-hand side . . . p. 78
SH	Southern hemisphere . . . p. 87
SICI	Small ice cap instability . . . p. 18
SIF	Seasonally ice free . . . p. 59
SSP	Shared socioeconomic pathway . . . p. 6
TOA	Top of atmosphere . . . p. 13

This page intentionally left blank.

List of symbols

This is a list of symbols used frequently throughout. Page cross references are to the first use or definition of each symbol. See also Table 2.1 containing EBM-specific parameters and default values.

Coordinates

t	Time (yr)	p. 12
λ	Longitude (°E)	p. 89
ϕ	Latitude (°N or °S)	p. 17
ϕ_0	Reference latitude (°N or °S)	p. 75
p_0	Reference pressure level (for T_a; hPa)	p. 47

Vertical heat fluxes

F_sw	Net shortwave radiation (W m^{-2})	p. 76
F_OLR	Outgoing longwave radiation (W m^{-2})	p. 33
F_up	Surface turbulent plus upwelling longwave flux (W m^{-2})	p. 32
F_dn	Surface downwelling longwave flux (W m^{-2})	p. 32
F_s	Net surface heat flux (W m^{-2})	p. 12

(continued overleaf)

Diagnostics

Chapter 1

Introduction and background

Sea ice plays many important roles in climate and is a notable metric of climate change. Understanding the long-term evolution of climate and informing environmental policy largely relies on projections by coupled general circulation models (GCMs). Yet, such models participating in the latest (sixth) phase of the Coupled Model Intercomparison Project (CMIP6) exhibit significant inter-model spread in their simulations of past, present, and future sea ice extent. To discern the origins of this, an understanding of the large-scale drivers of sea ice on decadal and longer timescales is required. This is a key step towards reducing uncertainty in climate projections.

The focus of this thesis is the impact of ocean heat transport (OHT) on sea ice extent on multidecadal timescales. Despite extensive evidence that larger heat transported by the ocean towards the poles is associated with smaller sea ice cover, there remain gaps in our theoretical understanding of the relationship and its relevance to the aforementioned problem of inter-model spread. Specifically, what are the factors setting and mechanisms underlying the sensitivity of sea ice to OHT, how important is OHT compared to other climate processes, and to what extent does OHT influence the rate of projected sea ice decline? This thesis aims to address these questions, first by developing and analysing an idealised

energy-balance climate model to generate theoretical insight, and then applying those results to the analysis of CMIP6 simulations.

This chapter starts with an overview of sea ice—its role in climate and the wider Earth system (section 1.1.1), its simulation by GCMs (section 1.1.2), and evidence for its physical drivers on multidecadal timescales (section 1.1.3). Section 1.2 describes current understanding of OHT and its relationship with sea ice. Next, the idealised energy balance model framework is explored in section 1.3, providing scientific context and the starting point for a major part of the methodology in this work. Finally, the specific objectives of this research project are laid out, and an outline of the remaining thesis structure is presented in section 1.4.

1.1 Sea ice in the climate system

1.1.1 Physical characteristics and importance

Sea ice is frozen sea water which, in the present-day climate, covers a substantial area of the high-latitude oceans. Arctic and Antarctic sea ice exhibit dramatic seasonality in extent, shaping the polar environment and affecting climate as well as human and biological activity. Arctic sea ice extent has been in decline in recent decades (Fig. 1.1, left), with significant attribution to anthropogenic climate change (Notz and Marotzke, 2012). Antarctic sea ice has not shown such a conspicuous trend, being insignificantly different from zero when considering the period 1979–2020 (Fig. 1.1, right; IPCC, 2021), for which the underlying reasons are not fully understood (Parkinson, 2019). This first section describes the general physical properties and main roles of sea ice in the Earth system, to emphasise the importance of understanding its drivers and how it responds to climate change.

A key large-scale impact of sea ice on climate is due to its high surface reflectivity compared to ocean and bare land, such that it greatly contributes to Earth's albedo. Sea ice albedo depends on its physical properties (such as thickness) and is affected by the presence of snow (increases) and melt ponds (decreases; e.g., Flocco et al., 2012). When considering the large-scale energy balance of the climate system as a whole, the planetary albedo becomes relevant, in which atmospheric effects (i.e., clouds) significantly attenuate the surface effects (Donohoe and Battisti, 2011). Still, this property gives rise to a major positive feedback mechanism, in which melting of ice exposes ocean, increasing absorption of shortwave radiation which reinforces the initial melting. This ice–albedo feedback plays a significant role in amplifying future climate change (Thackeray and Hall, 2019).

Sea ice acts as a physical barrier between the ocean and atmosphere, inhibiting surface exchanges of heat, moisture, and momentum (Bourassa et al., 2013). Thus, shrinking Arctic sea ice cover exposes more ocean, enhancing moisture fluxes and leading to local increases in cloud cover (Kay and Gettelman, 2014; Vihma, 2014; Huang et al., 2019) and precipitation (Bintanja and Selten, 2014; Kopec et al., 2016). Ocean heat release associated with retreating Arctic sea ice is a key part of the mechanism by which sea ice loss substantially contributes to polar amplification (the greater increases in surface temperature at high latitudes compared to that of the global mean in recent decades; Screen and Simmonds, 2010; Kim et al., 2016; Dai et al., 2019). Sea ice can affect global climate via influences on the large-scale atmospheric circulation. For instance, some studies link Arctic sea ice variability with mid-latitude precipitation via associated equatorward shifts in the mid-latitude jet stream (e.g., Screen, 2013; Ronalds et al., 2018). Similar effects on the southern hemisphere jet are suggested to occur in response to substantial Antarctic sea ice loss, although influences on precipitation are limited to high latitudes (England et al., 2018).

When sea water freezes, most of the salt content remains in the ocean, increasing its water density and so contributing to deep water formation as part of the ocean thermohaline circulation (e.g., Budikova, 2009). This and the associated Atlantic meridional overturning circulation (AMOC) affect the transport of heat around the globe (e.g., Rahmstorf, 2006, see also section 1.2.1). Some studies suggest that long-term Arctic sea ice loss and the resulting freshwater forcing could contribute to a weakening of the AMOC (Jahn and Holland, 2013; Sévellec et al., 2017; Li et al., 2021). Expansion of Antarctic sea ice is thought to partly explain ocean carbon uptake during the last glacial period by increasing Antarctic deep water formation, and the consequent reduced mixing of deep and shallow water masses (Bouttes et al., 2010; Ferrari et al., 2014).

While the basic physical properties of sea ice are the same in both hemispheres, the two polar regions are geographically and oceanographically distinct, leading to differences in behaviour and interactions with the ocean and atmosphere. The Arctic Ocean is centred on the North pole, surrounded by the North American and Eurasian continents, consisting largely of shallow, continental seas. Primarily as a result of land constraints, the distribution of Arctic sea ice cover is highly zonally-asymmetric (with some 20°N zonal variation in minimum latitude; Bitz et al., 2005). In contrast, the Southern Ocean and its sea ice cover surrounds the ice sheet-covered Antarctica, with no substantial land masses between 55°S (the approximate southern-most latitude of South America) and the Antarctic coast. The latitude of the Antarctic sea ice edge does not vary that much with longitude, and the ice pack has greater mobility and a larger seasonal cycle in extent compared with the Arctic. The oceanography of the two polar regions also influences the nature of their sea ice covers. In the Arctic, rivers from the surrounding continents input fresh water, while there is limited inflow from the Atlantic and Pacific Oceans at lower latitudes (Serreze et al., 2006). The result is a cold, fresh surface layer, separated from relatively warm, saline Atlantic and

deeper Arctic waters by a strong halocline. Due to the strong vertical stability of this setup, heat input from the Atlantic is largely prevented from reaching the surface, effectively shielding sea ice from its influence (Rudels, 2012; Carmack et al., 2015). In contrast, basal ocean heat fluxes are a key driver of Antarctic sea ice. The Southern Ocean is a major site of deep water upwelling, closing the inter-hemispheric overturning circulation (Marshall and Speer, 2012; Watson et al., 2013). This particularly affects the winter Antarctic sea ice cover, via the entrainment of heat into the mixed layer which slows the vertical sea ice growth rate (e.g., Wilson et al., 2019). Typical ocean–ice heat fluxes under Antarctic sea ice are $\sim$ 30 W m^{-2}, while only a few W m^{-2} under the central Arctic sea ice pack, largely explaining the existence of thicker, multi-year ice in the latter but not the former (Maksym, 2019).

Recent trends in sea ice extent feature prominently in public communication on anthropogenic climate change (Hardy and Jamieson, 2016; Christensen and Nilsson, 2017). This is in some part due to the impact of sea ice on human activity. An increasingly sea ice-free Arctic Ocean, for instance, enables shorter trans-Arctic shipping routes, carrying political and economic implications (Ho, 2010; Melia et al., 2016; Askenov et al., 2017). Another aspect is the integral role of sea ice in polar wildlife. For example, the increasingly early melt onset in the Arctic negatively impacts survival of polar bears (Regehr et al., 2010). Although Antarctic sea ice as a whole has not experienced the same long-term decline as the Arctic, regional changes in its seasonality are thought to disrupt the marine food web (e.g., by altering the timing of primary production; Raymond et al., 2009). However, owing to the disparity between observations and model simulations, and the wide spread in future estimates by the latter, the ongoing implications for Southern Ocean ecology remain uncertain (Massom and Stammerjohn, 2010).

1.1.2 Simulation and projections by GCMs

Figure 1.1 shows sea ice extent, S_i (total area with at least 15% sea ice coverage), in the historical (1850–2014; Eyring et al., 2016) and Tier 1 ScenarioMIP (2015–2100; O'Neill et al., 2016) experiments based on 15 CMIP6 models.[1] In the Arctic, models tend to capture the observed decline in annual mean and September sea ice extent. However, there is substantial inter-model spread, indicated by the standard deviation across models, which widens as the simulations extend into the late 21st century. The standard deviations of all four future scenarios overlap in summer. This translates into significant uncertainty on the rate of further ice loss, notably on the timing of the first sea ice-free Arctic summer. Following Senftleben et al. (2020), this is defined as the first year of the first consecutive 5 yr period with sea ice extent less than 1×10^6 km^2, and is computed for 17 CMIP6 models and plotted in Fig. 1.2. This shows that there is a wide range (several decades) in both the mean estimates across models and across ensemble members of individual models, and the considerable overlap of scenarios is evident. For the SSP1-2.6 (low emissions) scenario, the range of estimates is at least 80 yr (8 models have simulations with summer sea ice remaining in 2100). The lack of emergence of a coherent picture from the multi-model ensemble casts doubt on the reliability of projections by state-of-the-art models.

On average, models simulate retreating Antarctic sea ice, at odds with observations. Inter-model spread in Antarctic sea ice is about twice that of the Arctic, and is as large in the historical period as in the future. Five of the models listed in Fig. 1.2 already simulate a seasonally sea ice-free Southern Ocean in the historical period, while 8 have substantial summer sea ice extent at the end of the 21st century. These uncertainties in sea ice projections propagate into those of

[1] The ScenarioMIP experiments are labelled SSPi-j, where i is the Shared Socioeconomic Pathway (SSP) and j is the 2100 global-average radiative forcing. For the purposes of this thesis, details underlying the SSPs are not important and these experiments can be simply thought of as different degrees of future warming.

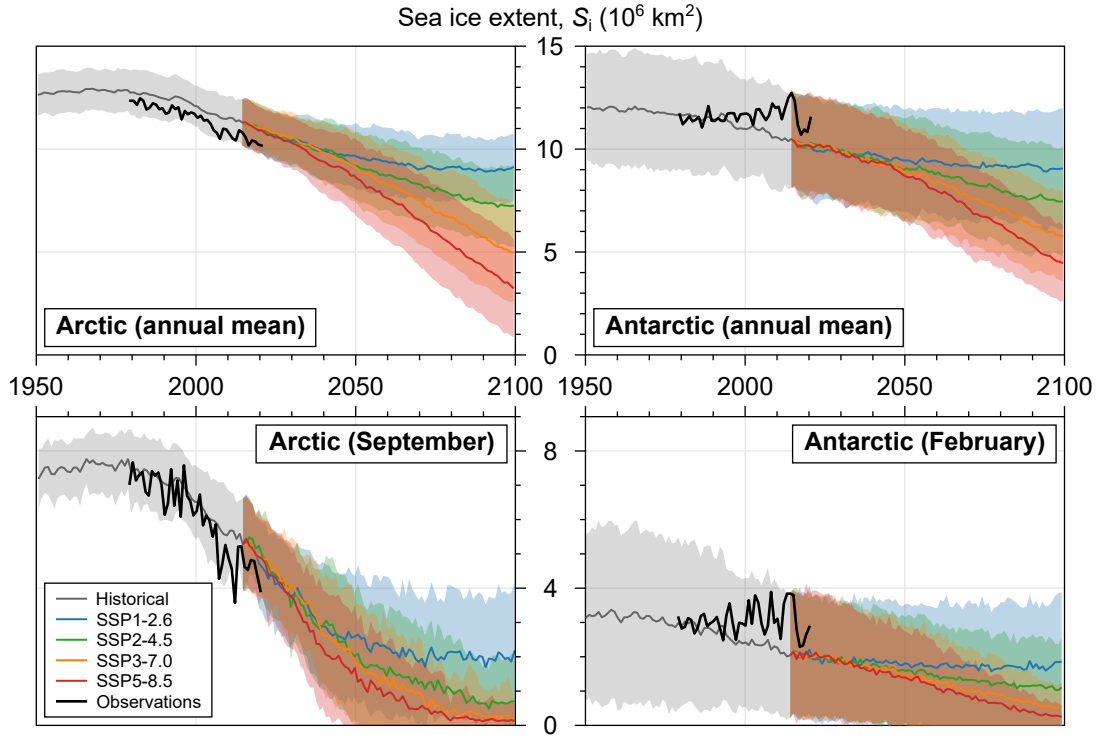

Figure 1.1: Historical simulations and future projections of (left) Arctic and (right) Antarctic sea ice extent, S_i, in 15 CMIP6 models, for four emission scenarios [SSPi-j, where i is the scenario label and j is the 2100 nominal, global-average radiative forcing (W m^{-2})]. See Fig. 1.2 for the models included. Top panels show the annual mean and the bottom panels show the summer time series. Solid lines are multi-model means of ensemble means, and shading indicates one standard deviation across ensemble means. Observations are taken from the National Snow and Ice Data Center (NSIDC).

other climate metrics such as surface temperature and precipitation (Bracegirdle et al., 2015).

The inter-model spread shown in Fig. 1.1 for CMIP6 models is comparable in magnitude to that in previous-generation model simulations (SIMIP Community, 2020; Roach et al., 2020), and the problem is not limited to 21st century projections. Marzocchi and Jansen (2017) find that model differences in Antarctic sea ice in CMIP5 simulations of the last glacial maximum (about 21 thousand years ago) contribute to uncertainty in the state of the ocean circulation at that time. This, for example, hampers understanding of the ocean role in CO_2 sequestration in such climates. Kageyama et al. (2021) show that Arctic sea ice differences

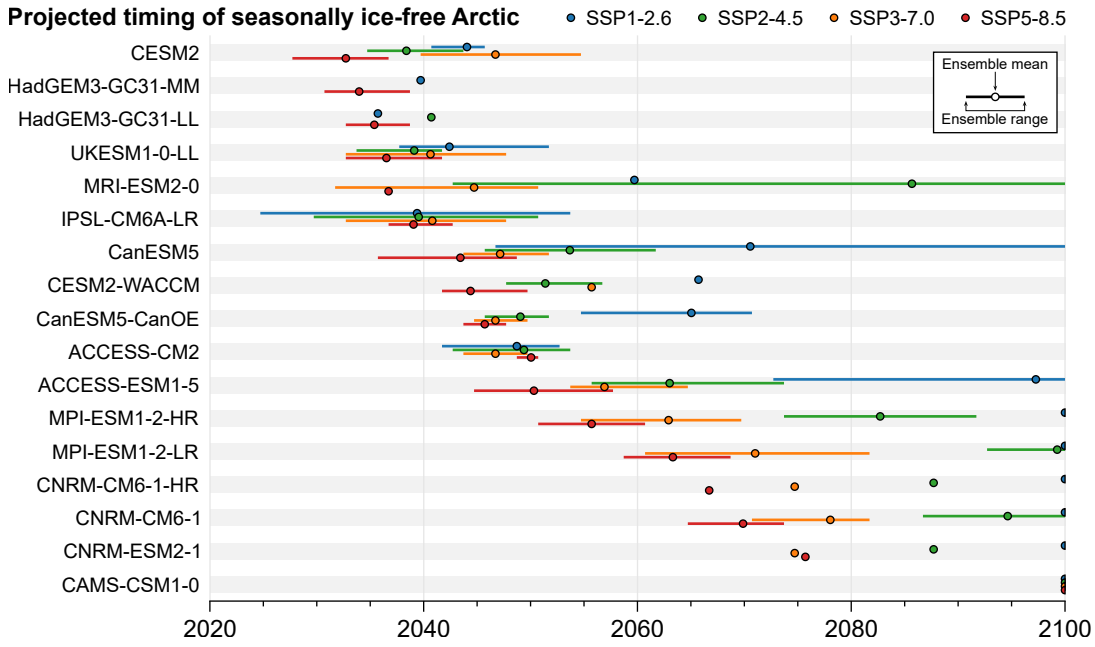

Figure 1.2: Projected timings of transition to a seasonally sea ice-free Arctic in CMIP6 models, ordered by that of SSP5-8.5. This is defined as the first year of the first consecutive 5 yr period for which the September sea ice extent is less than 1×10^6 km^2 (following Senftleben et al., 2020). Circles are ensemble means, and horizontal lines indicate the range of ensemble members, for each model. Half circles at 2100 indicate that sea ice remains in September at the end of the SSP simulation. Some of these models do not provide simulations for some of the ScenarioMIP experiments (see Table 5.1).

across CMIP6 simulations of the last inter-glacial period is larger than that of the corresponding pre-industrial (PI) control simulations. Understanding what causes inter-model spread thus remains an important step towards improving reliability of climate model simulations.

Possible factors contributing to inter-model spread are internal variability (fluctuations and the resulting ensemble divergence arising from the chaotic nature of the climate system), biases in atmosphere and ocean forcing, and the tuning and physical shortcomings of sea ice model components (Notz et al., 2016). Internal variability has been shown by Swart et al. (2015) to be sufficiently large to account for the discrepancy between the CMIP5-modelled and observed Arctic sea ice decline, and its contribution to the total uncertainty in future projections is comparable to that of inter-model spread. It has also been frequently suggested

to explain why most models do not capture the observed behaviour of Antarctic sea ice (Zunz et al., 2012; Polvani and Smith, 2013; Olonscheck and Notz, 2017; Singh et al., 2019). This rests on the notion that the observed (lack of) trend is a realisation of an extreme member of the hypothetical real-world ensemble of climate trajectories. There is some support for this: for example, Meehl et al. (2016) show that deepening of the Amundsen Sea low, associated with regional sea ice expansion, is driven by a shift to a negative phase of the interdecadal Pacific oscillation. Liu et al. (2013) showed that a dramatic reduction of the spread in the projected timing of an ice-free Arctic summer could be made by sub-sampling CMIP5 simulations best reproducing the observed sea ice trend. In terms of future-projection uncertainty, internal variability accounts for a substantial proportion ($\sim 50\%$), while scenario uncertainty only becomes important at the end of the 21st century and beyond (Roach et al., 2020; Bonan et al., 2021, and roughly apparent in Fig. 1.1).

On the tuning of sea ice model components, Eisenman et al. (2007) find that small adjustments in sea ice model parameters in GCMs intended to improve comparisons to observations often carries the cost of effectively cancelling errors arising from deficiencies in the atmospheric model. This means that models comparing well to observations in certain metrics such as winter Arctic sea ice thickness may do so for invalid reasons. It is difficult to quantify the contribution of this to projection uncertainty because modelling centres use different procedures for tuning (Mauritsen et al., 2012; Notz, 2015; Hourdin et al., 2017). The different representations of sea ice physics in models could also contribute to inter-model spread. Holland et al. (2010) find that CMIP3 models with thicker Arctic sea ice in the historical period tend to simulate more melt in the 21st century, related to the underlying ice thickness distribution. Keen et al. (2021) evaluate the Arctic sea ice mass budget in CMIP6 models. They do find relationships between, for example, specific melt-pond parameterisation schemes and

surface melt rates, but long-term changes in budget components across models are mostly a function of the mean ice state in response to climate change. This could suggest that physical differences between sea ice components of GCMs are less important than external drivers (i.e., atmosphere and ocean) on timescales relevant to long-term projections.

1.1.3 Multidecadal drivers

The previous section highlighted internal variability as a large contributor to uncertainty in future sea ice projections. But for sea ice extent specifically, what drives that variability? The influence of atmospheric and oceanic variability on that of sea ice has been investigated using observations and models. Using historical and paleoproxy records, Miles et al. (2013) show that Atlantic multidecadal variability (AMV) is strongly connected to variations in Atlantic sea ice extent, and suggest that this relationship is likely relevant to the rate of present-day sea ice loss. This is exhibited by GCMs, which show that positive anomalies in the meridional overturning circulation lead to Arctic sea ice loss via increased OHT (Mahajan et al., 2011; Day et al., 2012). On the other hand, Castruccio et al. (2019) highlight the effect of AMV-associated shifts in the atmospheric circulation on pan-Arctic sea ice loss, which occurs regardless of changes in OHT.

In paleoproxy reconstructions of the Southern Ocean over the last two millennia, repetitive El Niño and persistent positive phases of the southern annular mode (SAM) correlate with negative anomalies in Antarctic sea ice extent on multidecadal timescales (Crosta et al., 2021). Some studies suggest weakening of Southern Ocean convection over recent decades could account for observed increases in Antarctic sea ice (over the period 1979–2012; Zhang et al., 2019), while the sharp decrease since 2016 is mediated by upper ocean warming (Meehl et al., 2019), as a delayed effect in response to positive SAM (Ferreira et al., 2015;

Kostov et al., 2017). Goosse and Zunz (2014) describe how a positive feedback involving a reduction of the vertical oceanic heat flux sustains positive Antarctic sea ice anomalies on decadal and longer timescales in a GCM control simulation.

The ocean thus seems to play a key a role in both hemispheres, suggesting the hypothesis that ocean biases within and/or across models could explain a significant proportion of inter-model spread. There is support for this in some model intercomparison studies. In CMIP3 historical simulations, Mahlstein and Knutti (2011) find a significant anticorrelation between OHT and Arctic sea ice extent across models. They also find that models with larger OHT have larger Arctic amplification in future simulations. A similar result is found for CMIP5 models by Nummelin et al. (2017), while Burgard and Notz (2017) find that future sea ice loss is mainly driven by OHT in about half of a sample of CMIP5 future projections (the other half being mainly driven by net atmospheric surface fluxes). These strongly motivate the need for a deeper understanding of how OHT impacts sea ice and how important it is compared to other processes. The next section describes processes giving rise to OHT in the real world, compares it to atmospheric heat transport (AHT), and discusses previous studies which directly examine the impact of OHT and AHT on sea ice extent.

1.2 Ocean heat transport

1.2.1 Qualitative description

One of the main effects of the ocean circulation in climate is heat redistribution. Meridional OHT arises due to water masses being transported at different depths and/or latitudes with different temperatures (i.e., heat content). Large-scale features of the ocean circulation can then be broadly attributed to OHT. Notably, the AMOC leads to an inter-hemispheric northward heat transport that accounts

for roughly half the Atlantic OHT and roughly a quarter of the global OHT. The rest of the global OHT is primarily effected by the wind-driven gyres of the Atlantic and Pacific Oceans (Boccaletti et al., 2005; Ferrari and Ferreira, 2011).

The effect of OHT interacts with the atmosphere via air–sea fluxes, F_s (positive upwards), which follows from energy conservation:

$$\frac{\partial E_o}{\partial t} + F_s + \text{div OHT} = 0, \tag{1.1}$$

where E_o is the column-integrated ocean heat content and t is time. In other words, anomalous OHT divergence either decreases the local heat content (lowers its temperature) or is balanced by reduced heat loss to the atmosphere via F_s (or both). On long timescales the heat content tendency is small or zero, such that OHT divergence is effectively equivalent to F_s. Forget and Ferreira (2019) take an ocean reanalysis [Estimating the Climate and Circulation of the Ocean (ECCO) version 4; Forget et al. (2015)] and decompose OHT into divergent and rotational parts. The rotational part has, by construction, zero divergence so would drop out in Eq. (1.1). The other, divergent component thus allows the identification of basin contributions to the total meridional OHT, while removing 'heat loops' that are real parts of the ocean circulation but do not ultimately contribute to OHT. The result of their decomposition is reproduced in Fig. 1.3a. The Pacific Ocean is the dominant contribution to OHT and is poleward at all latitudes. Only in the mid northern latitudes does the Atlantic exceed the Pacific (attributable to the Gulf stream), while the Indian Ocean contributes to the poleward heat export in the southern hemisphere. Poleward of 60°N/°S, the majority of heat release occurs in the Pacific sector.

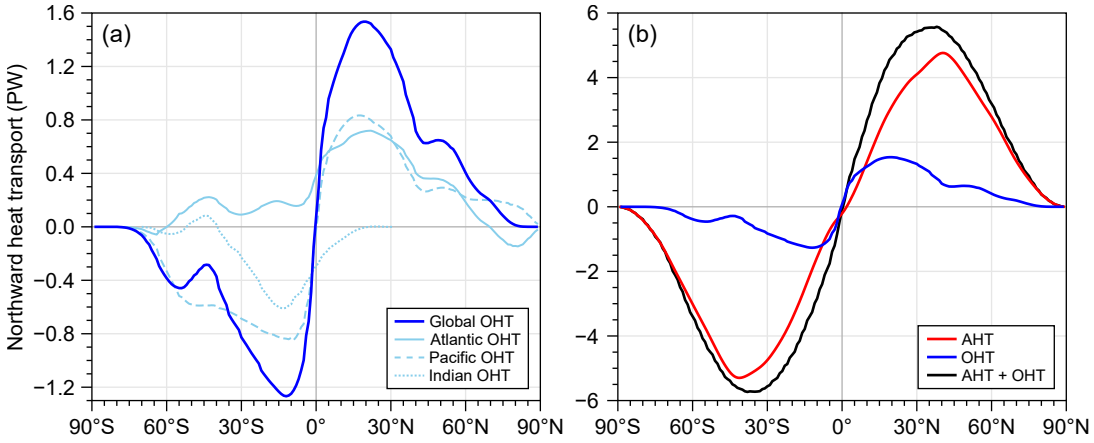

Figure 1.3: Independent estimates of ocean and atmospheric heat transport (OHT and AHT respectively) from reanalyses. (a) Global OHT (thick, dark blue) and basin OHT components (thin, light blue) derived from ECCO version 4 by Forget and Ferreira (2019). (b) The same estimate of global OHT (blue) plotted with AHT (red, derived from ERA-Interim by Liu et al., 2018) for comparison. Both are averaged over 1992–2011. Their sum is shown in black. 1 PW = 10^{15} W.

1.2.2 Comparison with atmospheric heat transport

Net OHT is small compared to AHT, except in the deep tropics where it is the slightly greater contribution to the net meridional heat transport (MHT); see Fig. 1.3b. In the tropics, poleward AHT is primarily driven by the mean meridional overturning circulation of the Hadley cells; in the extratropics transient eddies are the dominant contribution to AHT (Armour et al., 2019). The latitudinal distribution of OHT is significantly skewed, peaking at about 15°N/°S, compared to AHT, which peaks at about 45°N/°S.

Since the atmosphere and ocean are coupled via F_s, the AHT and OHT are not independent. Bjerknes (1964) proposed that if top-of-atmosphere (TOA) fluxes do not change much in steady state, then the total MHT cannot change, and therefore increases in OHT must be balanced by the equivalent decrease in AHT. Due to the sparseness of long-term oceanic observations it is currently difficult to investigate directly whether Bjerknes compensation (BC) occurs in the real world; however, Liu et al. (2020) show that it exists in several different

reanalysis products, and it is exhibited by coupled GCMs (e.g., Outten et al., 2018).

1.2.3 Relationship with sea ice

Extensive evidence exists for the impact of OHT on sea ice. In the classic ocean circulation GCM experiments of Winton (2003), when varying prescribed ocean current strengths by $\pm 50\%$ around $\mp 30\%$ change in sea ice extent occurs, despite compensating responses of comparable magnitude in AHT. An ocean energy budget analysis using the Community Climate System Model (CCSM) carried out by Bitz et al. (2005) showed that OHT convergence (OHTC) ~ 100 W m^{-2} is the main factor controlling the location of the sea ice edge in present-day conditions. Furthermore, they find that in response to CO_2 forcing there is an associated reduction of OHTC following the ice edge, implying that the rate of loss of sea ice is less than would otherwise be expected in a warming climate. In future climate simulations by the CMIP5 EC-Earth model, Koenigk and Brodeau (2014) find that OHT is largely lost to the atmosphere in the Atlantic sector and contributes to atmospheric warming, but direct melting by ocean heat does not occur in the central Arctic. Singh et al. (2017) analysed an updated version of CCSM finding that, in response to doubling CO_2, OHTC shifts poleward, coincident with sea ice retreat. They also highlight the ocean's role in enhancing polar amplification (by heat release warming the high latitudes, as in Koenigk and Brodeau, 2014), and how this is controlled by the partitioning of the total MHT into its atmospheric and oceanic components. Using the CMIP6 version of EC-Earth, Docquier et al. (2021) run perturbed northern hemisphere sea surface temperature experiments and find proportionate reductions in sea ice extent occur via basal melt. Analyses of the large ensemble simulations in the Community Earth System Model (CESM) find that atmospheric effects become more important than oceanic effects when

the sea ice cover is initially smaller (Auclair and Tremblay, 2018; Årthun et al., 2019).

Links between OHT and sea ice are also found in radically different climates of the distant past. In a coupled GCM with idealised land geometry, multiple sea ice states are exhibited, including one with sea ice extending into the mid-latitudes. This exotic state (which could be representative of the last glacial maximum) is stabilised by large OHTC near the ice edge, opposing the albedo feedback and preventing expansion of the ice cover (Ferreira et al., 2011, 2018). Similar results are found in simulations of the Neoproterozoic era ($\sim$ 500 Myr before present). Poulsen and Jacob (2004) identify the wind-driven ocean circulation as a key mechanism preventing global sea ice cover in a coupled-model simulation, while Rose (2015) shows that, in both comprehensive and idealised models, tropical ice caps can be supported by OHTC $\sim$ 100 W m^{-2}—comparable in magnitude to that found in simulations of present-day climate.

There are fewer examples in the literature of links between AHT and ice extent on climatic time and spatial scales. Thorndike (1992) presents an idealised single-column model of sea ice in thermal equilibrium with the atmosphere and a prescribed ocean heat flux. An increase of around 30 W m^{-2} in AHT convergence (AHTC) was sufficient to generate a transition from present-day to perennially-ice-free climate. However, this being a single-column model makes it difficult to infer the impact of AHT on ice extent. Atmospheric heat transport has been identified as a mechanism of polar amplification, although only a significant driver when the sea ice extent is fixed, playing a minor role (in terms of the equilibrium climate response) when the surface albedo feedback is active (Alexeev and Jackson, 2012). Other studies point to the influence of the atmosphere on sea ice extent on interannual timescales through feedbacks associated with enhanced moisture transport in the northern hemisphere (Kapsch et al., 2013; Olonscheck et al., 2019), and via large-scale modes of variability in the southern hemisphere

(Yuan, 2004; Simpkins et al., 2012; Serreze and Meier, 2019).

The question of the relative roles of AHT and OHT in setting sea ice extent has been partially addressed in previous studies. The aforementioned work by Thorndike (1992) found that the ice thickness was about twice as sensitive to basal (i.e., oceanic) than surface (i.e., atmospheric) heating. Eisenman (2012), also using a single-column model but of a different formulation, derived an expression for the enhanced rate of ice growth due to basal versus surface heating in terms of a single climate-feedback parameter, suggesting that the ocean is always a more effective driver of sea ice growth than the atmosphere. Singh et al. (2017, supplemental material) used an atmosphere–ocean box model to show that OHTC is a more effective driver of surface warming than AHTC, although there is no sea ice in their model. However, these results cannot be generalised to the impacts on sea ice extent due to the lack of latitudinal variation in those models.

1.3 Energy Balance Models

Latitudinally-varying energy balance models (EBMs) are highly idealised, zonal-average climate models constructed from simple parameterisations of large-scale physical processes. These include, at minimum: solar radiation, outgoing long-wave radiation (OLR), and net MHT. This basic configuration provides a framework that can be easily expanded with more detailed physics as required. Such conceptual models are useful for understanding the behaviour of the climate system that cannot always be inferred from the complex output of GCMs. This is due to their relative simplicity, such that parameter sensitivity experiments can be rapidly generated and there is scope for analytical relationships to be derived.

Section 1.3.1 provides theoretical background on the EBM framework, an extension of which constitutes a major part of the methodology in this thesis.

The classic diffusive EBM is presented, demonstrating how it can be used to estimate the sensitivity of the ice cap to MHT. This motivates the use of an EBM (with enhanced ocean and sea ice representation) to study the impact of OHT on sea ice extent. Section 1.3.3 then summarises more recent applications of EBMs, both to emphasise their ongoing utility and to identify improvements to EBMs in existing literature required for the purposes of the present work.

1.3.1 The diffusive EBM: formulation

The steady-state, annual-mean climate of one hemisphere is determined by a single variable $T_\mathrm{s}(x)$, the zonal-average, near-surface air temperature as a function of $x = \sin\phi$, where ϕ is latitude. At each latitude, net solar radiation is balanced by OLR and divergence of MHT. Of particular interest here is the MHT being modelled as diffusion of $T_\mathrm{s}(x)$, as implemented by North (1975a). The OLR is approximated as a linear function of $T_\mathrm{s}(x)$, and the net solar radiation is the product of the TOA incident solar radiation, $QS(x)$, and the planetary coalbedo, $a(x, x_\mathrm{i})$, where Q is one quarter of the solar constant,[2] $S(x)$ is the normalised distribution of incident solar radiation, and $x_\mathrm{i} = \sin\phi_\mathrm{i}$ is the location of the ice edge. The EBM is then expressed by the following second-order ordinary differential equation in $T_\mathrm{s}(x)$:

$$\underbrace{-\frac{\mathrm{d}}{\mathrm{d}x}\left[D\left(1-x^2\right)\frac{\mathrm{d}T_\mathrm{s}(x)}{\mathrm{d}x}\right]}_{\text{MHT divergence}} + \underbrace{A + BT_\mathrm{s}(x)}_{\text{OLR}} = \underbrace{QS(x)\,a(x, x_\mathrm{i})}_{\text{solar radiation}}, \tag{1.2}$$

where D is a diffusion coefficient, and A and B are constants. Horizontal heat transfer is given by $-D\nabla T_\mathrm{s}(x)$, the divergence of which evaluates as the first term on the left-hand side (LHS) of Eq. (1.2). North and Coakley (1979) showed

[2] The factor of 4 arises from the ratio of Earth's cross-sectional area normal to the solar flux, πR_E^2, and its irradiated surface area, $4\pi R_\mathrm{E}^2$, where R_E is the Earth radius.

that the real distribution of TOA solar radiation is well approximated by:

$$S(x) = 1 + S_2 P_2(x) \tag{1.3}$$

where P_2 is the degree-2 Legendre polynomial and S_2 is a fitted amplitude. This is shown in Fig. 1.4a, where Eq. (1.3)—with $S_2 = -0.48$ and multiplied by the present-day value of $Q = Q_0 = 340$ W m^{-2}—almost overlaps the observed profile.

The ice edge location, $x_\mathrm{i} = \sin\phi_\mathrm{i}$, is defined by assigning it a temperature $T_\mathrm{i} \equiv T_\mathrm{s}(x_\mathrm{i})$. Besides the albedo effect, there is no sea ice physics in this model, so here x_i is an ice-cap edge representing collectively the zonal-mean extent of ice sheets, sea ice, and the permanent snow line. The dependence of the coalbedo on x_i introduces non-linearity into the system. In its simplest form, the coalbedo is a step function such that $a = a_\mathrm{f}$ for $x < x_\mathrm{i}$ (ice free) and $a = a_\mathrm{i}$ for $x > x_\mathrm{i}$ (ice covered). This extreme transition strongly contributes to the emergence of the small ice cap instability (SICI), where solutions with high ϕ_i are unstable with respect to perturbations in Q (North, 1984). Since the SICI is not robustly exhibited by GCMs (Winton, 2006; Ridley et al., 2008, 2012; Tietsche et al., 2011) and stability is not the focus of this thesis, here the albedo transition across the ice edge is smoothed using the error function:

$$a(x, x_\mathrm{i}) = \frac{a_\mathrm{f} + a_\mathrm{i}}{2} - \frac{a_\mathrm{f} - a_\mathrm{i}}{2}\mathrm{erf}\left(\frac{x - x_\mathrm{i}}{\delta x}\right), \tag{1.4}$$

where δx is a characteristic smoothing scale. This eliminates the SICI (see section 1.3.2) and with appropriate choices of a_i, a_o, and δx, Eq. (1.4) gives a good representation of the net shortwave flux (Fig. 1.4a).

Equation (1.2) is subject to MHT = 0 boundary conditions at the equator ($x = 0$) and pole ($x = 1$), and is then solvable analytically (Held and Suarez, 1974; North, 1975a). The derivation and mathematical details of the solution are

omitted here (it is not relevant to the extended EBM developed in this thesis which must be solved numerically). In short, T_s can be expressed as an infinite series of even-order Legendre polynomials with coefficients depending on the model parameters. The series can be rearranged to express the hysteresis curve, $Q\left(x_\mathrm{i}\right)$ [North (1981) provides a summary of these equations]. It is sufficient to truncate the series at the second-order term (North, 1975b).

Figure 1.4 shows the terms in Eq. (1.2) for a solution comparable to the typical present-day climate. Parameter values are tuned from those of North (1981), by at most a few percent each, to improve the comparison to present-day northern hemisphere conditions as derived from ERA-Interim reanalysis data (Dee et al., 2011) averaged over 2008–2018. The present day zonal-mean sea ice edge is about 71°N, at which the zonal-mean surface temperature is about −5°C (Figure 1.4b), so this is used for T_i rather than −10°C as in North (1981). Figure 1.4b shows that $T_\mathrm{s}\left(\phi\right)$ in this solution of the EBM is a good idealisation of the observed profile.

Figure 1.4c compares OLR in the EBM to the real world. Poleward of about 30°N the distribution is correct, verifying the linear relationship with T_s, although there is an offset of about 10 W m^{-2}. The linearisation of OLR about T_s is originally due to Budyko (1969), who found such a relationship in observations. The relationship does not hold well in the tropics, where deep convective clouds substantially modify the OLR, and this breakdown is apparent in Fig. 1.4c. Outside of the tropics, the linearisation has been shown to be a robust property of the climate valid over the typical range of Earth surface temperatures, arising from a cancelling of the non-linearity of the Stefan–Boltzmann law (i.e., OLR $\sim T_\mathrm{s}^4$) by increased absorptivity of water vapour with temperature (Koll and Cronin, 2018; Zhang et al., 2020). For extratropical applications, it remains a powerful way of simplifying the representation of atmospheric radiation, and has also been used for turbulent and downwelling longwave fluxes in multi-layer EBMs (i.e., with

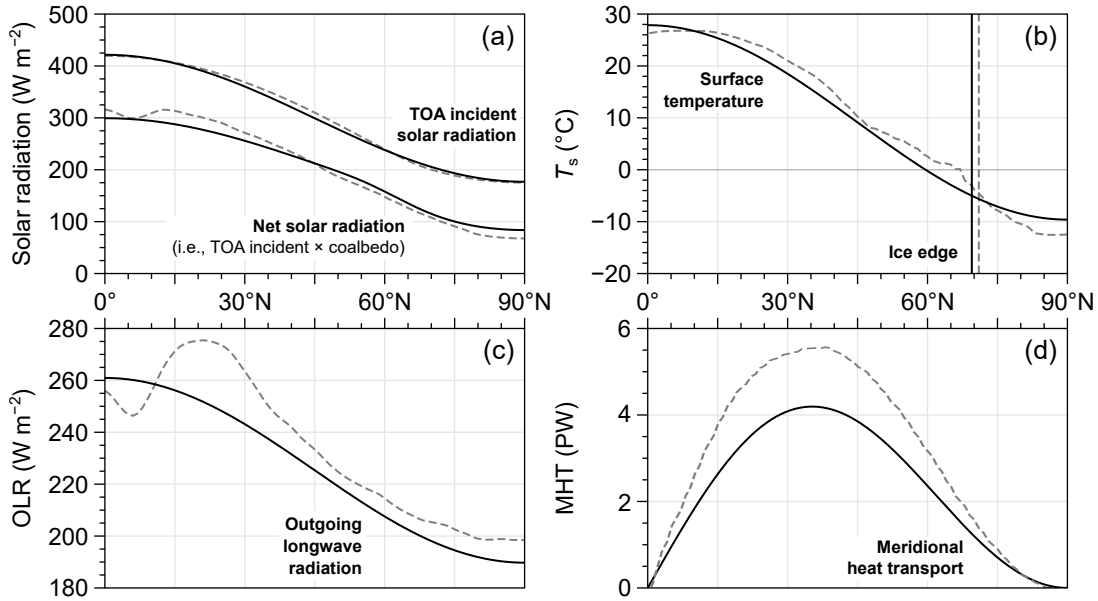

Figure 1.4: A solution of the diffusive EBM with smoothed coalbedo, Eqs. (1.2–1.4). Quantities in the EBM are shown by solid lines, and those for the present-day northern hemisphere state (derived from ERA-Interim, 2008–2018) are shown by dashed lines. (a) Incident solar radiation (upper curves; $Q_0 S$ in the EBM) and net downward solar radiation (lower curves; $Q_0 Sa$ in the EBM). (b) Surface temperature. Vertical lines indicate the ice edge, ϕ_i. (c) Outgoing longwave radiation (OLR; $A + BT_\mathrm{s}$ in the EBM). (d) Meridional heat transport (MHT; 1 PW$= 10^{15}$ W; proportional to $D\nabla T_\mathrm{s}$ in the EBM). Parameter values generating this solution: $Q = Q_0 = 340$ W m^{-2}, $D = D_0 = 0.57$ W m^{-2} °C^{-1}, $A = 208$ W m^{-2}, $B = 1.9$ W m^{-2} °C^{-1}, $a_\mathrm{i} = 0.42$, $a_\mathrm{f} = 0.71$, and $\delta x = 0.1$.

coupled surface and mid-tropospheric temperature profiles; Rose and Marshall, 2009; Rose, 2015).

Although diffusion of temperature is not the real mechanism of MHT, in the extratropics the total MHT is mostly attributed to atmospheric transient eddies which act to macroscopically diffuse heat poleward (Armour et al., 2019). This parameterisation thus produces a good approximation of the MHT at mid–high latitudes, but not in the tropics where the Hadley circulation is the dominant contribution to AHT (Armour et al., 2019) and OHT is comparable in magnitude (Trenberth and Fasullo, 2017), neither of which behave diffusively. This can be seen in Fig. 1.4d: the MHT distribution in the EBM is generally accurate on a hemispheric scale, with a peak of the correct order of magnitude

at the correct latitude (about 35°N). However, the EBM does not reproduce the cross-equatorial transport due to boundary conditions, and the inadequacy of the diffusion parameterisation at low latitudes leads to a smoother, more symmetric profile compared to observations.

1.3.2 The diffusive EBM: insights

Although ice-cap stability is not the theme of this thesis, it is worth a brief description for its historical significance in terms of EBM development, and as demonstration of how such a simple system generates physical insight. By varying Q relative to the default, present-day value Q_0, one or more solutions for the climate state, represented by x_i, can be found. Figure 1.5a shows the resulting curves of $Q\left(\phi_\mathrm{i}\right)$, repeated for various values of D. With respect to variations in Q, solutions are stable if $\partial\phi_\mathrm{i}/\partial Q > 0$ and unstable if $\partial\phi_\mathrm{i}/\partial Q < 0$ (Budyko, 1972; Cahalan and North, 1979). Variation of Q could be interpreted literally as a change in mean solar flux, or as a proxy for the radiative forcing arising due to changing atmospheric composition (such as greenhouse gases or volcanic dust; Sellers, 1969). These curves suggest the existence of multiple equilibria for given Q. For instance, at $Q = Q_0$ and $D = D_0$, Fig. 1.5a shows there are completely ice covered ($\phi_\mathrm{i} = 0$°N), polar ice cap ($\phi_\mathrm{i} \sim 70$°N), and tropical ice cap ($\phi_\mathrm{i} \sim 10$°N) solutions, although the last is unstable. Completely ice free ($\phi_\mathrm{i} = 90$°N) solutions also exist for slightly increased D or Q. If the coalbedo is represented as a step function, the polar ice cap is unstable (thin, grey curves in Fig. 1.5a). This occurs because the albedo feedback is stronger, i.e., the increase in absorbed solar radiation with an increase in Q is proportional to $(a_\mathrm{o} - a_\mathrm{i})$ in the step-function case, whereas in the smoothed case this is reduced by a factor depending on the smoothing scale δx and the functional form of the smoothing (North, 1984). The multiple states hypothesised by the EBM have since been

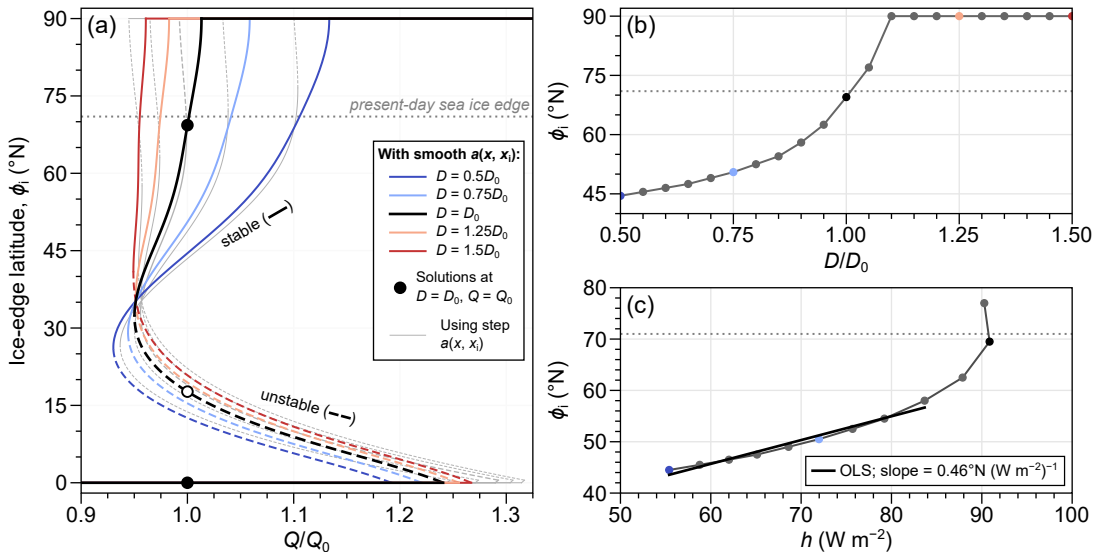

Figure 1.5: (a) Diffusive EBM ice cap hysteresis curves, $\phi_\mathrm{i}\,(Q)$, for various diffusivities, D. Solid (dashed) lines indicate stable (unstable) solutions. Thick curves are solutions using smooth albedo, Eq. (1.4); thin, grey curves are that when the albedo is a step function across the ice edge, producing the small ice cap instability at high latitudes. (b) Stable ϕ_i solutions as a function of D for $Q = Q_0$. (c) ϕ_i as a function of MHT convergence averaged over the ice cap, h, generated by varying D. An ordinary least squares (OLS) regression line to points with $0.5 \leq D/D_0 \leq 0.9$ is fitted, which has slope 0.46°N $(\mathrm{W\ m^{-2}})^{-1}$.

discovered in comprehensive GCMs, including the tropical ice cap solution which is rendered stable by strong OHT counteracting the albedo feedback (Ferreira et al., 2011, 2018; Rose, 2015). The tropical state becomes stable in EBMs when explicit OHT is included (Rose and Marshall, 2009; Rose, 2015).

The $Q\,(x_\mathrm{i})$ curve is strongly sensitive to D at high latitudes, such that the stable ice caps comparable to present-day conditions disappear after about a 10% increase in D (Fig. 1.5b). Increasing D enhances the poleward heat transport efficiency via implicit changes to the processes contained within D—for example, a strengthening of the mean meridional overturning circulation. The retreat of ϕ_i with increased D in Fig. 1.5b therefore implies a sensitivity of the ice cap to the MHT. Figure 1.5c plots the set of stable solutions as a function of h, the MHT convergence averaged over sea ice, as D varies, and suggests that the ice cap edge retreats by about 0.5°N per 1 W $\mathrm{m^{-2}}$ of MHT converging over the ice

pack. This result is limited, mainly because this EBM does not separate MHT into ocean and atmospheric components. This point is addressed in the first part of this thesis, building upon recent studies (discussed in the next section), and ultimately deriving new estimates of this sensitivity to OHT and AHT separately.

1.3.3 EBM variants

An important example of an EBM with extended physics is that of Wagner and Eisenman (2015), who incorporate a simplified single-column sea ice model (Eisenman and Wettlaufer, 2009) and seasonality into that of the diffusive EBM. This introduces sea ice thickness, H_i, renewing the definition of ϕ_i as the minimum latitude where $H_\mathrm{i} = 0$. Also, ϕ_i now specifically represents the sea ice edge, as opposed to the ice cap edge that it was before the introduction of sea ice physics. Further details of this model are given in section 2.1.3, but in short, sea ice is held at the freezing temperature, T_f, at the base, and diffuses heat vertically, with thermal conductivity k_i, assuming a linear variation in temperature up to the surface (T_s). The EBM is still one-dimensional, but requires a representation of OHT to enable sea ice basal melt. This is achieved by introducing a constant, uniform OHTC, denoted F_b ("basal flux"; Fig. 1.6a). The purpose of this model was to demonstrate that seasonality and MHT strongly influence sea ice stability, bridging the gap between low-order EBMs and high-order GCMs. Although it did not matter in this particular application, in general the representation of OHTC as a constant, F_b, is crude, because it does not represent the real-world meridional structure of OHT (Fig. 1.3a) and is a global heat source. Variation of F_b is therefore likely to overestimate the sensitivity of the sea ice cover to OHT. The result of varying F_b in this model is shown in Fig. 1.6b—indeed, the slope of the annual mean ϕ_i versus F_b is about four times larger than that in the standard diffusive EBM (Fig. 1.5c).

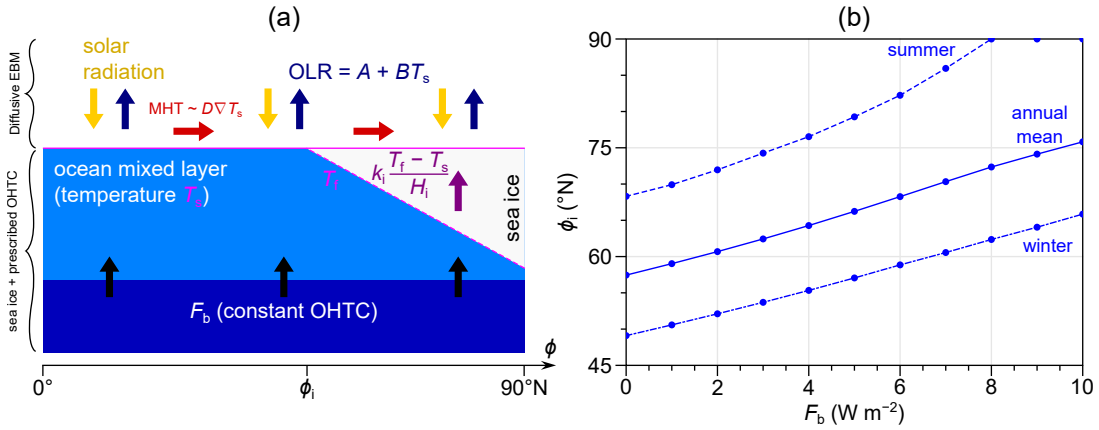

Figure 1.6: (a) Schematic of the 1D diffusive EBM (top) with added sea ice thickness, H_i, and prescribed OHTC, F_b (bottom) of Wagner and Eisenman (2015; adapted from their Fig. 1). Additional parameters are the ocean freezing temperature, T_f, and sea ice thermal conductivity, k_i. (b) Sensitivity of ϕ_i to F_b in this model.

Rose and Marshall (2009) explored a series of EBM extensions with increasingly complex representations of OHT, starting from a two-layer diffusive model (i.e., separate diffusive heat transport for the atmosphere and ocean), and ending with a complex parameterisation of the wind-driven gyres in an interactive energy–momentum balance model. These models all demonstrate the importance of OHT in maintaining sea ice cover. For example, the first model does not allow a tropical sea ice edge because the diffusive parameterisation leads to a broad OHT distribution like that in Fig. 1.4d (which is not realistic for OHT), whereas the more complex models with gyre parameterisation do. They also found that the inclusion of dynamics is not needed for the mechanism in which OHT maintains the sea ice cover. These variants do not include sea ice thickness. Rose (2015) used, effectively, the EBM of Wagner and Eisenman (2015) but allowed F_b to depend on ϕ, with a functional form better representing the real-world distribution of OHT (in particular, with a peak in the tropics rather than mid-latitudes). However, here the OHT and AHT do not interact (since OHT is prescribed).

Examples of recent EBM applications in other contexts include Hwang and Frierson (2010), who use a modified version of Eq. (1.2) representing transport

of atmospheric moist-static energy (by allowing the gradient term in Eq. 1.2 to depend on specific humidity as well as temperature), to interpret CMIP3 inter-model spread in future poleward AHT. A similar model has been used to study Bjerknes compensation—essentially by imposing OHT as a perturbation and examining the AHT response—developing expressions relating the rate of compensation to the climate feedback parameter (Liu et al., 2016, 2018). Roe et al. (2015) show that the EBM captures the surface temperature response to local climate feedbacks as simulated by GCMs, enabling the attribution of tropical-feedback uncertainty across GCMs to the global surface temperature uncertainty, while polar feedbacks mostly affect the regional uncertainty. Finally, Siler et al. (2018) add a parameterisation for the Hadley circulation to the EBM, and use it to explain how spatial variations in factors such as radiative feedbacks and ocean heat uptake contribute to GCM biases in the hydrological-cycle response to climate change.

1.3.4 Limitations and summary

This section has given an overview of the EBM framework, demonstrating that it is capable of mimicking the real world climate and generates useful physical insight. Given that they address the large-scale climate, work better in polar regions, and naturally incorporate MHT and ice extent (through ϕ_i), the suitability of an EBM for investigating the impact of OHT on sea ice extent is clear. Many of the principles described in this section—such as the OLR parameterisation and use of parameter sensitivities to modify heat transport—are applied in the implementation (chapter 2) and analysis (chapter 3) of a new EBM in the first part of this thesis.

While the EBM approach has major advantages, particularly in reducing a complex problem down to the essential physics, there are some limitations

which should be acknowledged. Simple examples include that EBMs are not well suited to smaller spatial- and time-scale processes, and can rapidly become too complex (defeating their purpose) if zonal variation needs to be explicitly accounted for (e.g., with the addition of land). They require, upfront, a choice of what physical processes need to be included, and how to effectively parameterise them. There is also a limit in relating their behaviour to the real world: although Fig. 1.4 shows that the classic EBM is able to reproduce typical climate metrics, this does not necessarily mean that, for instance, the sensitivity in Fig. 1.5c is realistic. In that example, an estimate of the sensitivity derived from observations would be required for comparison; but in this context, this is hindered by limited long-term ocean observations. In this thesis, some of these limitations are easily worked around: for example, constructing a new EBM by combining previous works in which various parameterisations have already been devised and tested against observations (in chapter 2, such analyses are also updated using more recent observations). Although land is particularly important for Arctic sea ice (section 1.1.1), it is undesirable to complicate the EBM by adding land. Instead, the reverse approach is taken: land is effectively removed from observations and GCM output by using a using a specific sea ice-edge diagnostic which only includes areas where sea ice can freely move meridionally (see sections 2.3.3 and 4.1.2; the latter also assesses this diagnostic against more conventional measures of sea ice cover).

1.4 Research aims and thesis outline

1.4.1 Research questions

The overarching aim of this thesis is to improve our understanding of the relationship between OHT and sea ice. Focus is on the large spatial scale (i.e., global

OHT and response of the Arctic or Antarctic sea ice cover as a whole), and the long, multidecadal timescale—particularly relevant to long-term climate projections (Fig. 1.1) and the expected sea ice response to OHT changes (section 1.2.3). The specific aims are expressed via three research questions:

1. **What sets the sensitivity of sea ice to OHT?**

   The first part of this thesis seeks to understand what factors control the sensitivity of sea ice to OHT on multidecadal timescales, and compare it to other processes—particularly, AHT. Such insights are a step toward understanding the role of heat transport biases in the spread of sea ice extent in coupled GCMs, by providing a theoretical framework to interpret emergent model trends in terms of physical processes.

2. **What is the relationship between unforced variability in OHT and sea ice in GCMs?**

   To better understand what role the ocean might play in sea ice uncertainties in coupled GCMs, an evaluation of the relationship between the ocean and sea ice in the latest generation of models is required. Previous studies have used sensitivity experiments or rely on rising-emissions simulations, and frequently emphasis is placed on the Arctic (section 1.2.3). As such, these describe a forced response of sea ice to OHT (and not addressing the direct effect of OHT in the case of global-warming experiments). Here, the impact of natural variability in OHT on both Arctic and Antarctic sea ice is investigated: what are the associated physical mechanisms, and how consistently is this exhibited by different models? Due to the contrasting oceanic settings, it is reasonable to suppose that such mechanisms may differ between the two hemispheres (section 1.1.1). By eliminating the influence of external forcing, these results can also be used as a 'baseline' for comparison of the sea ice response in future-climate simulations.

3. **To what extent does OHT explain uncertainties in future projections of sea ice?**

   Previous studies have shown that there is a relationship between present-day OHT and Arctic sea ice extent in previous-generation models (Mahlstein and Knutti, 2011). However, the existence of a similar relationship in the southern hemisphere, and the contribution of OHT to future sea ice losses, remain open questions. This work seeks to establish whether there is a relationship between future ice loss and OHT changes, within and across models, in both hemispheres. To further our physical understanding of this, the results of question (1) are applied to determine what factors set such relationships. Furthermore, it is investigated whether the basic mechanisms identified in question (2) are applicable, or modified, under the influence of external forcing.

1.4.2 Methodology

Question (1) is addressed using an EBM which, as discussed in section 1.3, first requires the formulation of a new EBM by combining elements from existing work. The EBM is used to estimate the sensitivity of sea ice to OHT, compare it to that of AHT, and generate simple equations describing the sea ice sensitivity to OHT. This yields physical insight into the factors setting the sensitivities and provides tools for the analysis of GCMs.

Analysis of CMIP6 PI-control simulations addresses question (2), in which the impact of natural variations in OHT on sea ice extent in both hemispheres is assessed. Simple diagnostics analogous to EBM quantities are used, which assists the physical interpretation of model behaviour and simplifies the analysis. It is beyond the scope to explain causes of variation in OHT itself (e.g., in terms of specific circulation changes), but this approach facilitates a large number of

models to be analysed, giving an indication of the robustness of the results across models of different resolutions and configurations.

The historical and Tier 1 ScenarioMIP simulations (Fig. 1.1) are investigated for question (3), as these are our most recent estimates of plausible future climate change and contain the uncertainties which are of most societal relevance. They also allow the determination of whether the magnitude of external forcing influences the results. Finally, it is tested whether the physical framework of the EBM captures the behaviour seen in coupled GCMs.

1.4.3 Thesis outline

The rest of this thesis is structured as follows. Chapter 2 describes the formulation of a new EBM, and demonstrates that it improves the representation of OHT and its interaction with sea ice compared to previous work. This EBM is then used to carry out sensitivity studies on the various parameters, generating theoretical insight into processes controlling the latitude of the sea ice edge and the relative impacts of ocean and atmospheric heat convergence (chapter 3). Next is the analysis of coupled GCMs, starting with the PI-control simulations of 20 CMIP6 models in chapter 4, which investigates the mechanisms underlying the impact of natural variability in OHT on sea ice. In chapter 5, analysis of the historical and ScenarioMIP experiments sheds light on the significance of the OHT–sea ice relationship to uncertainty in future-climate projections. Finally, chapter 6 brings all results together in a summary, implications and limitations are discussed, and avenues for further research are given.

This page intentionally left blank.

Chapter 2

A new energy balance model

This chapter presents a novel EBM which forms the foundation of results generated in this thesis. Processes represented and the defining prognostic equations are described in section 2.1. The implementation and testing of the model is given in section 2.2, and the default parameter values giving a suitable reference state are shown in section 2.3. This chapter is adapted from published work (Aylmer et al., 2020, material rearranged from section 2, appendix A, and online supplemental material).

2.1 Formulation

In essence, this model combines those of Eisenman and Wettlaufer (2009), Rose and Marshall (2009), and Rose (2015), with some additional improvements. The time, t, evolution of three temperature profiles, $T_{\mathrm{a}}(\phi, t)$, $T_{\mathrm{s}}(\phi, t)$, and $T_{\mathrm{ml}}(\phi, t)$, representing the atmosphere, surface, and ocean mixed layer respectively, and sea ice thickness, $H_{\mathrm{i}}(\phi, t)$, are determined by vertical energy fluxes and meridional heat transport convergence. All variables and heat fluxes represent zonal averages as a function of latitude, ϕ. The domain is one hemisphere ($0° \leq \phi \leq 90°\mathrm{N}$) and the system is subject to zero-horizontal-flux boundary conditions at the equator

and pole. The ice-edge latitude, $\phi_\mathrm{i}(t)$, is the lowest latitude containing a non-zero ice thickness. The heat fluxes between each model component, described in sections 2.1.1–2.1.3, are shown schematically in Fig. 2.1.

2.1.1 Atmosphere

The atmosphere is represented by a single 'layer' with temperature $T_\mathrm{a}(\phi, t)$, which evolves according to the net energy flux into the atmospheric column at each latitude:

$$C_\mathrm{a}\frac{\partial T_\mathrm{a}}{\partial t} = -\nabla \cdot F_\mathrm{AHT} + F_\mathrm{up} - F_\mathrm{dn} - F_\mathrm{OLR}, \tag{2.1}$$

where C_a is the (constant) atmospheric column heat capacity, F_AHT is the AHT per unit zonal distance, F_up and F_dn are upward and downward components of air–sea surface fluxes respectively, and F_OLR is the OLR (Fig. 2.1). AHT is parameterised as diffusion down the mean temperature gradient: $F_\mathrm{AHT} = -K_\mathrm{a}C_\mathrm{a}\nabla T_\mathrm{a}$, where K_a is a large-scale diffusivity for the atmosphere. The AHTC is then given by $-\nabla \cdot F_\mathrm{AHT}$.[1] This represents the net atmospheric moist-static energy transport, AHT—there is no separation of dry and moist transports in this model as this work is not concerned with the specific circulations that give rise to a certain heat transport.

The surface fluxes F_up and F_dn are bulk representations of the combined radiative, latent, and sensible heat fluxes (the latter two are contained within F_up only). These are parameterised as linear functions of the surface and air temperatures, respectively:

$$F_\mathrm{up} = A_\mathrm{up} + B_\mathrm{up}T_\mathrm{s} \tag{2.2}$$

[1] In the EBM coordinate system, the gradient of an arbitrary scalar d is given by $\nabla d = R_\mathrm{E}^{-1}\partial d/\partial\phi$, where R_E is the mean Earth radius, and the divergence of an arbitrary vector $\mathbf{d}$ is given by $\nabla \cdot \mathbf{d} = (R_\mathrm{E}\cos\phi)^{-1}\partial(d\cos\phi)/\partial\phi$.

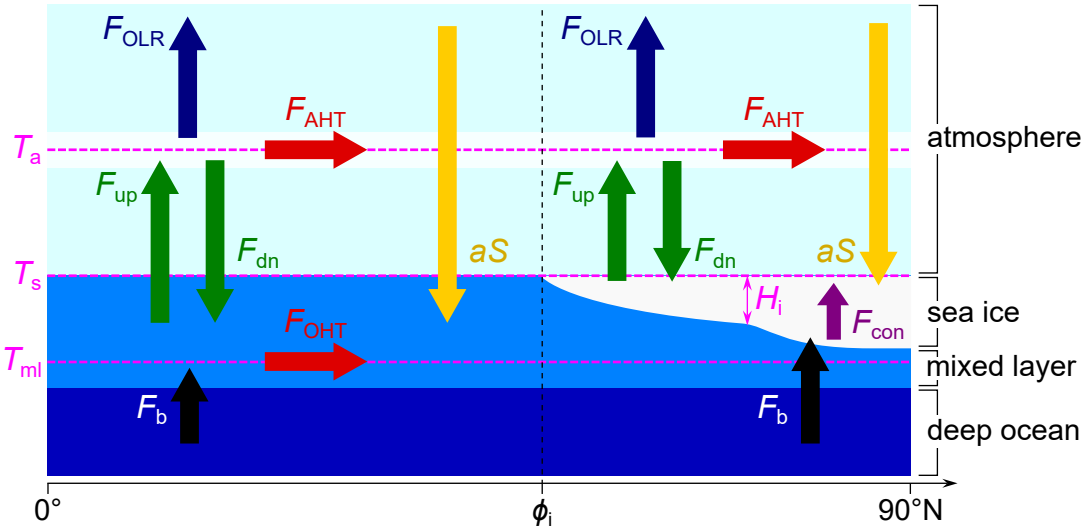

Figure 2.1: The EBM represents the climate system by an atmospheric 'layer' with temperature $T_a(\phi)$, an ocean mixed layer with temperature $T_{ml}(\phi)$, sea ice of thickness $H_i(\phi)$ and surface temperature $T_s(\phi)$ (pink), and a deep ocean layer with prescribed OHTC, $F_b(\phi)$. The ice-edge latitude is denoted ϕ_i. Vertical arrows represent zonally-averaged heat fluxes between components: absorbed solar radiation, $aS(\phi, t)$; outgoing longwave radiation, $F_{OLR}(T_a)$; upward and downward air–sea surface fluxes, $F_{up}(T_s)$ and $F_{dn}(T_a)$; and conduction through sea ice, $F_{con}(H_i, T_s)$. Horizontal arrows represent meridional heat transports in the atmosphere (F_{AHT}) and ocean mixed layer (F_{OHT}).

$$F_{dn} = A_{dn} + B_{dn}T_a. \tag{2.3}$$

Similarly, F_{OLR} is expressed as:

$$F_{OLR} = A_{OLR} + B_{OLR}T_a. \tag{2.4}$$

The A and B parameters in Eqs. (2.2–2.4) are constants. The Bs represent net climate feedbacks (e.g., Planck and water-vapour feedbacks). In particular, $1/B_{OLR}$ is approximately the climate-sensitivity parameter of the EBM (i.e., the global-average surface temperature change per unit TOA radiative forcing; see section 3.1.1). Spatial variations in the Bs are neglected for analytic simplicity (which is a reasonable approximation: see section 2.3.2). This formulation means that the atmosphere is implicitly opaque to surface upwelling longwave radiation,

because F_{OLR} does not have explicit T_{s} dependence. Transmission of such fluxes through the atmosphere contribute less than 10% of the net OLR (Costa and Shine, 2012) so this is a reasonable idealisation.

Following Rose and Marshall (2009), solar radiation is assumed to be absorbed entirely at the surface, making use of the planetary albedo, hence the absence of a radiative driving term in Eq. (2.1). Although atmospheric absorption is not negligible (Valero et al., 2000), this is a simplification which eliminates the need to handle surface and atmospheric reflections separately.

2.1.2 Ocean mixed layer

The prognostic equation for the ocean mixed-layer temperature T_{ml} is given by:

$$C_{\mathrm{o}}\frac{\partial T_{\mathrm{ml}}}{\partial t} = aS + (F_{\mathrm{b}} - \nabla \cdot F_{\mathrm{OHT}}) + F_{\mathrm{dn}} - F_{\mathrm{up}}, \tag{2.5}$$

which applies at latitudes where ice is not present, $\phi < \phi_{\mathrm{i}}(t)$. Here, the mixed-layer column heat capacity $C_{\mathrm{o}} = c_{\mathrm{o}}\rho_{\mathrm{o}}H_{\mathrm{ml}}$, with c_{o}, ρ_{o} and H_{ml} the ocean specific heat capacity, density, and mixed-layer depth, respectively, taken to be constants. Absorbed solar radiation is the product of the planetary coalbedo, a, and the incident solar radiation, S. The total OHTC is given by contributions from the mixed layer, $-\nabla \cdot F_{\mathrm{OHT}}$, and the deep ocean, F_{b} [section 2.1.2(b)]. For latitudes where ice is present, $\phi \geq \phi_{\mathrm{i}}(t)$, T_{ml} is fixed at the freezing temperature, T_{f} (which is constant: salinity variations are neglected). If Eq. (2.5) produces a temperature $T_{\mathrm{ml}} > T_{\mathrm{f}}$ for $\phi \geq \phi_{\mathrm{i}}$, T_{ml} is reset to T_{f} and the surplus energy is used to melt sea ice: by this mechanism, the mixed layer can directly melt ice just poleward of the ice edge. How this is done in practice is described in section 2.2.

(a) Absorbed solar radiation

The planetary coalbedo takes a constant value a_i where sea ice is present ($\phi \geq \phi_\mathrm{i}$), a spatially-varying value $a_\mathrm{o}(\phi) > a_\mathrm{i}$ over open ocean ($\phi < \phi_\mathrm{i}$), and the transition across the ice edge is smoothed over a characteristic latitude scale $\delta\phi$ using the error function:

$$a(\phi, \phi_\mathrm{i}) = \frac{a_\mathrm{o}(\phi) + a_\mathrm{i}}{2} - \frac{a_\mathrm{o}(\phi) - a_\mathrm{i}}{2} \mathrm{erf}\left(\frac{\phi - \phi_\mathrm{i}}{\delta\phi}\right), \tag{2.6}$$

where

$$a_\mathrm{o}(\phi) = a_0 - a_2\phi^2. \tag{2.7}$$

Note that $a(0°) \approx a_0$ and $a(90°\mathrm{N}) \approx a_\mathrm{i}$, both tending to equality in the limit $\delta\phi \to 0$. The parameter a_2 roughly accounts for geometric factors (i.e., the change in angle of incidence of solar radiation) and typical changes in cloud distribution that reduce the planetary coalbedo at higher latitudes. Equations (2.6) and (2.7) are motivated by previous idealised albedo formulas (e.g., Wagner and Eisenman, 2015) but here are expressed in terms of ϕ instead of $\sin\phi$. There is no physical motivation for the specific functional form, although Eq. (2.7) could be thought of as a Taylor expansion truncated at the quadratic term and dropping the linear term for the sake of hemispheric symmetry. Figure 2.2a shows that this gives a good representation of the typical real-world zonal-average planetary coalbedo, as determined from ERA-Interim. Although including higher-order terms may improve the fit, this would sacrifice simplicity and resemblance with previous studies.

Typically, EBMs use an idealised analytical function for the TOA incident solar radiation, $S(\phi, t)$, such as the series expansion:

$$S(x,t) = S_0 + S_1 \cos(2\pi t)\, P_1(x) + [S_2 + S_{22} \cos(4\pi t)]\, P_2(x), \tag{2.8}$$

from North and Coakley (1979), where $x = \sin\phi$, P_n are Legendre polynomials and S_n are fitted amplitudes. This is analogous to Eq. (1.3) but includes the seasonal cycle. The time-dependent part was found to be a poor fit, particularly at high latitudes. Since an analytic expression for S is not required, the present EBM is forced with an accurate dataset of daily-mean insolation, generated using the program of Huybers (2016). Figure 2.2b shows S from this data set at various times, compared to S from Eq. (2.8). Although the annual mean is a reasonable fit (as already shown in section 1.3.1), at some times Eq. (2.8) gives unphysical $S < 0$ (e.g., in winter; Fig. 2.2b) and the error can be several tens of W m^{-2} (e.g., in Autumn at high latitudes; Fig. 2.2b).

(b) Ocean heat transport

Unlike for the AHT, a purely diffusive parameterisation does not well represent the observed OHT (Rose and Marshall, 2009; Ferreira et al., 2011). A purely prescribed OHT is also not appropriate because the ocean must interact dynamically with the atmosphere and sea ice. Additionally, it is worth keeping in mind that Arctic and Antarctic sea ice are likely to respond differently to OHT variation, because of oceanographic differences between the Arctic and Southern Oceans (section 1.1.1). The interpretation of EBM behaviour is mainly kept 'hemisphere-neutral' in chapter 3 before more insight is gained in chapter 4, but it is wise to equip the EBM with means to directly vary ocean–ice fluxes and, separately, to increase OHT at lower latitudes without substantially modifying direct ocean–ice fluxes. Therefore, a combination of the two approaches is used: a prescribed part, represented by its convergence, $F_\mathrm{b}(\phi)$, and an interactive part, $F_\mathrm{OHT} = -K_\mathrm{o} C_\mathrm{o} \nabla T_\mathrm{ml}$, where K_o is a large-scale ocean diffusivity. The F_OHT component is not meant to represent a mixed-layer OHT but may be loosely interpreted as an upper OHT which responds to and drives changes in surface fluxes, and for simplicity is parameterised as a function of T_ml. The prescribed part,

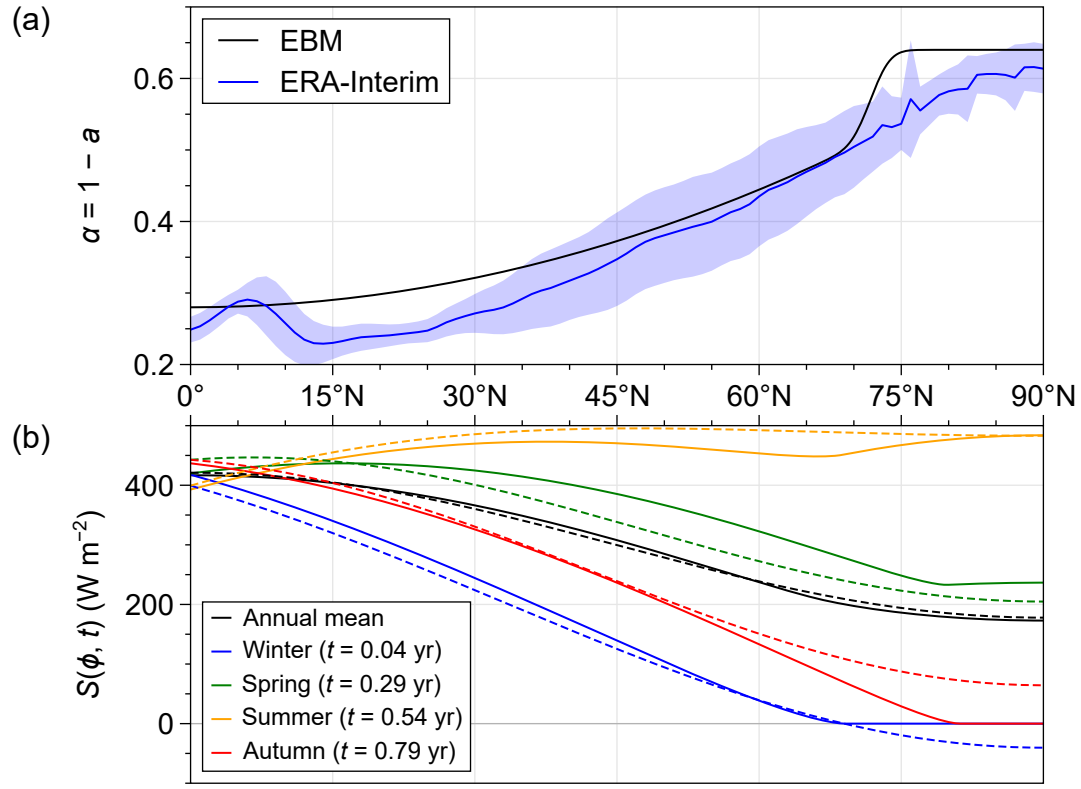

Figure 2.2: (a) Planetary albedo, $\alpha = 1 - a$, derived from ERA-Interim TOA shortwave flux data for 2010: the annual mean is shown by the blue line and the standard deviation is shown in the pale-blue shading. The EBM profile (i.e., one minus Eq. 2.6 with standard parameter values as given in Table 2.1) is also shown (black). (b) Top-of-atmosphere incident solar radiation, S, from the dataset used in the EBM (solid) and according to Eq. (2.8) (dashed), at various times throughout the seasonal cycle. The parameters $S_0 = 340$, $S_1 = -271$, $S_2 = -162$, and $S_{22} = 50$, all in W m^{-2}.

F_b, encapsulates the effects of the wind-driven gyres and meridional overturning circulation. Note that since OHT will be varied by adjusting its underlying parameters $\{p\}$, F_b must not represent a net heat source, i.e.,

$$2\pi R_\mathrm{E}^2 \int_0^{90^\circ} F_\mathrm{b}\left(\phi, \{p\}\right) \cos\phi \, \mathrm{d}\phi = 0. \tag{2.9}$$

Due to boundary conditions, the OHTC associated with F_OHT automatically satisfies Eq. (2.9).

The analogous quantity to F_b in many previous studies is taken to be a constant, which does not satisfy Eq. (2.9). Rose (2015) uses an EBM with prescribed

total OHTC (originally from Rose and Ferreira, 2013) for which the associated OHT is more consistent with observations, given by

$$f(\phi) = -\frac{\psi}{2\pi R_{\mathrm{E}}^2} \cos^{2N-2}\phi \left[1 - (2N+1)\sin^2\phi\right], \tag{2.10}$$

where ψ is a constant and $N \geq 1$ is an integer. This satisfies Eq. (2.9) for any ψ and N, but it also decays rapidly to zero at high latitudes for $N > 1$. To satisfy the requirements described above, F_{b} in the present EBM is set as:

$$F_{\mathrm{b}}(\phi) = f(\phi) + F_{\mathrm{bp}} g(\phi), \tag{2.11}$$

where F_{bp} (W m^{-2}) is an adjustable parameter and

$$g(\phi) = \frac{1 - 3\cos 2\phi}{4}, \tag{2.12}$$

which is just Eq. (2.10) with $N = 1$ and normalised. This gives a broad hemispheric-scale transport with maximum convergence at the pole. A schematic plot of the two components of F_{b}, Eqs. (2.10) and (2.12), is shown in Fig. 2.3. For any choice of F_{bp}, which is the value of F_{b} at the pole, Eq. (2.9) is satisfied. The analytic functions $f(\phi)$ and $g(\phi)$ are left fixed, while F_{bp} is varied. This allows the mean ocean–ice basal flux to be directly changed; specifically, $F_{\mathrm{bp}} g(\phi)$ can be thought of as a perturbation to a background state $f(\phi)$ which redistributes a relatively small amount of tropical OHTC into high latitudes.

Globally, F_{b} and $\nabla \cdot F_{\mathrm{OHT}}$ contribute roughly equally to the total OHT, with the former dominating in the tropics and polar latitudes and the latter dominating in the mid-latitudes. This effective partitioning, which depends on the choice of ocean parameters, is somewhat arbitrary, but unimportant because it is only the total OHT which matters and there is no attempt to attribute a certain OHT(C) to a specific circulation. Ultimately this does not have a significant impact on

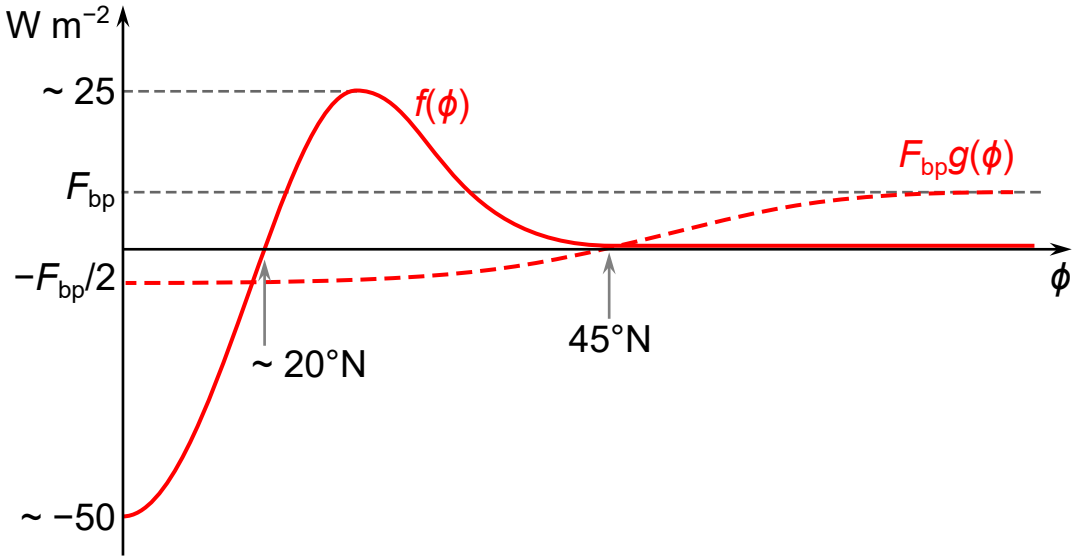

Figure 2.3: Schematic of components and typical magnitudes of the prescribed deep ocean heat transport convergence, $F_b(\phi)$; see Eq. (2.11). For $\phi < 45°$N, F_b is dominated by $f(\phi)$ (Eq. 2.10, solid), which sets the peak heat transport at around 20°N. This component decays rapidly to zero at high latitudes, where F_b is dominated by $F_{bp}g(\phi)$ (Eq. 2.12, dashed). In the reference state, $F_{bp} = 2$ W m^{-2}. The position of the zero in $f(\phi)$ is determined by N (here $N = 5$).

the results (see the end of section 3.2.3).

2.1.3 Sea ice

The simplified sea ice model of Eisenman and Wettlaufer (2009) makes up the sea ice component of the EBM, which is derived from the more complex thermodynamic sea ice model of Maykut and Untersteiner (1971) after making a number of idealisations. A summary of this is given here. Changes in latent heat content associated with melting and freezing are assumed to dominate changes in sensible heat content, such that the net energy content of ice at each latitude is $-L_f H_i$, where L_f is a bulk latent heat of fusion of sea ice. Salinity variations, snow, and shortwave penetration are neglected. The surface of ice in contact with the ocean is assumed to remain at the freezing temperature T_f. The temperature within the ice is assumed to vary linearly with depth, such that there is uniform vertical

conduction of heat given by:

$$F_{\text{con}} = k_{\text{i}} \frac{T_{\text{f}} - T_{\text{s}}}{H_{\text{i}}}, \tag{2.13}$$

where k_{i} is a bulk thermal conductivity of sea ice. The surface temperature (at the ice–air interface) is determined by first calculating a 'diagnostic' temperature T_{d}, which is the surface temperature required for the top-surface heat balance to be zero, i.e.,

$$k_{\text{i}} \frac{T_{\text{f}} - T_{\text{d}}}{H_{\text{i}}} = A_{\text{up}} + B_{\text{up}} T_{\text{d}} - F_{\text{dn}} - aS. \tag{2.14}$$

If $T_{\text{d}} > T_{\text{m}}$, where T_{m} is the melting temperature, this implies surface melt, which occurs at the melting temperature so $T_{\text{s}} = T_{\text{m}}$. Otherwise $T_{\text{d}} \leq T_{\text{m}}$, which is allowed:

$$T_{\text{s}} = \begin{cases} T_{\text{m}} & T_{\text{d}} > T_{\text{m}} \\ T_{\text{d}} & T_{\text{d}} \leq T_{\text{m}}. \end{cases} \tag{2.15}$$

In Eisenman and Wettlaufer (2009), $T_{\text{m}} = T_{\text{f}}$; here this assumption is relaxed. Typical salinities at the top ice surface are much lower than the underlying ocean (due to brine rejection and drainage), such that the melting temperature is closer to the freshwater value. This improves the comparison of typical ice thicknesses in the EBM to observational estimates for the Arctic (shown in section 2.3.3).

Top-surface melt and the bottom-surface melt/growth rates are implied by the imbalance of fluxes at the respective surfaces, but the evolution of the ice thickness only depends on the net energy input to the column:

$$-L_{\text{f}} \frac{\partial H_{\text{i}}}{\partial t} = aS + F_{\text{b}} + F_{\text{dn}} - F_{\text{up}}. \tag{2.16}$$

The surface temperature diagnostic, Eqs. (2.14) and (2.15), and the ice-thickness prognostic, Eq. (2.16), together describe the sea ice component of the EBM. These equations apply where $\phi \geq \phi_{\text{i}}(t)$. Where ice is not present, the surface

temperature is equal to the mixed-layer temperature.

2.2 Implementation

The EBM is determined by the three prognostic Eqs. (2.1), (2.5), and (2.16) and the surface-temperature diagnostic Eq. (2.15). The time-dependent vertical heat fluxes are approximated as constants over time step Δt (i.e., T_a, T_ml, T_s, and H_i at $t = (n+1)\Delta t$ are solved subject to fluxes calculated at $t = n\Delta t$). The spatial discretisation of the divergence terms in Eqs. (2.1) and (2.5) is handled using the partial differential equation solver `pdepe()` of MATLAB. Equation (2.16) is solved using a simple first-order forward time stepping routine, at each latitude. Although it imposes a time-step restriction for numerical accuracy, this is a simple approach to handling the non-smoothness at the ice edge and the model is computationally cheap to run anyway.

Equations (2.5) and (2.16) apply to open-ocean and ice-covered latitudes, respectively. The ice edge $\phi_\mathrm{i}(t)$ evolves as either open ocean freezes (T_ml falls below T_f) or ice retreats (H_i falls to zero at the edge). In practice, as the system is solved numerically, a correction is applied at the end of each time step to update ϕ_i. If $T_\mathrm{ml} < T_\mathrm{f}$ at any latitude (freezing has occurred), the ice thickness there is increased by $\Delta H_\mathrm{i} = C_\mathrm{o}(T_\mathrm{f} - T_\mathrm{ml})/L_\mathrm{f}$ and T_ml is reset to T_f. Similarly, if $H_\mathrm{i} < 0$ at any latitude (heat in excess of that required to completely melt the ice has converged at that latitude), the mixed-layer temperature is increased by $\Delta T_\mathrm{ml} = -L_\mathrm{f} H_\mathrm{i}/C_\mathrm{o}$ and H_i is reset to zero.

2.2.1 Test of implementation

Averaging over the seasonal cycle, steady-state solutions to the EBM should have zero net TOA flux. This provides a simple test that the EBM has been imple-

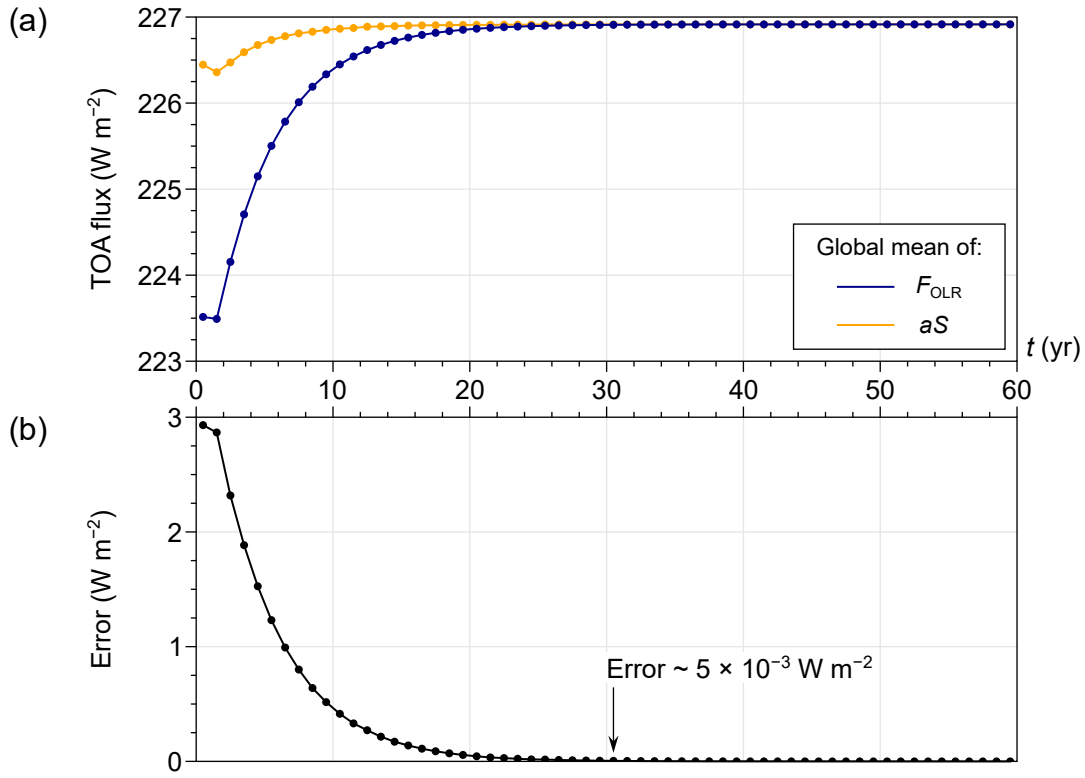

Figure 2.4: (a) Global-mean OLR (blue) and net solar radiation (orange), annually-averaged, in a 60 yr spin-up simulation of the EBM starting from arbitrary initial conditions with default parameters at $t = 0$. (b) Difference between the curves in (a).

mented correctly and is used to identify a suitable spin-up time for sensitivity experiments. Starting from a set of arbitrary initial conditions, and with parameters set to the defaults listed in Table 2.1, a 60 yr spin-up simulation was run. For this and all EBM simulations generating results in this thesis, the time step $\Delta t = 0.5$ days and grid resolution $\Delta\phi = 0.25°$N, as a balance between well resolving changes in the ice-edge latitude and reasonable computation time. The global-mean F_{OLR} and net shortwave radiation, aS, are plotted in Fig. 2.4a.

After about 30 yr the net TOA flux is sufficiently close to zero to consider the system to be in equilibrium: the flux imbalance is about 5×10^{-3} W m^{-2} (Fig. 2.4b). At $t = 60$ yr, this reduces by another order of magnitude. In practice, simulations are not initiated from an arbitrary state, but rather from a saved previous simulation in which the system had reached equilibrium, and then

a small adjustment to a parameter is made. Therefore, 30 yr is ample spin-up time for the sensitivity experiments (chapter 3).

2.3 Reference state

The reference state is the steady-state solution to the EBM in the default parameter space. This reference state is tuned to the present-day northern hemisphere and forms the starting point about which to vary parameters in sensitivity experiments. The ability of the EBM to reproduce typical climate metrics also serves as model validation. In section 2.3.1, brief justifications of default parameter values are given, and in section 2.3.2 the derivation of the A and B atmospheric radiation parameters (Eqs. 2.2–2.4) is described in more detail. Finally, section 2.3.3 compares key climate metrics in the reference state to observational estimates.

2.3.1 Parameter values

Default parameter values, used to obtain the EBM reference state, are given in Table 2.1. The ocean density and specific heat capacity correspond to those of average temperatures and salinities in the ocean. The parameters of the deep OHT, ψ and N, are tuned until the peak of the net OHT is close to the observed value of about 1.5 PW at around 20°N (Fig. 1.3a). Previous studies suggest a typical range of ocean–ice basal heat fluxes of around 2–4 W m^{-2}, and here the default value of $F_{\mathrm{bp}} = 2$ W m^{-2}.

The diffusivities K_{a} and K_{o} are tuned to best match the reference state to observations. Compared to values used by Rose and Marshall (2009), the value of K_{a} here is about a factor of 2 larger, and K_{o} is about a factor of 50 smaller. The difference in K_{o} is accounted for by the difference in mixed-layer depth: their model effectively uses a shallow mixed layer of about 2 m depth (inferred

from their column heat capacity of 10^7 J m^{-2} °C^{-1}), while here the value of $H_{\mathrm{ml}} = 75$ m from Wagner and Eisenman (2015) is used. The difference in K_{a} reflects the difference in formulations of surface and OLR fluxes between models. The atmospheric column heat capacity, C_{a}, is a rough estimate based on the mass-weighted vertical integral of the specific heat capacity assuming hydrostatic balance.

Planetary coalbedo parameters a_0, a_2, a_{i}, and $\delta\phi$ were determined by fitting Eq. (2.6) to the fraction of solar radiation absorbed, deduced from net TOA shortwave fluxes in the ERA-Interim atmospheric reanalysis (Dee et al., 2011)—as in Fig. 2.2a.

The ice thermal conductivity, k_{i}, takes the pure-ice value, as in Eisenman and Wettlaufer (2009). The latent heat of fusion, L_{f}, is also given the value corresponding to pure ice. Although salinity reduces k_{i} and L_{f} for sea ice (Affholder and Valiron, 2001; Marshall, 2012), in section 3.1 it is found that the system sensitivity is low as either k_{i} or L_{f} are varied over ±10% of these default values.

2.3.2 Atmospheric radiation parameters

The determination of the A and B parameters in Eqs. (2.2–2.4) is described in more detail than the other parameters in this section, because (i) these provide updated estimates of the radiation parameters typically used in EBMs; (ii) the formulation of the upward and downward components differs slightly from previous studies; and (iii) a similar procedure is carried out on GCM output in chapter 4. Here, they are derived from ERA-Interim, using synoptic monthly-mean data for the period 2010–2014, on a 1° grid. The analysis is separated by hemisphere (Fig. 2.5a,c,e) and by ocean versus land-covered points (Fig. 2.5b,d,f) to determine how important these factors are for the resulting parameter values.

For the upward surface flux, A_{up} and B_{up} are found from a linear fit to

Table 2.1: EBM reference state parameter values.

Parameter		Reference state value
K_a	Atmosphere diffusivity	630×10^4 m^2 s^{-1}
K_o	Ocean diffusivity	1.4×10^4 m^2 s^{-1}
F_bp	Deep OHTC at 90°N	2.0 W m^{-2}
ψ	Deep OHT amplitude	13 PW
N	Deep OHT spatial parameter	5
c_o	Ocean specific heat capacity	4.0 kJ kg^{-1} °C^{-1}
ρ_o	Ocean density	1025 kg m^{-3}
H_ml	Mixed-layer depth	75 m
C_a	Atmosphere heat capacity	0.95×10^7 J m^{-2} °C^{-1}
L_f	Sea ice latent heat of fusion	3.2×10^8 J m^{-3}
k_i	Sea ice thermal conductivity	2.0 W m^{-1} °C^{-1}
T_f	Ocean freezing temperature	−1.8°C
T_m	Sea ice surface melting temperature	−0.1°C
A_up	Surface flux up: constant term	380 W m^{-2}
B_up	Surface flux up: linear term	7.9 W m^{-2} °C^{-1}
A_dn	Surface flux down: constant term	335 W m^{-2}
B_dn	Surface flux down: linear term	5.9 W m^{-2} °C^{-1}
A_OLR	OLR: constant term	241 W m^{-2}
B_OLR	OLR: linear term	2.4 W m^{-2} °C^{-1}
a_0	Coalbedo at equator	0.72
a_2	Coalbedo spatial dependence	0.15 rad^{-2}
a_i	Coalbedo over sea ice	0.36
$\delta\phi$	Coalbedo smoothing scale	0.04 rad

the zonal-average 2 m air temperature and the zonal-average sum of upward longwave (F_lw), sensible (F_sens) and latent (F_lat) heat fluxes (Fig. 2.5a–b). The near-surface air temperature is used rather than the sea surface temperature to avoid complications of combining the sea ice and land surface temperatures, and to get a global dataset. For the purposes of this work, T_2m is sufficiently accurate. There is some deviation from a linear dependence on T_2m across the full temperature range shown in (Fig. 2.5a–b). From the separation of points it can be seen that the parameterisation is working least well over Antarctica (the lowest temperatures). This is attributed to the F_lat component: over Antarctica, F_lat is

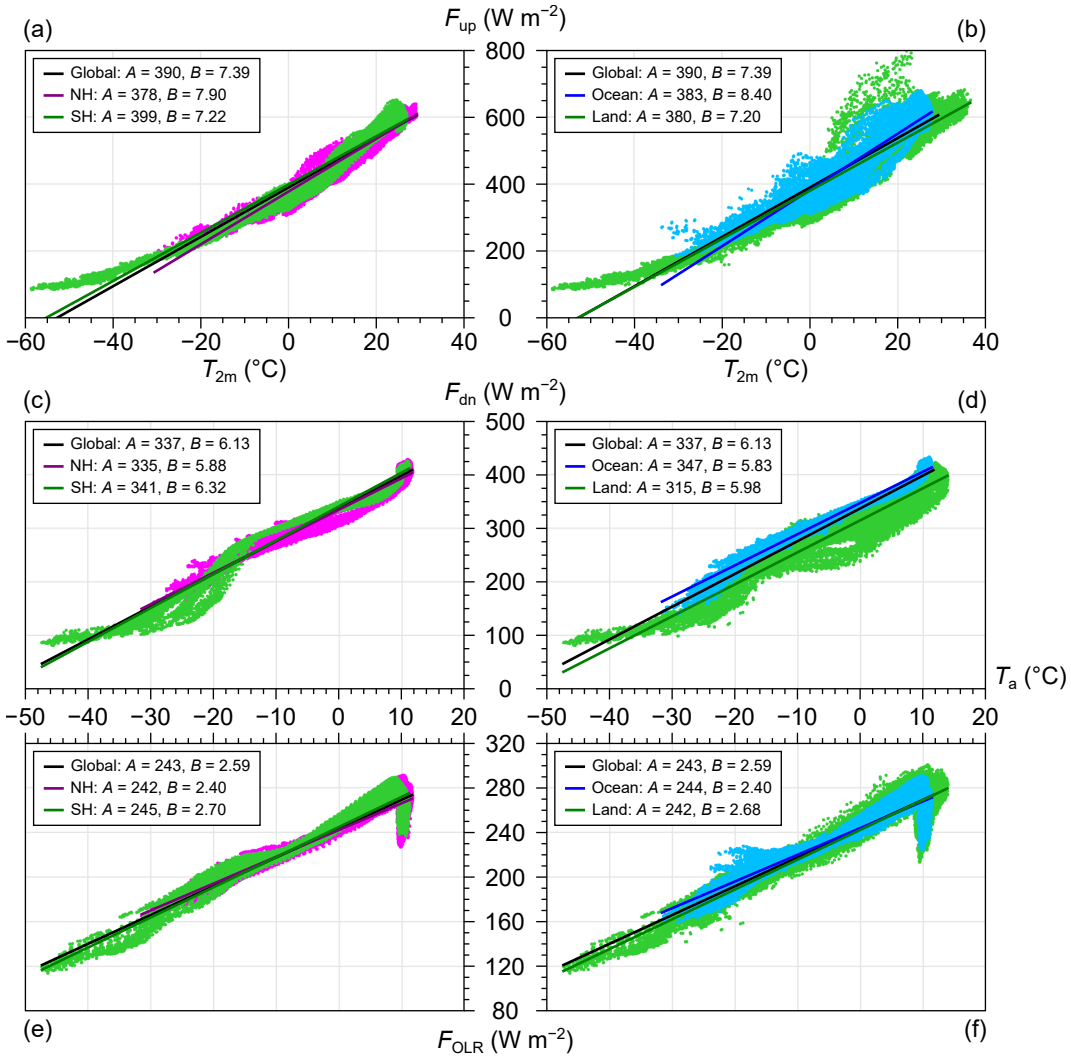

Figure 2.5: (a) Net upward surface flux (sensible, latent, and upwelling longwave radiation; F_{up}) plotted against near-surface air temperature, $T_{2\mathrm{m}}$. Each point is a zonal average corresponding to a certain time and latitude, and points are separated into northern (pink) and southern (green) hemispheres. A linear fit is added for all points together (global, black) and for each hemisphere. The legend gives the intercept, A (W m^{-2}), and slope, B (W m^{-2} °C^{-1}), in each case. (b) As in (a) but points are separated by ocean (blue) and land (green) covered points. (c)–(d) As in (a)–(b) but for the downwelling longwave radiation, F_{dn}, and air temperature at $p_0 = 700$ hPa, T_{a}. (e)–(f) As in (c)–(d) but with F_{OLR} on the vertical axis.

significantly reduced (close to zero) because the extreme low surface temperature limits moisture fluxes to the atmosphere. Here the EBM is being tuned to the northern hemisphere, where the fit for F_{up} works much better, but this caveat should be kept in mind as a potential limitation in generalising EBM results to the southern hemisphere.

Table 2.2: Values of A_{dn}, B_{dn}, A_{OLR}, and B_{OLR} as a function of the reference pressure p_0. The units of the A parameters are W m^{-2} and of the B parameters are W m^{-2} °C^{-1}. These are obtained using the global dataset. The final column shows that the ratio $\beta = B_{\mathrm{OLR}}/B_{\mathrm{dn}}$ is not sensitive to p_0.

p_0	A_{dn}	B_{dn}	A_{OLR}	B_{OLR}	$\beta = B_{\mathrm{OLR}}/B_{\mathrm{dn}}$
900	280	5.8	220	2.5	0.43
800	306	6.0	230	2.5	0.42
750	320	6.0	240	2.5	0.42
700	337	6.1	243	2.6	0.43
650	360	6.4	250	2.7	0.42
600	383	6.7	260	2.8	0.42
550	410	6.8	270	2.9	0.43
500	440	6.8	290	2.9	0.43
450	470	6.8	300	2.9	0.43
400	520	6.9	320	2.9	0.42
350	570	7.2	340	3.0	0.42
300	660	8.1	380	3.4	0.42
250	800	10	440	4.3	0.43

The downward surface flux parameters A_{dn} and B_{dn} are determined in a similar way, by fitting to the downwelling longwave flux at the surface and air temperature (Fig. 2.5c–d), and for A_{OLR} and B_{OLR} the TOA longwave flux is used (Fig. 2.5e–f). Here there is a choice of pressure level, p_0, on which to take T_{a}. The sensitivity of the fitted parameters A_{dn}, B_{dn}, A_{OLR}, and B_{OLR}, is assessed qualitatively in Table 2.2. The A parameters are affected more substantially than the B parameters, but the former just set the mean state while the latter contain the important physics. It is notable that the ratio $\beta = B_{\mathrm{OLR}}/B_{\mathrm{dn}}$ is insensitive to p_0. In section 3.3 it is shown analytically that results from the EBM depend on β and not B_{OLR} or B_{dn} individually; therefore, the choice of p_0 is immaterial.

The downwelling longwave flux, F_{dn}, is well approximated by a linear dependence on T_{a} (Fig. 2.5c–d). Noting that latitude decreases from left to right on the T_{a} axis, some large-scale meridional deviations can be seen, but on average, globally, the linearisation works well. Those deviations are mostly associated

with land covered points (Fig. 2.5c–d), but this does not make a significant difference to the slopes (i.e., B_{dn}). The OLR is also well approximated by a linear dependence on T_{a} except in the lowest latitudes (highest T_{a}), as can be seen in (Fig. 2.5e–f). As discussed in section 1.3.1, the breakdown of the parameterisation in the tropics is associated with significant longwave absorption of deep convective clouds reducing the OLR without affecting T_{a}. This effect is also seen in the F_{dn} plots, but is less prominent there.

For the reference state, the values are taken with $p_0 = 700$ hPa and for the northern hemisphere. However, A_{OLR} and A_{up} are modified by a few W m^{-2} from the fitted values for tuning purposes: this is because all metrics are highly sensitive to these parameters, so they do not need to be adjusted much to change the mean state (see section 3.1).

2.3.3 Comparison to observational estimates

Figure 2.6 shows the main metrics of interest for the EBM reference state in comparison to observational estimates for the present-day northern hemisphere. It is tuned to best match the quantities of interest for this study: ice-edge latitude ϕ_{i}, mean ice thickness $\langle H_{\mathrm{i}} \rangle$, annual-mean surface temperature $\overline{T_{\mathrm{s}}}$, $\overline{\mathrm{AHT}}$ and $\overline{\mathrm{OHT}}$.[2]

The ice-edge latitude, ϕ_{i}, is compared to that derived from ERA-Interim over the period 2010–2014. This dataset is chosen because it provides a complete set of gridded sea ice concentration consistent with the data used to determine the various atmospheric parameters. Essentially, ϕ_{i} is identified as the zonal-average 15% concentration contour, ignoring longitudes where land obstructs the immediate meridional evolution of sea ice (a procedure due to Eisenman, 2010, implemented and described in section 4.1.2). Figure 2.6a shows the annual cycle of ϕ_{i} in the EBM (solid) compared to the estimate from ERA-Interim (dashed).

[2] Throughout, $\langle d \rangle$ denotes the spatial average of diagnostic d, and $\overline{d}$ denotes its time average.

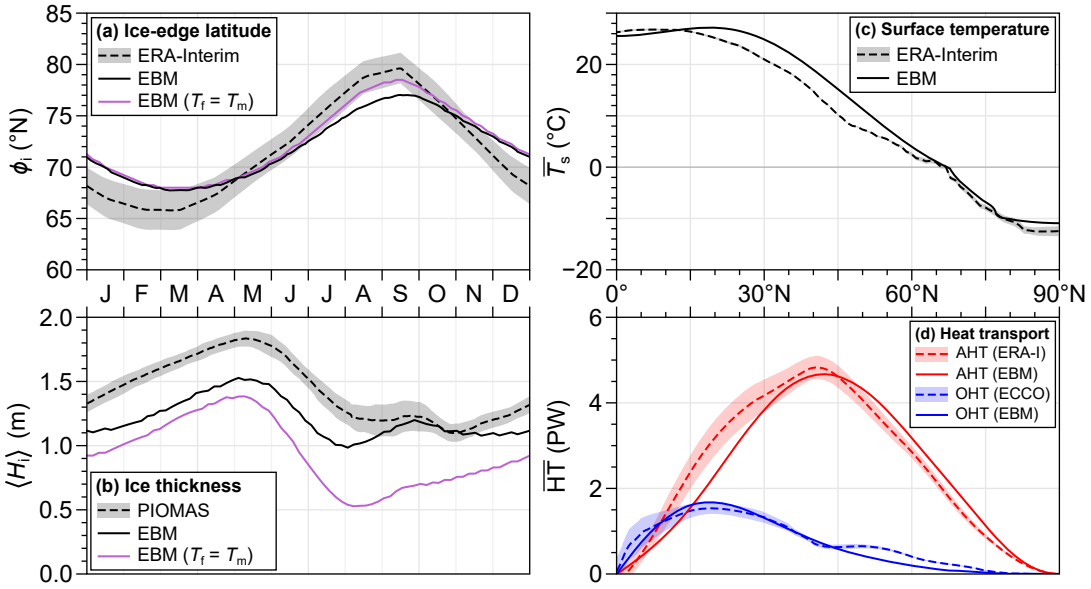

Figure 2.6: Key metrics of the EBM reference state compared to various estimates of present-day conditions in the northern hemisphere. (a) Ice-edge latitude in the EBM (black, solid) and zonal-average sea ice-edge latitude in ERA-Interim (dashed). (b) Mean sea ice thickness in the EBM (black, solid) and in PIOMAS (dashed). Also shown in (a)–(b) are those diagnostics if $T_f = T_m = -1.8°C$ (purple). (c) Annual-mean surface temperature, $\overline{T_s}$, in the EBM (solid) and zonal-average 2 m air temperature in ERA-Interim. (d) Annual-mean Heat Transports ($\overline{HT}$; 1 PW = 10^{15} W). The EBM AHT (red, solid) is compared to an estimate from ERA-Interim (red, dashed), and the EBM net OHT (blue, solid) is compared to an estimate from ECCO (blue, dashed). In (a)–(d), shaded regions indicate one standard deviation of annual means over the period of observational estimates shown (see main text).

The EBM mean ice-edge latitude (72°N) compares well with the mean in ERA-Interim (71°N). The seasonal range is approximately 5°N too small. However, the maximum error is less than 2°N.

The mean ice thickness, $\langle H_i \rangle$, is compared to the estimate from the Pan-Arctic Ice–Ocean Modeling and Assimilation System (PIOMAS; Schweiger et al., 2011) averaged over the period 2010–2018 (Fig. 2.6b). The annual mean $\langle \overline{H_i} \rangle$ = 1.21 m in the EBM, which is of the right order of magnitude when compared to PIOMAS which has an annual mean thickness of 1.39 m. The EBM is about 30 cm too thin in late winter to summer, but the agreement in autumn to early winter is good, and the lag between maximum ice thickness and maximum ice

extent is reproduced (cf. Fig. 2.6a).

Figure 2.6a,b also show ϕ_i and H_i when $T_\mathrm{m} = T_\mathrm{f} = -1.8°\mathrm{C}$ (without changing other parameters). The annual mean ice edge increases a little (by about 0.5°N) but the seasonal range improves. However, on average sea ice is substantially thinner, by about 40 cm. The other metrics are negligibly affected. These differences to the original reference state make physical sense: less heat is required to melt ice in summer because T_m is lower, so the summer ice edge retreats further and the average ice thickness must decrease. On balance, using different T_f and T_m is better because it is physically motivated and improves the ice thickness representation for only a minor change in ice extent.

The annual-mean surface temperature in the EBM compares well with the annual-mean zonal-average 2 m air temperature in ERA-Interim averaged over 2010–2014 (within 5°C; Fig. 2.6c). The comparison is not made to the sea-surface temperature (SST) from ERA-Interim because in regions occupied by sea ice the SST is not the sea ice-surface temperature. However, as discussed in section 2.3.2, the 2 m air temperature is close to the surface temperature regardless of surface type and was used to obtain default values of A_up and B_up. The EBM annual and global mean surface temperature (18.6°C) is slightly higher than that of ERA-Interim (16.7°C).

Atmospheric heat transport is diagnosed in the EBM by zonally integrating F_AHT. This is compared to the AHT in ERA-Interim, using processed data provided by Liu et al. (2015). Figure 2.6d shows that the broad hemispheric structure of AHT is represented well by the EBM diffusive transport. Due to boundary conditions the EBM cannot reproduce the non-zero transport across the equator, which leads to some error in low latitudes (similarly to the classic diffusive EBM; section 1.3.1).

The mixed-layer OHT is diagnosed by zonally integrating F_OHT, and the

OHT associated with F_b is found by integrating F_b meridionally and zonally. Here, a land fraction factor $f_\mathrm{L}(\phi)$, the fraction of longitudes occupied by land as a function of latitude, is included for the zonal integral. Note that f_L is only used for diagnosing OHT and comparing to observations, and does not appear in the EBM itself. The recent estimate of global OHT from the ECCO reanalysis by Forget and Ferreira (2019)—as in Fig. 1.3a—is used for comparison to the EBM OHT (Fig. 2.6d). The overall structure agrees well. There is some discrepancy around 60°–70°N, because the EBM does not reproduce the structure of the subpolar gyres.

2.4 Chapter summary

This chapter establishes the implementation of an EBM suitable for addressing the research aims of this thesis. The main novelties of this model are:

1. An improved representation of ocean heat transport, which has:
   a) a more realistic meridional structure compared to the real world;
   b) a means to vary high-latitude OHTC while conserving heat;
   c) interaction with other model components;
2. Separate sea ice melting temperature for top and bottom ice surfaces, which improves sea ice thickness without compromising other metrics;
3. Improved radiative heat flux parameterisations with updated estimates of parameter values, which helped to establish a reference state carefully tuned to observations.

This page intentionally left blank.

Chapter 3

Sensitivity studies

The EBM developed in the previous chapter is now used to explore the relationship between sea ice and OHT. Firstly, in section 3.1, the sensitivity to all parameters is briefly presented, which provides general context (i.e., situating the impact of ocean parameters in comparison to the others) and further establishes the reliability of the EBM by computing its climate sensitivity. Next, in section 3.2, the effects of varying key parameters controlling OHT and AHT are examined in more detail, producing estimates of the sensitivity of the sea ice edge to OHTC and AHTC in perennial and seasonal ice climates. In section 3.3, the analytical simplicity of the EBM is exploited to derive equations explaining the ice edge sensitivities found in section 3.2. These develop the qualitative interpretation and will guide the analysis of coupled GCMs in chapters 4–5. In section 3.4 the limitations of the EBM approach are discussed, and finally a summary of the key insights are given in section 3.5. Sections 3.2, 3.3.1, and 3.4 are adapted from the author's published work (Aylmer et al., 2020).

3.1 General parameter sensitivities

Taking each parameter, p, in turn, the EBM is spun up from the reference state as initial conditions, but with p adjusted slightly from its reference-state value, p_{ref}. The perturbed prognostic-variable data is saved and this is repeated over the required range of variation in p. Figure 3.1 shows the sensitivity of $\overline{\phi_{\mathrm{i}}}$ to p/p_{ref}, grouped into separate plots for clarity. Steeper lines indicate greater sensitivities to fractional changes in p. For the atmospheric radiation parameters (a) and albedo parameters (c), the ranges of variation are based on the uncertainty of fitting the associated parameterisations (Eqs. 2.2–2.4 and 2.6) to ERA-Interim data (see section 2.3.2). The sensitivities of the global mean surface temperature, $\langle\overline{T_{\mathrm{s}}}\rangle$, and mean ice thickness, $\langle\overline{H_{\mathrm{i}}}\rangle$, are shown in Figs. 3.2 and 3.3, respectively.

The three metrics $\overline{\phi_{\mathrm{i}}}$, $\langle\overline{T_{\mathrm{s}}}\rangle$, and $\langle\overline{H_{\mathrm{i}}}\rangle$ are most sensitive to A_{OLR} and (with the opposite sign) a_0. These parameters directly control the mean OLR and net absorbed shortwave radiation, respectively, and are thus leading-order determinants of the mean heat content of the system. This explains the high sensitivities and why these are suitable tuning parameters (section 2.3). The sea ice coalbedo, a_{i}, has a similar role to a_0 but operates over a smaller area such that the sensitivity is lower. There is also strong sensitivity to A_{dn} and A_{up}, the constant heat fluxes toward and away from the surface, respectively, consistent with the signs of the sensitivities. The sensitivities to the Bs are substantial compared to the remaining parameters, but are weaker than their A counterparts.

The sensitivities of $\overline{\phi_{\mathrm{i}}}$ and $\langle\overline{T_{\mathrm{s}}}\rangle$ to K_{o} and K_{a} are similar but slightly larger for K_{a}. These parameters provide a point of contact to classic diffusive EBM (section 1.3.1): the sensitivity to $\overline{\phi_{\mathrm{i}}}$ is about a factor of 10 larger when varying D in that model (Fig. 1.5b) compared to varying K_{o} or K_{a} here. This reflects the more resolved physics in the new EBM. Here, varying the diffusivities has

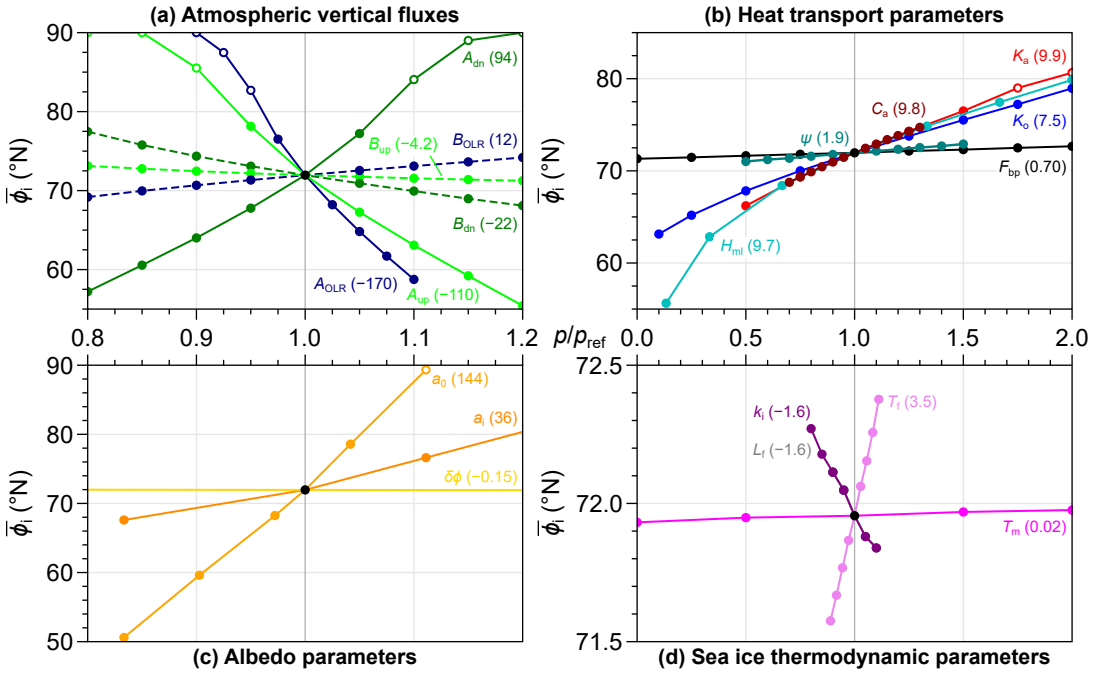

Figure 3.1: Sensitivity of the annual-mean ice edge, $\overline{\phi_i}$, to model parameters, p, plotted relative to their reference-state values, p_{ref}. Filled (hollow) points indicate that the equilibrium state has perennial ice (is seasonally ice free). Values in brackets of each label are the slopes (°N) at $p = p_{ref}$. Note that the axes scales are different across (a)–(d). In (a), the A parameters are the solid lines and the B parameters are the dashed lines.

less effect because the heat transports are separated and comparatively small, and melting sea ice requires latent heat absorption making $\overline{\phi_i}$ inherently more resistant to retreat compared to the classic EBM (in which ϕ_i is defined by a reference temperature, $T_i \equiv T_s(\phi_i)$—see section 1.3.1). For $\langle\overline{H_i}\rangle$, K_a is about 5 times more effective than K_o, and the response to K_a is non linear over the whole range shown (Fig. 3.3b). This is because K_o has, by construction, no impact under sea ice, suggesting that increasing K_o indirectly causes ice retreat. The range of F_{bp} shown in Figs. 3.1–3.3 is limited for comparison with other parameters: corresponding roughly to a range of 0–4 W m^{-2} in mean ocean–ice flux, it could plausibly be at least 2.5 times higher (Wagner and Eisenman, 2015). Both $\overline{\phi_i}$ and $\langle\overline{T_s}\rangle$ are about a factor of ten less sensitive to F_{bp} than K_o, but the sensitivity of $\langle\overline{H_i}\rangle$ is about the same to both. This suggests different mechanisms can be found from further analysis of the K_o and F_{bp} sensitivities.

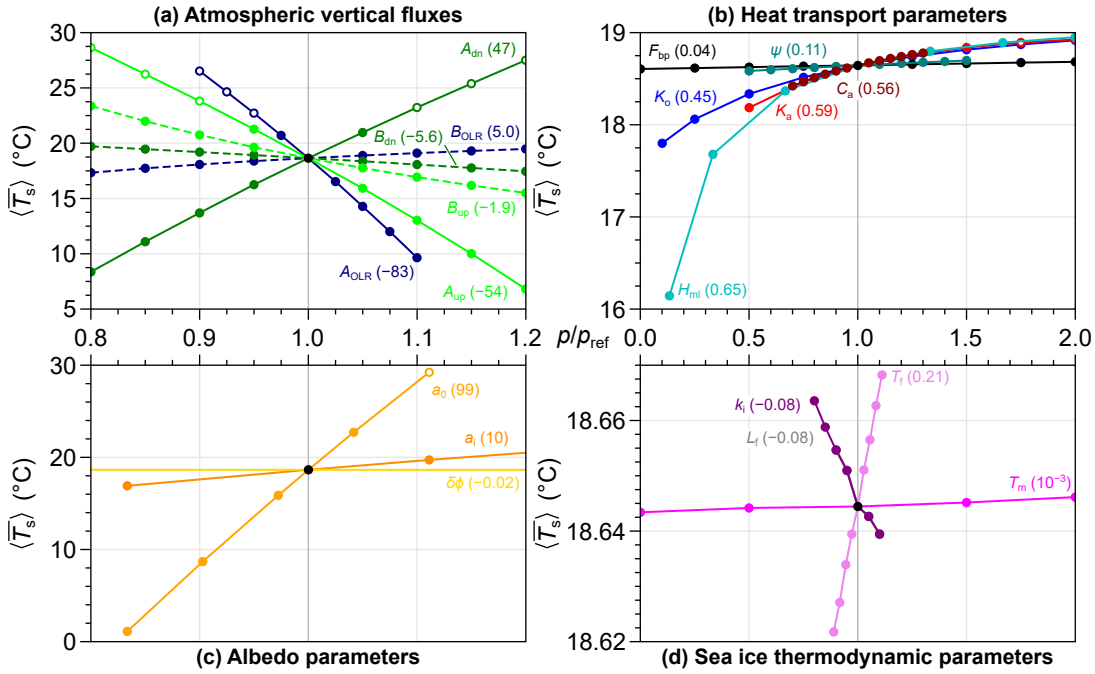

Figure 3.2: As in Fig. 3.1 but for the annual mean, global mean surface temperature, $\langle \overline{T_s} \rangle$ (slopes at $p = p_{ref}$ in °C).

Varying C_a has the same effect as varying K_a because time-averaged metrics are being considered, rendering them mathematically equivalent (i.e., the T_a tendency averages to zero in Eq. 2.1, such that only the product $K_a C_a$ appears in the EBM prognostic equations). Since the value of K_a is an unknown only determined by tuning, whereas C_a is well constrained by simple physical considerations, it makes more sense to vary K_a to study the effect of AHT variations in section 3.2. For the ocean, K_o does not behave the same as H_{ml} (equivalently, c_o or ρ_o), particularly at low H_{ml}, because the ocean heat capacity plays a role in the melting and freezing of sea ice. With a much lower H_{ml}, it takes very little cooling for T_{ml} to reach T_f, such that sea ice forms more easily and $\overline{\phi_i}$ decreases. Under ice, K_o has no effect. The sensitivity of each metric to ψ is relatively low, because it mainly determines the peak OHT in the tropics without substantially affecting latitudes occupied by sea ice.

There is notably low sensitivity of all three metrics to sea ice thermodynamic parameters, indicating that the large-scale sea ice state is determined mainly by

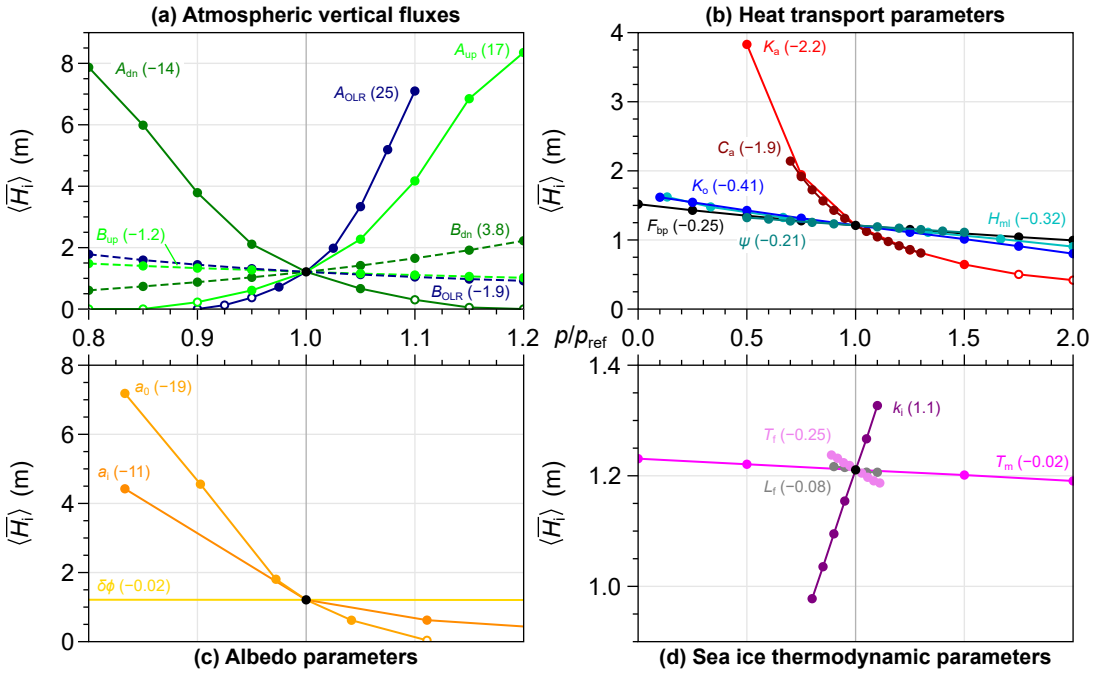

Figure 3.3: As in Fig. 3.1 but for the annual mean, global mean sea ice thickness, $\langle \overline{H_\mathrm{i}} \rangle$ (slopes at $p = p_\mathrm{ref}$ in m).

the oceanic and atmospheric forcing. Only for $\langle \overline{H_\mathrm{i}} \rangle$ does k_i matter more than ocean parameters. These parameters affect $\langle \overline{H_\mathrm{i}} \rangle$ more than they do $\overline{\phi_\mathrm{i}}$ or $\langle \overline{T_\mathrm{s}} \rangle$, which explains why the separation of top and bottom surface melting/freezing temperatures improves the ice thickness in the reference state. The default surface melting temperature, $T_\mathrm{m}^\mathrm{ref}$, would need to be multiplied by 18 to set it equal to the bottom freezing temperature, $T_\mathrm{f}^\mathrm{ref}$ (Table 2.1). Assuming the sensitivities to T_m remain roughly linear as T_m is increased by a factor of 18, the slope in Fig. 3.3 implies $\langle \overline{H_\mathrm{i}} \rangle$ would decrease by about 40 cm, while $\langle \overline{T_\mathrm{s}} \rangle$ would increase by only 0.02°C (Fig. 3.2) and $\overline{\phi_\mathrm{i}}$ by 0.4°N (Fig. 3.1; consistent with the discussion in section 2.3.3).

3.1.1 Climate sensitivity of the EBM

Applying a TOA forcing F (positive downward) in the EBM is equivalent to decreasing A_OLR (Eqs. 2.1 and 2.4). Thus, the sensitivity experiment on A_OLR

gives the EBM climate-sensitivity parameter:

$$\lambda_{\mathrm{EBM}} = -\frac{\partial\langle\overline{T_{\mathrm{s}}}\rangle}{\partial A_{\mathrm{OLR}}} = \frac{83}{241} = 0.34\text{°C (W m}^{-2})^{-1}, \tag{3.1}$$

where the local slope in Fig. 3.2a for A_{OLR} and the value of $A^{\mathrm{ref}}_{\mathrm{OLR}}$ from Table 2.1 was used. The physics setting λ_{EBM} is contained mostly within B_{OLR} and the parameters defining the planetary coalbedo. This can be seen from the definition:

$$F = \Delta\langle\overline{F_{\mathrm{OLR}}}\rangle - \Delta\langle\overline{aS}\rangle = \frac{\Delta\langle\overline{T_{\mathrm{s}}}\rangle}{\lambda_{\mathrm{EBM}}}, \tag{3.2}$$

but because there is no simple expression for $\Delta\langle\overline{aS}\rangle$ it is not possible to write λ_{EBM} directly in terms of those parameters. Crudely, $\lambda_{\mathrm{EBM}} \approx 1/B_{\mathrm{OLR}}$ as mentioned in section 2.1.1. This follows from Eq. (3.2) assuming $\Delta\langle\overline{F_{\mathrm{OLR}}}\rangle \gg \Delta\langle\overline{aS}\rangle$ and that $\Delta\langle\overline{T_{\mathrm{a}}}\rangle \approx \Delta\langle\overline{T_{\mathrm{s}}}\rangle$, which for the reference state gives $\lambda_{\mathrm{EBM}} \approx 0.4\text{°C (W m}^{-2})^{-1}$.

Using $F_{2\times} = 3.44$ W m^{-2} for the effective radiative forcing of doubling CO_2 concentrations (Otto et al., 2013) gives the Equilibrium Climate Sensitivity (ECS): $\mathrm{ECS}_{\mathrm{EBM}} = \lambda_{\mathrm{EBM}} F_{2\times} = 1.2$°C. This is below the range of values for CMIP5/6 models ($\mathrm{ECS}_{\mathrm{CMIP}} = 1.84$–$5.66$°C; Nijsse et al., 2020). However, it is just in agreement with observation-constrained estimates ($\mathrm{ECS}_{\mathrm{obs}} = 2$°C with a 95% confidence interval of $[1.2, 3.9]$°C; Otto et al., 2013). The low λ_{EBM} is likely attributed to an overestimation of the Bs (particularly B_{up} at high latitudes; see section 2.3.2). The fact that $\mathrm{ECS}_{\mathrm{EBM}}$ does not wildly differ from $\mathrm{ECS}_{\mathrm{obs}}$ suggests that other sensitivities derived from EBM (as in the next section) can be taken as reasonable estimates of real-world values.

3.2 Focus on heat transports

This section focuses on varying the parameters K_{o}, K_{a}, and F_{bp}, as these allow the most direct determination of the sensitivities of the ice edge to OHT and AHT.

The main metrics of interest are the mean ice-edge latitude, $\overline{\phi_\mathrm{i}}$, and the AHTC and OHTC averaged over times and latitudes where ice is present, hereafter:

$$h_\mathrm{a} = \langle \overline{-\nabla \cdot F_\mathrm{AHT}} \rangle, \tag{3.3}$$

and

$$h_\mathrm{o} = \langle \overline{F_\mathrm{b} - \nabla \cdot F_\mathrm{OHT}} \rangle, \tag{3.4}$$

respectively. This lets the analysis focus on the average heat transport convergence that ice covered regions are subject to, rather than the heat transport across a fixed latitude, because this more directly quantifies the impact of heat transport on the sea ice cover.[1]

3.2.1 Varying the ocean diffusivity

The ocean diffusivity, K_o, was varied between 10–500% of the reference state value $K_\mathrm{o}^\mathrm{ref}$. With larger K_o, the OHT increases and ϕ_i retreats in an approximately linear response (Fig. 3.4a). The winter and summer ice edges, shown by the shading in Fig. 3.4a, respond at similar rates. The system becomes seasonally ice free (SIF) when K_o is increased by about a factor of 2.5 from its reference value, $K_\mathrm{o}^\mathrm{ref}$, and sea ice completely vanishes when it is increased by just over a factor of 4. The mean ice-edge latitude may either be calculated as (i) an annual mean, or (ii) the average only when ice is present (as is done for h_a and h_o). When the ice cover is perennial, (i) and (ii) are equal. When the ice cover is seasonal, these lead to slightly different interpretations of the sensitivities. Averages (i), shown by hollow circles in Fig. 3.4a, capture the general high-latitude warming influence of the heat transports in summer which affects the amount of ice growth in autumn/winter. Averages (ii), shown by hollow squares in Fig. 3.4a, misses

[1] The effect of heat transport across a fixed latitude is returned to in section 3.3.2.

this but instead quantifies the more immediate impact of the heat transports in melting ice. Both have merit and the results of both are discussed for the seasonal cases.

The increase of K_o causes an increase in the net ocean–ice heat flux, h_o (Fig. 3.4b). Although $F_{OHT} = 0$ under ice because the mixed-layer temperature is fixed at the freezing temperature, across the ice edge there is a temperature difference such that $F_{OHT}(\phi_i)$ is non-zero. Therefore in this case the increase in h_o is due to an increase in OHTC at the ice edge. It should be emphasised that h_o and h_a are dependent variables. Here, K_o is the independent variable which changes the heat transport, triggering a shift of the coupled climate and hence an adjustment of h_o.

Figure 3.4c shows $\overline{\phi_i}$ as a function of h_o, as K_o varies. For the seasonal cases, both averaging methods for the ice edge are shown: (i) annual means and (ii) averages only when ice is present. Taken across the whole range the ice edge retreat with increasing h_o is non-linear but there is no abrupt transition to a SIF climate. However, reasonable linear fits can be made to the perennial and SIF regimes separately, excluding some of the points around the transition. The edge of a seasonal ice cover is approximately 40 times less sensitive to h_o than is the edge of a perennial ice cover. In this case, the two averaging methods do not make a major difference to the sensitivities (see values in the legend of Fig. 3.4c). While changes in OHTC are being imposed via the change in K_o, other parts of the system respond. Figure 3.4d shows how h_a varies as a function of h_o. For small values of h_o, h_a increases slightly, then decreases more rapidly when the ice becomes seasonal. Again there is no abrupt transition to the SIF regime. Linear fits were made across the same subsets of simulations used for the fits in Fig. 3.4c. For SIF climates, there is a clear compensating effect where h_a decreases by about 0.2 W m^{-2} for every 1 W m^{-2} increase in h_o. The response of h_a suggests that the sensitivities to h_o in Fig. 3.4c are being exaggerated in the perennial ice cases and

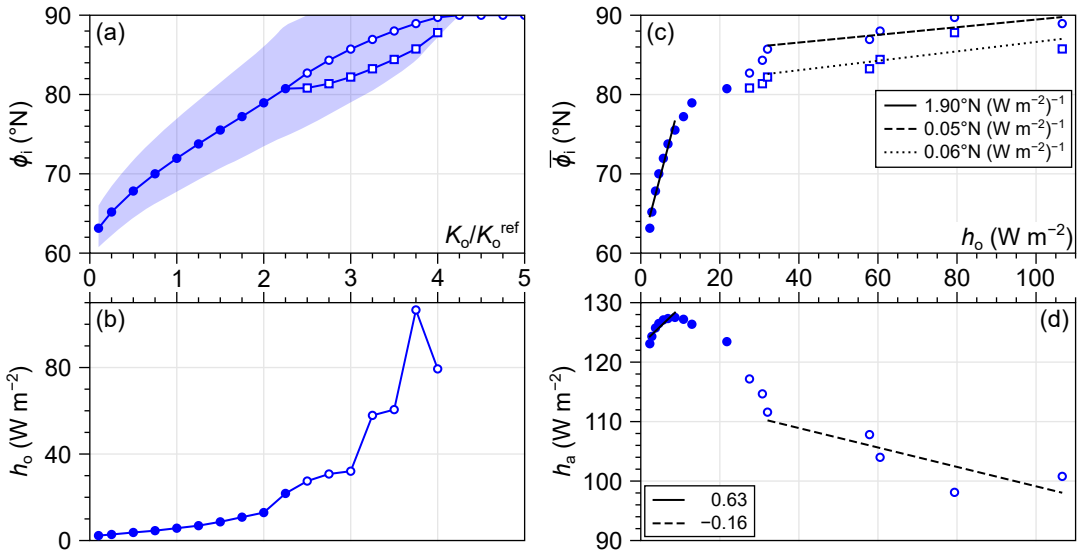

Figure 3.4: Sensitivity experiments for the ocean mixed-layer diffusivity, K_o. (a) Ice-edge latitude, ϕ_i, as K_o varies relative to the reference-state value, K_o^{ref}. The annual mean is plotted and shading indicates the seasonal range. (b) Net OHTC, averaged over times and latitudes where ice is present, h_o, as K_o varies. (c) Annual-mean ice-edge latitude, $\overline{\phi_i}$, as a function of h_o as K_o varies. (d) AHTC, averaged over times and latitudes where ice is present, h_a, as a function of h_o, as K_o varies. In (c) and (d), ordinary least squares (OLS) fits are added for perennial (filled points, solid black lines) and seasonally ice-free (hollow points, dashed and dotted black lines) simulations, excluding some near the transition between regimes, and the legends give the slopes. For the seasonal cases in (a) and (c), circles indicate that the mean ice-edge latitude is calculated as an annual mean (OLS fit in dashed line) and squares indicate that it is calculated as the mean only when ice is present (OLS fit in dotted line).

suppressed in the seasonal ice cases. This highlights that impacts of the two heat transport components on the ice edge are interconnected, and the importance of Bjerknes compensation (BC; Bjerknes, 1964) in modulating the impact of OHT. This point is returned to in the next section, in order to distinguish between 'effective' (with BC) and 'actual' (in the absence of BC) sensitivities and thus quantify the role of BC.

For the perennial-ice cases, why does h_a increase when h_o increases (for $h_o \approx 0$–10 W m^{-2} in Fig. 3.4d)? As K_o is increased and OHT increases near the ice edge, some is lost to the atmosphere via air–sea exchanges which is then transported poleward by the atmosphere. For example, in the reference state about 10% of the open-ocean OHTC is lost to the atmosphere rather than trans-

ported under sea ice. This proportion increases with increasing K_o (e.g., to about 15% with $K_o = 2K_o^{ref}$). Thus, although changing K_o only directly affects OHT at the ice edge, the ice edge retreats more than it otherwise would because the atmosphere continues transporting heat further poleward (Fig. 3.4d), reducing the ice thickness at higher latitudes (e.g., by about 0.3 m when K_o is doubled from K_o^{ref}). Increased OHTC at the ice edge thus indirectly causes melt over the entire ice pack, mediated by the atmosphere. This same mechanism applies for the SIF regime, but only for the portion of the year where ice is present. For the rest of the year, OHT reaches the pole and warms the high latitudes directly. This reduces the temperature gradient in the atmosphere (e.g., by about 25% between $K_o = 2.5K_o^{ref}$ and $K_o = 5K_o^{ref}$), reducing h_a. The magnitude of this summer reduction in h_a is larger than the winter increase in h_a due to increasing OHTC at the ice edge, such that on average h_a is smaller. The magnitudes of the summer reduction in h_a and winter increase in h_a depend on how far the ice edge advances in winter and on the magnitude of h_o—hence the relatively smooth transition between over-compensation and under-compensation (Fig. 3.4d).

3.2.2 Varying the atmospheric diffusivity

The atmospheric diffusivity K_a was varied between 50–500% of the reference value, K_a^{ref}. Figure 3.5a shows the response of ϕ_i. For the SIF cases, as with K_o both the annual mean (i; hollow circles) and ice-only mean (ii; hollow squares) ice-edge latitudes are plotted. Starting at small K_a, the mean ϕ_i increases approximately linearly with K_a. The summer ice edge is more sensitive than the winter ice edge, as shown by the edges of the shaded region in Fig. 3.5a. The system becomes SIF when K_a approaches $1.75K_a^{ref}$. Beyond this value, a perennially-ice-free solution was not obtained despite K_a being increased to $5K_a$, although the winter ice edge continues to retreat with further increases in K_a. This is unlike

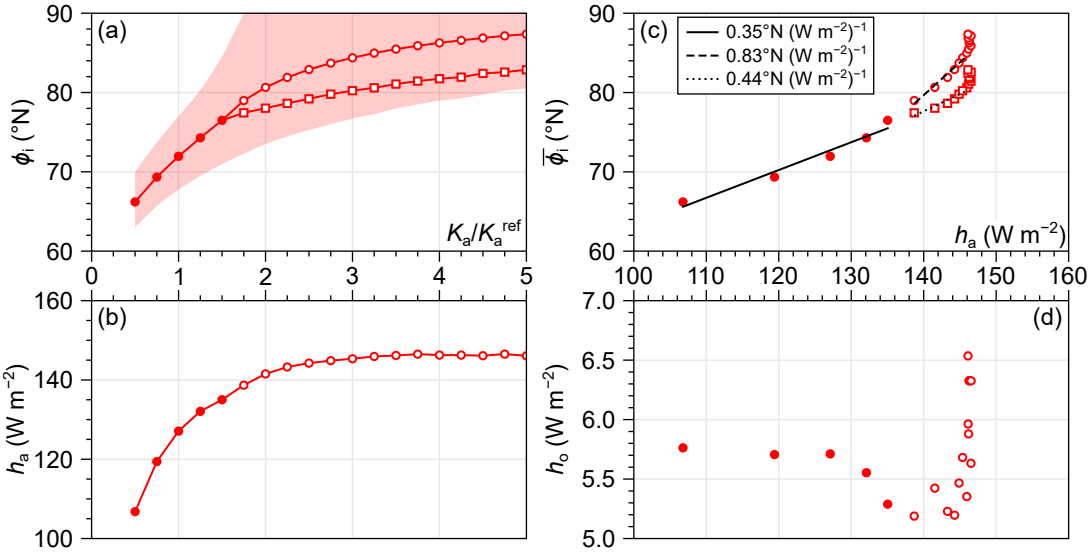

Figure 3.5: As in Fig. 3.4 but for the K_a sensitivity experiments, with K_a taking the place of K_o and h_a exchanged with h_o. The last few simulations where h_a tends to its limit value are excluded from the fits to the seasonally ice free regime in (c).

the behaviour of K_o, in which a SIF climate was generated with about $2.5K_o^{ref}$ and a perennially-ice-free climate at about $4K_o^{ref}$. This is consistent with the notion of OHT being a more effective driver of the ice-edge latitude than AHT.

As K_a is increased, h_a tends toward a limit value of about 150 W m^{-2} (Fig. 3.5b). Although the EBM representation of AHT is not sophisticated and does not explicitly describe any features of the atmospheric circulation, the large-scale heat transport depends on the existence of a temperature gradient, so this may suggest a limit on h_a which may be insufficient to completely eliminate the ice cover. Clearly, such climates with small hemispheric air-temperature gradients are unrealistic. This limit should thus be taken with caution.

Figure 3.5c shows the response of $\overline{\phi_i}$ to h_a in this K_a sensitivity experiment. As was done in the case of K_o, a line of best fit is added for perennial and seasonal ice cover simulations separately. For the seasonal cases, the last few solutions where h_a does not change much are excluded. While h_a changes by about 40 W m^{-2} across the whole set of simulations, h_o varies by only about 1 W m^{-2}, with no major trend except the slight increase when h_a reaches its

limiting value (Fig. 3.5d). Since $\Delta h_o \ll \Delta h_a$, it is approximated that there is no BC across this sensitivity experiment. This suggests that the actual sensitivity of ϕ_i to AHT is about 0.35°N sea ice loss per 1 W m^{-2} increase in AHTC averaged over the ice pack while ice survives in summer. The sensitivity in the seasonal case depends on how the average ice-edge latitude is calculated: the annual-mean ice edge is about 2.5 times more sensitive to AHT when the ice cover is seasonal than when it is perennial, but the sensitivity of the ice edge when averaged only during ice-covered times is not significantly changed across regimes. This suggests roughly equal contributions of the indirect (high-latitude warming) and direct (melting ice) mechanisms in setting the sensitivity of the ice edge to AHT.

Returning to the K_o sensitivity experiment, the actual sensitivity of ϕ_i to h_o (in the absence of variations in h_a) can be determined. As described in the previous section, Fig. 3.4c shows the effective sensitivity of ϕ_i to h_o while both h_o and h_a vary. Approximating all responses of the ice edge to changes in heat transport convergence as linear:

$$\Delta\overline{\phi_i} = s_a \Delta h_a + s_o \Delta h_o, \tag{3.5}$$

where s_a is the actual sensitivity of the ice edge to h_a, when h_o does not vary, and vice versa for s_o. Note that s_o is a function of model parameters too because, as will be seen, different parameters change h_o in different ways; for brevity of notation this is left implicit. As described above, in the K_a sensitivity experiment $\Delta h_o \approx 0$, giving $s_a \approx \Delta\overline{\phi_i}/\Delta h_a \approx 0.35$°N (W m^{-2})$^{-1}$ for perennial ice and ≈ 0.83°N (W m^{-2})$^{-1}$ for seasonal ice (focusing first on values derived using the annual-mean ice edge). These values can now be used in Eq. (3.5) for the K_o sensitivity experiment, in which the BC rate $\Delta h_a/\Delta h_o = -0.16$ for seasonal ice (Fig. 3.4d). Thus, the effective sensitivity $\Delta\overline{\phi_i}/\Delta h_o \approx 0.05$°N (W m^{-2})$^{-1}$ is a suppression of the actual sensitivity, $s_o \approx 0.18$°N (W m^{-2})$^{-1}$. Alternatively, using

the mean ice-edge latitude only when ice is present gives an actual sensitivity $s_o \approx 0.13°\text{N (W m}^{-2})^{-1}$. The estimate of the actual sensitivity in the case of perennial ice is not as straightforward here because the response of h_a is small and highly nonlinear over those simulations (Fig. 3.4d). A rough estimate suggests the actual sensitivity of $\overline{\phi_i}$ to h_o for perennial ice is about $1.7°\text{N (W m}^{-2})^{-1}$, compared to the effective sensitivity of $1.9°\text{N (W m}^{-2})^{-1}$.

When interpreting these numbers it should be kept in mind that the spatial distribution of the increase in h_o due to increasing K_o is concentrated at the ice edge. In the next section, a sensitivity experiment is carried out in which the h_o variation is distributed across the ice pack, making a better comparison with the impact of h_a. Nevertheless, large OHTC near the ice edge does occur in models (e.g., Bitz et al., 2005), and this analysis suggests that the ice edge is highly sensitive to such anomalies in OHTC when the ice cover is perennial (such as in the present-day climate). This is consistent with previous studies showing a link between OHTC and the ice-edge latitude (section 1.2.3). These results suggest further that in a SIF climate the role of such OHTC near the ice edge plays a less dramatic role.

3.2.3 Varying directly the ocean–ice flux

Global OHTC in the EBM can also be varied by changing the shape of the prescribed part, $F_b(\phi)$. Here, this is accomplished with the parameter F_{bp}, which sets the OHTC at the pole by conservatively redistributing the pattern of OHTC associated with $F_b(\phi)$. This changes the ocean–ice flux smoothly across the whole ice pack.

The parameter F_{bp} was thus varied between 0–20 W m^{-2} which gives rise to a variation in h_o of about 4–22 W m^{-2}. Both $\overline{\phi_i}$ and h_o increase linearly with F_{bp} (Figs. 3.6a and 3.6b, respectively). The slope of h_o versus F_{bp} is not exactly

1 because $F_b(\phi)$ is non-uniform, and there is a contribution from the mixed-layer transport, F_{OHT}, at the ice edge [see section 2.1.2(b)]. Ice-edge retreat in response to h_o and BC of h_a are also linear in both perennial and SIF regimes (Figs. 3.6c and 3.6d, respectively). It is worth emphasising that increasing F_{bp}, K_o, or K_a only redistribute heat: increases in heat content of the system are due to ice-edge retreat which exposes the ocean, thus increasing net shortwave radiation. The system becomes SIF when F_{bp} is about 11 W m^{-2}, or when h_o is roughly 13 W m^{-2}. This is about half the value of h_o required to obtain a SIF solution when K_o is varied (Fig. 3.4b), reflecting that ϕ_i is more sensitive to ocean heat fluxes near the ice edge than in the central ice pack. As with the K_a and K_o sensitivity analyses, Figs. 3.6a and 3.6c show the mean ice-edge latitude calculated as the annual mean (hollow circles) and as the mean only when ice is present (hollow squares). There is a smooth transition between the perennial and SIF regimes, but the difference in effective sensitivities between regimes (legend of Fig. 3.6c) is not as large as in the case of K_o, regardless of how the mean ice edge is calculated. Bjerknes compensation is present in both regimes, but the rate of BC halves in SIF climates (legend of Fig. 3.6d).

The actual sensitivities can be determined following the same procedure as described in section 3.2.2. Figure 3.6d shows the associated decrease in h_a as h_o increases; from this and Eq. (3.5), $s_o \approx 0.7°\text{N (W m}^{-2})^{-1}$ for perennial ice, about a third of the value $1.7°\text{N (W m}^{-2})^{-1}$ obtained for the perennial-ice simulations when K_o was varied. The reason for the difference is that increasing F_{bp} increases the ocean–ice flux uniformly over the ice pack, compared to increasing K_o which increases h_o only at the ice edge. Clearly, ice is thinner at and near to the edge, such that heat fluxes there have more impact on the ice-edge latitude than equal heat fluxes at the pole. A given h_o due to varying K_o thus has a greater effect on the ice edge than the same h_o due to varying F_{bp}. It is therefore not surprising that the ice edge is more sensitive to h_o when K_o is varied.

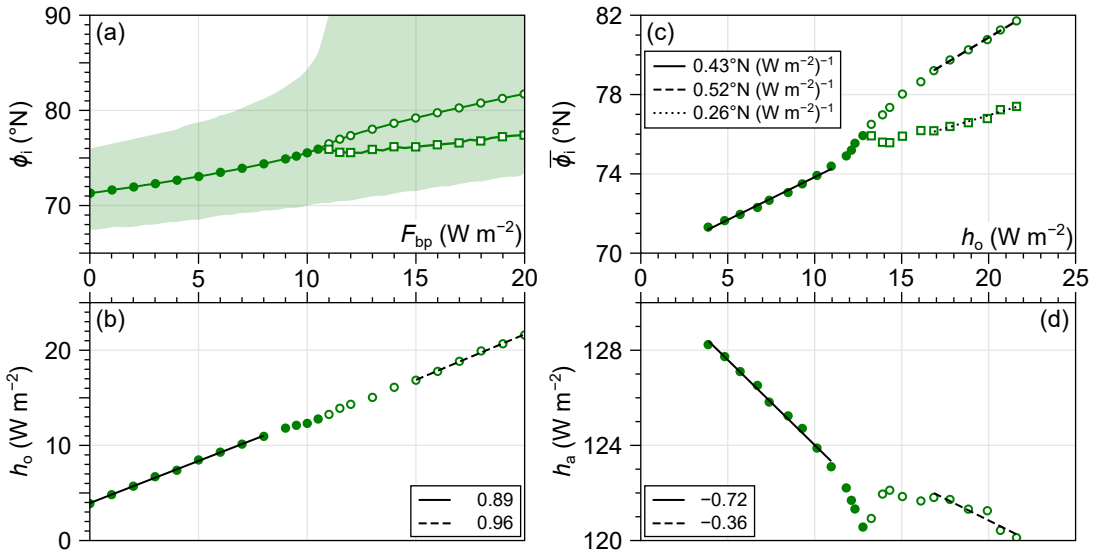

Figure 3.6: As in Fig. 3.4, but for the F_{bp} sensitivity experiments, with F_{bp} taking the place of K_o. Simulations near the transition between perennial and seasonal ice-cover regimes are excluded in the linear fits in (b)–(d).

When the ice cover is seasonal, $s_o \approx 0.8°\text{N (W m}^{-2})^{-1}$, calculated from annual-mean ice edges. This is notably similar to the value of s_a for seasonal ice cover, suggesting that the two heat transports have similar impacts on ice extent in the seasonal regime. If the calculation here is done using the mean ice-edge latitudes calculated only when ice is present, it is found that $s_o \approx 0.4°\text{N (W m}^{-2})^{-1}$ which is also similar to the value of s_a obtained when calculating the ice-edge latitude in the same way. The effective sensitivities to h_o are about two-thirds the actual sensitivities, in both perennial and seasonal regimes and independent of how the mean ice-edge latitude is calculated in the latter. Therefore, the relative impacts of AHT and OHT in the seasonal regime are independent of the calculation method.

In terms of the annual-mean method, the sensitivities for SIF conditions are larger than the sensitivities for perennial-ice conditions (for the atmosphere, compensated and uncompensated ocean). Sensitivities derived based on averaging method (ii)—the mean over times only when ice is present—are smaller for SIF conditions. When ice is not present in summer, the role of the heat trans-

Table 3.1: Summary of results [°N (W m^{-2})$^{-1}$] obtained from sensitivity experiments in which the parameters $p = K_o$, K_a and F_{bp} are varied. The 'effective' (i.e., with Bjerknes compensation) sensitivities $\Delta\phi_i/\Delta h$ and 'actual' (i.e., with compensation removed) sensitivities s are given in the perennial and seasonal ice cover regimes. For the seasonal case, values obtained when the ice-edge latitude is calculated as a mean only when ice is present (rather than the annual mean) are indicated with *.

p	Ice cover	$\Delta\phi_i/\Delta h_a$	$\Delta\phi_i/\Delta h_o$	s_a	s_o
K_a	perennial	0.35	—	0.35	—
	seasonal	0.83	—	0.83	—
	seasonal*	0.44	—	0.44	—
K_o	perennial	—	~ 1.9	—	~ 1.7
	seasonal	—	0.05	—	0.18
	seasonal*	—	0.06	—	0.13
F_{bp}	perennial	—	0.43	—	0.68
	seasonal	—	0.52	—	0.82
	seasonal*	—	0.26	—	0.42

ports is to warm the high latitudes to resist ice formation in winter. Since there is no ice to act as a barrier to surface fluxes, it is reasonable to expect that AHT would have roughly the same warming effect as OHT, and thus similar sensitivities (regardless of how the mean ice edge is calculated). The lack of ice in summer also enhances solar absorption and thus warming at high latitudes. This effect is captured when using the annual-mean ice edge, explaining why the seasonal sensitivities in this case are larger than when calculated as a mean only when ice is present.

The sensitivities of the ice-edge latitude to h_o and h_a are given in Table 3.1 and summarised graphically in Fig. 3.7, including the impacts of BC in each ice-cover regime and the difference in using the annual mean and ice-only mean ice-edge latitude. In Fig. 3.7, for the ocean only those sensitivities derived from the F_{bp} sensitivity experiments are shown, rather than from the K_o ones: since varying h_o via F_{bp} varies the ocean–ice flux more uniformly than doing so with K_o, this provides a fairer comparison with the h_a sensitivities.

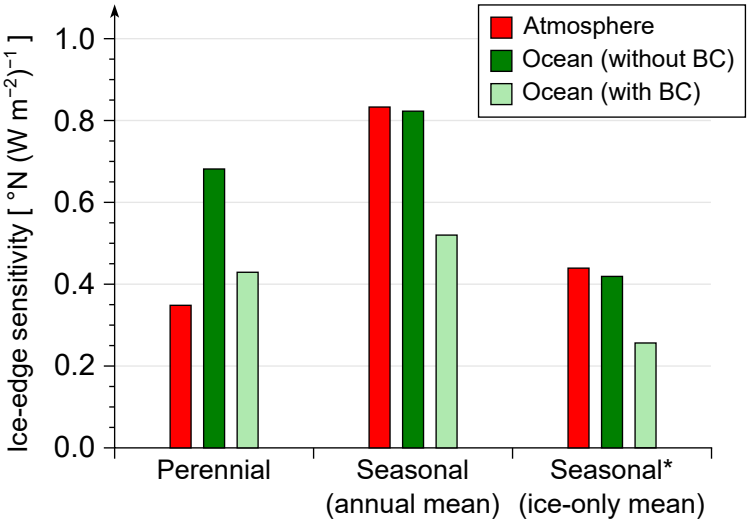

Figure 3.7: Summary of sensitivities of the ice edge to AHTC (red), to OHTC in the absence of compensation (dark green), and to OHTC in the presence of compensation (light green). These are given for (left) perennial ice cover, (centre) seasonal ice cover based on calculating the ice-edge latitude as an annual mean, and (right) seasonal ice cover based on calculating the ice-edge latitude as the mean value only when ice is present. For the OHTC, values derived from the F_{bp} sensitivity experiment are shown rather than those from the K_{o} sensitivities as this provides a fairer comparison to the AHTC sensitivities.

In section 2.1.2(b), it was mentioned that the partitioning of OHT between the mixed layer (controlled by K_{o}) and prescribed component (controlled by F_{bp}) was arbitrary. The results are not sensitive to this: for example, when $K_{\mathrm{o}} = 0.75K_{\mathrm{o}}^{\mathrm{ref}}$ (i.e., reducing the mixed layer component) and $F_{\mathrm{bp}} = 7$ W m^{-2} (i.e., reducing the prescribed component), the total OHT and ϕ_{i} of the reference state remain largely unchanged, despite roughly 25% of the mixed layer OHT being 'moved' into the prescribed part. With respect to this alternate reference state, the derived actual sensitivities change by only a few percent.

3.3 Analytical relationships from the EBM

3.3.1 Ratio of sensitivities to OHTC and AHTC

In section 3.2 it was shown that, after accounting for Bjerknes compensation, the sensitivity of the ice-edge latitude to OHTC is approximately twice that to AHTC when ice remains in summer. In this section, that result is generalised by deriving an analytic relation for the ratio of the two sensitivities. The parameter dependence of $s_\mathrm{o}/s_\mathrm{a}$ facilitates a physical interpretation of the difference between s_o and s_a. The reader, if uninterested in the mathematical details, may skip the derivation in subsection (a) and go to the result, Eq. (3.15), and its discussion in subsection (b).

(a) Derivation

A relationship between h_a, h_o, and ϕ_i, derived from the EBM equations, with minimum dependence on the background state (i.e., the prognostic variables T_a, T_ml, T_s, and H_i), is sought, to linearise about small perturbations. In essence, the aim is to arrive at an equation of the form of Eq. (3.5). Since there are four independent prognostic equations it is not possible to eliminate the background state entirely, so the final result is an approximation assuming perturbations to that background state are sufficiently small so as to not change it too much.

First, the domain dependence is eliminated from the mixed-layer and sea ice-thickness prognostic equations, (2.5) and (2.16) respectively, as this complicates the time averaging. In the continuous limit, $\nabla \cdot F_\mathrm{OHT} = 0$ for $\phi \geq \phi_\mathrm{i}$, so those equations may be combined into one:

$$\frac{\partial E}{\partial t} = aS + (F_\mathrm{b} - \nabla \cdot F_\mathrm{OHT}) + F_\mathrm{dn} - F_\mathrm{up}, \tag{3.6}$$

where

$$E = \begin{cases} -L_\mathrm{f} H_\mathrm{i} & E \leq 0 \\ C_\mathrm{o} \left(T_\mathrm{ml} - T_\mathrm{f}\right) & E > 0 \end{cases} \tag{3.7}$$

(recalling the approach of Wagner and Eisenman, 2015). Taking the time and spatial average over latitudes occupied by sea ice of the T_a prognostic equation, (2.1), and rearranging, gives:

$$-h_\mathrm{a} = \left(A_\mathrm{up} - A_\mathrm{dn} - A_\mathrm{OLR}\right) + B_\mathrm{up}\langle\overline{T_\mathrm{s}}\rangle - \left(B_\mathrm{dn} + B_\mathrm{OLR}\right)\langle\overline{T_\mathrm{a}}\rangle, \tag{3.8}$$

where Eqs. (2.2–2.4) were also used. Doing the same averaging on Eq. (3.6), and rearranging, gives:

$$-h_\mathrm{o} = \left(A_\mathrm{dn} - A_\mathrm{up}\right) + B_\mathrm{dn}\langle\overline{T_\mathrm{a}}\rangle - B_\mathrm{up}\langle\overline{T_\mathrm{s}}\rangle + a_\mathrm{i}\langle\overline{S}\rangle, \tag{3.9}$$

where smoothing of coalbedo across the ice edge has been neglected. Next, $\langle\overline{T_\mathrm{a}}\rangle$ is eliminated by solving Eq. (3.9) for $\langle\overline{T_\mathrm{a}}\rangle$:

$$\langle\overline{T_\mathrm{a}}\rangle = \frac{A_\mathrm{up} - A_\mathrm{dn} + B_\mathrm{up}\langle\overline{T_\mathrm{s}}\rangle - a_\mathrm{i}\langle\overline{S}\rangle - h_\mathrm{o}}{B_\mathrm{dn}}, \tag{3.10}$$

then substituting this into Eq. (3.8) and rearranging, which gives:

$$h_\mathrm{a} + (1+\beta)\, h_\mathrm{o} = \gamma_0 + \beta B_\mathrm{up}\langle\overline{T_\mathrm{s}}\rangle - (1+\beta)\, a_\mathrm{i}\langle\overline{S}\rangle, \tag{3.11}$$

where $\gamma_0 = A_\mathrm{OLR} + \beta\left(A_\mathrm{up} - A_\mathrm{dn}\right)$, and $\beta = B_\mathrm{OLR}/B_\mathrm{dn}$. Note that while γ_0 just combines some constants for brevity and ultimately has no significance, β will become an important part of the interpretation of the final result here, and in that of section 3.3.2.

Next, $\langle\overline{T_\mathrm{s}}\rangle$ is eliminated in favour of $\langle\overline{H_\mathrm{i}}\rangle$. Approximating that for roughly half the time the ice surface is melting and the rest of the time it is sub-freezing,

as described in Eqs. (2.14) and (2.15), $\langle\overline{T_\mathrm{s}}\rangle \approx (T_\mathrm{m} + \langle\overline{T_\mathrm{d}}\rangle)/2$. Averaging Eq. (2.14) and neglecting cross correlations between variables (such that $\langle\overline{T_\mathrm{d}H_\mathrm{i}}\rangle \approx \langle\overline{T_\mathrm{d}}\rangle\langle\overline{H_\mathrm{i}}\rangle$, and so on) gives an expression for $\langle\overline{T_\mathrm{d}}\rangle$, resulting in:

$$\langle\overline{T_\mathrm{s}}\rangle = \frac{T_\mathrm{m}}{2} + \frac{A_\mathrm{dn} - A_\mathrm{up} + B_\mathrm{dn}\langle\overline{T_\mathrm{a}}\rangle + a_\mathrm{i}\langle\overline{S}\rangle + k_\mathrm{i}T_\mathrm{f}/\langle\overline{H_\mathrm{i}}\rangle}{2\left(B_\mathrm{up} + k_\mathrm{i}/\langle\overline{H_\mathrm{i}}\rangle\right)}. \tag{3.12}$$

Now, $\langle\overline{T_\mathrm{a}}\rangle$ is eliminated by substituting Eq. (3.10) into Eq. (3.12) and then solving for $\langle\overline{T_\mathrm{s}}\rangle$. Upon rearrangement and simplification, this gives the following expression for $\langle\overline{T_\mathrm{s}}\rangle$ in terms of $\langle\overline{H_\mathrm{i}}\rangle$:

$$\langle\overline{T_\mathrm{s}}\rangle = \frac{B_\mathrm{up}T_\mathrm{m} + k_\mathrm{i}\left(T_\mathrm{m} + T_\mathrm{f}\right)/\langle\overline{H_\mathrm{i}}\rangle - h_\mathrm{o}}{B_\mathrm{up} + 2k_\mathrm{i}/\langle\overline{H_\mathrm{i}}\rangle}. \tag{3.13}$$

Equation (3.13) is then substituted back into Eq. (3.11), and after collecting like terms and simplifying this leads to:

$$\begin{aligned} &h_\mathrm{a} + \left[1 + \beta\left(1 + \frac{B_\mathrm{up}}{B_\mathrm{up} + 2k_\mathrm{i}/\langle\overline{H_\mathrm{i}}\rangle}\right)\right] h_\mathrm{o} \\ &\qquad = \gamma_0 + \beta B_\mathrm{up}\frac{B_\mathrm{up}T_\mathrm{m} + k_\mathrm{i}\left(T_\mathrm{m} + T_\mathrm{f}\right)/\langle\overline{H_\mathrm{i}}\rangle}{B_\mathrm{up} + 2k_\mathrm{i}/\langle\overline{H_\mathrm{i}}\rangle} - (1+\beta)\, a_\mathrm{i}\langle\overline{S}\rangle. \end{aligned} \tag{3.14}$$

Finally, for sufficiently small perturbations around a given background state with ice edge $\overline{\phi_\mathrm{i}}$, $\langle\overline{S}\rangle \approx s_0 - s_1\overline{\phi_\mathrm{i}}$, where s_0 and $s_1 > 0$ are empirical parameters which depend weakly on the background state.[2] This does not work if the system becomes SIF because the averaging includes the annual mean and spatial mean over sea ice. Although it is intuitive that $\langle\overline{S}\rangle$ can be linearised about $\overline{\phi_\mathrm{i}}$ for perennial ice cover because S depends only on t and ϕ, this was verified by plotting $\langle\overline{S}\rangle$ against $\overline{\phi_\mathrm{i}}$ for all sensitivity experiments described in section 3.1, shown in Fig. 3.8a. Here it can be seen that the approximation is good even over

[2] The parameters s_0 and s_1 are not to be confused with S_0 and S_1 in Eq. (2.8).

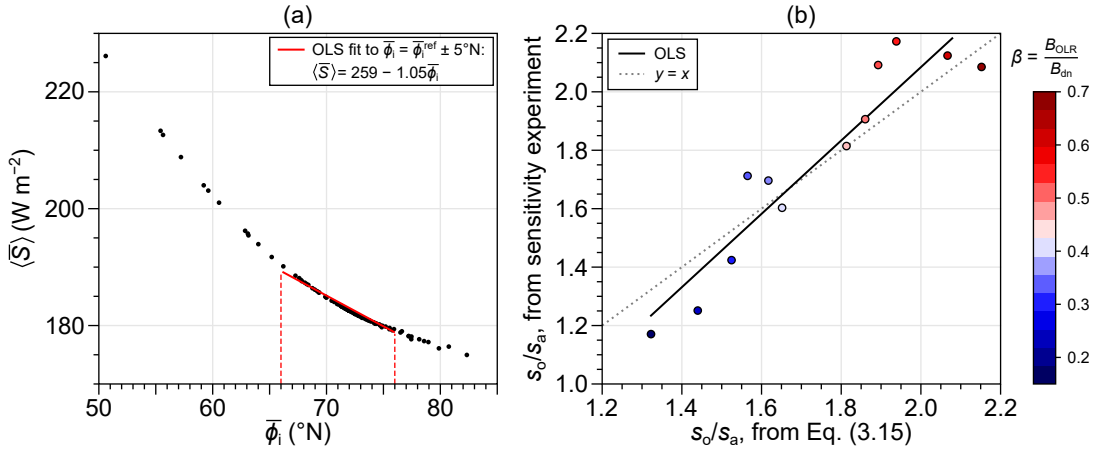

Figure 3.8: (a) Annual-mean TOA solar radiation averaged over sea ice, $\langle\overline{S}\rangle$, as a function of the mean ice-edge latitude, $\overline{\phi_i}$. These points come from the general parameter sensitivity experiments (i.e., the points in Fig. 3.1 for all parameters). Seasonally ice free points are excluded. An OLS fit is added to points with $\overline{\phi_i}$ within ±5°N of the reference state value, $\overline{\phi_i}^{ref}$. (b) Sensitivity ratio, s_o/s_a, for various choices of B_{OLR} and B_{dn}, plotted as the experimentally-derived value versus the value predicted by Eq. (3.15). An OLS fit (black, solid) and $y = x$ line (grey, dotted) are shown. Points are coloured according to the value of $\beta = B_{OLR}/B_{dn}$.

a substantial variation in $\overline{\phi_i}$ of about ±5°N around the reference state, and the value of s_1 is about 1 W m^{-2} °N^{-1}. It also shows that the relationship between $\overline{\phi_i}$ and $\langle\overline{S}\rangle$ only depends on the background state, because the points in Fig. 3.8a lie approximately along a common curve despite being obtained by changing different parameters. Substituting $s_0 - s_1\overline{\phi_i}$ for $\langle\overline{S}\rangle$ in Eq. (3.14) introduces dependence on $\overline{\phi_i}$. Again assuming small perturbations such that $\langle\overline{H_i}\rangle$ does not change much, it then follows, by comparing the coefficients of h_o and h_a in Eq. (3.14) (cf. Eq. 3.5), that the ratio of sensitivities is given by:

$$\boxed{\frac{s_o}{s_a} \approx 1 + \beta\left(1 + \frac{B_{up}}{B_{up} + 2k_i/\langle\overline{H_i}\rangle}\right)} \tag{3.15}$$

where, to reiterate, $\beta = B_{OLR}/B_{dn}$. Since a number of approximations are involved in deriving this equation, it was tested by repeating the sensitivity studies with different values of B_{OLR} and B_{dn}. Values of s_o/s_a derived from experiment agree with the predicted values from Eq. (3.15) within about 5% (Fig. 3.8b).

In particular, it correctly predicts that a larger value of β results in a larger sensitivity of $\overline{\phi_\mathrm{i}}$ to h_o relative to h_a (also depicted in Fig. 3.8b).

(b) Interpretation

In the derivation of Eq. (3.15), the main assumptions are that ice remains in the summer, prognostic-variable correlations are neglected, and h_a and h_o are smoothly distributed across the ice cap. This last point means the appropriate sensitivity to h_o is that when F_bp varies rather than K_o. Also, since the ratio depends on the climate state (via the mean ice thickness, $\langle\overline{H_\mathrm{i}}\rangle$), the result applies to small perturbations around a given reference state.

The factor in brackets in Eq. (3.15) is at least 1 in the limit $\langle\overline{H_\mathrm{i}}\rangle \to 0$, and at most 2 in the limit $\langle\overline{H_\mathrm{i}}\rangle \to \infty$. For the reference state values of B_up, k_i, and $\langle\overline{H_\mathrm{i}}\rangle$, this factor is about 1.7. In practice neither of the limits can be reached since they correspond to the extreme cases of perennially ice free and snowball-Earth climates, respectively, in which cases Eq. (3.15) certainly does not hold. This suggests that the ratio of sensitivities is fairly insensitive to the background climate.

Equation (3.15) shows that the ratio of sensitivities is set, to leading order, by atmospheric feedbacks described by B_OLR and B_dn. An interesting property is that the ice edge is always more sensitive to OHTC than AHTC, with equality of sensitivities only in the (unrealistic) limits $B_\mathrm{OLR} \to 0$ or $B_\mathrm{dn} \to \infty$. Both of these parameters relate to how much AHTC is transferred to the surface. Larger values of either B_OLR or B_dn lead to larger loss of heat from the atmosphere; in the former case heat is lost to space (thus reducing the relative impact of AHTC on the ice edge) and in the latter case it is lost to the surface where it is absorbed by sea ice (thus increasing the relative impact of AHTC on the ice edge).

The third, higher-order term in Eq. (3.15) suggests that the sensitivity of the

ice edge to OHTC relative to AHTC decreases with k_i, increases with $\langle\overline{H_\mathrm{i}}\rangle$ and increases with B_up. This term represents two additional processes relating to the diversion of heat away from the ice surface. Firstly, any increase in downwelling longwave radiation attributed to an increase in AHTC may simply be re-emitted to the atmosphere, the proportion of which depends on B_up. A larger B_up thus decreases s_a, increasing $s_\mathrm{o}/s_\mathrm{a}$. Secondly, the ocean–ice heat flux melts ice directly at the base. The subsequently thinner ice then conducts heat to the surface more effectively, increasing the surface temperature and longwave component of F_up, counteracting the initial melting (this is analogous to the ice-thickness feedback; e.g., Bitz and Roe, 2004). For larger $\langle\overline{H_\mathrm{i}}\rangle$, smaller k_i, or smaller B_up, this effect is smaller. Note that B_up controls both processes, but the atmosphere–surface effect dominates the ice-thickness effect [$\partial(s_\mathrm{o}/s_\mathrm{a})/\partial B_\mathrm{up} > 0$ for all parameter choices]. Overall, Eq. (3.15) describes the difference in sensitivities in terms of how perturbations to AHTC and OHTC are diverted to/from the ice pack.

3.3.2 Effective sensitivity to OHT

Equation (3.15) provides insight on why heat converging under sea ice has a larger impact than the same heat converging over it. Here, a more general equation in terms of the heat transport across a fixed latitude is discussed. This does not require a specific underlying mechanism to be applicable, and ultimately bridges the gap between the EBM and behaviour of coupled GCMs in chapters 4–5.

(a) Derivation

Consider the annual-mean, spatial-mean energy balance of the region between a fixed reference latitude ϕ_0 and the pole. From conservation of energy, changes in

heat fluxes at the boundaries (TOA and at ϕ_0) of this region must satisfy:

$$\Delta\langle\overline{F_{\mathrm{sw}}}\rangle = \Delta\langle\overline{F_{\mathrm{OLR}}}\rangle - \frac{\Delta\overline{\mathrm{OHT}} + \Delta\overline{\mathrm{AHT}}}{A}, \tag{3.16}$$

where F_{sw} is net shortwave radiation, $A = 2\pi R_{\mathrm{E}}^2(1 - \sin\phi_0)$ is the surface area between ϕ_0 and the pole, and $\overline{\mathrm{OHT}}$ and $\overline{\mathrm{AHT}}$ are evaluated at ϕ_0. In the EBM, $F_{\mathrm{sw}} \equiv aS$. Here, shortwave radiation is written as a general flux F_{sw}, as this makes more sense when the result of this section (Eq. 3.23a) is later applied to CMIP6 models, where the explicit decomposition of net shortwave into the incident solar radiation and planetary coalbedo is not required.

Assuming $\overline{\mathrm{OHT}}$ and $\overline{\mathrm{AHT}}$ are strongly coupled by Bjerknes compensation, with $b_{\mathrm{c}} = \Delta\overline{\mathrm{AHT}}/\Delta\overline{\mathrm{OHT}}$, the Bjerknes compensation rate, allows $\Delta\overline{\mathrm{AHT}}$ to be eliminated:

$$\Delta\langle\overline{F_{\mathrm{sw}}}\rangle = B_{\mathrm{OLR}}\Delta\langle\overline{T_{\mathrm{a}}}\rangle - \frac{1}{A}\left(1 + b_{\mathrm{c}}\right)\Delta\overline{\mathrm{OHT}}, \tag{3.17}$$

where Eq. (2.4) was also used on the OLR term. The mean air temperature, $\langle\overline{T_{\mathrm{a}}}\rangle$, is eliminated in favour of the mean surface temperature, $\langle\overline{T_{\mathrm{s}}}\rangle$, using the energy balance of the atmospheric layer:

$$\Delta\langle\overline{F_{\mathrm{OLR}}}\rangle = \Delta\langle\overline{F_{\mathrm{up}}}\rangle - \Delta\langle\overline{F_{\mathrm{dn}}}\rangle + \frac{b_{\mathrm{c}}\Delta\overline{\mathrm{OHT}}}{A} \tag{3.18}$$

(cf. Eq. 2.1), or, using Eqs. (2.2–2.4):

$$B_{\mathrm{OLR}}\Delta\langle\overline{T_{\mathrm{a}}}\rangle = B_{\mathrm{up}}\Delta\langle\overline{T_{\mathrm{s}}}\rangle - B_{\mathrm{dn}}\Delta\langle\overline{T_{\mathrm{a}}}\rangle + \frac{b_{\mathrm{c}}\Delta\overline{\mathrm{OHT}}}{A}. \tag{3.19}$$

Rearranging for $\Delta\langle\overline{T_{\mathrm{a}}}\rangle$:

$$\Delta\langle\overline{T_{\mathrm{a}}}\rangle = \frac{B_{\mathrm{up}}}{B_{\mathrm{OLR}} + B_{\mathrm{dn}}}\Delta\langle\overline{T_{\mathrm{s}}}\rangle + \frac{b_{\mathrm{c}}}{A\left(B_{\mathrm{OLR}} + B_{\mathrm{dn}}\right)}\Delta\overline{\mathrm{OHT}}. \tag{3.20}$$

Substituting Eq. (3.20) into Eq. (3.17) and simplifying the $\Delta\overline{\mathrm{OHT}}$ terms:

$$\Delta\langle\overline{F_{\mathrm{sw}}}\rangle = \frac{\beta B_{\mathrm{up}}}{1+\beta}\Delta\langle\overline{T_{\mathrm{s}}}\rangle - \frac{1}{A}\left(1+\frac{b_{\mathrm{c}}}{1+\beta}\right)\Delta\overline{\mathrm{OHT}}. \tag{3.21}$$

Finally, it is assumed that changes in $\langle\overline{F_{\mathrm{sw}}}\rangle$ are purely a function of $\overline{\phi_{\mathrm{i}}}$. Physically, this assumption is based on the coalbedo difference between sea ice and ocean, δa, which increases net shortwave absorption when the area of ocean proportional to $\cos\overline{\phi_{\mathrm{i}}}\Delta\overline{\phi_{\mathrm{i}}}$ is exposed, such that:

$$\Delta\langle\overline{F_{\mathrm{sw}}}\rangle = \langle\overline{S}\rangle\delta a\cos\overline{\phi_{\mathrm{i}}}\Delta\overline{\phi_{\mathrm{i}}} \equiv s\Delta\overline{\phi_{\mathrm{i}}}, \tag{3.22}$$

where $\langle\overline{S}\rangle$ is the time- and spatial-mean TOA solar radiation. In practice, it is simpler to use the empirical constant s, i.e., the far-RHS of Eq. (3.22), to make this 'conversion' between F_{sw} and ϕ_{i}, rather than computing δa (which is not trivial because of the smoothing in the coalbedo formulation of Eq. 2.6).[3] Substitution of Eq. (3.22) into Eq. (3.21) then gives

$$\boxed{s\Delta\overline{\phi_{\mathrm{i}}} = \frac{\beta B_{\mathrm{up}}}{1+\beta}\Delta\langle\overline{T_{\mathrm{s}}}\rangle - \frac{1}{A}\left(1+\frac{b_{\mathrm{c}}}{1+\beta}\right)\Delta\overline{\mathrm{OHT}}} \tag{3.23a}$$

or, dividing through by $s\Delta\overline{\mathrm{OHT}}$ to get the effective sensitivity of the ice edge to OHT:

$$\boxed{\frac{\Delta\overline{\phi_{\mathrm{i}}}}{\Delta\overline{\mathrm{OHT}}} = \frac{\beta B_{\mathrm{up}}}{s\,(1+\beta)}\frac{\Delta\langle\overline{T_{\mathrm{s}}}\rangle}{\Delta\overline{\mathrm{OHT}}} - \frac{1}{sA}\left(1+\frac{b_{\mathrm{c}}}{1+\beta}\right)} \tag{3.23b}$$

(b) Interpretation

Two clarifying remarks should be made. Firstly, note that the LHS of Eq. (3.23a) is really just $\Delta\langle\overline{F_{\mathrm{sw}}}\rangle$. This equation thus relies on a strong linear relationship

[3] This is not the same as the 'conversion' between mean solar radiation and the ice edge in the derivation of Eq. (3.15): in that case, spatial averages are taken over sea ice, whereas here, spatial averages are over a fixed region.

between ϕ_i and F_sw averaged between ϕ_0 and the pole in order to connect changes in ϕ_i with OHT and T_s. Secondly, it should be emphasised that Eq. (3.23a) describes the effective (to use the same terminology distinguishing 'effective' and 'actual' sensitivities in the previous sections) responses of each variable $\overline{\phi_\mathrm{i}}$, $\langle\overline{T_\mathrm{s}}\rangle$, and $\overline{\mathrm{OHT}}$. Thus, the minus sign on the term multiplying $\Delta\overline{\mathrm{OHT}}$ does not imply that increases in $\overline{\mathrm{OHT}}$ should increase the sea ice cover, because $\Delta\langle\overline{T_\mathrm{s}}\rangle$ and $\Delta\overline{\mathrm{OHT}}$ are highly correlated—that is, the effect of $\Delta\overline{\mathrm{OHT}}$ is partly captured by $\Delta\langle\overline{T_\mathrm{s}}\rangle$.

Equation (3.23a) expresses energy conservation in a manner which parallels the classic diffusive EBM formulation of Eq. (1.2): net shortwave radiation (the LHS of Eq. 3.23a), is balanced by OLR [first term on the right-hand side (RHS) of Eq. 3.23a] and net heat transport into the region (second term on the RHS of Eq. 3.23a). The first term on the RHS of Eq. (3.23a) represents the contribution to the OLR from surface heat loss to the atmosphere. The upward surface flux appears directly as $\Delta\langle\overline{F_\mathrm{up}}\rangle = B_\mathrm{up}\Delta\langle\overline{T_\mathrm{s}}\rangle$, and is weighted by a factor which represents the fraction of it partitioned into OLR: $B_\mathrm{OLR}/\left(B_\mathrm{OLR}+B_\mathrm{dn}\right)$. This is similar to the partitioning of AHTC into upward and downward components which, being controlled by the relative values of B_OLR and B_dn, lead to the factor of β in Eq. (3.15). This factor also appears in Eq. (3.23a): since $b_\mathrm{c}\Delta\overline{\mathrm{OHT}} = \Delta\overline{\mathrm{AHT}}$, the coefficient in front of the 'hidden' $\Delta\overline{\mathrm{AHT}}$ in Eq. (3.23a) is smaller than that in front of $\Delta\overline{\mathrm{OHT}}$ by the same factor of $1+\beta$.

The EBM effective sensitivity of the ice edge to OHT can be determined from the K_o and F_bp sensitivity experiments, as shown in Fig. 3.9a. To focus on a relatively small perturbation to the reference state, only the $K_\mathrm{o} = (1\pm0.25)K_\mathrm{o}^\mathrm{ref}$ simulations, and the varied-F_bp simulations falling in the same range of OHT, are shown. The OLS fits give the effective sensitivities to OHT at $\phi_0 = 60°\mathrm{N}$ when K_o varies (blue, $16.7°\mathrm{N\ PW^{-1}}$) and when F_bp varies (green, $13.7°\mathrm{N\ PW^{-1}}$). Equation (3.23b) shows that these effective sensitivities depend on the terms $\Delta\langle\overline{T_\mathrm{s}}\rangle/\Delta\overline{\mathrm{OHT}}$, b_c, and s. These are given by the OLS slopes in panels (b), (c),

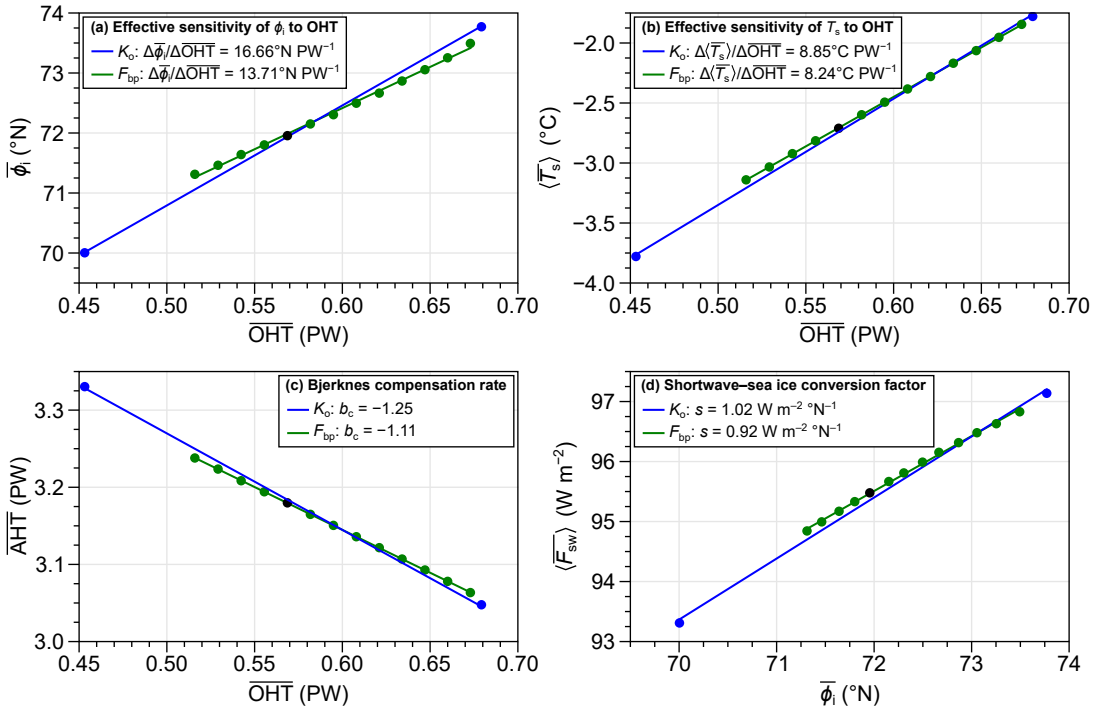

Figure 3.9: (a) Effective sensitivity of the ice edge to OHT across 60°N as K_o varies (blue) and as F_{bp} varies (green). The reference state is shown in black. Only a subset of simulations are shown in each case (see main text). Slopes of the OLS fits in the legends of (b)–(d) give the terms in Eq. (3.23b), respectively: $\Delta\langle\overline{T}_s\rangle/\Delta\overline{\mathrm{OHT}}$, $b_c = \Delta\overline{\mathrm{AHT}}/\Delta\overline{\mathrm{OHT}}$, and $s = \Delta\langle\overline{F}_{sw}\rangle/\Delta\overline{\phi}_i$.

and (d) respectively of Fig. 3.9, which show plots of the required quantities in both sensitivity experiments. Inserting the reference state constants (from Table 2.1) and these terms for the K_o case, the RHS of Eq. (3.23b) evaluates to 16.6°N PW^{-1}, and repeating this for the F_{bp} case gives 13.7°N PW^{-1}. Both of these calculated sensitivities agree with the OLS-determined sensitivities within 1%. Considering the results of section 3.2 showing clear differences in the qualitative behaviour of varying K_o and varying F_{bp}, this verifies that Eq. (3.23a) is unaffected by the underlying mechanism.

The differences in the terms on the RHS of Eq. (3.23b) between the K_o and F_{bp} cases are not striking, but are enough to give rise to an effective sensitivity about 25% larger when K_o varies than when F_{bp} varies. This can be understood from the values of the terms in Eq. (3.23b). First, the effective sensitivity

of surface temperature to OHT is slightly larger when K_o varies (Fig. 3.9b), contributing to a larger effective sensitivity of the ice edge, consistent with the description in section 3.2.1 where intense OHTC near the ice edge is partially lost to the atmosphere, contributing to poleward warming. This also explains the more negative value of b_c when K_o varies (Fig. 3.9c), since some of that heat loss will be transported equatorward by the atmosphere. A more negative b_c also increases the sea ice sensitivity to OHT according to Eq. (3.23b). Finally, s is larger when K_o varies (Fig. 3.9d): this would decrease $\Delta\overline{\phi_i}/\Delta\overline{\mathrm{OHT}}$, so the T_s and b_c effects explain the larger sensitivity in the K_o case.

It is worth emphasising the simplicity of Eq. (3.23a), which is perhaps obscured by the number of parameters appearing in it. This is particularly important since it represents the first attempt at providing a simple diagnostic equation to interpret the emergent sea ice–OHT relationship in GCMs. As mentioned in section 1.2.2, such models typically exhibit BC robustly and strongly. Thus, b_c might be treated as a constant, with a value close to -1. Assuming the same can be done for s, and that the atmospheric radiation parameters B_{up}, B_{dn}, and B_{OLR}, can be derived following a similar procedure as for the reanalysis data (section 2.3.2), Eq. (3.23a) can be expressed as:

$$\Delta\overline{\phi_i} = X\Delta\langle\overline{T_s}\rangle - Y\Delta\overline{\mathrm{OHT}}, \tag{3.24}$$

where the various parameters, including s and b_c on the above assumptions, are bundled into the constants X and Y. The Δ operators in this equation could refer to a variation across ensemble members of a GCM simulation, across a collection of different GCMs, or to a time difference (e.g., in a climate change simulation). In these contexts, Eq. (3.24) suggests that variations in sea ice extent are determined simply by surface temperature and OHT, with coefficients depending on what are essentially atmospheric properties. This is investigated in chapters 4 and 5.

3.4 Discussion

The sensitivity experiments in section 3.2 showed that the ice-edge latitude is more sensitive to OHTC than AHTC, but results depend on whether the ice cover exists perennially or seasonally. In the perennial case, ϕ_i is more sensitive to OHTC than AHTC by roughly a factor of 2 (found by varying the ocean–ice flux parameter, F_bp), and by a further factor of 2 (i.e., 4 times more sensitive in total) if the OHTC perturbation is concentrated at the ice edge (found by varying the mixed-layer diffusivity, K_o). This higher sensitivity to oceanic than atmospheric heat is consistent with previous studies (Thorndike, 1992; Singh et al., 2017); in particular, Eq. (3.15) appears to be an expanded form of the result found by Eisenman (2012, Eq. 17). These results are built upon here by quantifying the sensitivity of ice extent (rather than thickness) in a two-layer, latitudinally-varying system, making explicit the role of meridional energy transports.

It is worth recalling the estimate of the effective sensitivity of ϕ_i to net MHT convergence, 0.46°N (W m^{-2})$^{-1}$, in the classic diffusive EBM (Fig. 1.5c). This is similar to the sensitivities derived in the new EBM, and lies between the perennial and seasonal h_a (close to the net MHT convergence) sensitivities of the new EBM. The classic EBM does not yield information about the ocean, but the effect on ϕ_i when varying F_bp can be compared to that of varying the constant F_b in the model of Wagner and Eisenman (2015, WE15), as discussed in section 1.3.3. Varying the constant F_b in WE15 gave a sensitivity of about 2°N (W m^{-2})$^{-1}$, which is closer to the K_o sensitivities in the present EBM. In WE15, however, the large sensitivity arises due to an increase in net heat content: raising their F_b has a similar effect to lowering A_OLR in the present EBM, for which about 0.7°N (W m^{-2})$^{-1}$ sensitivity occurs (Fig. 3.1a). The sensitivity to F_b in WE15 exceeds this because it is directly coupled to sea ice. Note the analogy of this argument to the simple upward versus downward partitioning of h_a via Eq. (3.15).

The ratio of perennial sensitivities is fairly robust to the background climate and is set to leading order by atmospheric feedback parameters according to Eq. (3.15), which suggests OHT is always a more effective driver of the ice edge compared to AHT. This is because only a fraction of AHTC is transferred to the ice since some of it is lost to space via OLR (or re-emission from the surface). In contrast, any OHT converging under sea ice must be absorbed by it. Part of the absorbed ocean heat flux melts ice at the base, although a mechanism similar to the ice-thickness feedback plays a role in which the resulting thinner ice more effectively conducts heat to the surface where it may be radiated away.

When the ice cover is seasonal, the sensitivities of the ice edge to AHTC and OHTC are roughly the same, but both are larger than the perennial sensitivities. This is associated with uninhibited air–sea fluxes in ice free months making the two heat transports have similar roles to play in warming the high latitudes, and increased solar absorption which further enhances warming. Sensitivities for the SIF regime should be considered with more caution than those for the perennial regime, because it is possible that under the former conditions the B values would change: for instance, in response to increasing Arctic cloud cover (Kay and Gettelman, 2014; Vihma, 2014; Huang et al., 2019).

Bjerknes compensation, in which the AHTC counteracts a change in OHTC, was shown to play a major role by modulating the impact of OHTC on the ice edge. The effective sensitivity of the ice edge to increasing OHTC is about two-thirds its actual sensitivity in both regimes. This is likely relevant to coupled GCMs: Outten et al. (2018) established the presence of BC in a number of CMIP5 models' historical simulations, with typical rates of compensation similar to that found in the present EBM. They report an average ratio of heat-transport anomalies of -0.78 ± 0.35, and that BC mainly occurs in regions of strong air–sea fluxes (particularly the high latitudes and near the northern mid-latitude storm track). Supported by theoretical ideas developed by Liu et al. (2016), they explain

that the rates of compensation in models are related to local climate feedbacks. This suggests that there may be a deeper link between the ice-edge sensitivities and BC than found in the present work, since the rate of BC is affected by the very parameters found to control the relative actual sensitivities. Nevertheless, the qualitative significance of AHT partly cancelling the effect of increasing OHT is a notable, novel result, discovered due to the formulation of independent OHT and AHT in the newly-developed EBM.

The simple, physical explanation for the sensitivities encapsulated in Eq. (3.15) suggests it is relevant to the real world. Of course, there are some caveats in making this connection. The EBM is zonally averaged and effectively applies to an aquaplanet: land and zonal asymmetries in surface fluxes and heat transport convergences clearly affect the real-world distribution of sea ice. Results have been interpreted against the northern hemisphere (by tuning the reference state to such conditions and allowing sea ice to exist up to the pole). It is plausible that these results, at least in the perennial regime, are relevant to the southern hemisphere as well (for example, the southern hemisphere value of β is the same as the northern hemisphere value; see section 2.3.2). As alluded to in section 2.1.2(b), and based on the description in section 1.1.1, it is plausible to expect that Arctic sea ice would behave more in line with the K_o sensitivity experiment, while Antarctic sea ice might behave more like the F_bp sensitivity experiment. This would have implications for the sea ice sensitivities to OHT in the two hemispheres of GCMs and the real world, but the investigation of chapter 4 is required to gather more evidence of this.

Some other caveats relate to the physical realism of the EBM. For example, it does not represent leads in the ice pack, thereby assuming that 100% of OHT converging under ice melts it (rather than escaping to the atmosphere). This is reasonable though since, although surface fluxes may indeed reach ~ 100 W m^{-2} over such areas of exposed ocean, these persist on sub-daily timescales (Heorton

et al., 2017) and so is averaged out on the EBM scale. Sea ice dynamics have not been included, which may be particularly important in relating these results to the southern hemisphere where sea ice export to warmer latitudes is a key process (section 1.1.1). However, to first order this would likely only affect the reference state (for the same thermodynamic conditions, the sea ice edge would move poleward), and this could simply be re-tuned. Of particular importance to Eq. (3.23a) is how changes in net shortwave radiation, F_{sw}, only depend on the position of the ice edge (Eq. 2.6). Net shortwave radiation can also be affected by changes in cloud cover, for example, which can occur independently of changes in sea ice. Equation (3.21) shows that there is a sensitivity of F_{sw} to OHT arising from maintenance of the TOA radiation balance. Assuming that all of this sensitivity directly translates into sea ice sensitivity is true in the EBM as constructed, but for the real world this implies that the sensitivities from the EBM are overestimated.

Heat transports are usually quantified in terms of the transport (in W) across a fixed latitude, whereas here the sensitivity experiments mainly used the average convergences (in W m^{-2}) over a variable area, h_{a} and h_{o}. In the EBM these are linearly related, but this may not be so in the real world or a coupled GCM. There may also be some point between the results of the K_{o} and F_{bp} sensitivity experiments which gives the most realistic picture, dependent on the real-world distribution of incoming OHT across the ice pack, or that in GCMs. This point is addressed to some extent by the second analytical result, Eq. (3.23a), which only assumes energy conservation and is valid for any underlying mechanism. It does, however, rely on a strong conversion between the sea ice edge and net shortwave radiation (i.e., a strong influence of sea ice cover on the planetary albedo) in order to yield information about sea ice sensitivity. It remains to be seen whether such a relationship emerges in the average behaviour of GCMs (or whether it is obscured by other factors determining the planetary albedo, or zonal asymmetries). The

first analytical result, Eq. (3.15), nevertheless remains useful in providing an explanation of a fundamental difference between atmospheric and oceanic forcing on sea ice—as alluded to in previous work (Thorndike, 1992; Eisenman, 2012; Singh et al., 2017)—in simple physical terms.

3.5 Chapter summary

A summary of the key results from the EBM sensitivity studies in this chapter is as follows:

1. **A general sensitivity study was carried out on all parameters:**
   a) Broadly, sea ice is most sensitive to radiation parameters, least sensitive to sea ice parameters, with OHT parameters in between;
   b) The climate sensitivity of the EBM is comparable to observational estimates, suggesting that other sensitivities derived from the EBM are relevant to the real world.
2. **By calculating AHTC and OHTC averaged over sea ice (h_a and h_o respectively), it was found that the ice edge latitude ϕ_i:**
   a) is about twice as sensitive to h_o than to h_a;
   b) is a further factor of 2 more sensitive to h_o when OHTC is concentrated near the ice edge;
   c) is 'effectively' about $1/3$ less sensitive to OHTC in practice due to Bjerknes compensation, because reduced AHTC partially offsets the 'actual' sensitivity to OHTC;
   d) is equally sensitive to h_o and to h_a in a seasonally ice-free climate.

3. **An equation (3.15) was derived explaining why the impact of h_a is reduced relative to h_o:**

   a) AHTC is partly transferred downward to sea ice and partly lost via OLR, as controlled by atmospheric radiative feedback parameters;

   b) Surface cooling further reduces the impact of AHTC, with higher-order corrections due to vertical heat diffusion through sea ice depending on its thickness and thermal conductivity.

4. **Another equation (3.23) directly describes the effective sensitivity of ϕ_i to OHT, which:**

   a) connects changes in sea ice, OHT, and surface temperature;

   b) does not depend on an underlying mechanism of OHT;

   c) parameterises specific processes (particularly Bjerknes compensation), providing a simple diagnostic that could be applied to GCMs.

Chapter 4

How does natural ocean variability affect sea ice?

This chapter begins the analysis of coupled GCMs, by assessing the role of natural variations in OHT in driving sea ice extent on multidecadal timescales. Here, the focus is on explicating the underlying mechanisms, comparing the behaviour of the northern (NH) and southern (SH) hemisphere, within and across models. The relationship between OHT and sea ice extent is also cast into the theoretical framework of the EBM analysis in the previous chapter. This provides a test of the EBM results, generates insight into GCM behaviour, and sets up the analysis of future-climate simulations in chapter 5.

In section 4.1, the data and methodology are described, including details of the diagnostic procedures and an assessment of their shortcomings. The analysis begins in section 4.2, firstly by computing correlations between sea ice, OHT, and AHT, which suggests different mechanisms in the northern and southern hemispheres. This is examined in more detail by looking at spatial patterns of the changes in sea ice extent, OHTC, and AHTC, in a selected model. The similarity to other models is then verified, making use of the EBM diagnostics of OHTC and AHTC averaged over sea ice (h_o and h_a, respectively). Section 4.3 tests whether

the analytical result derived in the EBM analysis connecting variations in sea ice, OHT, and surface temperature (Eq. 3.23a) can explain the relationship between OHT and sea ice extent in models (considered individually and collectively). The results from this chapter are discussed in section 4.4 and summarised in section 4.5. The material in sections 4.1–4.2 has been adapted from the author's published work (Aylmer et al., 2022).

4.1 Data and methods

4.1.1 Models and simulations

The CMIP6 pre-industrial (PI) control runs provide a set of multi-century simulations of unforced climate variability suitable for this analysis. All models providing the raw fields needed to calculate the main diagnostics required (section 4.1.2) are included. This gives 20 models from various modelling groups, with a range of physical cores and resolutions. Eleven provide a 500 yr time series, one is shorter (CNRM-CM6-1-HR, 300 yr), and the remaining eight are longer (Table 4.1). Most models have one PI-control ensemble member. For MPI-ESM1-2-LR and MRI-ESM2-0, which provide more than one, the longest time series is used (both having realisation label r = 1). For CanESM5 and CanESM5-CanOE, the members with perturbed-physics label p = 2 are used, in which a different interpolation procedure couples wind stress from the atmosphere to the ocean. The developers explain that this improves the representation of local ocean dynamics but otherwise does not substantially impact the large-scale climate relative to the standard configuration with p = 1 (Swart et al., 2019). The first 1000 yr of the 2000 yr IPSL-CM6A-LR simulation with initialisation label i = 1 is analysed (because sections of data were missing for some fields). NorCPM1 provides three 500 yr realisations, but only that with r = 1 is

included. For further details, see the references cited in Table 4.1.

4.1.2 Diagnostics

(a) Sea ice

Sea ice extent, S_i, is calculated directly from the monthly-mean sea ice concentration, c_i, and ocean grid cell area, A_o, fields by summing A_o over cells with $c_\mathrm{i} \geq c_\mathrm{i}^\star$, in each hemisphere separately, as a function of time. The concentration threshold, $c_\mathrm{i}^\star$, is taken to be 15%. A similar procedure is used for sea ice area, A_i, but weighting A_o by c_i and including all grid cells (i.e., not just those with $c_\mathrm{i} > c_\mathrm{i}^\star$). For consistency S_i and A_i are computed from c_i regardless of whether they are provided as standard outputs, since the c_i data are required for other diagnostics. Note also that S_i and A_i are only needed to validate the computation and use of the ice-edge latitude, ϕ_i, which serves as the main quantification of 'sea ice cover'. For this, c_i is interpolated onto a regular, fixed grid, then the algorithm described by Eisenman (2010) is applied. This determines ϕ_i as a function of longitude, λ, by identifying meridionally adjacent grid cells where the equatorward cell satisfies $c_\mathrm{i} < c_\mathrm{i}^\star$ and the poleward cell satisfies $c_\mathrm{i} \geq c_\mathrm{i}^\star$. If land is present in any cell within a meridional distance y_L of the identified pair, it is rejected. In the case of multiple ice edges for a given longitude, the one nearest the equator is chosen. This procedure results in a set of ice edges representative of the thermodynamically-driven evolution of the sea ice cover, eliminating locations where the ice edge is temporarily fixed simply because there is no ocean for it to move into. Using the cf-python package (Hassell et al., 2017), c_i is linearly interpolated onto a fixed grid of resolution $\delta\phi = 0.5°$. For the land checking, $y_\mathrm{L} = 100$ km is chosen which corresponds to 2 nearest grid cells when $\delta\phi = 0.5°$.[1]

[1] In the original implementation by Eisenman (2010), land checking was done directly on the meridionally-adjacent cells.

Table 4.1: Physical models and approximate resolutions of the atmosphere, ocean, and sea ice components of the CMIP6 models analysed in this thesis. Lengths t_{PI} (yr) of the PI controls are also given. The last column gives references for full details. In each case, sea ice is on the ocean grid. CNRM-CM6-1 is not analysed in this chapter because (at the time of analysis) it does not provide sea ice concentration data for its PI control simulation, but does for the historical and ScenarioMIP simulations and is thus included in the analysis in chapter 5.

Model	t_{PI}	Atmosphere		Ocean		Sea ice	Reference
ACCESS-CM2	500	MetUM GA7.1	250 km	MOM5	1°	CICE 5.1.2	Bi et al. (2020)
ACCESS-ESM1-5	900	MetUM GA1	250 km	MOM5	1°	CICE 4.1	Ziehn et al. (2020)
CAMS-CSM1-0	500	ECHAM 5	100 km	MOM4	1°	SIS 1.0	Rong et al. (2018)
CanESM5	1050	CanAM5	500 km	NEMO 3.4.1	1°	LIM 2	Swart et al. (2019)
CanESM5-CanOE	500	CanAM5	500 km	NEMO 3.4.1	1°	LIM 2	Swart et al. (2019)
CESM2	1200	CAM6	100 km	POP2	1°	CICE 5.1	Danabasoglu et al. (2020)
CESM2-FV2	500	CAM6	250 km	POP2	1°	CICE 5.1	Danabasoglu et al. (2020)
CESM2-WACCM	500	WACCM6	100 km	POP2	1°	CICE 5.1	Danabasoglu et al. (2020)
CESM2-WACCM-FV2	500	WACCM6	250 km	POP2	1°	CICE 5.1	Danabasoglu et al. (2020)
CNRM-CM6-1	—	ARPEGE 6.3	250 km	NEMO 3.6	1°	GELATO 6.1	Voldoire et al. (2019)
CNRM-CM6-1-HR	300	ARPEGE 6.3	100 km	NEMO 3.6	0.25°	GELATO 6.1	Voldoire et al. (2019)
CNRM-ESM2-1	500	ARPEGE 6.3	150 km	NEMO 3.6	1°	GELATO 6.1	Séférian et al. (2019)
HadGEM3-GC31-LL	500	MetUM GA7.1	250 km	NEMO 3.6	1°	CICE 5.1	Menary et al. (2018)
HadGEM3-GC31-MM	500	MetUM GA7.1	100 km	NEMO 3.6	0.25°	CICE 5.1	Menary et al. (2018)
IPSL-CM6A-LR	1000	LMDZ 6	250 km	NEMO 3.6	1°	LIM 3	Boucher et al. (2020)
MPI-ESM-1-2-HAM	780	ECHAM 6.3	250 km	MPIOM 1.63	1.5°	In ocean model	Mauritsen et al. (2019)
MPI-ESM1-2-HR	500	ECHAM 6.3	100 km	MPIOM 1.63	0.4°	In ocean model	Müller et al. (2018)
MPI-ESM1-2-LR	1000	ECHAM 6.3	250 km	MPIOM 1.63	1.5°	In ocean model	Mauritsen et al. (2019)
MRI-ESM2-0	700	MRI-AGCM3.5	100 km	MRI-COM 4.4	0.5°	In ocean model	Yukimoto et al. (2019)
NorCPM1	500	CAM-OSLO4.1	250 km	MICOM 1.1	1°	CICE 4	Counillon et al. (2016)
UKESM1-0-LL	1880	MetUM GA7.1	250 km	NEMO 3.6	1°	CICE 5.1	Sellar et al. (2019)

An example of the identification of ϕ_i using this algorithm is shown in Fig. 4.1, which plots c_i contours and $\phi_\mathrm{i}(\lambda)$ in March and September in the first year of the PI-control simulation of HadGEM3-GC31-LL. Note the difference between the $c_\mathrm{i}^\star$ contour and $\phi_\mathrm{i}(\lambda)$, which is particularly evident in the NH. In the SH when sea ice is close to its maximum seasonal extent, the $c_\mathrm{i}^\star$ contour and $\phi_\mathrm{i}(\lambda)$ happen to be identical in this case (Fig. 4.1, bottom right) because the ice edge is sufficiently far from land everywhere. Since this analysis is considering long-term averages, the sensitivity to the choice of interpolation resolution, the land-checking parameter y_L, and selecting nearest the pole instead of the equator in the case of multiple ice edges, is low. This is demonstrated in Fig. 4.2, which plots the time series of 25 yr averages (explained in section 4.1.3) of $\overline{\phi_\mathrm{i}}$, zonally averaged, in HadGEM3-GC31-LL, for various combinations of the diagnostic options. In the SH, there is little sensitivity to $\delta\phi$ and even less to y_L because land does not obstruct Antarctic sea ice that much. In the NH, the most important option is y_L which causes a poleward shift of ~ 0.5°N when doubling y_L (at fixed $\delta\phi$). Overall, different choices result mostly in an offset of the time series without affecting multidecadal variability (i.e., anomalies $\Delta\overline{\phi_\mathrm{i}}$) which is of interest here. Python code implementing this algorithm is archived online (Aylmer, 2021).

The ice-edge latitude diagnosed in this way and zonally averaged is an effective way of quantifying the sea ice cover. In addition to the connection with the EBM analysis, this is because it can be easily compared across models and works naturally when analysing heat transported across a fixed latitude. The three metrics, S_i, A_i, and ϕ_i, are strongly correlated in each model (Fig. 4.3), and are thus effectively interchangeable; i.e., correlations based on ϕ_i can be applied to S_i or A_i (with sign reversal). However, the slope $\Delta\phi_\mathrm{i}/\Delta S_\mathrm{i}$ (or $\Delta\phi_\mathrm{i}/\Delta A_\mathrm{i}$) is about twice as large in the NH compared to the SH. This is partly because the area change associated with a latitude increment $\phi \to \phi + \Delta\phi$ is proportional to $\cos\phi$, and so is larger in the SH where the mean ice edge is at a lower latitude,

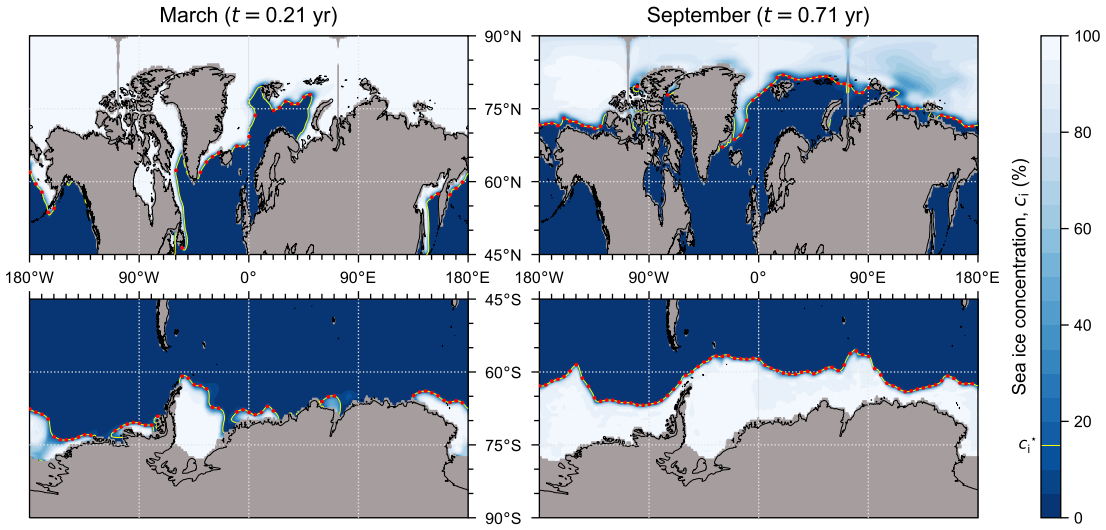

Figure 4.1: Ice-edge latitude as a function of longitude, $\phi_i(\lambda)$ (red points), at two selected times during the first year of the PI-control simulation of HadGEM3-GC31-LL: (left) March and (right) September. The $c_i^\star = 15\%$ concentration contour is shown in yellow. The algorithm described in section 4.1.2 was used, with $\delta\phi = 0.5°$, $y_L = 100$ km, and choosing nearest the equator in the case of multiple possible $\phi_i(\lambda)$. Points of $\phi_i(\lambda)$ are only shown in 5°E intervals of λ for clarity. Grey shading indicates missing data (land mask) in the model. Coastlines (thin, black) are added for illustration and are not part of the model.

$\sim 64°$S, than in the NH, $\sim 68°$N. The dominant effect, however, is due to land: in the NH, about 50% of longitudes at 68°N are occupied by land, whereas 64°S is land free (see Fig. 4.6). Both geometric effects mean that a given change in ϕ_i represents a larger areal change in sea ice cover in the SH compared to that in the NH, resulting in the factor of 2 difference in the slopes of Fig. 4.3. This means, for example, that equal sensitivities of the NH and SH ice edge to OHT implies a factor of 2 difference in the S_i sensitivities. Figure 4.3 also shows that the inter-model spread in Antarctic sea ice-extent variability is about twice as large as that for the Arctic.

In section 4.2.2, sea ice thickness, H_i, is considered. This is computed from the `sivol` field, which is the ice volume per unit grid-cell area. Dividing by c_i gives the actual floe thickness. However, H_i could not be produced for CanESM5, CanESM5-CanOE, and NorCPM1, because `sivol` was not available for these models. Also required in that section is the near-surface air temperature (field:

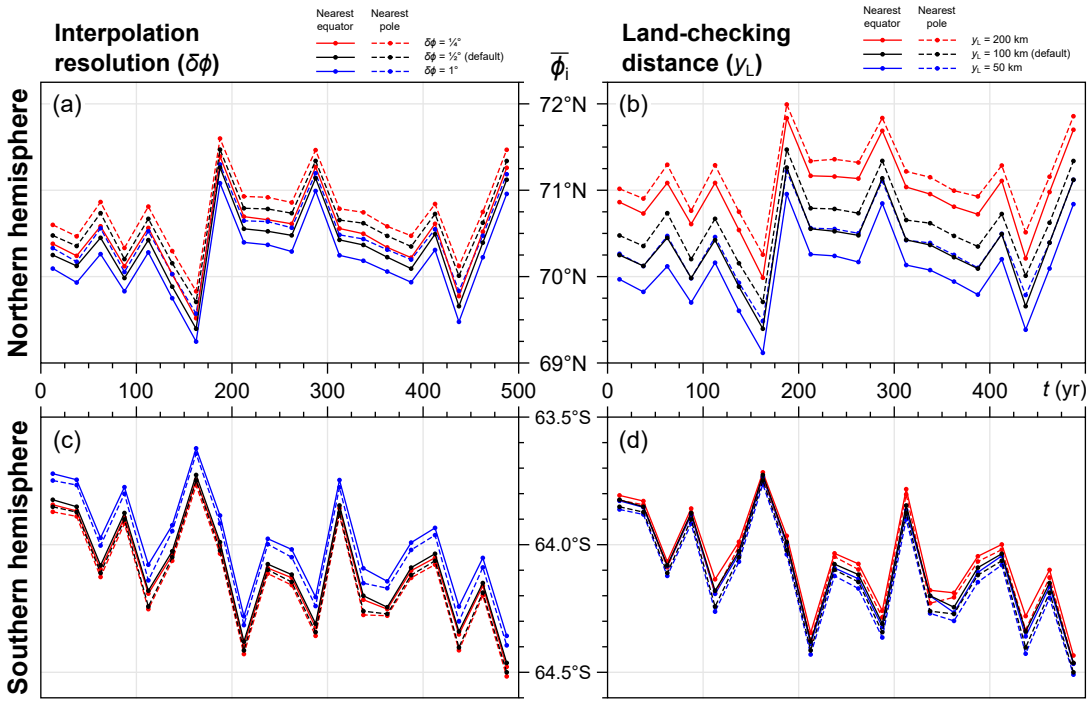

Figure 4.2: Time series of 25 yr averages of the zonal-mean ice edge latitude, $\overline{\phi_\mathrm{i}}$, in the PI-control simulation of HadGEM3-GC31-LL, for various choices of the ice-edge algorithm parameters. (a,c) Sensitivity to choosing a different interpolation resolution, $\delta\phi$, in the NH and SH respectively (in all cases with $y_\mathrm{L} = 100$ km). (b,d) Sensitivity to choice of land-checking distance, y_L, in the NH and SH respectively (in all cases with $\delta\phi = 0.5°$). Also shown in each case in (a)–(d) is the difference between choosing nearest the equator (solid) or pole (dashed) in the case of multiple ice edges at a given longitude.

`tas`), which is provided by all models in Table 4.1 and does not require manipulation other than averaging.

(b) Meridional heat transport

At the time of analysis, few models provided northward OHT already diagnosed (field: `hfbasin`). Computing OHT directly from the ocean current and temperature fields for each model is impractical due to data volume, non-trivial grid geometries, and issues with closing heat budgets which may be worsened by interpolation. Here, Eq. (1.1) is exploited: since most models provide the net downward energy flux into the top of the ocean column (field: `hfds`; i.e., $-F_\mathrm{s}$ in Eq. 1.1), northward OHT is approximated at each latitude ϕ by integrating `hfds`

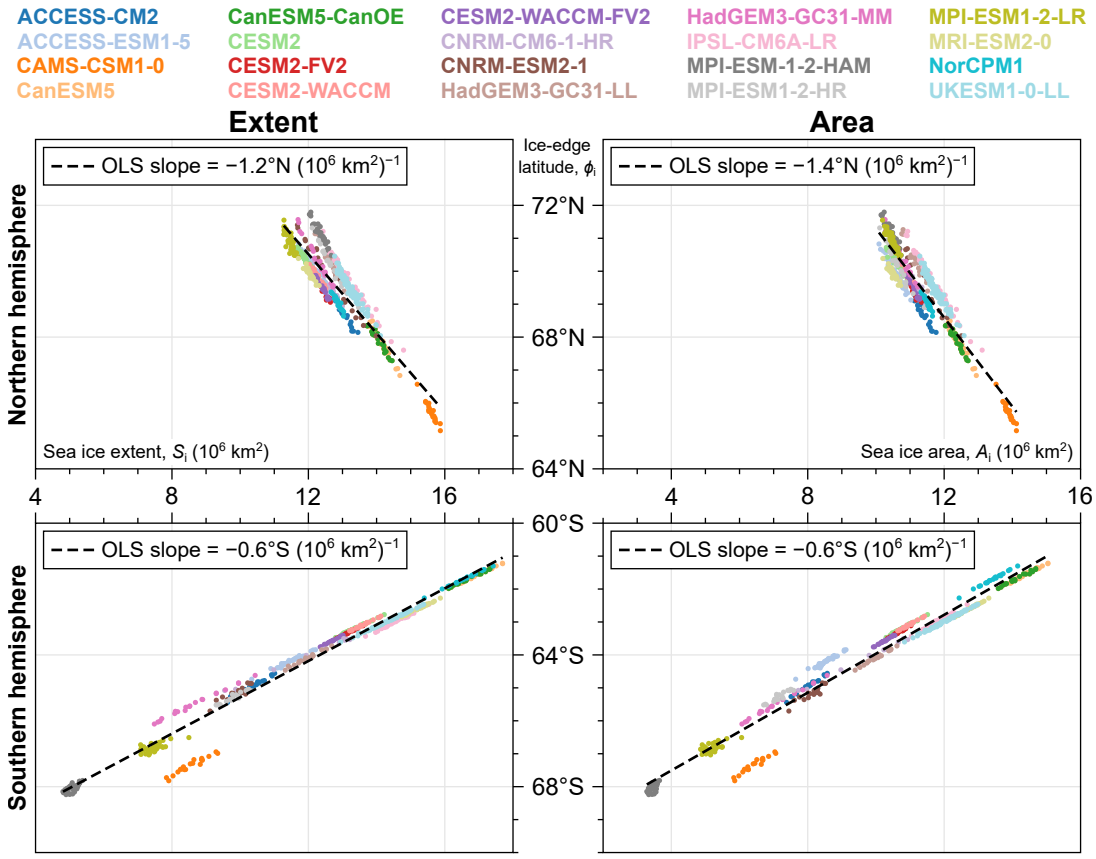

Figure 4.3: Zonal-mean sea ice edge latitude, ϕ_i, plotted against (left) sea ice extent, S_i, and (right) sea ice area, A_i, in the (top) NH and (bottom) SH. Each point is a 25 yr average from the corresponding model's (legend) PI-control simulation (see section 4.1.3). Ordinary least squares (OLS) lines are fitted to all points in each panel, with slopes given in the legends. Individual model correlations between each pair of diagnostics are all statistically significant at the 95% confidence level based on a t-test.

over the area north of ϕ. This neglects heat storage tendency (i.e., the LHS of Eq. 1.1, also not commonly provided), which on timescales relevant to this work manifests as a non-zero heat transport at the south pole of typical magnitude 0.1 PW (Fig. 4.4, top left), or less than 1 W m^{-2} averaged over the world ocean. For the SH analysis, a second version of OHT is computed by starting the integration at the south pole and proceeding north, which shifts the accumulated error into the NH (Fig. 4.4, bottom left).

The turbulent, longwave, and shortwave heat fluxes evaluated at the surface and TOA are combined to give the net heat flux into the atmospheric column which, neglecting atmospheric heat storage, gives the column-integrated moist-

static energy convergence. Then AHT follows from integrating in a similar manner as is done for OHT. Although neglecting the heat capacity of the atmosphere is a very good approximation, the same error arising in the OHT calculation manifests in the AHT calculated in this way (since AHT and OHT are coupled via F_s; Fig. 4.4, top right), so a second version of AHT is computed, integrating from the south pole (Fig. 4.4, bottom right), for the SH analysis.

Finally, under the same approximations just discussed, the heat transport divergences are given by `hfds` ($-$OHTC) and the net flux into the atmospheric column ($-$AHTC). Again, these neglect heat storage tendencies. To compute h_o and h_a, the OHTC and AHTC averaged over sea ice as defined in section 3.2, simply requires averaging the aforementioned fields over locations where $c_i \geq c_i^\star$. In the case of AHTC, this requires interpolation of c_i from the ocean grid to the atmospheric grid, which is done using the same procedure as for calculating ϕ_i (linear interpolation onto a fixed grid with resolution $\delta\phi = 0.5°$ using cf-python).[2]

4.1.3 Time-series analysis

To analyse how sea ice responds to natural variations in oceanic and atmospheric heat fluxes during the PI control simulations, a simple approach is taken by dividing each time series into consecutive, non-overlapping Δt year averages, and calculating Pearson correlations, r, between each pair of diagnostics. The choice $\Delta t = 25$ yr is sufficiently long to study multidecadal variability. To give a sense of the significance of r, critical values r_{crit} of a two-tailed Student's t-test on the null hypothesis that $r = 0$, at the 95% confidence level, are computed. Values of r exceeding r_{crit} in magnitude are then significant at the 95% confidence level. These depend on the time series length: for the shortest (300 yr), most common (500 yr), and longest (1880 yr) time series respectively, $r_{crit} = 0.50$, 0.38, and 0.19.

[2] Although some models provide c_i already interpolated onto their atmospheric grid, for consistency the interpolation of the ocean-grid version of c_i is done for all models.

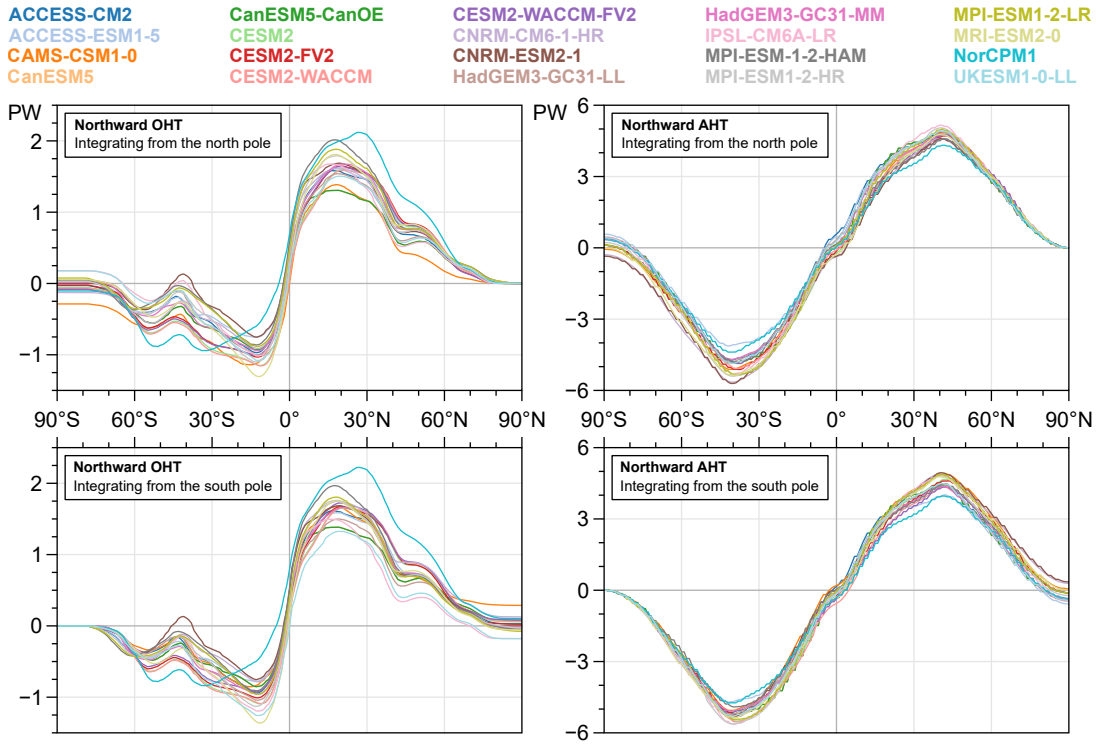

Figure 4.4: Northward OHT (left) and AHT (right) as a function of latitude, ϕ, calculated by integrating column heat fluxes north of each ϕ. In the top panels, the integration is started from the north pole, and in the bottom panels it is started from the south pole [see section 4.1.2(b)].

Computing critical values in this way assumes that the sets of 25 yr averages for individual diagnostics are uncorrelated. Figure 4.5 shows autocorrelations, r_a, of the main diagnostics for each model. In most cases r_a becomes insignificant at a lag of 25 yr. The worst case is r_a (ϕ_i), which is significant for 5 models in the NH and 9 in the SH. While this does not affect the correlations between diagnostics in the next section, it does mean that r_{crit} is a lower bound for models with significant autocorrelation at 25 yr lag.

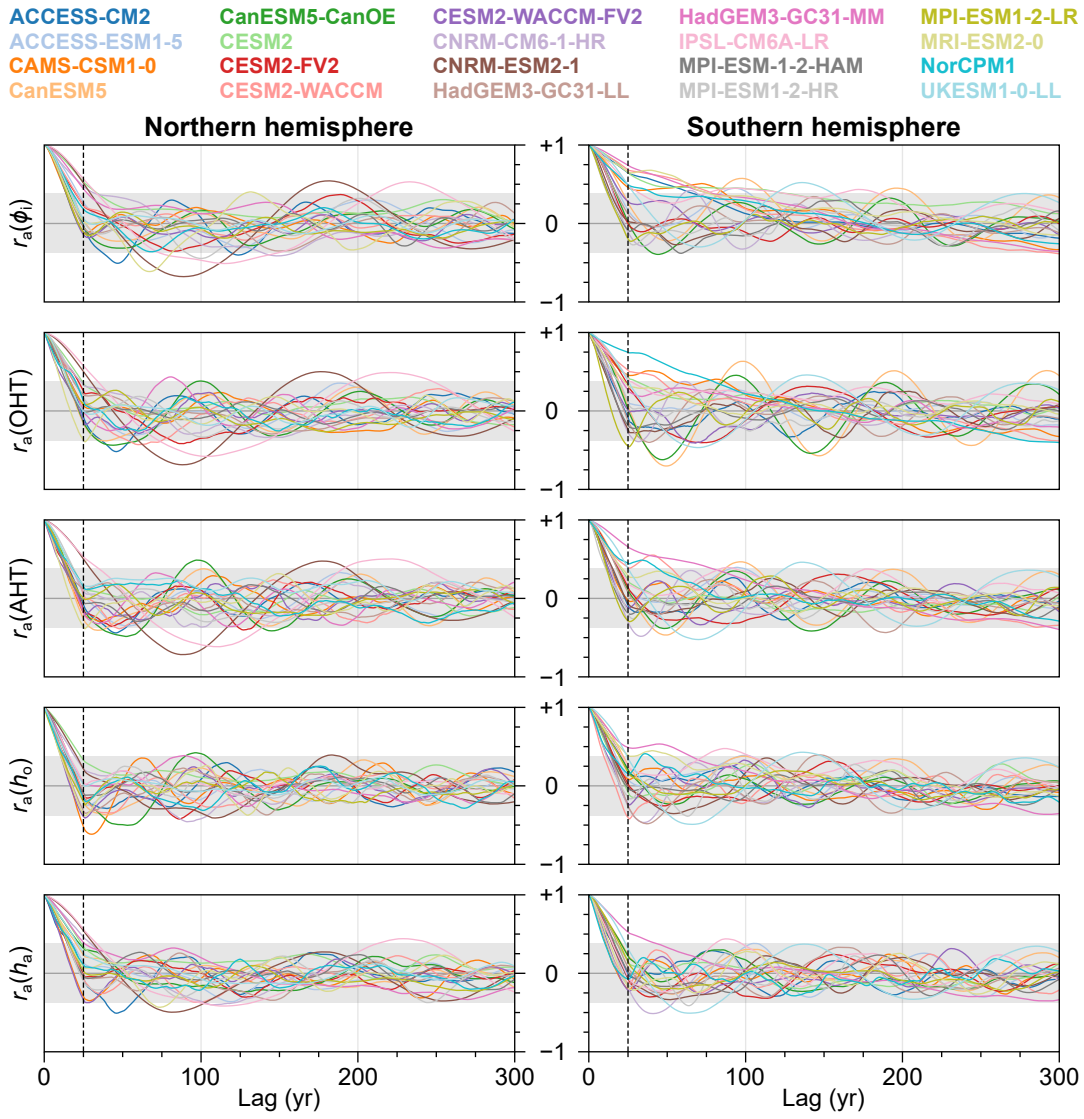

Figure 4.5: Autocorrelation, r_a, of, from top to bottom: ice-edge latitude, ϕ_i, poleward OHT across 60°N/°S, poleward AHT across 60°N/°S, OHTC averaged over sea ice, h_o, and AHTC averaged over sea ice, h_a. Autocorrelations are computed from 25 yr moving averages of the diagnostics for the purpose of smoothing. Shading indicates statistical insignificance at the 95% confidence level based on a Student's t-test of the consecutive, non-overlapping 25 yr periods for 500 yr time series ($r_{crit} = 0.38$).

4.2 Unravelling the mechanisms

4.2.1 Correlation analysis

(a) Northern hemisphere

To start, the correlations, r, between ϕ_i, OHT, and AHT, as a function of the latitude at which the heat transports are evaluated, ϕ_0, are computed. In the NH, 19 of 20 models show a positive correlation between OHT and ϕ_i equatorward of the ice edge (Fig. 4.6a, right). This is physically intuitive (increased heat is associated with less sea ice) and consistent with previous studies (section 1.2.3). All models have $r > r_\mathrm{crit}$ for at least one latitude equatorward of their mean ice edges. In many cases the correlations are strong and do not vary that much with latitude. There is an abrupt change in r poleward of the ice edge, occurring roughly at the seasonal minimum ice extent: some r become quite strongly negative, whereas most (11) drop to an insignificant value. One model, CNRM-ESM2-1, retains a significantly strong positive correlation up to the pole. The same 19 of 20 models have a negative correlation between AHT and ϕ_i equatorward of the ice edge, although there is more variation across models and fewer retain $|r| > r_\mathrm{crit}$ up to the ice edge (Fig. 4.6c, right). Such negative correlations are physically non-intuitive, but can be understood as a consequence of BC, which manifests as a negative correlation between OHT and AHT, present in all models equatorward of the mean ice edge (Fig. 4.6d, right). For many models, AHT and OHT become uncorrelated over sea ice, which can be attributed to minimal air–sea exchanges necessary for the compensation to occur. As with OHT there is a sharp change in $r(\mathrm{AHT}, \phi_\mathrm{i})$ across the ice edge but, in contrast, all 20 models have significant positive $r(\mathrm{AHT}, \phi_\mathrm{i})$ over the permanent ice cover.

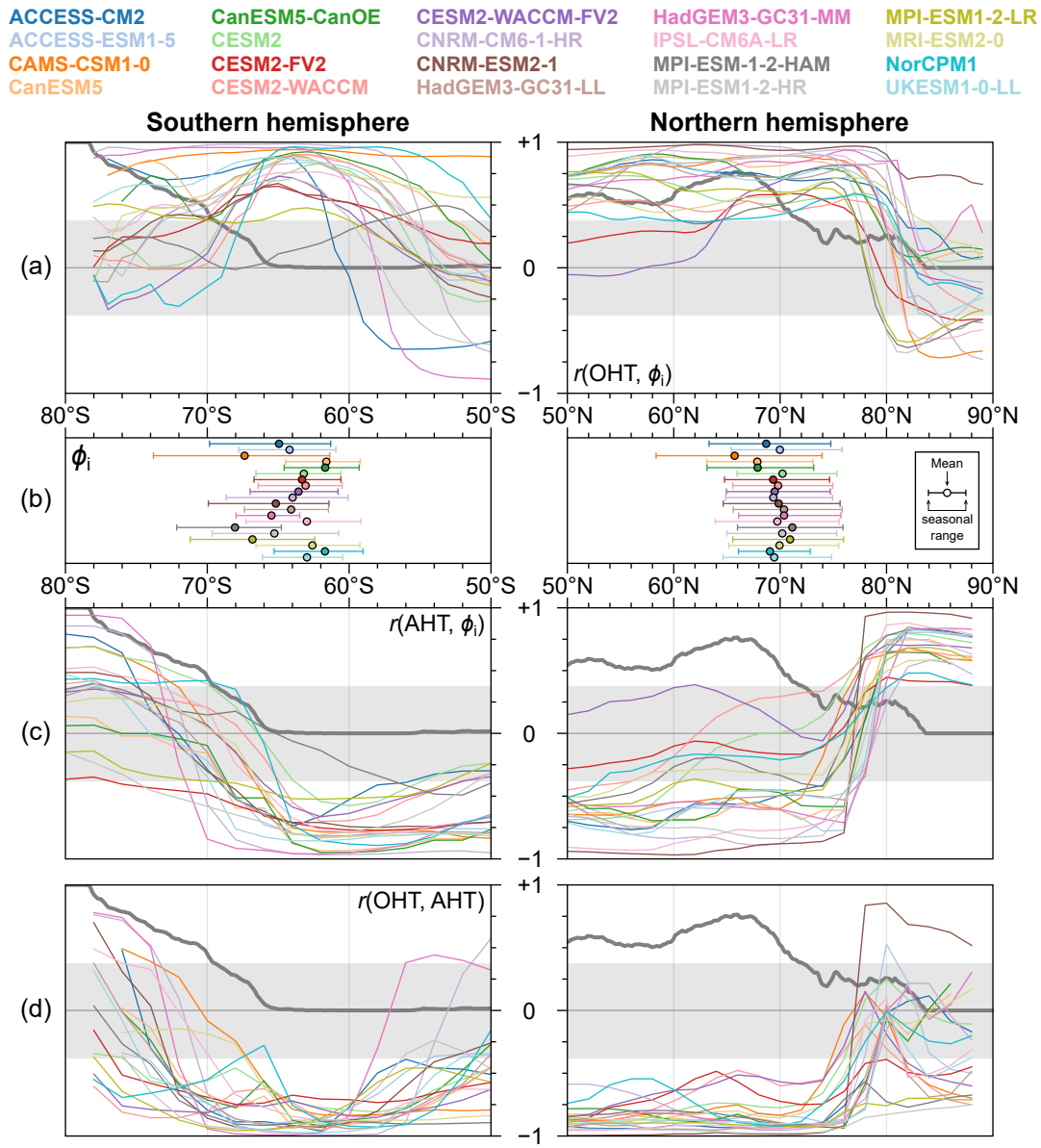

Figure 4.6: (a) Correlation (r) between 25 yr mean, zonal-mean sea ice edge latitude, ϕ_i, and poleward OHT as a function of latitude in the (left) southern and (right) northern hemispheres. (b) Mean ϕ_i in each model (circles) and their seasonal ranges (horizontal bars). (c) As in (a) but for poleward AHT. (d) Correlation between OHT and AHT as a function of latitude. Shading indicates where r is insignificant at the 95% confidence level based on a t-test for 500 yr time series. Thick grey lines in (a), (c), and (d) show the fraction of longitudes occupied by land at each latitude. Note the reversed horizontal axis in the left panels.

(b) Southern hemisphere

The picture in the SH does not mirror that in the NH. There is a large variation in $r(\mathrm{OHT}, \phi_i)$ across models between 50°–60°S (Fig. 4.6a, left), with four having sig-

nificantly negative $r(\mathrm{OHT}, \phi_\mathrm{i})$. Excluding MPI-ESM-1-2-HAM, these correlations converge at high positive values near 65°S—roughly at the mean ice edge. When considering higher southern latitudes, it must be borne in mind that the area of enclosed ocean reduces to zero as the Antarctic coastline is approached, such that the correlations become less meaningful. This is addressed more directly in the next sections, but for now the left panels of Fig. 4.6 show the zonal land fraction as a function of latitude (thick grey lines; i.e., the fraction of longitudes occupied by land, exploiting the 0–1 scale on the vertical axes) to approximately indicate the location of Antarctica. A similar issue arises for the NH when approaching 90°N, but the important qualitative change in the behaviour of the correlations already occurs by 80°N. For all models except MPI-ESM-1-2-HAM, there is at least one latitude equatorward of its mean ϕ_i which has $r(\mathrm{OHT}, \phi_\mathrm{i}) > r_\mathrm{crit}$. Atmospheric heat transport is significantly negatively correlated with ϕ_i for most models between 50°–65°S (Fig. 4.6c, left). For some, $r(\mathrm{AHT}, \phi_\mathrm{i})$ becomes significantly positive at higher latitudes, from about 72°S. However, the land fraction here is above 0.5, so that AHT across these latitudes mostly converges over Antarctica. In contrast, $r(\mathrm{OHT}, \phi_\mathrm{i})$ remains generally positive between ϕ_i and the 0.5 land-fraction latitude. Bjerknes compensation is indicated in the southern hemisphere (Fig. 4.6d, left), although less strongly than in the NH and two models (CNRM-CM6-1-HR and HadGEM3-GC31-MM) do not show the signal at the lower latitudes of the range plotted. All models have significantly strong compensation at about 65°S, coincident with the location of strongest $r(\mathrm{OHT}, \phi_\mathrm{i})$.

This correlation analysis points towards qualitatively different behaviours of the Arctic and Antarctic sea ice cover. In both hemispheres, there tends to be less sea ice when poleward OHT increases just equatorward of the ice edge. This holds, roughly, with OHT under the Antarctic ice pack, which implies that sea ice contracts via increased basal melting. However, reduced Arctic sea ice cover is associated with increased AHT over the permanent ice pack, where there

is no consistent relation with OHT across models, i.e., direct ocean–ice fluxes do not seem relevant in the NH in most cases. Possible explanations for the NH correlations are OHT driving AHTC at higher latitudes, causing melt from above, and/or OHT having a more localised effect by increasing OHTC close to the ice edge (mimicking the behaviour of the K_o sensitivity experiment in the EBM in chapter 3). Such potential mechanisms are not mutually exclusive and could be exhibited to different degrees across models. To examine this in a more direct and physical way, the next section presents the spatial patterns of changes in ocean and atmospheric heat fluxes, and key sea ice metrics (concentration, thickness, and surface temperature).

4.2.2 Spatial distribution of changes in heat fluxes

The changes in the various diagnostics between two 25 yr mean states corresponding to the minimum and maximum mean ϕ_i are computed. This is presented for one model, HadGEM3-GC31-LL, which is a typical case (i.e., having about the average value and magnitude of variability of ϕ_i in both hemispheres; Fig. 4.6b). This facilitates presentation and overall there are no major differences in the qualitative, large-scale behaviour when repeating this procedure on the other models. It should not be taken that HadGEM3-GC31-LL is the 'best' case that other models should be measured against—rather, this is merely a simplification of presentation and the reader is directed to the supplemental material of Aylmer et al. (2022) which contains the analogous plots for all 20 models (which are described in this section). Furthermore, in section 4.2.3, summary statistics of all models are provided (which also assess the whole time series rather than just the extrema; Tables 4.2 and 4.3).

(a) Northern hemisphere

Most of the change in Arctic sea ice from the period of minimum to maximum ϕ_i occurs in the Atlantic sector. Between the two periods, a concentrated increase in OHTC $\sim$ 60 W m^{-2} occurs in the Barents Sea where ϕ_i retreats by $\sim$ 2°N (Fig. 4.7c), coincident with substantial reductions in sea ice concentration (Fig. 4.7a) and thickness (Fig. 4.7b). Comparable poleward shift in ϕ_i also occurs in the Greenland Sea, but with strong localised OHTC slightly further poleward of the ice edge compared with the Barents Sea. Between these areas, near Svalbard, is a patch of decreased OHTC $\sim$ 20 W m^{-2}, and the change in ϕ_i is about half that in the Barents Sea. Strong OHTC also occurs in the Labrador Sea where ϕ_i retreats by $\sim$ 2°N, although the change in thickness is less striking than in the Greenland and Barents Seas. Across the open ocean, ΔAHTC (Fig. 4.7d) is approximately the same magnitude as ΔOHTC but of the opposite sign, which implies the TOA flux does not change much and confirms the presence of BC. In the Pacific sector, sea ice expands by a very small amount in the Bering Sea, contracts by a similarly small amount in the Sea of Okhotsk, and in both cases the local ΔOHTC and ΔAHTC is small. In sum, ϕ_i retreats more wherever OHTC increases more.

In the central Arctic, OHTC and c_i barely change between the two time periods, yet H_i decreases by a substantial $\sim$ 50 cm, similar to the reduction near the Atlantic ice edge where OHTC is strong. Over sea ice, ΔAHTC indicates the sign of the change in net downward surface flux[3], which increases over most of the Arctic ice pack. Averaged over sea ice, the mean change in OHTC is approximately zero while that of AHTC is a few W m^{-2} (this is quantified in section 4.2.3 and Fig. 4.10). Thus the reduction in H_i at high latitudes must be attributed primarily to surface rather than basal melt. This is verified by the

[3]The actual net downward surface flux was plotted to verify this but is not included here because it is almost identical to Fig. 4.7d. This is also the case in the southern hemisphere.

surface air temperature (T_s, Fig. 4.7e) and downwelling longwave radiation (F_{dn}, Fig. 4.7f). Both T_s and F_{dn} increase over most of the Arctic ice pack, skewed towards the Atlantic sector where OHTC is sufficiently high to both erode the ice edge and promote surface warming. Since AHT and OHT are highly anticorrelated between 50°–70°N (Fig. 4.6d), the increase in AHTC in the central Arctic must be primarily driven by oceanic heat loss close to the ice edge. On the other side of the Arctic, a modest increase in ice thickness occurs ($\sim$ 30 cm) in the Chukchi Sea, coincident with slightly reduced T_s and F_{dn}, supporting the notion that ice thickness changes are surface driven. There is possibly a dynamical component to the explanation of sea ice changes in the central Arctic; this is beyond the scope of the present investigation, but it can be reasonably speculated that the changes in H_i are mostly thermodynamically driven because of the timescales considered and the apparent spatial correlation of ΔH_i with ΔF_{dn} and ΔT_s. This interpretation is also reminiscent of Ding et al. (2017), who argue a major role of strengthening atmospheric circulation on recent summer Arctic sea ice decline acting, ultimately, via increased downwelling longwave radiation at high latitudes. It is also consistent with the work of Olonscheck et al. (2019), in which recent interannual variability in Arctic sea ice is linked with that of atmospheric temperature, the latter being partly driven by ocean heat release. However, this study focuses on the shorter, interannual timescale: caution should of course be taken in drawing comparisons of processes across different timescales.

The spatial distributions of the changes in these diagnostics are largely the same when considering the difference between the maximum and minimum sea ice states in the other 19 models, with only minor exceptions. All models show increased OHTC somewhere in the vicinity of the Atlantic ice edge of several tens of W m^{-2}, and only a few have similarly high values in the Pacific sector. In CNRM-ESM2-1, ΔOHTC reaches 150 W m^{-2} in the Greenland sea where ϕ_i retreats by about 5°N. CanESM5 and CanESM5-CanOE stand out as having

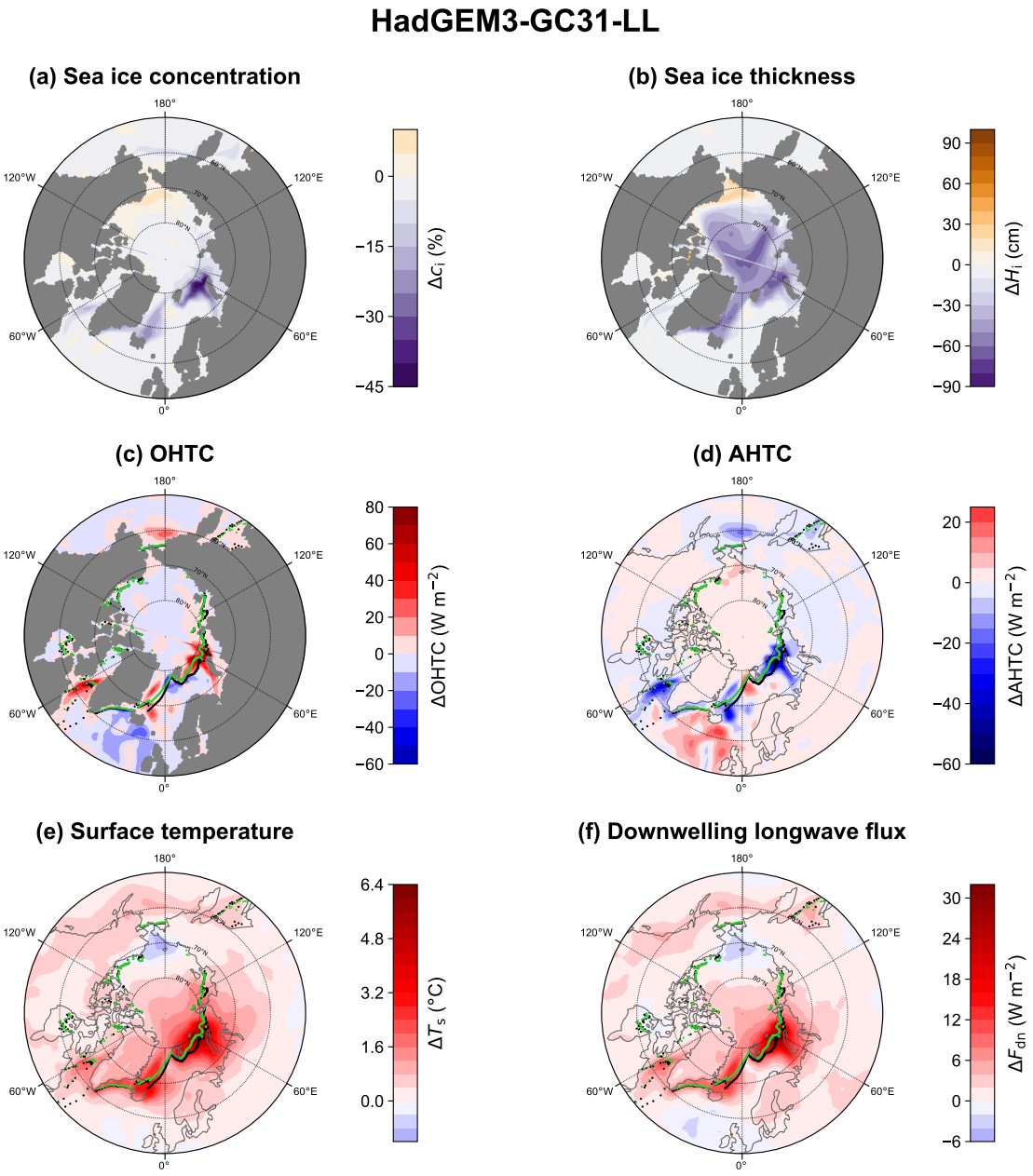

Figure 4.7: Change in (a) sea ice concentration, c_i, (b) sea ice thickness, H_i, (c) OHTC, (d) AHTC, (e) surface air temperature, T_s, and (f) downwelling longwave radiation, F_dn, between the maximum (green) and minimum (black) 25 year mean Arctic sea ice-edge latitude in the PI-control simulation of HadGEM3-GC31-LL. Note that there is at most one ice-edge point per longitude (see section 4.1.2).

relatively extensive ice cover in the Denmark Strait, in which OHT converges nearer the coast of Greenland (i.e., well under sea ice). High-latitude ice thickness decreases by several tens of centimetres in all models, even in cases with modest variations in overall sea ice extent (e.g., CESM2 which only has strong

ΔOHTC in the Labrador sea). As in HadGEM3-GC31-LL, many models have some areas of increased H_i, usually in the Pacific sector. Reduction in sea ice concentration is always localised near the ice edge; in a few models c_i increases by a few percent in the central Arctic. These results strongly suggest that, on multidecadal timescales, variations in Arctic sea ice extent are primarily driven by local OHT convergence causing the ice edge to retreat in the vicinity. This has a secondary effect of enhancing AHT into higher latitudes where the ice volume decreases [explaining the change in sign of $r(\mathrm{AHT}, \phi_\mathrm{i})$ across the summer (i.e. perennial) ice edge in Fig. 4.6c, right].

(b) Southern hemisphere

Like in the Arctic, the largest reductions in Antarctic sea ice cover between the minimum and maximum ϕ_i states occur where the largest increases in OHTC occur: for HadGEM3-GC31-LL, this is primarily in the Ross Sea (Fig. 4.8c). The difference is that OHTC increases by several W m^{-2} at most longitudes and well under the Antarctic ice pack. Consequently, the reductions in concentration and thickness (Fig. 4.8a,b) are relatively spatially uniform; although the largest reductions in c_i and H_i do occur in the Ross Sea. There are a few regional exceptions: in the Amundsen–Bellingshausen Sea, ΔOHTC is smaller and the ice edge does not move much, and decreased OHTC at about 110°–120°E coincides with slight ice expansion.

Figure 4.8d shows that ΔAHTC is approximately the same magnitude but opposite sign to ΔOHTC—as seen in the Arctic, but in the Antarctic this is true over sea ice as well as open ocean. This can be attributed to the lower mean sea ice concentration (43% in the Antarctic compared to 70% in the Arctic at maximum sea ice extent in HadGEM3-GC31-LL), such that air–sea exchanges are significantly less inhibited. Figure 4.8e–f show that T_s and F_dn increase quite

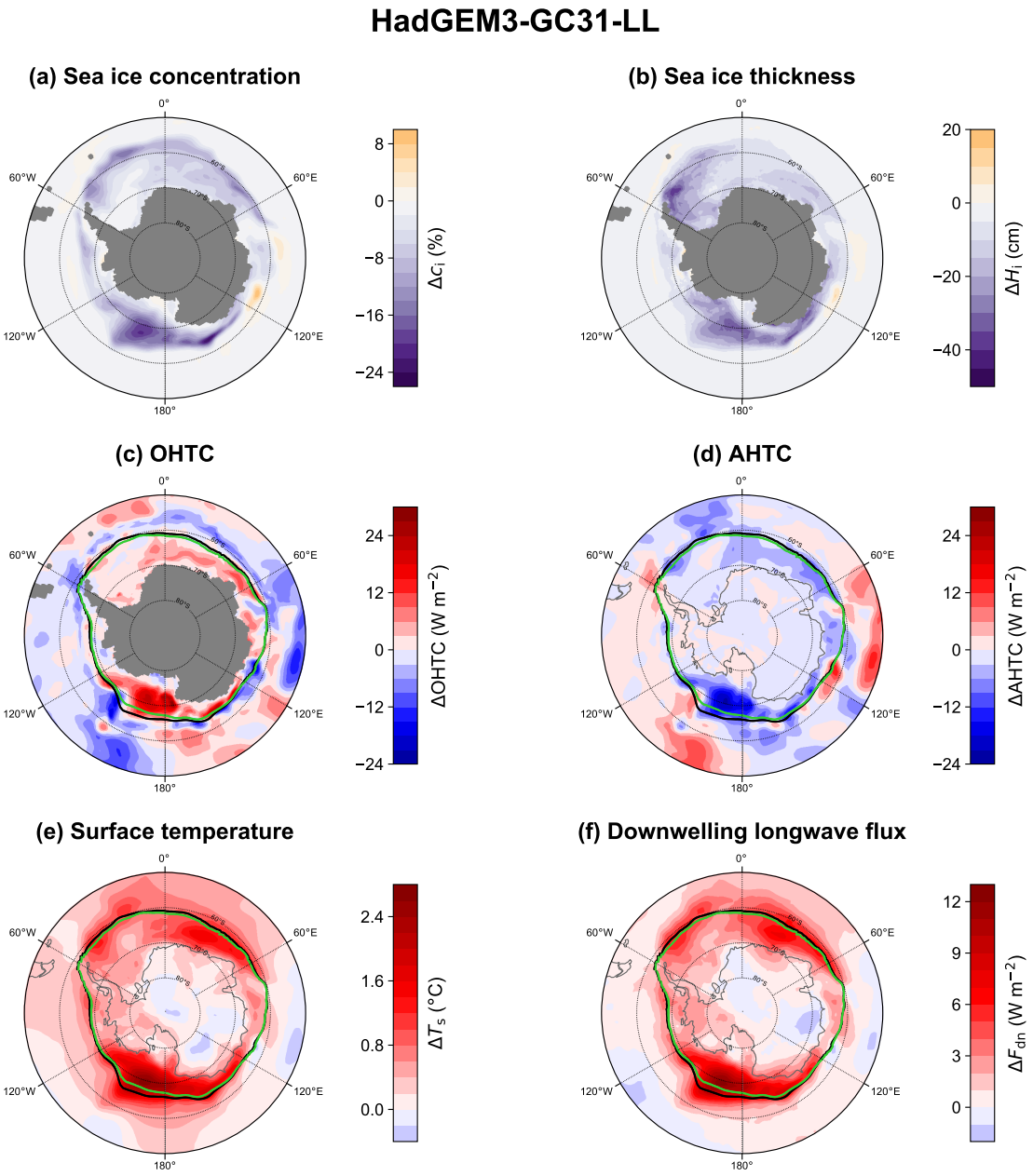

Figure 4.8: As in Fig. 4.7 but for the southern hemisphere.

uniformly over sea ice, with the largest increases roughly coinciding with the largest increases in OHTC. Over Antarctica, T_s, F_{dn}, and AHTC do not change that much. Thus the increased surface warming and downwelling longwave radiation are an effect of OHTC but are not attributed to the loss of ice thickness or concentration, because the net surface flux (roughly, AHTC) decreases (which, by itself, would have a surface cooling effect). Figure 4.8c clearly shows heat be-

ing transported under sea ice, and explains why $r(\mathrm{OHT}, \phi_\mathrm{i})$ is largest with OHT evaluated near to the ice edge (Fig. 4.6a, left).

All models show the same basic features as HadGEM3-GC31-LL. Between their minimum and maximum ϕ_i states, OHTC broadly increases under the Antarctic ice pack, ΔAHTC is roughly the same but with opposite sign, and T_s increases most wherever OHTC is largest. Although the increase in OHTC is fairly spatially uniform (compared to the NH), roughly half of models have the largest ΔOHTC in the Ross Sea, while for the others it occurs in the Weddell Sea. CNRM-CM6-1-HR, with the largest variation in Antarctic sea ice extent, exhibits strong $\Delta\mathrm{OHTC} \sim 40$ W m^{-2} in the Weddell Sea where the ice edge retreats by $\sim 8°$. NorCPM1 is slightly unusual in that most of its strong increase in OHTC is concentrated closer to the ice edge in the Amundsen Sea, Ross Sea, and East Antarctica, such that the behaviour looks more like that in the NH. Its mean sea ice concentration (42%) is comparable to that in HadGEM3-GC31-LL. However, there is still clearly non-zero OHTC increase under the ice, particularly in the Weddell Sea (~ 10 W m^{-2}). CESM2-WACCM-FV2 has the smallest variation in Antarctic sea ice extent, and it has small changes in both OHTC and AHTC even though the ice concentration and thickness vary by similar amounts to HadGEM3-GC31-LL. This is possibly indicative of a higher intrinsic sensitivity in this model.

4.2.3 Heat fluxes averaged over sea ice

The previous section showed the changes in various heat fluxes in HadGEM3-GC31-LL as the system moved from the minimum to maximum sea ice cover during the PI control simulation. This is useful for illustration but only shows the extrema—is the interpretation valid for the whole time series? To check this, diagnostics that quantify the inferred mechanisms are required.

Specifically, the analysis suggested that most of the positive anomalies in OHT are lost near the ice edge in the NH, while most converges under sea ice in the SH. Concurrently, AHTC increases (decreases) over sea ice in the NH (SH). This naturally suggests the analogues of the EBM diagnostics h_o and h_a used in section 3.2. These also conveniently eliminate land-covered points from AHTC and zonal asymmetries. To reiterate, h_o and h_a are OHTC and AHTC, respectively, averaged over sea ice [i.e. where $c_i \geq c_i^\star$, thus 'following' changes in sea ice; see section 4.1.2(b)]. The annual series of h_o and h_a are then converted to series of 25 yr averages in the same way as the previous diagnostics, and correlations between those and ϕ_i are computed.

(a) Northern hemisphere

The correlations $r(h_o, \phi_i)$ and $r(h_a, \phi_i)$ in the NH [Table 4.2 columns (a)–(b)] largely confirm what is suggested by Fig. 4.6 and are consistent with the discussion in section 4.2.2. All models have $r(h_a, \phi_i) > 0$, although two (CanESM5-CanOE and CNRM-CM6-1-HR) are statistically insignificant. The correlation of ϕ_i with h_o varies across models: four have strong positive $r(h_o, \phi_i)$, and a few (notably all CESM models) have strong negative $r(h_o, \phi_i)$. The ones with strong positive $r(h_o, \phi_i)$ are those which have more extensive ice in the Denmark Strait/Labrador Sea area (both CanESM models) or have larger overall variations (CNRM-ESM2-1), such that h_o captures the direct effect of OHTC. In contrast, all but two models have statistically-significant positive $r(h_a, \phi_i)$. Most have $r(\mathrm{OHT}, h_a) > 0$, suggesting that the increase in AHTC over sea ice is at least partly ocean driven, but many are relatively weak [Table 4.2, column (b)]. The reduced correlation between OHT and h_a could be attributed to the reduction in AHT as OHT increases, such that there are two competing influences on h_a: (i) the overall decrease in heat available from AHT, and (ii) the increase in heat available from ocean heat loss near the ice edge. In Table 4.2, column (c) lists correlations with

f_{dn}, the downwelling longwave flux averaged over sea ice, computing f_{dn} in an analogous procedure to h_{a}. All models have significant positive $r(f_{\mathrm{dn}}, \phi_{\mathrm{i}})$, and most have significant positive $r(\mathrm{OHT}, f_{\mathrm{dn}})$ [Table 4.2, column (c)]. This supports the atmosphere acting as a 'bridge' connecting incoming OHT to the top ice surface. From a more general perspective, surface warming is associated with both loss of sea ice and increased OHT [Table 4.2, column (d)]. Studies have already shown a relation between global mean surface temperature and sea ice extent in both hemispheres (e.g., Rosenblum and Eisenman, 2017). Given the correlations between OHT, T_{s}, and ϕ_{i}, these results imply a potential role of OHT in explaining model differences in such relationships.

(b) Southern hemisphere

Thirteen models exhibit strong (> 0.7) positive correlation of ϕ_{i} with h_{o} and correspondingly strong negative correlation with h_{a}, confirming again the description in section 4.2.2 (Table 4.3). Some models do not fit this, including all CESM models: CESM2 is the only model to show a significant (although weak) negative $r(h_{\mathrm{o}}, \phi_{\mathrm{i}})$ despite having significantly positive $r(\mathrm{OHT}, \phi_{\mathrm{i}})$, while the other CESM models show statistically insignificant $r(h_{\mathrm{o}}, \phi_{\mathrm{i}})$. These models have among the smallest variance in h_{o} and ϕ_{i}, so the signal-to-noise ratio could be too small to draw a meaningful interpretation in these cases (or the Antarctic sea ice sensitivity to OHT is relatively small). CAMS-CSM1-0 has practically no correlation between h_{o} and ϕ_{i}, despite strong positive $r(\mathrm{OHT}, \phi_{\mathrm{i}}) > 0.75$ up to the Antarctic coast. However, this model has cancelling regions of positive and negative OHTC under ice in the Weddell Sea (Aylmer et al., 2022, supplemental material, Fig. S.6) and h_{o} averages over both regions. Similar reasoning explains the small $r(h_{\mathrm{o}}, \phi_{\mathrm{i}})$ and $r(h_{\mathrm{a}}, \phi_{\mathrm{i}})$ in MPI-ESM-1-2-HAM (Aylmer et al., 2022, supplemental material, Fig. S.28), which also has the smallest mean Antarctic sea ice extent (Fig. 4.6b, left). The fact that BC is maintained over much of the Antarctic sea

ice pack (Fig. 4.6d, left), suggests that the negative correlation between ϕ_i and h_a mostly reflects heat loss from the ocean into the atmosphere via leads. There could be a negative feedback such that the resulting AHT divergence offsets the effect of OHTC, however it is difficult to ascertain this in the present analysis.

Comparing Tables 4.2 and 4.3, columns (a)–(b), emphasises the broad hemispheric asymmetry in the response of ϕ_i to h_o and h_a. To illustrate this further, let $\Delta\phi_\mathrm{i}$ be the difference between the maximum and minimum ϕ_i (from the 25 yr averages), and Δd be the difference in diagnostic d between the same times at which $\max(\phi_\mathrm{i})$ and $\min(\phi_\mathrm{i})$ occur—exactly as was done for Figs. 4.7 and 4.8. While $\Delta\phi_\mathrm{i}$ could loosely be interpreted as a 'signed standard deviation', the aim with this is just to concisely summarise the general qualitative conclusions. This metric is conducive to this end, as it gives single data points per model, eliminates differences in mean states, and retains the sign of the relationship between variables. Figure 4.9 shows that models with larger increases in ϕ_i are associated with larger increases (decreases) in poleward OHT (AHT) in both hemispheres (matching individual model descriptions). Here, it makes sense to use the same reference latitude ϕ_0 in both hemispheres and for all models for the sake of comparison. Since the mean value of ϕ_0 at which $r(\mathrm{OHT}, \phi_\mathrm{i})$ is strongest across models is close to 60°N/°S in both hemispheres, this is taken for OHT and AHT in Fig. 4.9. This plot is not qualitatively affected (nor do the correlations become insignificant) if $\phi_0 = 65$°N/°S is chosen instead.

This page intentionally left blank.

Table 4.2: Northern hemisphere correlations (r) between various pairs of diagnostics. The first two columns list the latitude, ϕ_0 (°N), where the maximum correlation between OHT and ϕ_i occurs and the corresponding value. (a)–(d) list correlations of the stated diagnostic with (left) OHT, and with (right) ϕ_i. (a) OHTC averaged over sea ice, h_o. (b) AHTC averaged over sea ice, h_a. (c) Downwelling longwave radiation averaged over sea ice, f_{dn}. (d) Surface air temperature averaged over ϕ_0–90°N, T_s. Values in **bold** are statistically significant at the 95% confidence level. Cells are shaded on a red (+1) through white (0) to blue (−1) color scale as a visual aid.

	max $r(\text{OHT}, \phi_i)$		(a) h_o		(b) h_a		(c) f_{dn}		(d) T_s	
Model	ϕ_0	r	r_{OHT}	r_{ϕ_i}	r_{OHT}	r_{ϕ_i}	r_{OHT}	r_{ϕ_i}	r_{OHT}	r_{ϕ_i}
ACCESS-CM2	58	**+0.86**	**+0.67**	+0.30	+0.28	**+0.63**	**+0.42**	**+0.72**	**+0.71**	**+0.92**
ACCESS-ESM1-5	69	**+0.94**	−0.03	**−0.35**	**+0.58**	**+0.82**	**+0.63**	**+0.72**	**+0.86**	**+0.93**
CAMS-CSM1-0	65	**+0.89**	+0.18	−0.02	+0.07	**+0.40**	**+0.52**	**+0.50**	**+0.81**	**+0.88**
CanESM5	59	**+0.88**	**+0.79**	**+0.67**	**+0.32**	**+0.46**	**+0.50**	**+0.62**	**+0.78**	**+0.88**
CanESM5-CanOE	58	**+0.91**	**+0.88**	**+0.72**	+0.16	+0.35	**+0.52**	**+0.55**	**+0.78**	**+0.86**
CESM2	55	**+0.73**	**−0.43**	**−0.85**	**+0.45**	**+0.73**	**+0.58**	**+0.86**	**+0.75**	**+0.95**
CESM2-FV2	69	**+0.59**	−0.26	**−0.76**	−0.18	**+0.41**	+0.15	**+0.61**	**+0.41**	**+0.87**
CESM2-WACCM	56	**+0.55**	−0.30	**−0.82**	+0.38	**+0.83**	+0.30	**+0.68**	**+0.57**	**+0.91**
CESM2-WACCM-FV2	69	**+0.82**	−0.06	**−0.61**	+0.00	**+0.63**	+0.33	**+0.84**	**+0.52**	**+0.95**
CNRM-CM6-1-HR	62	**+0.98**	**+0.56**	**+0.53**	+0.36	+0.40	**+0.65**	**+0.66**	**+0.85**	**+0.86**
CNRM-ESM2-1	62	**+0.98**	**+0.69**	**+0.68**	**+0.91**	**+0.92**	**+0.92**	**+0.95**	**+0.97**	**+0.99**
HadGEM3-GC31-LL	58	**+0.84**	+0.21	−0.13	+0.36	**+0.64**	**+0.63**	**+0.73**	**+0.84**	**+0.96**
HadGEM3-GC31-MM	68	**+0.94**	+0.10	−0.35	**+0.44**	**+0.81**	**+0.71**	**+0.87**	**+0.82**	**+0.97**
IPSL-CM6A-LR	58	**+0.94**	**−0.32**	**−0.27**	**+0.91**	**+0.92**	**+0.82**	**+0.91**	**+0.94**	**+0.98**
MPI-ESM-1-2-HAM	50	**+0.69**	−0.09	**−0.55**	**+0.36**	**+0.78**	+0.29	**+0.75**	**+0.60**	**+0.89**
MPI-ESM1-2-HR	70	**+0.90**	+0.09	−0.21	+0.27	**+0.61**	**+0.60**	**+0.77**	**+0.85**	**+0.96**
MPI-ESM1-2-LR	51	**+0.77**	−0.29	**−0.46**	**+0.48**	**+0.77**	**+0.58**	**+0.66**	**+0.70**	**+0.87**
MRI-ESM2-0	69	**+0.72**	**+0.52**	−0.05	+0.08	**+0.65**	**+0.36**	**+0.70**	**+0.56**	**+0.90**
NorCPM1	51	**+0.59**	**+0.43**	−0.20	−0.08	**+0.47**	+0.19	**+0.49**	**+0.48**	**+0.74**
UKESM1-0-LL	57	**+0.89**	**+0.30**	+0.12	**+0.55**	**+0.69**	**+0.56**	**+0.76**	**+0.82**	**+0.94**

Table 4.3: As in Table 4.2 but for the southern hemisphere, and here ϕ_i and ϕ_0 are in °S.

	max $r(\mathrm{OHT}, \phi_\mathrm{i})$		(a) h_o		(b) h_a		(c) f_dn		(d) T_s	
Model	ϕ_0	r	r_OHT	r_{ϕ_i}	r_OHT	r_{ϕ_i}	r_OHT	r_{ϕ_i}	r_OHT	r_{ϕ_i}
ACCESS-CM2	64	**+0.88**	**+0.87**	**+0.90**	**−0.87**	**−0.85**	**+0.61**	**+0.73**	**+0.83**	**+0.97**
ACCESS-ESM1-5	63	**+0.84**	**+0.79**	**+0.79**	**−0.47**	**−0.49**	+0.26	+0.11	**+0.82**	**+0.87**
CAMS-CSM1-0	64	**+0.94**	−0.10	+0.02	**−0.38**	**−0.47**	**+0.50**	**+0.58**	**+0.91**	**+0.92**
CanESM5	61	**+0.90**	**+0.79**	**+0.91**	**−0.64**	**−0.76**	+0.22	**+0.43**	**+0.80**	**+0.93**
CanESM5-CanOE	61	**+0.92**	**+0.77**	**+0.91**	**−0.55**	**−0.71**	+0.19	+0.32	**+0.84**	**+0.93**
CESM2	62	**+0.83**	−0.13	**−0.48**	**−0.64**	**−0.57**	**+0.46**	**+0.71**	**+0.73**	**+0.97**
CESM2-FV2	63	**+0.65**	**+0.74**	+0.26	**−0.48**	**−0.72**	+0.13	+0.20	+0.26	**+0.72**
CESM2-WACCM	63	**+0.90**	+0.04	−0.17	**−0.55**	**−0.42**	**+0.40**	**+0.62**	**+0.67**	**+0.89**
CESM2-WACCM-FV2	63	**+0.73**	+0.24	−0.29	**−0.53**	**−0.60**	+0.17	+0.24	**+0.42**	**+0.91**
CNRM-CM6-1-HR	63	**+0.99**	**+0.97**	**+0.98**	**−0.86**	**−0.86**	**+0.79**	**+0.82**	**+0.97**	**+0.99**
CNRM-ESM2-1	65	**+0.67**	**+0.70**	**+0.85**	**−0.46**	**−0.79**	**+0.64**	**+0.44**	**+0.78**	**+0.72**
HadGEM3-GC31-LL	64	**+0.89**	**+0.88**	**+0.76**	**−0.75**	**−0.57**	**+0.54**	**+0.71**	**+0.70**	**+0.89**
HadGEM3-GC31-MM	64	**+0.96**	**+0.95**	**+0.95**	**−0.87**	**−0.89**	**+0.69**	**+0.79**	**+0.96**	**+0.99**
IPSL-CM6A-LR	62	**+0.77**	**+0.74**	**+0.77**	**−0.51**	**−0.45**	+0.17	**+0.57**	**+0.60**	**+0.91**
MPI-ESM-1-2-HAM	54	**+0.49**	**+0.34**	+0.08	−0.18	+0.20	−0.01	+0.15	**+0.62**	**+0.56**
MPI-ESM1-2-HR	64	**+0.71**	**+0.85**	**+0.78**	**−0.79**	**−0.74**	**−0.40**	−0.35	**+0.58**	**+0.72**
MPI-ESM1-2-LR	63	**+0.51**	**+0.58**	**+0.35**	**−0.42**	−0.19	−0.07	−0.05	**+0.67**	**+0.58**
MRI-ESM2-0	62	**+0.88**	**+0.90**	**+0.88**	**−0.64**	**−0.52**	−0.01	+0.23	**+0.65**	**+0.88**
NorCPM1	58	**+0.96**	**+0.86**	**+0.92**	**−0.55**	**−0.63**	**+0.56**	**+0.53**	**+0.97**	**+0.97**
UKESM1-0-LL	62	**+0.88**	**+0.88**	**+0.73**	**−0.83**	**−0.71**	**+0.75**	**+0.85**	**+0.74**	**+0.96**

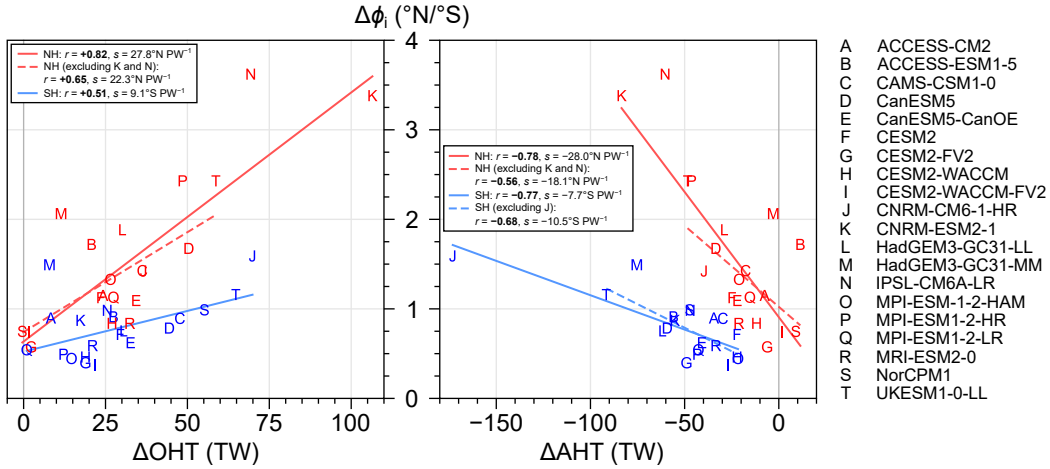

Figure 4.9: Maximum increase in 25 yr mean ice-edge latitude, $\Delta\phi_i$, plotted against the corresponding change in poleward (left) OHT and (right) AHT. Heat transports are here evaluated at 60°N/S. Red points are northern hemisphere (NH) and blue points are southern hemisphere (SH). Ordinary least-squares regression lines are added to all models for the NH (red, solid) and SH (blue, solid), and also excluding certain models (dashed; see legends). The legends give the corresponding correlation coefficients (r) and slopes of the regression lines (s). 1 TW$= 10^{12}$ W.

Figure 4.10 shows that h_o does not change much between the maximum and minimum sea ice states across models in the NH, but that h_o increases by a few W m^{-2} in the SH. In all models, h_a increases from the minimum to maximum ϕ_i in the NH, but decreases in the SH. The analysis in section 4.2.2 suggests that, in the SH, h_a decreases in response to Bjerknes compensation (which does not occur in the NH because the ice concentration is too high). Figure 4.11 shows ΔT_s averaged between $\phi_0 = 60$°N/°S against (a) $\Delta\phi_i$ and (b) ΔOHT evaluated at 60°N/°S. This reinforces the earlier point that the OHT–sea ice relationships revealed here could be in part responsible for the previously noted relation between sea ice extent and surface temperature (Rosenblum and Eisenman, 2017). It is worth noting the non-zero intercepts of the fitted linear relations between $\Delta\phi_i$ and the other diagnostics in Figs. 4.9 and 4.11. This indicates that the variability of ϕ_i cannot be wholly attributed to anomalies in heat transports.

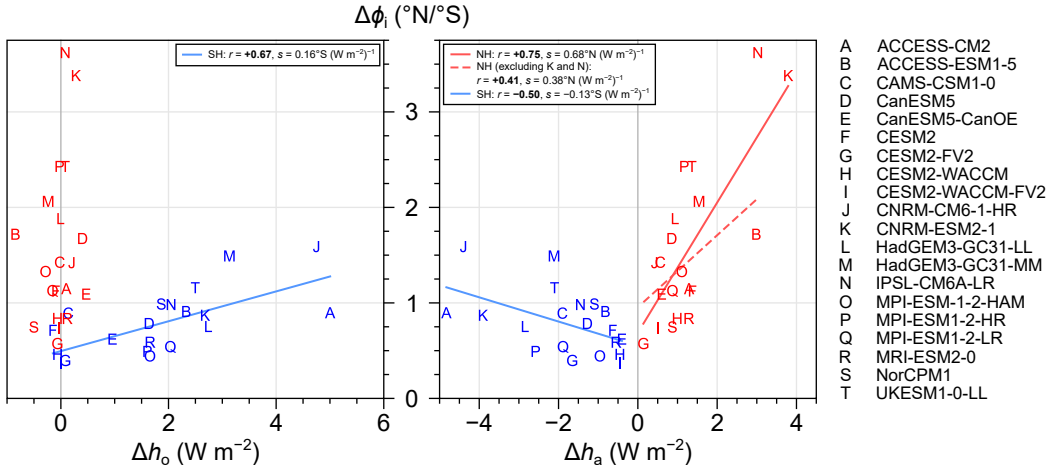

Figure 4.10: As in Fig. 4.9 but for (left) OHTC averaged over sea ice, h_o, and (right) AHTC averaged over sea ice, h_a.

4.2.4 Section summary and discussion

Analysis of the PI-control simulations of 20 CMIP6 models has revealed distinct mechanisms of how natural OHT variability impacts sea ice between the northern and southern hemispheres. In summary:

1. Arctic and Antarctic sea ice extent contract with increased poleward OHT, with significant correlation in all models.

2. Due to Bjerknes compensation, anomalous AHT towards the polar regions is counterintuitively associated with larger sea ice cover.

3. In the northern hemisphere, for most models:

    a) the direct effect of OHT is concentrated convergence and melting at the ice edge in the Atlantic sector;

    b) there is no substantial role of OHTC in the central Arctic;

    c) a secondary Arctic-wide ice thinning occurs, mediated by increased high-latitude AHTC.

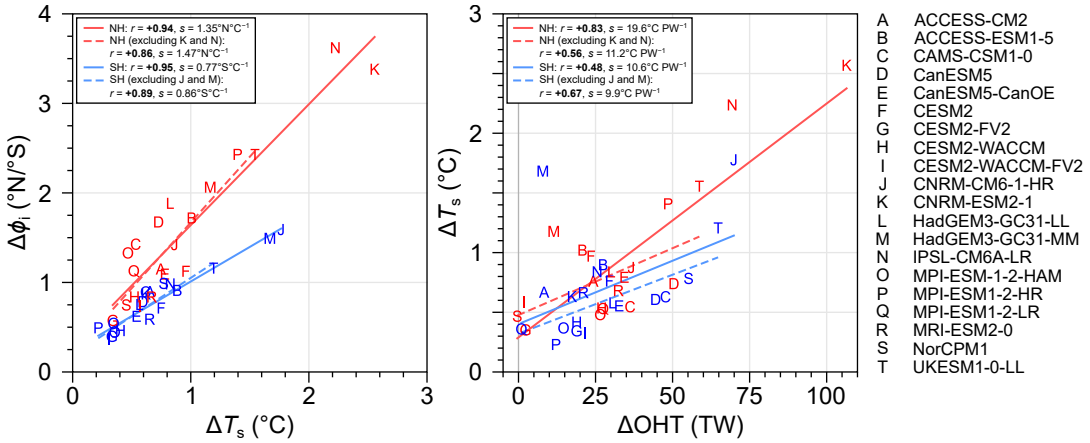

Figure 4.11: As in Fig. 4.9 but for (left) ϕ_i and mean near-surface air temperature, T_s, and (right) T_s and OHT. Here, OHT is evaluated at 60°N/S and T_s is averaged between 60°N/S and the pole.

4. In the southern hemisphere, for most models:

   a) the effect of OHT is relatively-uniform convergence and consequent melting under the entire Antarctic ice pack;

   b) AHT does not have a direct impact on the ice cover, but transports some ocean heat away from the ice pack.

The difference between Arctic and Antarctic sea ice behaviours is summarised by Figs. 4.9 and 4.10: the former emphasises point (1), similarly to Mahlstein and Knutti (2011) for CMIP3 in the NH,[4] while the latter shows the key result of this section: that OHT takes different 'pathways' in each hemisphere (points 3–4; Fig. 4.12). Point (2) is noteworthy as such relationships between the natural variability of AHT and sea ice have not been widely acknowledged in prior studies (although found in the controlled ocean experiments by Winton, 2003).

Figure 4.9a implies that the Arctic sea ice edge is about twice as sensitive to poleward OHT than the Antarctic sea ice edge, although there are caveats in this statement: it could depend on the choice of reference latitude for OHT,

[4]The relationship between the mean states of OHT and sea ice across models, found in CMIP3 models by Mahlstein and Knutti (2011), is addressed directly for the CMIP6 models in the next chapter (section 5.2.1).

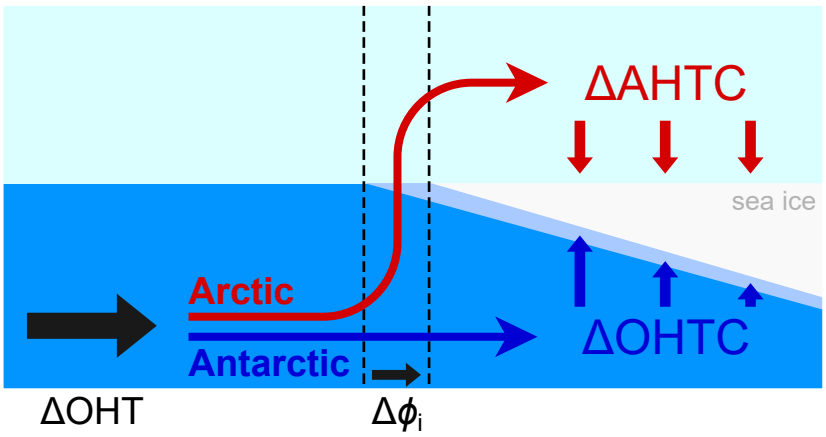

Figure 4.12: Schematic summary of the mechanisms of OHT influence on the sea ice edge (ϕ_i) inferred from CMIP6 PI-control analysis in section 4.2.

and the cross-model behaviour does not necessarily reflect individual model behaviours. Also, the extrema of ϕ_i and OHT defining the points in Fig. 4.9 are not necessarily representative of the whole time series [depending on $r\,(\mathrm{OHT}, \phi_i)$]. The change of slope between hemispheres in Fig. 4.9a is plausibly due to the difference in mechanism, since local OHTC along the ice edge in the North Atlantic is several times larger than OHTC under the Antarctic ice pack (Figs. 4.7c and 4.8c), even though ΔOHT is similar for HadGEM3-GC31-LL in both hemispheres (Fig. 4.9a). Switching to sea ice extent, S_i, using the conversion factors in Fig. 4.3, the sensitivities of S_i to OHT are about the same in each hemisphere. This differs from the sensitivities in terms of ϕ_i because of differences in land distribution between the hemispheres. In using ϕ_i, it is possible to understand how the land influence matters relative to the difference in sensitivities arising from other factors, including the OHT mechanisms. This and the sensitivities of the ice edge to OHT are explored in more detail in section 4.3.

Insight into the mechanisms in this chapter is based mostly on correlations, which support but do not prove causal relationships. While clearly an important caveat to acknowledge, the alternative would be to carry out controlled experiments (e.g., imposing an OHT change) in every model, which is computationally

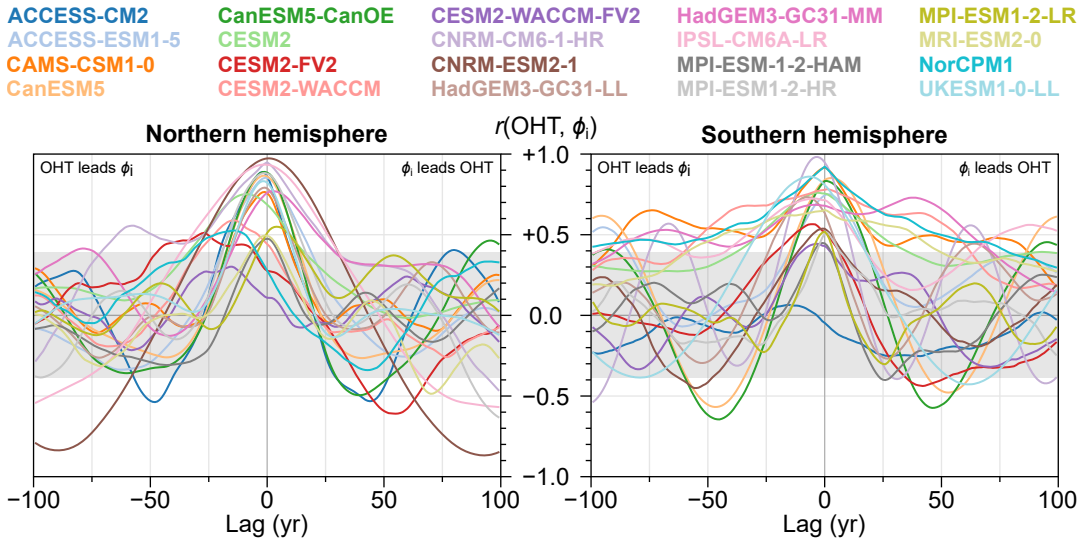

Figure 4.13: Correlation between OHT and ϕ_i as a function of lag. As in Fig. 4.5, correlations are computed from 25 yr moving averages for smoothing. Shading indicates insignificance at the 95% confidence level based on a t-test of the non-overlapping 25 yr averages for 500 yr time series. At negative lags, OHT leads ϕ_i (and vice-versa for positive lags).

expensive and done on a smaller scale in previous studies (section 1.2.3). The key here is to understand what happens in the climate system without external interference, and the correlation analysis is the simplest starting point from which such insight can be generated with simulations which have already run. After analysing multiple diagnostics, simple physical reasoning has been used to deduce the qualitative mechanisms that are most consistent with all data. However, this raises the question: is there an alternative description which also fits the data? Specifically, in the NH it could be argued that negative anomalies in sea ice cover allow increased upward air–sea heat fluxes due to newly exposed ocean which, in turn, is compensated for by increased OHT. If this were the case, a lag in the OHT response relative to the sea ice change would be expected because of the long timescales associated with ocean heat content and circulation adjustments. However, this alternative interpretation is not supported by the lagged correlation between OHT and ϕ_i, for which the maximum occurs at zero or slightly negative (ocean leads sea ice) lag in most models (Fig. 4.13). This suggests that

the sea ice state at some time-averaging period is primarily influenced by OHT at the same period, consistent with the interpretation in section 4.2.2, whereas the alternative would be indicated by sea ice leading OHT.

Why does OHT continue under and through sea ice in the SH but is lost nearer the ice edge in the NH? The methodology used here does not provide the tools to rigorously answer this, but an explanation could be speculated based on current understanding of the Arctic and Southern Oceans in today's climate, as described in section 1.1.1. In the central Arctic, sea ice is thick and high in concentration, preventing ocean–atmosphere exchanges, and the upper ocean is stably stratified, limiting heat release from the already limited Atlantic inflow. This probably explains why OHTC does not change in the central Arctic in the PI-control simulations. The Southern Ocean does not have such stability, such that ocean heat loss is less restricted. However, this description is based on shorter timescales than considered here and, despite the clear parallel, should not be naively generalised to the multidecadal processes. Whatever the reasons, the fact that robustly-different behaviours are exhibited in the NH and SH indicates different approaches for tackling Arctic and Antarctic sea ice uncertainties. For example, CMIP6 models also exhibit wide spread in simulations of the Atlantic meridional overturning circulation (AMOC; Todd et al., 2020). Although here there is no identification of specific processes such as AMOC causing OHT variability, it is clear that most changes in Arctic sea ice occur in the Atlantic sector, suggesting a plausible link between AMOC and sea ice uncertainties.

The qualitative mechanisms can be compared with the EBM sensitivity studies in chapter 3. The CMIP6 model NH mechanism is reminiscent of the qualitative behaviour of the EBM K_o sensitivity experiment, and the SH mechanism is reminiscent of that in the EBM F_{bp} sensitivity experiment. There it was found (via the K_o experiment) that OHTC concentrated near the ice edge is about twice as effective at shrinking the ice cover as the equivalent OHTC spread uni-

formly over the ice pack (via the F_{bp} experiment). Consistent with this analogy, the CMIP NH sensitivity is larger than that in the SH. However, the factor of 2 difference in the EBM refers to the 'actual' sensitivity of ϕ_{i} to h_{o}, s_{o}, with the effect of BC removed. In the CMIP6 models, the ratio of NH to SH sensitivities is about a factor of two, but BC has not been eliminated and it is impractical to do so and compute s_{o}. Therefore the comparison should be made to the 'effective sensitivities' of ϕ_{i} to OHT in the EBM as shown in Fig. 3.9a. There, $\Delta\phi_{\mathrm{i}}/\Delta\mathrm{OHT}$ is only about 25% larger in the K_{o} case compared to the F_{bp} case. This suggests that the larger difference between the NH and SH CMIP6 effective sensitivities arises due to substantial hemispheric differences in the various terms making up Eq. (3.23b). This is investigated in the next section.

4.3 Explaining sensitivities with the EBM

The effective sensitivities of ϕ_{i} to OHT in the CMIP6 models are now examined and cast into the theoretical framework of the EBM. Specifically, the applicability of Eq. (3.23b)—which proposes how the relationship between ϕ_{i} and OHT arises based on simple energy-conservation principles—is tested. For convenience this equation is repeated here:

$$\frac{\Delta\phi_{\mathrm{i}}}{\Delta\mathrm{OHT}} = \frac{\beta B_{\mathrm{up}}}{s\,(1+\beta)}\frac{\Delta T_{\mathrm{s}}}{\Delta\mathrm{OHT}} - \frac{1}{sA}\left(1+\frac{b_{\mathrm{c}}}{1+\beta}\right) \qquad \text{(3.23b revisited)}$$

where, for ease of notation, the explicit indication of time and spatial averaging (overlines and angular brackets, respectively) is now dropped. In section 4.3.1 this is applied to models individually (i.e., assessing internal variability), and in section 4.3.2 this is done on models collectively (i.e., effectively assessing inter-model spread). This is preamble for the analysis of future simulations in the next chapter, providing an assessment of how well the EBM fits the model relationships

in the simpler case of the control simulations. At the same time, insight is gained into the difference between the NH and SH sensitivities alluded to in Fig. 4.9a.

4.3.1 Application to models individually

Consider again the example model, HadGEM3-GC31-LL, in which poleward OHT (across ϕ_0), ϕ_i, and T_s (averaged between ϕ_0 and the pole), are strongly positively correlated in both hemispheres ($r > 0.7$; Tables 4.2 and 4.3). According to the EBM analysis discussed in section 3.3.2, changes in these quantities should be related according to Eq. (3.23a), under the reasonable assumption that energy conservation holds. The simplest approach to verifying this is to use the effective sensitivity ($\Delta\phi_\mathrm{i}/\Delta\mathrm{OHT}$) version, Eq. (3.23b), and follow the same procedure outlined in section 3.3.2 for the EBM sensitivity experiments. First, the values of B_up, B_OLR, B_dn, s, b_c, and $\Delta T_\mathrm{s}/\Delta\mathrm{OHT}$ for HadGEM3-GC31-LL are required. The atmospheric radiation parameters are obtained as described in section 2.3.2, replacing ERA-Interim data with the appropriate fields of the model's PI-control simulation. One difference here is that, since only the region between latitude ϕ_0 and the pole is of interest now, only data within this spatial range is used to determine B_up, B_dn, and B_OLR. The values of the B parameters for all models and for various ϕ_0 are tabulated in appendix A, Tables A.1–A.5. In both hemispheres, the model values are comparable to those derived from ERA-Interim. The values of $\beta = B_\mathrm{OLR}/B_\mathrm{dn}$, as with ERA-Interim, are found to be insensitive to the choice of reference pressure level used for air temperature.

The other parameters in Eq. (3.23b), s, b_c, and $\Delta T_\mathrm{s}/\Delta\mathrm{OHT}$, are each obtained from linear regression coefficients of anomalies in 25 yr mean values of the quantities defining them. Specifically, s is given by the slope of ΔF_sw (net shortwave radiation averaged between ϕ_0 and the pole) and $\Delta\phi_\mathrm{i}$, and b_c is given by that of $\Delta\mathrm{AHT}/\Delta\mathrm{OHT}$. These are shown in Fig. 4.14 for HadGEM3-GC31-LL

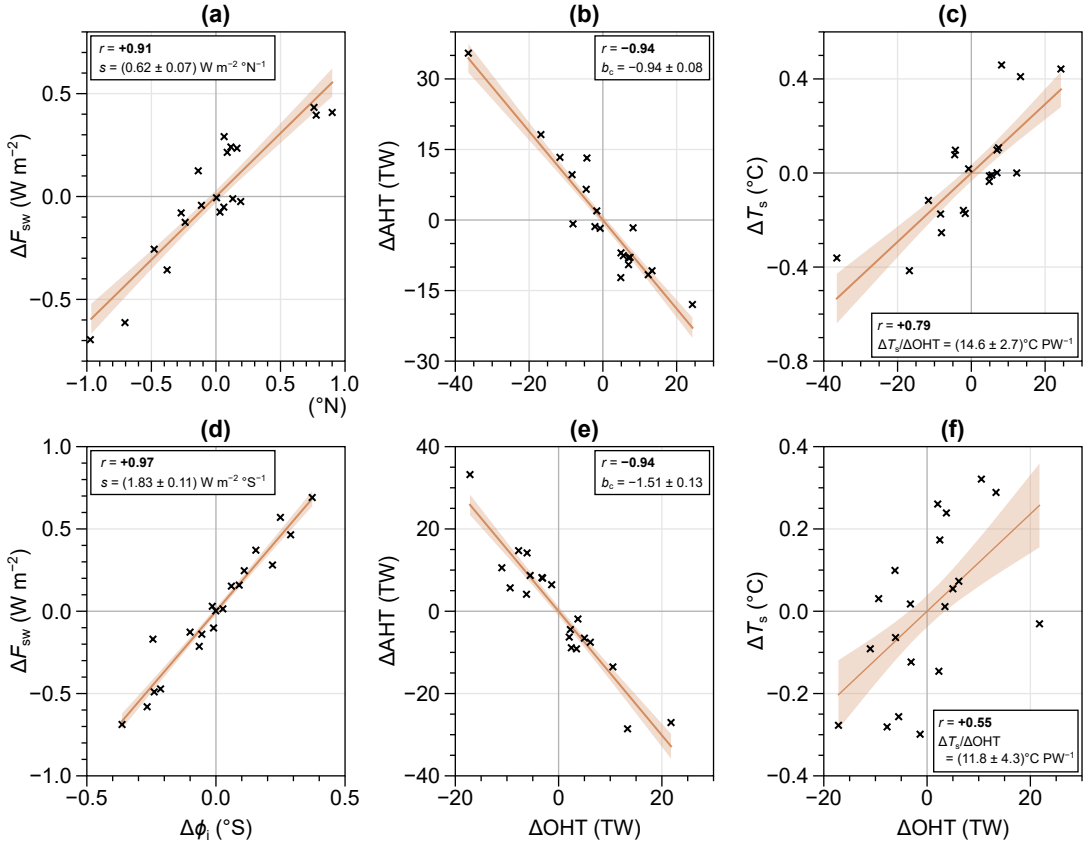

Figure 4.14: Values of s, b_c, and $\Delta T_s/\Delta\text{OHT}$, determined from the PI-control simulation of HadGEM3-GC31-LL. Each point is a 25 yr average, as an anomaly relative to the mean of the whole time series. Plots (a)–(c) are for the NH, and (d)–(f) are for the SH. (a,d) Net shortwave radiation, F_{sw}, and ice edge latitude, ϕ_i, the OLS slope of which defines s. (b,e) AHT versus OHT; the slope of which gives b_c. (c,f) Surface temperature, T_s, versus OHT. F_{sw} and T_s are averaged between $\phi_0 = 60°\text{N}/°\text{S}$ and the pole, and OHT and AHT are evaluated at ϕ_0.

with $\phi_0 = 60°\text{N}/°\text{S}$, which suggests that the values of s, b_c, and $\Delta T_s/\Delta\text{OHT}$ are well defined in the sense that there is a strong relationship between the quantities on each set of axes. Particularly, a key requirement for Eq. (3.23b) to work is the 'conversion' between F_{sw} and ϕ_i, and $r(\phi_i, F_{sw}) > 0.9$ in both hemispheres (Fig. 4.14a,d). The worst case is $\Delta T_s/\Delta\text{OHT}$ in the SH, in which $r(\Delta T_s, \Delta\text{OHT}) = 0.55$ is relatively weak (Fig. 4.14f). This is due partly to the small range of variation in T_s ($< 1°\text{C}$), and partly to the choice of $\phi_0 = 60°\text{S}$. As explained in section 4.2.3 it makes sense to use the same ϕ_0 for both hemispheres for comparison purposes. For HadGEM3-GC31-LL, the actual ϕ_0 at

which $r(\mathrm{OHT}, \phi_\mathrm{i})$ is strongest is closer to 65°S, for which $r(\Delta T_\mathrm{s}, \Delta\mathrm{OHT}) = 0.66$. Below, the result of fitting the EBM equation with different ϕ_0 is discussed.

Having now gathered all terms appearing on the RHS of Eq. (3.23b), it is possible to check the estimate of the EBM-derived effective sensitivity of ϕ_i to OHT and compare it to the real, OLS-derived effective sensitivity exhibited by HadGEM3-GC31-LL. Figure 4.15a,b plots the anomalies in ϕ_i versus those of OHT, showing the OLS fit to $\Delta\mathrm{OHT}$ and $\Delta\phi_\mathrm{i}$ (black) and the 'predicted slope' from the combination of the other terms according to Eq. (3.23b) (brown). Taking into account the uncertainties (standard deviations), the EBM slope is consistent with the OLS fit in both hemispheres (i.e., the shaded regions in Fig. 4.15a,b overlap). There is some sensitivity to the choice of ϕ_0, largely reflecting the latitude dependence of $r(\mathrm{OHT}, \phi_\mathrm{i})$ (Fig. 4.6a). In the NH, the EBM equation works well for $\phi_0 = 50°$–$60°$N (Fig. 4.15c), even though $r(\mathrm{OHT}, \phi_\mathrm{i}) = 0.45$ is relatively weak at $\phi_0 = 50°$N. At southern latitudes lower than 60°S, $r(\mathrm{OHT}, \phi_\mathrm{i})$ becomes small and statistically insignificant ($r < r_\mathrm{crit} = 0.38$). The EBM equation agrees well with the OLS fit at these latitudes anyway (Fig. 4.15d), but the error bars are quite large, attributed to poorly-defined values of s and $\Delta T_\mathrm{s}/\Delta\mathrm{OHT}$. At 65°S, where $r(\mathrm{OHT}, \phi_\mathrm{i})$ is larger, the EBM does not quite agree with the OLS but the gap between the OLS lower limit and EBM upper limit is not large ($\sim 10\%$ difference). Also indicated in Fig. 4.15a,b are the minimum and maximum 25 yr averages of $\Delta\phi_\mathrm{i}$ (and the corresponding values of $\Delta\mathrm{OHT}$) which determine the points in Fig. 4.9. The EBM interpretation discussed next thus explains the origin of the corresponding point for this model on Fig. 4.9.

Despite some discrepancies which can be at least partly understood in terms of the previous correlation analysis, Fig. 4.15 shows that the EBM broadly captures the emergent relationship between ϕ_i and OHT in HadGEM3-GC31-LL. This suggests that the EBM equation and the terms in Fig. 4.14 can provide insight into the sensitivity of ϕ_i to OHT in this model. For example, why is the

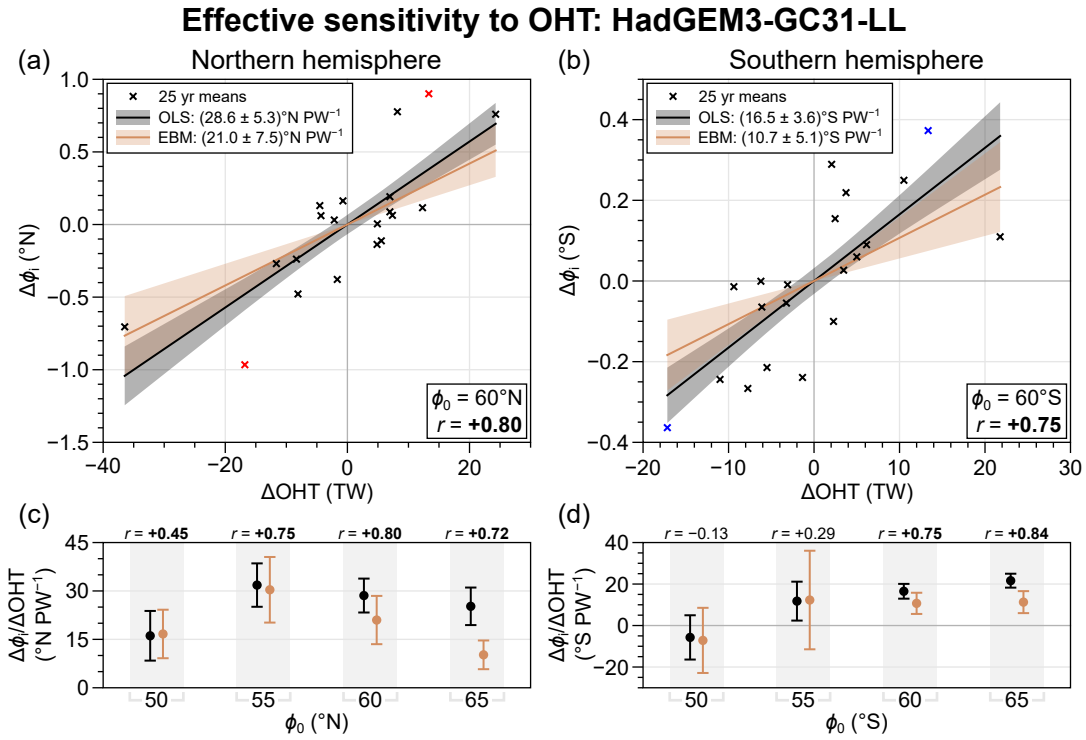

Figure 4.15: (a) Anomalies in 25 yr mean ice-edge latitude, $\Delta\phi_i$, plotted against those of poleward OHT, ΔOHT, in the PI-control simulation of HadGEM3-GC31-LL for the NH. The upper legend gives the slopes of the OLS fit (black) and EBM (brown), with standard deviations indicated by shading. The lower legend gives the reference latitude, ϕ_0, and correlation coefficient, r, of the anomalies. (b) As in (a) but for the SH. The highlighted points in (a, red) and (b, blue) are the maximum and minimum 25 yr mean ϕ_i used to compute $\Delta\phi_i$ in Fig. 4.9. (c) Summary of results for (a) when using different ϕ_0: the vertical axis is the sensitivity (i.e., slope of $\Delta\phi_i$ versus ΔOHT) with error bars indicating the standard deviations, derived from OLS (black) and from the EBM (brown). Values of r are given at the top. (d) As in (c) but for the SH.

sensitivity larger in the NH compared to the SH? The differences between the values of B_{up} and β in the NH and SH are small compared to the hemispheric differences in the other terms in Eq. (3.23b), so these can be neglected for simplicity. The temperature-sensitivity term, $\Delta T_s/\Delta$OHT, is slightly larger ($\sim$ 25%) in the NH than in the SH (Fig. 4.14c,f), which would tend to increase the NH sensitivity relative to the SH according to Eq. (3.23b). Bjerknes compensation, b_c, is substantially more negative in the SH than in the NH (Fig. 4.14b,e) which, according to Eq. (3.23b), would tend to increase $\Delta\phi_i/\Delta$OHT of the SH compared to NH. Thus, the overwhelming influence is the shortwave-conversion factor, s,

which is about 3 times larger in the SH than in the NH (Fig. 4.14a,b). This factor is the main reason why the effective sensitivity is smaller in the SH. Physically, this is indicative of the larger albedo contrast across the ice edge (Eq. 3.22), which incorporates the effects of relative zonal symmetry in sea ice cover and lack of land in the SH (Figs. 4.7a and 4.8a). Per unit ΔOHT across ϕ_0, the TOA fluxes, including the net shortwave F_{sw}, must adjust to restore the energy balance. In the SH with larger s, ϕ_{i} does not need to retreat as much to generate the additional F_{sw} required compared to the NH. The sensitivity $\Delta\phi_{\mathrm{i}}/\Delta\mathrm{OHT}$ is not, then, 3 times larger in the NH because the other factors are still important. The $\Delta T_{\mathrm{s}}/\Delta\mathrm{OHT}$ term is larger in the NH, which, consistent with the EBM analysis, is due to the underlying mechanisms identified in section 4.2 in which ΔOHT is primarily lost near the ice edge (NH/K_{o}) rather than uniformly under it (SH/F_{bp}). This lowers the SH sensitivity relative to the NH. However, BC acts to reduces the gap between the NH and SH sensitivities: in the SH, AHT strongly overcompensates ΔOHT, whereas in the NH it slightly under-compensates. The response of AHT in the SH strongly counteracts ΔOHT such that the required adjustment in TOA fluxes is reduced relative to the NH in addition to the s effect. All of these processes do not occur independently, but conspire to give the 'resultant' effective sensitivities shown in Fig. 4.15.

The EBM fitting was repeated on the other models, and the real (OLS) effective sensitivities of ϕ_{i} to OHT are plotted against the EBM predictions in Fig. 4.16. In the NH, the two models with insignificant $r(\mathrm{OHT}, \phi_{\mathrm{i}})$ at $\phi_0 = 60°\mathrm{N}$ (CESM2-FV2 and CESM2-WACCM-FV2) are excluded. Similarly, ACCESS-CM2 and MPI-ESM-1-2-HAM are excluded in the SH because they have insignificant $r(\mathrm{OHT}, \phi_{\mathrm{i}})$ at $\phi_0 = 60°\mathrm{S}$. CAMS-CSM1-0 is also excluded in the NH because the EBM equation is unable to estimate the sensitivity due to this model having no relationship between F_{sw} and ϕ_{i} [$r(\phi_{\mathrm{i}}, F_{\mathrm{sw}}) = 0.09$, despite having $|r| > 0.8$ in the other required terms]. Accounting for error bars, for 11 of

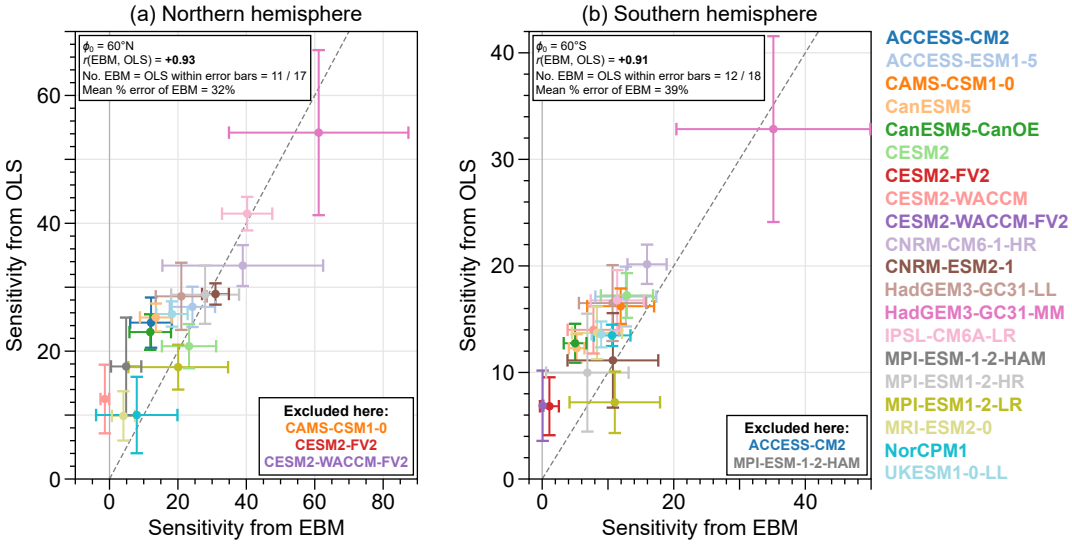

Figure 4.16: (a) Northern hemisphere effective sensitivity of the ice edge to poleward OHT, determined by OLS regression of anomalies in 25 yr means of the respective quantities, plotted against the fitted sensitivity of the EBM Eq. (3.23b). Error bars indicate standard deviations, and both axes are in °N PW^{-1}. The dashed line indicates OLS = EBM. (b) As in (a) but for the southern hemisphere (axes units: °S PW^{-1}).

17 models (65%) the EBM and OLS sensitivities overlap in the NH, and in the SH this 'success rate' is 12 of 18 (67%). The mean percentage error of the EBM slope is about 32% in the NH and 40% in the SH. In most cases, the EBM equation underestimates the sensitivity seen in the model. However, it correctly estimates larger sensitivities in models where the sensitivity is actually larger: the correlation between the EBM and OLS estimates is $r(\mathrm{EBM}, \mathrm{OLS}) > 0.9$ in both hemispheres [ignoring the extreme case of HadGEM3-GC31-MM, $r(\mathrm{EBM}, \mathrm{OLS}) > 0.75$].

In all models, the NH $\Delta\phi_\mathrm{i}/\Delta\mathrm{OHT}$ are larger than their SH counterparts. Overall, the magnitude of the sensitivities is determined by the $\Delta T_\mathrm{s}/\Delta\mathrm{OHT}$ term in Eq. (3.23b) (indicating the well-established relation between T_s and ϕ_i; Notz and Stroeve, 2016; Rosenblum and Eisenman, 2017). The interpretation for the difference in NH and SH sensitivities for HadGEM3-GC31-LL is also applicable to the majority of models included in both panels of Fig. 4.16, with some minor differences. The HadGEM3-GC31-MM model has the largest over-compensation in the SH with $b_\mathrm{c} = -2.5$, and $\Delta T_\mathrm{s}/\Delta\mathrm{OHT}$ is larger in the SH than in the

NH (opposite to HadGEM3-GC31-LL). However, it still has about a factor of 3 larger s in the SH compared to the NH, which, as described before, is the most important factor setting the difference in NH and SH sensitivities. The CESM2 and NorCPM1 models have similar b_c in both hemispheres but, again, this is not enough to override the effect of s which is a factor of 2 larger in the SHs of these models. Finally, CNRM-CM6-1-HR has the largest hemispheric difference in s at 5 times larger in the SH than in the NH, but it also has a substantial over-compensation of $b_c = 2.3$ in the SH such that the extreme s difference does not result in a substantially larger NH/SH sensitivity ratio than in the other models.

4.3.2 Application to models collectively

In section 4.2 it was shown that there are significant correlations between ϕ_i, OHT, AHT, and T_s across models, when defining $\Delta\phi_i$ as the maximum increase in the 25 yr-average time series of ϕ_i, and ΔOHT, ΔAHT, and ΔT_s as the corresponding changes in the respective quantities. This raises the question: does the EBM equation explain such inter-model relationship between OHT and ϕ_i? Rather than fitting to the diagnostics defined in that way, here the cross-model effective sensitivity of ϕ_i to OHT is assessed using the 25 yr anomalies for all models collectively. This increases the number of data points, which reduces the uncertainty in fitting the EBM equation and takes the whole time series into account rather than just model extrema. This first requires a slight reinterpretation of the other parameters in Eq. (3.23b), which now represent 'cross-model' relationships.

For the atmospheric radiation parameters B_{up}, B_{dn}, and B_{OLR}, the simplest approach is to calculate regression coefficients of the relevant heat flux and temperature anomalies. This is similar to the previous determination of these parameters from ERA-Interim data (section 2.3.2) and for single models (sec-

tion 4.3.1), but accounts for temporal and spatial variations in a different way. Specifically, let ΔF_{up} be the anomaly (relative to the model mean) in the net upward turbulent plus upwelling longwave flux, averaged between the reference latitude $\phi_0 = 60°\mathrm{N}/°\mathrm{S}$ and the pole, and averaged over a 25 yr period. Surface temperature anomalies ΔT_{s} are calculated as before. The multi-model ensemble of ΔF_{up} and ΔT_{s} are strongly positively correlated in both hemispheres ($r > 0.95$; Fig. 4.17a,c) and the slopes (i.e., B_{up}) are comparable to the values of B_{up} derived from ERA-Interim and from individual models (Table A.2). A similar procedure is carried out to determine the multi-model B_{dn}, using air temperature and downwelling longwave flux anomalies, ΔT_{a} and ΔF_{dn} respectively (Fig. 4.17b,e), and B_{OLR} using the TOA longwave flux, F_{OLR} (Fig. 4.17c,f).[5] There is more scatter associated with B_{dn} and B_{OLR}, particularly in the southern hemisphere. However, the correlation coefficients are still significant and strong ($r > 0.8$) in all cases, and the uncertainties of the regression slopes are at most a few percent.

The same procedure is used to compute s, b_{c}, and $\Delta T_{\mathrm{s}}/\Delta\mathrm{OHT}$ as for single models, but by including anomalies of the relevant quantities for all models together. Figure 4.18 shows the results of these regressions. In all cases the correlations are significant and strong ($r > 0.75$) and the slopes are comparable to previous single-model estimates (e.g., Fig. 4.14) and EBM values (Fig. 3.9). This is partly expected since this is effectively averaging the individual-model results, but it is still notable that these relationships hold with strong correlation across models. For example, BC relies on the assumption that the net TOA flux remains constant. This assumption is invalid across models (different models have different values of the TOA flux), but in removing the model means (by computing anomalies), Fig. 4.18b,e shows that a consistent AHT response to OHT perturbations emerges in the multi-model ensemble.

[5] Since only $\beta = B_{\mathrm{OLR}}/B_{\mathrm{dn}}$ is required, the slope in a plot of ΔF_{OLR} versus ΔF_{dn} gives β directly, eliminating the choice of pressure level for T_{a}. However, the full derivation with T_{a} provides a comparison with ERA-Interim and individual-model values of B_{OLR} and B_{dn}.

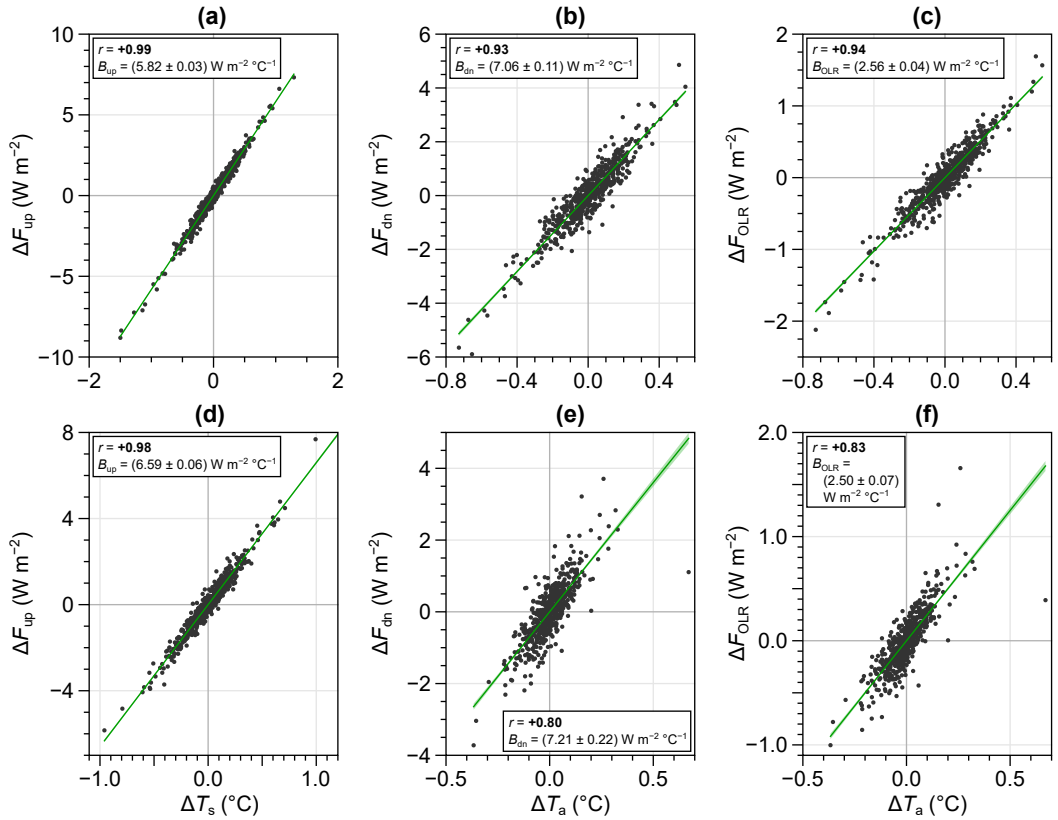

Figure 4.17: Values of B_{up}, B_{dn}, and B_{OLR} determined from the 20 CMIP6 PI-control simulations analysed in this chapter. Plots (a)–(c) are for the NH, and (d)–(f) are for the SH. Each point represents a 25 yr average from one of the (here, unidentified) models, as an anomaly relative to the model mean. (a,d) Net upward turbulent and longwave flux, ΔF_{up}, and surface temperature, ΔT_{s}. (b,e) Downwelling longwave flux, ΔF_{dn}, and air temperature, ΔT_{a}. (c,f) OLR, ΔF_{OLR}, and ΔT_{a}. All quantities are averaged between 60°N/°S and the pole. Air temperature is taken on pressure level (NH) $p_0 = 700$ hPa, (SH) $p_0 = 500$ hPa. Slopes of the OLS fits (green) give the multi-model values of (a,d) B_{up}, (b,e) B_{dn}, and (c,f) B_{OLR}.

As before, the EBM predicts that the terms in Figs. 4.17 and 4.18 should combine according to Eq. (3.23b), to give the multi-model effective sensitivity of ϕ_{i} to OHT, in each hemisphere. Firstly, the OLS regression of the multi-model $\Delta\phi_{\mathrm{i}}$ and ΔOHT anomalies are found: the correlations are about 0.8 in each hemisphere, but the slope is about 2 times larger in the NH than in the SH, as shown in Fig. 4.19. Here, the EBM predicted slope is also shown in green. The EBM underestimates the sensitivities by about 10% in the NH and 20% in the SH. Considering the uncertainty estimates of the OLS and EBM slopes, they do

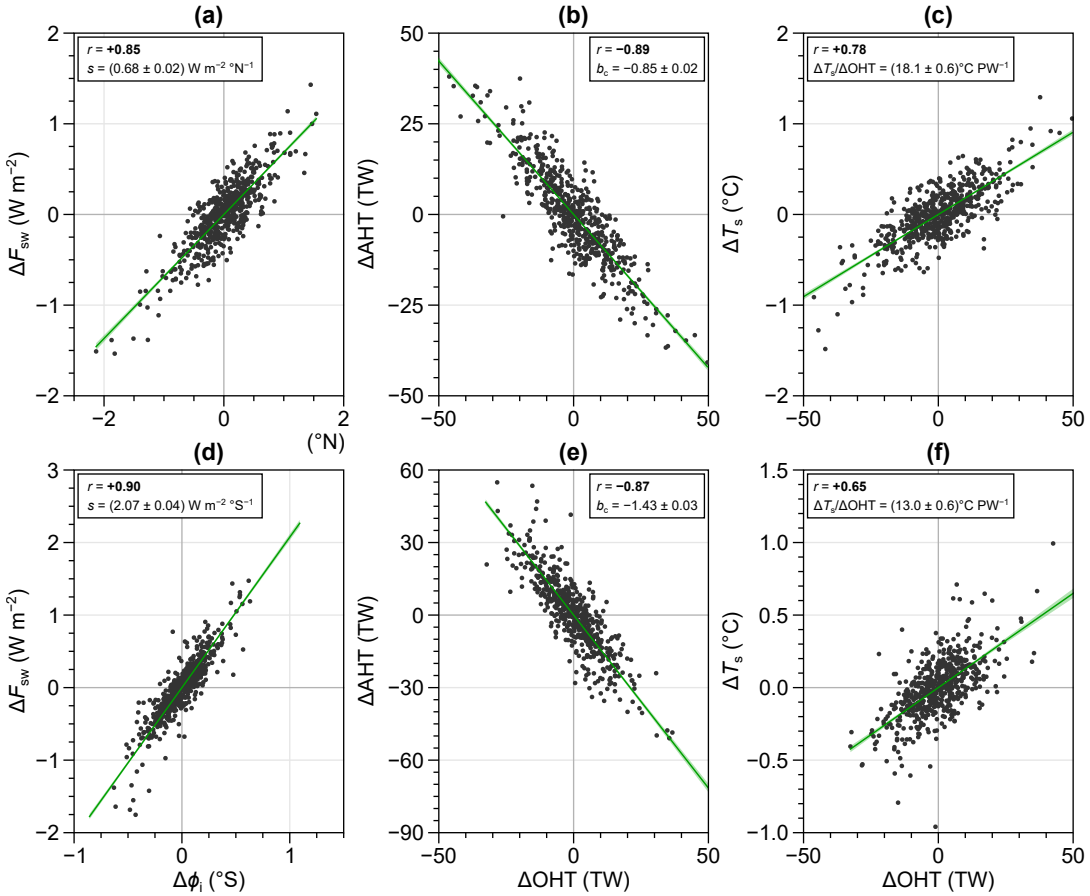

Figure 4.18: As in Fig. 4.14 but for all 20 CMIP6 models analysed in section 4.2 together, i.e., each point is a 25 yr average of a certain (here, unidentified) model.

overlap in the NH but not quite in the SH (about 7% error between the lower OLS and upper EBM limits). However, the ratio of NH to SH EBM slopes is about 2, matching the OLS ratio of slopes. Comparing the values of s, b_c, and $\Delta T_s/\Delta\text{OHT}$ in both hemispheres in Figs. 4.14 and 4.18 suggests that the explanation for the difference in NH and SH sensitivities across models (or, the mean model behaviour) can be explained in the same way as with HadGEM3-GC31-LL. In particular, it is primarily the difference in s that explains the factor of two larger sensitivity in the NH compared to the SH. Finally, note that there is sensitivity of $\Delta\phi_i/\Delta\text{OHT}$ to the reference latitude, ϕ_0. In the NH, the effective sensitivity is proportional to ϕ_0 (determined by OLS regression; Fig. 4.19c), but the EBM does not well capture this. In going from $\phi_0 = 55°\text{N}$ through to $\phi_0 = 65°\text{N}$, it

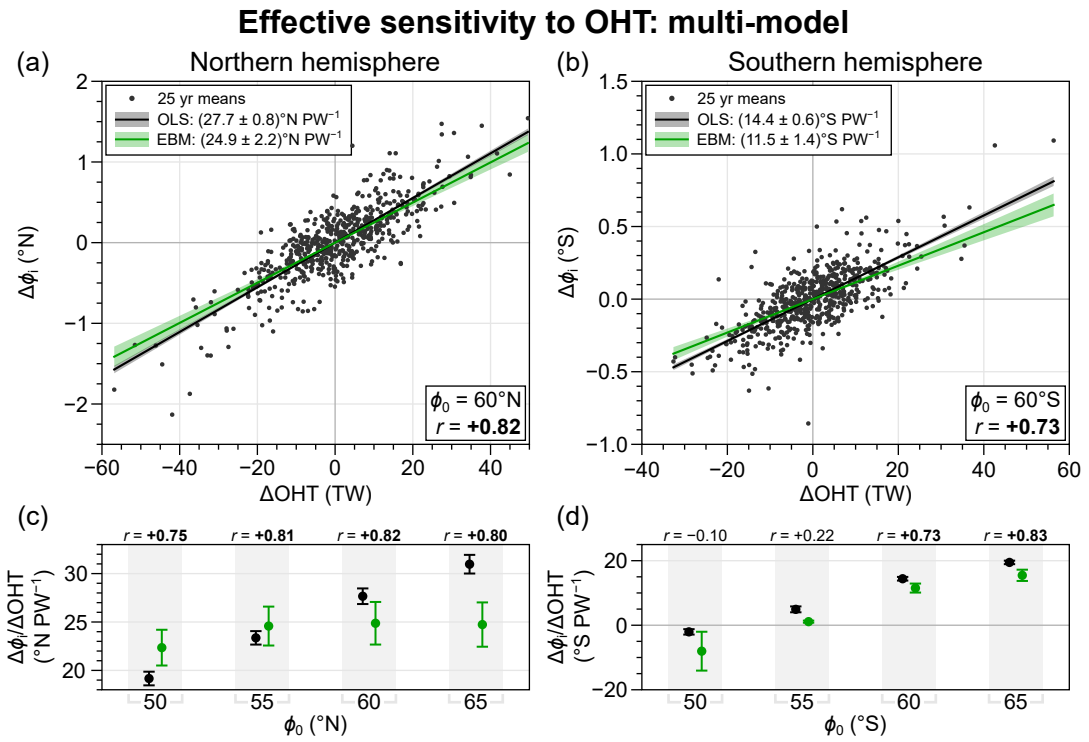

Figure 4.19: As in Fig. 4.15 but for all 20 CMIP6 models analysed in section 4.2 taken collectively, i.e., each point in (a) and (b) is a 25 yr average of a certain (here, unidentified) model.

happens that both terms on the RHS of Eq. (3.23b) increase by the same amounts, such that the EBM fits similar sensitivities over this range of ϕ_0. Specifically, $\Delta T_s/\Delta\text{OHT}$ and the area factor $1/A$ increase by similar proportions per 5°N increment in ϕ_0, while B_{up}, β and b_c do not change much. The cause of the equal sensitivities is that s also increases with ϕ_0, whereas it would be expected to decrease because F_{sw} decreases with latitude (Fig. 1.4a). If this were the case, it would result in larger $\Delta\phi_i/\Delta\text{OHT}$ with higher ϕ_0. However the opposite (s increases with ϕ_0) occurs because of zonal asymmetry in the Arctic ice cover: higher ϕ_0 start to substantially intersect the sea ice perimeter, so that the effect on ΔF_{sw} due to $\Delta\phi_i$ is not fully captured by s. Indeed, Eq. (3.23b) requires that $\phi_0 < \phi_i$ in order for the energy-balance underpinning the relation to hold. The sensitivities also increase with higher southern reference latitudes [taking $\phi_0 = 50°\text{S}$ and $\phi_0 = 55°\text{S}$ with caution due to the insignificant $r(\text{OHT}, \phi_i)$;

Fig. 4.19d]. Here, the EBM does capture this trend, albeit with a slight offset. Also, in the SH s decreases with ϕ_0 as expected, because the above effect of mixing ice-covered areas poleward and equatorward of ϕ_0 is less of an issue due to the relatively zonally-symmetric Antarctic sea ice cover.

4.4 Discussion

This chapter has assessed the impact of natural, multidecadal variability in OHT on sea ice in the NH and SH of 20 CMIP6 models' PI-control simulations. This has revealed that while poleward OHT is strongly correlated with the latitude of the sea ice edge in both hemispheres, this hides different underlying mechanisms for each hemisphere which are qualitatively robust across models. The theoretical framework of the EBM in chapter 3 broadly captures the relationship between ϕ_i and OHT in both hemispheres within and across these models. The different NH and SH mechanisms are analogous to two key EBM sensitivity experiments, and the effective sensitivities ($\Delta\phi_\mathrm{i}/\Delta\mathrm{OHT}$) can be explained qualitatively by computing terms in the EBM-derived Eq. (3.23b).

These results add to the growing evidence that OHT is a key player in the long-term evolution of sea ice extent, and are generally consistent with previous work. In particular, the effect of OHT being concentrated near the ice edge in the North Atlantic sector has been noted in individual model studies (see section 1.2.3). The novel aspect of the present analysis is that it shows this relationship exists within simulated unforced climate variability. Furthermore, it provides evidence that such relationships are robust across models, and contributes physical insight into the factors setting the sensitivity via the EBM analysis.

It was stated in section 4.3.1 that the EBM equation typically underestimates the sensitivity $\Delta\phi_\mathrm{i}/\Delta\mathrm{OHT}$. This suggests a systematic bias—possibly a process

missing from, or an inaccurate assumption built into, Eq. (3.23b). The most likely explanation is that the EBM equation does not include land and thus assumes that OHT converges over the whole spherical cap at latitude ϕ_0, when in reality it converges over a smaller area. This suggests that Eq. (3.23b) underestimates the direct ocean–ice flux effect, which reduces the predicted sensitivity relative to the real (OLS) sensitivity. This cannot be trivially accounted for by allowing OHT to converge over area $(1 - f_\mathrm{L})\,A$, where f_L is the land fraction of the spherical cap, because this would break energy conservation (Eq. 3.16). The point of Eq. (3.23b) is to explain the relationship between OHT and ϕ_i regardless of the underlying mechanism. In the NH of models (or the K_o sensitivity experiment of the EBM), a major part of the process is heat losses in the open ocean between ϕ_0 and ϕ_i. So another aspect here is that on the timescales being considered, the system roughly equilibrates such that the air–sea flux effect of OHT is already averaged over the whole region. In other words, ocean heat lost to the atmosphere is included in the atmospheric response (e.g., in the TOA fluxes) which applies to the whole region.

Ordinary least-squares (OLS) regression has been used to estimate parameter values in Eq. (3.23b) and effective sensitivities, $\Delta\phi_\mathrm{i}/\Delta\mathrm{OHT}$. This assumes that, in the latter for instance, all variability in $\Delta\mathrm{OHT}$ manifests in $\Delta\phi_\mathrm{i}$. If this is not the case, the value of the OLS slope is negatively biased from the true value (regression dilution; e.g., Draper and Smith, 1998). Although it is convenient to view Eq. (3.23b) with $\Delta\mathrm{OHT}$ as the independent variable, in the context of the PI control simulations this is not so. For example, OLS regression could be done on the same data in Fig. 4.15a but switching the horizontal and vertical axes to estimate $\Delta\mathrm{OHT}/\Delta\phi_\mathrm{i}$. Doing this and then taking the reciprocal gives $\Delta\phi_\mathrm{i}/\Delta\mathrm{OHT} = 45.2 \pm 8.3°\mathrm{N\ PW^{-1}}$, which is about 1.5 times the sensitivity estimated directly from regression of $\Delta\phi_\mathrm{i}$ against $\Delta\mathrm{OHT}$. It could be argued that both estimates of $\Delta\phi_\mathrm{i}/\Delta\mathrm{OHT}$ are upper and lower limits on the true value which lies

somewhere between. However, for the present purposes the individual sensitivity values are not used for anything except qualitative comparisons between hemispheres, and by repeating this on the SH data it can be seen that such insights are not substantially affected. For HadGEM3-GC31-LL, the SH sensitivity calculated from 'inverted' regression of ΔOHT onto $\Delta\phi_\mathrm{i}$ is 29.3 ± 6.4°S PW^{-1}. The ratio of 'inverted'-calculation sensitivities (1.5) is similar to that of the 'direct'-calculation (1.7). There is also no impact on the EBM fitting: for example, using Eq. (3.23b) with 'inverted' terms (regressing $\Delta\phi_\mathrm{i}$ onto ΔF_sw to obtain $1/s$, etc.) gives $\Delta\phi_\mathrm{i}/\Delta\mathrm{OHT} = 39.0 \pm 13.9$°N PW^{-1}, which agrees with the 'inverted' OLS estimate within error bars, to the same extent that the direct calculation does as presented in Fig. 4.15a. Note also that the 'inverted' EBM sensitivity is lower than the 'inverted' OLS sensitivity, so that this bias does not contribute to the systematic underestimation by the EBM discussed before. Since the method does not affect the qualitative results, and viewing ΔOHT as the 'independent' variable in Eq. (3.23b) is physically motivated in light of the mechanisms unveiled in section 4.2 (particularly keeping Fig. 4.13 in mind), the 'direct' OLS estimates are arguably more reliable than the 'inverted' ones. Nevertheless, there is clearly a limitation in estimating them from climate simulations in which ΔOHT is not controlled, so that the values should be taken cautiously as qualitative estimates.

A notable result from the EBM analysis is that the difference in ϕ_i sensitivities between the two hemispheres is mostly explained by the factor s (the change in net shortwave radiation per change in ϕ_i). Whether considering models individually or collectively, the SH value of s is about 3 times greater than the NH value (Figs. 4.14a,d and 4.18b,d). This factor would set the SH ϕ_i to be about 3 times less sensitive to OHT than the NH ϕ_i. However, two other factors are relevant: the mechanism of OHT (contained in the $\Delta T_\mathrm{s}/\Delta\mathrm{OHT}$ term of Eq. 3.23b) which further reduces the SH sensitivity relative to the NH, and the BC rate which, being over-compensating ($b_\mathrm{c} < -1$) in the SH while under-compensating

($-1 < b_c < 0$) in the NH, increases the SH sensitivity relative to the NH. The BC difference partially cancels the s and OHT-mechanism effects so that the net result is a ratio of NH to SH sensitivities being roughly 2. To leading order, then, the difference in s between hemispheres explains the difference in ϕ_i sensitivities. As explained in section 4.3.1, this means that primarily geometric effects of the NH land distribution account for the difference in ϕ_i sensitivities.

If the end result is that the difference in sensitivities is mostly explained by land effects, and one of the purposes of using ϕ_i rather than sea ice extent, S_i, is to eliminate the influence of land, does this mean that the problem has just been shifted into the EBM equation? Using the factors in Fig. 4.3 to convert from ϕ_i to S_i suggests that the ratio of NH to SH sensitivities of S_i to OHT is approximately 1. Both ways of quantifying the sea ice sensitivities are consistent and have their own merits, but by switching to ϕ_i it is clear that more insight is gained. Suppose that the ϕ_i diagnostic and EBM framework were not known, and that Arctic and Antarctic S_i sensitivities to OHT being about equal was found. From this 'naive' perspective it is not obvious how the land effect manifests because it is hidden in S_i itself. Therefore, by introducing ϕ_i and the EBM equation describing its response to OHT, it has been identified that land primarily influences the sea ice sensitivity to OHT by modifying how much shortwave fluxes must adjust to restore the TOA fluxes. This new insight into the behaviour of the CMIP6 models reflects a major advantage of the EBM approach.

The approach taken in this chapter has some limitations. Although using PI-control simulations means that results are not dependent on a forced response, a disadvantage is that some models have quite small magnitudes of internal variability, which hides the signal of the effect of OHT on sea ice behind noise. This potentially contributes to the error in fitting the EBM equation to models individually and across models in section 4.3. Also, in the multi-model fit of Fig. 4.19a,b, extreme anomalies in $\Delta\phi_i$ and ΔOHT are mostly contributed by a

few particular models with largest internal variability (notably the CNRM models and IPSL-CM6A-LR). Of course, considering climate change simulations and the forced responses of each diagnostic (which are larger than their internal variations) is an obvious way of increasing the signal-to-noise ratio. Therefore, the analysis of CMIP6 future simulations in chapter 5 provides a better assessment of how well the EBM captures the model behaviour. Analysing a large sample of GCMs comes at the cost of it being impractical to analyse every detail of the simulations—for example, sea ice dynamics were not considered. This could be relevant to both Arctic sea ice (e.g., as in Castruccio et al., 2019, who suggest a dynamic response of Arctic sea ice to atmospheric circulation changes) and Antarctic sea ice (e.g., Sun and Eisenman, 2021, showing improved comparison of simulated to observed trends after manually correcting Antarctic sea ice drift in CESM). The thermodynamic interpretations put forward are not called into question by this—on the contrary, they strengthen the conclusions of previous studies finding similar behaviours in the NH (e.g., Bitz et al., 2005; Koenigk and Brodeau, 2014; Singh et al., 2017) and SH (e.g., Goosse and Zunz, 2014). Still, the role of dynamics in the identified NH/SH mechanisms would make a worthwhile future study, potentially highlighting a specific area of model improvement for sea ice simulation.

Finally, this analysis has focused on multidecadal variability by computing 25 yr averages. It is worth noting that some models show evidence of significant centennial-scale variability in all key diagnostics: particularly, in the NH of CNRM-ESM2-1 and IPSL-CM6A-LR (Fig. 4.5). In these models, this longer-timescale variability probably explains why they have the largest anomalies in $\Delta\phi_\mathrm{i}$ and ΔOHT (Figs. 4.9–4.11). It is possible that different mechanisms could occur on different timescales: for example, this could be indicated by the strong, positive correlation between OHT, h_o, and ϕ_i in the NH of CNRM-ESM2-1 (Table 4.2).

4.5 Chapter summary

The key results of this chapter are as follows:

1. **Natural multidecadal fluctuations in poleward OHT are strongly correlated with sea ice extent, or equivalently the zonal-mean latitude of the sea ice edge:**

   a) The correlations with poleward AHT are opposite in sign, which is attributed to Bjerknes compensation;

   b) The correlations depend strongly on the latitude at which OHT and AHT are evaluated, reflecting differences in the underlying mechanisms.

2. **Different mechanisms of the sea ice response to OHT are evident in the northern and southern hemispheres:**

   a) NH: OHT primarily converges along the Atlantic sea ice edge, efficiently eroding the ice edge and enhancing AHT to the central Arctic where surface melt occurs. This is analogous to the behaviour of the K_o sensitivity experiment of the EBM (section 3.2.1).

   b) SH: OHT is released uniformly under the Antarctic ice pack. This is analogous to the behaviour of the F_{bp} sensitivity experiment in the EBM (section 3.2.3).

3. **The effective sensitivity of the ice edge to OHT is broadly captured and explained by the EBM:**

   a) The Arctic sensitivity is larger than that of the Antarctic in models primarily because of the inherently larger sensitivity associated with localised OHT convergence, and the smaller reduction in planetary

albedo when sea ice retreats in the north Atlantic compared to the Southern Ocean;

b) A multi-model relationship between changes in sea ice extent and OHT emerges, which is captured by the EBM, and strengthens the case for a substantial role of inter-model OHT biases in the spread of sea ice projections.

Chapter 5

Ocean role in projected future sea ice loss

An important motivation behind this thesis is the possible contribution of OHT to inter-model spread in sea ice projections of coupled GCMs (Fig. 1.1). Returning to this point, this chapter presents analyses of 21st-century climate simulations with plausible future emission scenarios from CMIP6. In essence, the aim here is to establish what relationships exist between OHT and sea ice under a forced climate response with substantial changes in sea ice cover, and interpret how these arise in light of the results of previous chapters.

The models, data availability, and experiments analysed, are described briefly in section 5.1. Section 5.2 presents correlation analyses on the time series of the ice-edge latitude and the other key diagnostics identified in chapter 4, which shows again the strong role of OHT, here in terms of the mean state and rates of sea ice decline across models. The EBM is then used to explain the inter-model relationship between sea ice and OHT changes across different time periods, in section 5.3. Next, section 5.4 investigates whether the distinct NH versus SH mechanisms identified in section 4.2 also apply to the relation between OHT and ϕ_{i} changes in the future. Finally, the seasonally sea ice-free Arctic state—

which occurs in many model projections but with high uncertainty on the timing (Fig. 1.2)—is briefly explored in section 5.5. Results are discussed in section 5.6, and the key points are summarised in section 5.7.

5.1 Data and methods

The ScenarioMIP simulations (O'Neill et al., 2016) project the global climate state to the end of the 21st century under different greenhouse-gas emission and socioeconomic development scenarios. In this chapter, the four Tier 1 experiments are analysed. These are labelled SSP1-2.6, SSP2-4.5, SSP3-7.0, and SSP5-8.5, which for the purposes of the present work may be simply interpreted as increasing levels of emissions, respectively. The last two digits in the labels indicate the nominal, global-mean radiative forcing, in W m^{-2}, in the year 2100. To enable comparisons with contemporary and pre-industrial conditions, the historical simulations (1850–2014; Eyring et al., 2016) are also used. These are combined with the ScenarioMIP simulations (which start in 2015, being initiated from the end of a historical realisation), to give continuous time series over 1850–2100. Different realisations of a given model's historical simulation are initialised from different times of its PI-control simulation (Eyring et al., 2016, appendix A.2). Therefore, the first 25 yr average period, 1850–1875, is considered to approximate the PI-control state (i.e., neglecting the effect of the 1850–1875 forcing).

The models included are a subset of those analysed in chapter 4, because not all of the models in Table 4.1 contribute to ScenarioMIP. Table 5.1 lists the number of ensemble members available per experiment for each model, based on data availability. Of the 20 models analysed in the previous chapter, 4 are thus excluded (CESM2-FV2, CESM2-WACCM-FV2, MPI-ESM-1-2-HAM, and NorCPM1), but CNRM-CM6-1 is added to the sample. This still gives a variety of models with different resolutions and configurations.

Table 5.1: Number of ensemble members available for the historical and ScenarioMIP experiments of the 17 CMIP6 models analysed in this chapter.

Model	Historical	SSP1-2.6	SSP2-4.5	SSP3-7.0	SSP5-8.5
ACCESS-CM2	3	3	3	3	3
ACCESS-ESM1-5	12	10	10	10	10
CAMS-CSM1-0	2	2	2	2	2
CanESM5	40	25	25	25	25
CanESM5-CanOE	3	3	3	3	3
CESM2	11	3	3	3	3
CESM2-WACCM	3	1	3	1	3
CNRM-CM6-1	20	6	6	6	6
CNRM-CM6-1-HR	1	1	1	1	1
CNRM-ESM2-1	5	1	1	1	1
HadGEM3-GC31-LL	3	1	1	0	3
HadGEM3-GC31-MM	4	1	0	0	4
IPSL-CM6A-LR	32	6	11	11	6
MPI-ESM1-2-HR	10	1	2	10	2
MPI-ESM1-2-LR	10	10	10	10	10
MRI-ESM2-0	5	1	1	5	1
UKESM1-0-LL	16	13	5	13	5
Total simulations:	180	88	87	104	88

Following the methodology of chapter 4, 25 yr averages of each diagnostic are computed to capture the transient mean state on multidecadal timescales. The primary focus here is on inter-model relationships. Rather than analysing individual time series, differences and correlations across ensemble members are considered. Taking models collectively in each future scenario, this gives ~ 100 data points (Table 5.1). While this analysis could be applied to models individually, there needs to be a sufficient number of realisations to extract meaningful relationships, and most models provide less than 10 (Table 5.1). The main exception is CanESM5: 25 ensemble members are available for all four scenarios, and this is exploited for the seasonally sea ice-free Arctic analysis in section 5.5.2.

All required raw data and physical diagnostics are as described in section 4.1.2.

One subtlety arises with the ice-edge latitude, ϕ_i, because many models become seasonally ice free (SIF) in the future. In the EBM analysis of section 3.2, it was noted that in computing the annual-mean ϕ_i there is a choice of whether to include times of the year when the ice edge is effectively at 90°N. There, both averages were considered as they incorporate slightly different information: if all times of the year are included [average (i)], the effect of warmer open ocean is included. If only times of the year when ice is present is included [average(ii)], this represents only immediate effects on sea ice. For the GCMs, years which are SIF are identified when the minimum sea ice extent, S_i—which occurs in September in the NH, and in February in the SH—is less than a threshold, $S_\mathrm{i}^\star = 1\times10^6$ km^2. This is better than determining SIF years from the ϕ_i diagnostic directly, because it is consistent across models and between hemispheres, and it is not obvious how to construct an equivalent SIF threshold in terms of ϕ_i. Until otherwise explicitly indicated in section 5.5, the average (i) is used throughout this chapter and does not affect the interpretation of analyses in sections 5.2–5.4. Note that in the previous chapter, average (i) was also implicitly used, but this choice was ultimately immaterial. For the NH, none of the models analysed are SIF in the PI-control simulations. Although 7 of 20 models exhibit SIF Southern Oceans in the PI-control simulations (only 3 of which are SIF throughout the whole time series), using average (ii) instead has negligible impact on results since the two averages have almost the same variability [i.e., when average (i) is anomalously high, so is average (ii)].

Finally, it is worth commenting from the outset about the use of correlations in this chapter. The issue that correlations do not inherently prove causal relationships was discussed in section 4.2.4. Here, this is potentially more problematic because forced climate change scenarios are analysed, in which correlations may emerge between two variables merely because they both evolve with time. However, the advantage of this simple methodology remains: it enables the 547

existing simulations (Table 5.1) to be rapidly analysed and, aided by the EBM framework, a physically plausible interpretation consistent with the data can be found. How this affects the findings of this chapter is discussed more thoroughly in section 5.6.

5.2 Relating future sea ice loss to OHT

5.2.1 Mean-state biases in OHT

To begin, the result of Mahlstein and Knutti (2011) for CMIP3 models is revisited, repeating the analysis on CMIP6 models with some modifications to their approach. Specifically, they found a strong anticorrelation ($r = -0.72$) between OHT and sea ice extent, S_i, in CMIP3 simulations, averaging over the period 1970–1999. However, they used single ensemble members per model and their study was focusing on the Arctic. Here, all available ensemble members of the CMIP6 historical simulations are included and both hemispheres are assessed. The existence of an anticorrelation between OHT and S_i across models suggests a role for mean-state biases of OHT in the inter-model spread of S_i as the historical and future simulations evolve. Such biases originate in the PI-control simulations from which the historical simulations are initialised. Therefore, the time average over 1850–1875 is considered (at first), which approximates the PI-control state. Finally, since it has already been demonstrated that S_i and the ice-edge latitude diagnostic of Eisenman (2010), ϕ_i, are strongly correlated in the PI-control simulations (Fig. 4.3), here S_i is exchanged for ϕ_i to link with the previous results in chapters 3–4, and ϕ_i is later used in sections 5.3–5.5.

Figure 5.1 plots ϕ_i against poleward OHT, each averaged over 1850–1875, in the historical simulations of CMIP6 models listed in Table 5.1. For the NH, CAMS-CSM1-0 is excluded because both of its ensemble members are substan-

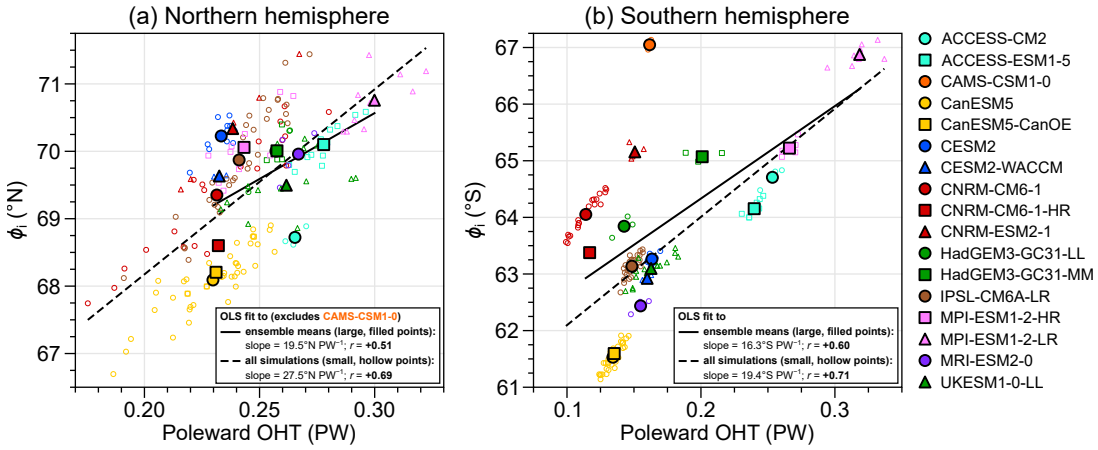

Figure 5.1: Ice-edge latitude, ϕ_i, plotted against poleward OHT evaluated at 65°N/°S, each averaged over 1850–1875, in the CMIP6 historical simulations. Individual ensemble members are plotted in small, hollow points, and ensemble means are the large, filled points. Ordinary least squares (OLS) regression lines are fitted to ensemble means (solid) and to all simulations collectively (dashed). For the NH in (a), CAMS-CSM1-0 is excluded, which is outside the axis limits at OHT ∼ 0.1 PW, ϕ_i ∼ 65°N.

tially out of the range of the other models (OHT ∼ 0.1 PW and ϕ_i ∼ 65°N), such that it exaggerates the inter-model correlation. For the remaining models, OHT and ϕ_i exhibit significant (based on a t-test with 95% confidence level as described in section 4.1.3) correlation in the NH, and when taking all points together the correlation $r = 0.69$ is comparable to the result for CMIP3 models from Mahlstein and Knutti (2011). The correlation of ensemble means is still significant but weaker ($r = 0.51$). There is substantial overlap and variation in the degrees of internal model spreads, which reflects the different magnitudes of internal variability of the PI-control simulations identified in the previous chapter (e.g., Fig. 4.9). Since 1850–1875 approximates the PI controls, Fig. 5.1a is analogous to Fig. 4.19a except that model means are not subtracted in the former. Because of the model overlap, in this case the OLS slopes in the two figures are similar. Significant correlations across model means ($r = 0.60$) and across all simulations collectively ($r = 0.71$) are also found in the SH (Fig. 5.1b). Unlike the NH, different models are more separated and there is less overlap of internal spreads in the SH. The ranges of model means in OHT and ϕ_i in the SH are about

twice those of the NH, and dominates the internal variabilities (i.e., intra-model spreads) in setting the total spread. Overall, Fig. 5.1 shows that simulations with larger initial poleward OHT tend to have smaller initial sea ice cover, and the multi-model ensemble spread is dominated by model differences in the SH. When poleward OHT in the NH is large, the SH poleward OHT is also typically large ($r = 0.75$ for ensemble means, $r = 0.61$ for all simulations). Similarly, models with larger sea ice cover in one hemisphere also tend to have larger sea ice cover in the other hemisphere ($r = 0.66$).

If the time-averaging period is changed to 1975–2000, the relationship between OHT and ϕ_i is similar to that shown in Fig. 5.1. This suggests that the behaviour of CMIP3 models identified by Mahlstein and Knutti (2011) is still exhibited by CMIP6 models, also applies to Antarctic sea ice, and supports the notion of a significant role of mean-state OHT biases in future projections of sea ice. To explore this further, the analysis is now extended to other time periods and other diagnostics. Figure 5.2 shows the correlations between 25 yr averages of ϕ_i, OHT, AHT, and T_s, across models, as a function of time-averaging period, from model ensemble means (solid lines) and from the multi-model ensemble (dashed lines). Note that slightly different sets of models and ensemble members enter into each future scenario (Table 5.1), and for the historical period the subset for SSP3-7.0 is used for a fairer comparison with the future simulations (since there are about twice the number of historical simulations available in total).

The correlation of OHT with ϕ_i across all simulations remains mostly significant and moderately strong throughout the 20$^{\mathrm{th}}$ century in the NH, but weakens to insignificant levels in all future scenarios (Fig. 5.2a). This indicates a divergence away from a coherent inter-model relationship between OHT and ϕ_i like that in Fig. 5.1a in the NH, suggesting a weakened role of mean-OHT biases in the future. There is no relationship between ϕ_i and AHT (Fig. 5.2c), despite there being a cross-model Bjerknes compensation (BC) between AHT and OHT (Fig. 5.2g).

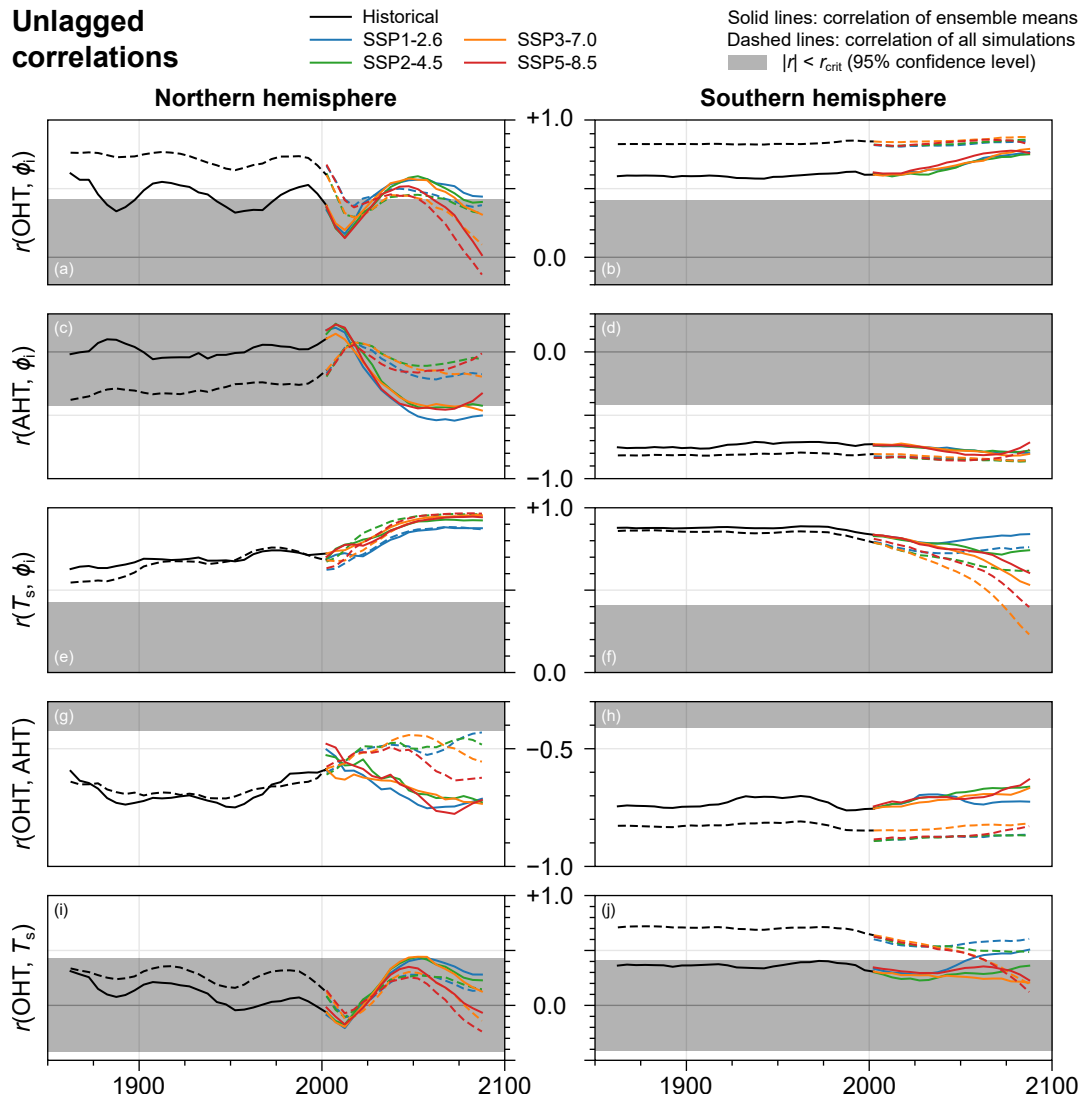

Figure 5.2: Correlations between various diagnostics (25 yr averages) in the historical and ScenarioMIP experiments across CMIP6 models, as a function of time. For the solid lines, ensemble means are first calculated for each model before computing r. For the dashed lines, all simulations for all models are taken together in computing r. Here, OHT and AHT are evaluated at 65°N/°S, and T_s is averaged between 65°–90°N/°S. Time coordinates are the centre of the averaging period (e.g., values of r for the average over 1850–1875 are plotted at 1862.5). Shading indicates statistical insignificance at the 95% confidence level based on a t-test of the ensemble means. Historical simulations do not join exactly with the future simulations because the latter have different sets of models/simulations (see Table 5.1). In the NH (left panels), CAMS-CSM1-0 is excluded.

Unsurprisingly, models and simulations with less sea ice (larger ϕ_i) tend to have a warmer Arctic (Fig. 5.2e), although it is notable that $r\,(T_s, \phi_i)$ starts relatively weak and strengthens towards the end of the 21st century—opposite to the case

of $r\,(\mathrm{OHT}, \phi_\mathrm{i})$. At no time in the historical period or in any future scenario is there a significant correlation between OHT and the mean surface temperature, T_s (Fig. 5.2i), even when $r(\mathrm{OHT}, \phi_\mathrm{i})$ is strong. There are no major differences between these correlations in any of the four future scenarios, despite large differences in the amount of sea ice loss. In the NH, models become SIF over a wide range of times in all four scenarios (spanning ~ 50 yr; Fig. 1.2). This could affect the correlations at later times as an increasing proportion of models have qualitatively different climate states. This point is returned to in section 5.5.

Correlations in the SH are more consistent in time compared to the NH. That between OHT and ϕ_i remains about as strong throughout the 20$^{\mathrm{th}}$ and 21$^{\mathrm{st}}$ centuries as it is initially in the PI state, as shown in Fig. 5.2b. Unlike in the NH, there is an anticorrelation between AHT and ϕ_i, persisting across time roughly symmetrically with $r\,(\mathrm{OHT}, \phi_\mathrm{i})$ (Fig. 5.2d), indicating again the cross-model BC which is slightly stronger in the SH (Fig. 5.2h). Another difference is the behaviour of T_s. Initially, $r\,(T_\mathrm{s}, \phi_\mathrm{i}) \sim 0.9$ across models (Fig. 5.2f), but this weakens in the future and becomes insignificant in the high-emission scenarios (SSP3-7.0 and SSP5-8.5), while at the same time $r\,(\mathrm{OHT}, \phi_\mathrm{i})$ increases slightly (Fig. 5.2b). This suggests that OHT is more important than warming in the SH in the future, consistent with the weakening of $r\,(\mathrm{OHT}, T_\mathrm{s})$ (Fig. 5.2j). Again, there are no substantial differences between the different future scenarios, but here this is unlikely to be related to a seasonal Antarctic sea ice cover since about 20% of simulations are already SIF in the historical period (Fig. 5.14b).

5.2.2 Changes in OHT

From the analyses in chapters 3–4 which show how variations in sea ice, $\Delta\phi_\mathrm{i}$, are sensitive to variations in OHT, ΔOHT, it is reasonable to hypothesise that differences across models in ΔOHT, i.e., a change across time, contribute to

differences in the rates of sea ice decline. For each diagnostic d, let $\Delta d = \Delta d\,(t)$ be the average of d over the 25 yr time period centred at time t, minus that at a fixed time-averaging period t_0, here taken as 1975–2000 ($t_0 = 1987.5$). These are computed for each model simulation, in each future scenario, and the correlations between key combinations of diagnostics are plotted as a function of t in Fig. 5.3.

Correlations between the changes in diagnostics are generally stronger than those between the corresponding mean states (compare Figs. 5.2 and 5.3), mainly because the model mean differences have effectively been removed. Larger increases in OHT are strongly and significantly correlated with larger sea ice losses in both hemispheres (Fig. 5.3a,b), which remains so until the end of the 21$^{\text{st}}$ century, except in SSP5-8.5 for the NH. The fact that $r\,(\Delta\text{OHT}, \Delta\phi_\text{i})$ becomes insignificant in the high-emission scenario for the NH could be related to fundamental changes in the behaviour of the Arctic as it becomes SIF: nearly all SSP5-8.5 simulations are SIF after 2080 (Fig. 5.14a). However, this is also the case for SSP3-7.0, in which $r\,(\Delta\text{OHT}, \Delta\phi_\text{i})$ does not drop that much compared to earlier times, so the effect of the Arctic becoming SIF is not clear. A cross-model BC, manifesting as a strong anti-correlation between ΔOHT and ΔAHT, is revealed in Fig. 5.3g,h. This results in the opposite relationship between $\Delta\phi_\text{i}$ and ΔAHT, such that larger sea ice losses are associated with reduced AHT (Fig. 5.3c,d). In the NH, the strength of $r\,(\Delta\text{OHT}, \Delta\text{AHT})$ decreases with time: this is another instance where the emergence of SIF states in the ensemble of simulations could be relevant due to the increased area of open ocean for air–sea exchanges to occur. This also applies in the SH, with the additional effect that SH BC is confined near the ice edge (Fig. 4.6d, left), so that here the strength of BC is weakened at 65°S as the ice edge retreats in the future and inter-model spread widens (i.e., 65°S becomes a less suitable reference latitude for an increasing subset of ensemble members as time evolves). Changes in OHT are also strongly correlated with the change in surface temperature, ΔT_s (Fig. 5.3i,j), and, unsur-

prisingly, the latter is strongly correlated with $\Delta\phi_\mathrm{i}$ (Fig. 5.3e,f). This is similar to the other findings of Mahlstein and Knutti (2011): models/simulations with greater increases in OHT into the Arctic simulate larger degrees of future polar warming, which is also associated with greater reductions in sea ice. A similar result applies to the SH. Figure 5.3 shows that the diagnostics ΔOHT, $\Delta\phi_\mathrm{i}$, and ΔT_s are strongly related across models, in both hemispheres. This indicates that the EBM analysis, particularly Eq. (3.23b), could provide insight into the role of OHT in future sea ice projections (section 5.3).

While the correlations between OHT and ϕ_i (the mean values) are not as strong in the NH (Fig. 5.2a) compared to the changes ΔOHT and $\Delta\phi_\mathrm{i}$ (Fig. 5.3a), the former should not be disregarded. This is especially considering that the inter-model relationship shown in Fig. 5.1a in conjunction with the results of Mahlstein and Knutti (2011) implies it is a persistent feature across generations of GCMs. One possibility is that the initial spread in sea ice extents associated with OHT is retained in the future—in other words, there could be a relationship between initial OHT and future sea ice. To check this, Fig. 5.4 plots the correlation of the 25 yr mean $\phi_\mathrm{i}(t)$ with OHT averaged over a fixed time period: in the top row, this is the approximated PI control, 1850–1875, and in the bottom row this is the late 20$^\mathrm{th}$ century, 1975–2000. In the NH, the correlation of ϕ_i with the PI-control OHT mainly drops to the insignificant range around 2000 (Fig. 5.4a), but relative to 1975–2000 there is significant anticorrelation (Fig. 5.4c). This means that models with initially (in the late-historical period; Fig. 5.4c) larger OHT tend to have more Arctic sea ice by the end of the 21$^\mathrm{st}$ century, regardless of the future scenario (i.e., strength of ice decline). This result—which is counterintuitive in light of previous results—is not replicated in the SH (Fig. 5.4d): instead, the end-of-century Antarctic sea ice cover tends to be smaller when the initial poleward OHT is larger.

The reversed sign of correlation between historical OHT and future Arctic

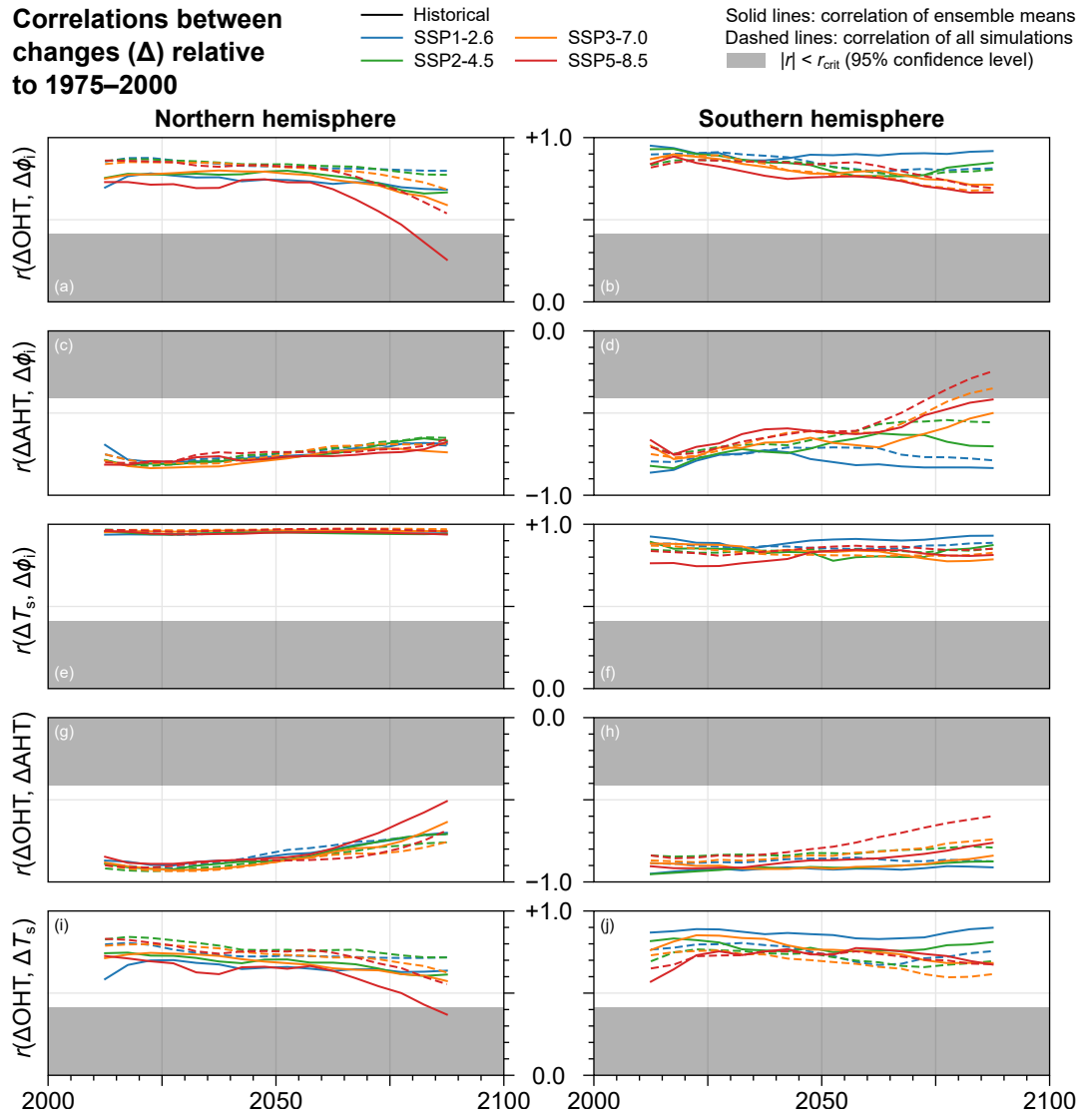

Figure 5.3: Correlations across models between the changes in various diagnostics relative to 1975–2000 in the ScenarioMIP experiments. Each diagnostic $\Delta d\,(t)$ is its 25 yr average centred at time t (horizontal axes) minus that over the fixed time period 1975–2000. Otherwise, as in Fig. 5.2, except here CAMS-CSM1-0 is included in the NH (left panels).

sea ice cover can be explained by considering again the change in future OHT. Figure 5.5a plots the change in OHT averaged over a near-future period, 2025–2050,[1] relative to the late-historical period, 1975–2000, against the OHT at the same late-historical period. Simulations with initially larger OHT show larger decreases/smaller increases in OHT (generally, more negative ΔOHT) going into

[1]For now, end-of-century time periods are avoided since more than half of the SSP5-8.5 simulations become seasonally ice free in the Arctic after 2050; see section 5.5.

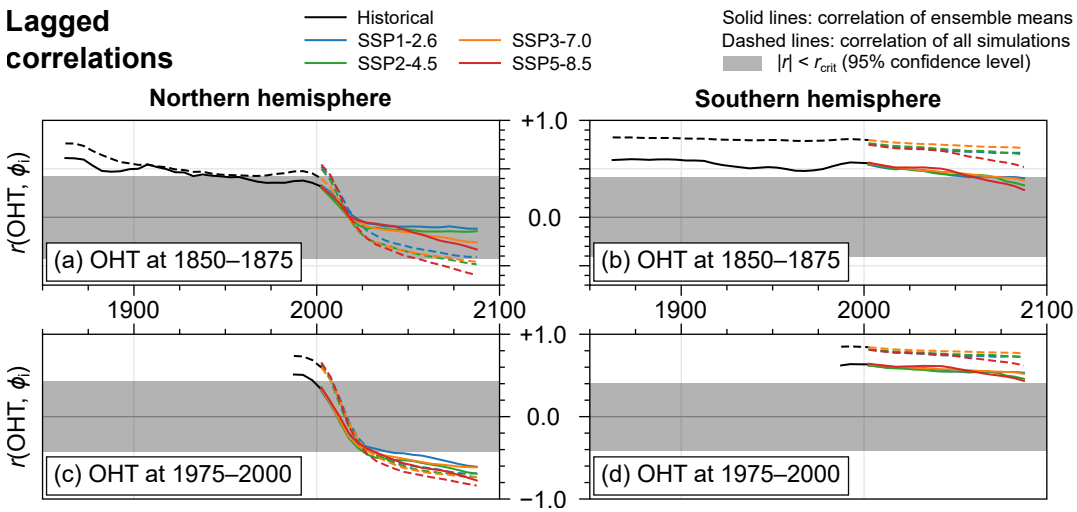

Figure 5.4: Correlation across all simulations (dotted) and ensemble means (solid) between the 25 yr mean ϕ_i centred at time t (horizontal axes) and OHT averaged over a fixed time period: (a,b) 1850–1875; (c,d) 1975–2000.

the future, which results in smaller sea ice declines (Fig. 5.5b) and thus the negative lagged correlation between OHT and ϕ_i in Fig. 5.4c. Similar relationships between initial OHT, future OHT change, and future sea ice decline, are seen in the SH (Fig. 5.5c,d). However, there is no change of sign of the lagged correlation between initial OHT and future sea ice cover in the SH (Fig. 5.4d). This is because the inter-model differences in mean initial OHT (i.e., the horizontal axis of Fig. 5.5c) are larger than that of the future changes ΔOHT (i.e., the vertical axis of Fig. 5.5c).

To summarise, this section has compared the effects of mean-state biases in OHT and temporal changes in OHT on sea ice in CMIP6 historical and future simulations, expanding upon the result of Mahlstein and Knutti (2011). Based on correlation analyses, both aspects of OHT are associated with future spread in sea ice projections, and their impacts are summarised schematically in Fig. 5.6. Models which initially have larger OHT also have initially less sea ice, but have smaller increases in OHT in the future. In the NH, the change ΔOHT dominates the effect of the initial mean OHT on future sea ice states (explaining the counter-

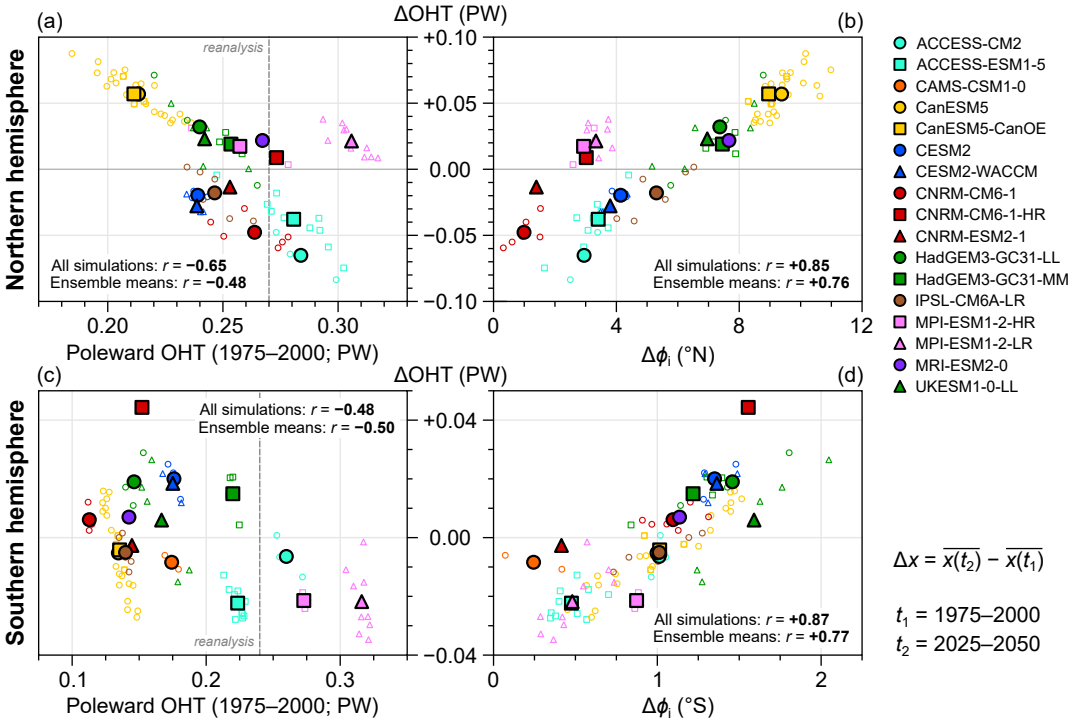

Figure 5.5: (a,c) Change in poleward OHT between the average over 1975–2000 and over 2025–2050, ΔOHT, plotted against OHT averaged over 1975–2000, in the NH and SH respectively. Vertical dashed lines indicate the values of OHT estimated from the ECCO reanalysis (as in Fig. 1.3a, and averaged over the slightly later period 1992–2011 due to data availability). (b,d) ΔOHT as in (a,c) plotted against the change in ϕ_i between the same times. For times later than 2015, data comes from the SSP5-8.5 experiment. As in Fig. 5.1, large, filled points are ensemble means and small, hollow points are individual ensemble members.

intuitive result that models with larger historical OHT are associated with more sea ice at the end of the century). In the SH, the influence of the initial mean OHT spread persists throughout the whole period 1850–2100, although this is partly offset by the same correlation between larger increases ΔOHT and larger sea ice losses $\Delta\phi_i$.

5.3 Explaining trends with the EBM

The previous section revealed strong multi-model correlations between projected rates of sea ice loss ($\Delta\phi_i$), warming (ΔT_s), and ΔOHT (Fig. 5.3). Here, the

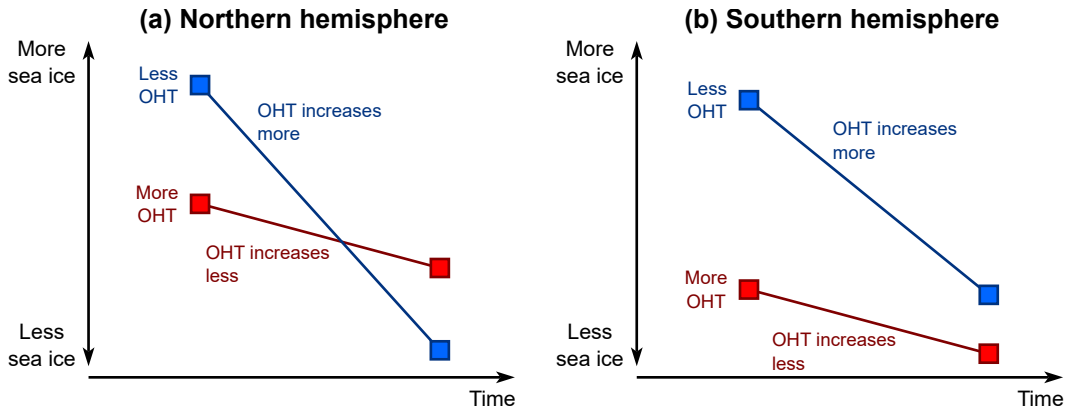

Figure 5.6: Schematic summary of the correlation analysis in section 5.2. The blue and red squares represent models with anomalously high and low initial sea ice covers respectively. Blue has less OHT than red initially, but OHT increases more in the future for blue. In both hemispheres, this enhances the rate of ice loss (steepness of lines) for blue compared to red. In the NH (a), this overwhelms the initial spread such that blue ends up with less ice than red. In the SH (b), initial spread is larger so that the difference in future OHT just reduces the gap between blue and red.

EBM is applied to these relationships and used to develop qualitative insight, in a similar manner to section 4.3. The EBM equation describing the relationship between ϕ_i, T_s, and OHT in terms of the various atmospheric parameters is again repeated here for reference:

$$\frac{\Delta\phi_\mathrm{i}}{\Delta\mathrm{OHT}} = \frac{\beta B_\mathrm{up}}{s\,(1+\beta)}\frac{\Delta T_\mathrm{s}}{\Delta\mathrm{OHT}} - \frac{1}{sA}\left(1+\frac{b_\mathrm{c}}{1+\beta}\right). \qquad \text{(3.23b revisited)}$$

In section 5.3.1, this is applied to the near-term future state (specifically, before a substantial number of models become SIF) in comparison to historical conditions. Then in section 5.3.2 the fitting is done to model simulations over a relatively short recent time period, which allows a superficial comparison of model trends to those of the real world.

Table 5.2: Values of the terms in Eq. (3.23b) derived in the PI control and future simulations, with reference latitude $\phi_0 = 65°\text{N}/°\text{S}$. For the PI, these are derived from 25 yr anomalies as described in section 4.3.2. For the future simulations, they are derived from the difference in states averaged over 1975–2000 and 2025–2050.

Experiment	s	b_c	$\Delta T_s/\Delta\text{OHT}$
Northern hemisphere ($\phi_0 = 65°\text{N}$)			
PI control	0.77 ± 0.02	-0.89 ± 0.02	21.8 ± 0.8
SSP1-2.6	0.89 ± 0.04	-0.93 ± 0.05	30.3 ± 3.0
SSP2-4.5	0.75 ± 0.04	-0.95 ± 0.05	31.9 ± 2.7
SSP3-7.0	0.72 ± 0.06	-1.01 ± 0.04	35.4 ± 2.9
SSP5-8.5	0.77 ± 0.04	-0.99 ± 0.06	32.5 ± 3.2
Southern hemisphere ($\phi_0 = 65°\text{S}$)			
PI control	1.66 ± 0.04	-1.22 ± 0.02	17.4 ± 0.6
SSP1-2.6	1.67 ± 0.10	-1.22 ± 0.07	22.2 ± 1.8
SSP2-4.5	1.78 ± 0.13	-1.17 ± 0.08	22.7 ± 2.2
SSP3-7.0	1.70 ± 0.12	-1.20 ± 0.07	22.7 ± 2.1
SSP5-8.5	1.82 ± 0.14	-1.20 ± 0.09	24.4 ± 2.3

5.3.1 Near-term future projections

In section 4.3, $\Delta\phi_i$, ΔOHT, and ΔT_s in Eq. (3.23b) were taken as anomalies in the PI control simulations. Here, as in the previous section, they are interpreted as the forced responses of each diagnostic and computed as the change between an initial and a final 25 yr average. The initial time is taken to be the approximate 'present-day' period, 1975–2000, and the final time is a 'near future' period: 2025–2050. Later in this section, other final time periods are considered.

There are a few considerations for parameter choices in Eq. (3.23b) to be discussed first. For the atmospheric radiative feedback parameters—B_{up}, B_{OLR}, and B_{dn}—the values derived in the PI-control simulations are used. This neglects changes in the relation between atmospheric radiation and air or surface temperature in the near future. Slightly different sets of models and simulations are available for each scenario (Table 5.1), so in principle separate values of B_{up}, B_{OLR}, and B_{dn} should be derived based on the relevant subsets for each scenario. However, it turns out that this does not substantially affect the values of B_{up}

Table 5.3: Sources of the terms in Eq. (3.23b) entering into the three different EBM fitting procedures in Figs. 5.7–5.8.

EBM fitting label	s	b_c	$\Delta T_s/\Delta$OHT
‘Future’	Future	Future	Future
‘Mixed’	PI	PI	Future
‘PI’	PI	PI	PI

or $\beta = B_{OLR}/B_{dn}$ (appendix A, Table A.6), and thus has negligible impact on EBM-derived sensitivities. Therefore, for simplicity, the same values as derived from all 17 models listed in Table 5.1 (i.e., the ‘historical’ subset in Table A.6) are used for all scenarios here.

For the other terms in Eq. (3.23b)—s, b_c, and $\Delta T_s/\Delta$OHT—the literal interpretation of the equation is to compute them from the future data. For example: $s = \Delta F_{sw}/\Delta\phi_i$, where ΔF_{sw} is the change in net shortwave radiation averaged between the reference latitude, ϕ_0, and the pole, between the initial and final time periods. This directly captures the physical processes and changes that ultimately give rise to the EBM-predicted relationship between ΔOHT and $\Delta\phi_i$. It is also reasonable to suggest that some of these terms represent constant, intrinsic properties of the multi-model ensemble, given by the PI-control derived values. For instance, s describes the change in shortwave radiation in response to changes in sea ice cover. It is plausible that this is no different when considering the near-term forced response than in the natural variability of the control simulations, barring other influences on the planetary albedo (future changes in cloud cover) or geometric effects relating to the change in area of exposed ocean per change in ϕ_i when ϕ_i reaches higher latitudes (Eq. 3.22). It is less clear whether b_c is affected: there are strong anticorrelations between ΔOHT and ΔAHT (Fig. 5.3g,h), but the correlation strength decreases with time and this does not show the rate of BC. The TOA fluxes are not constant in the future simulations, so the value of b_c derived as ΔAHT/ΔOHT could change with time. The changes in OHT

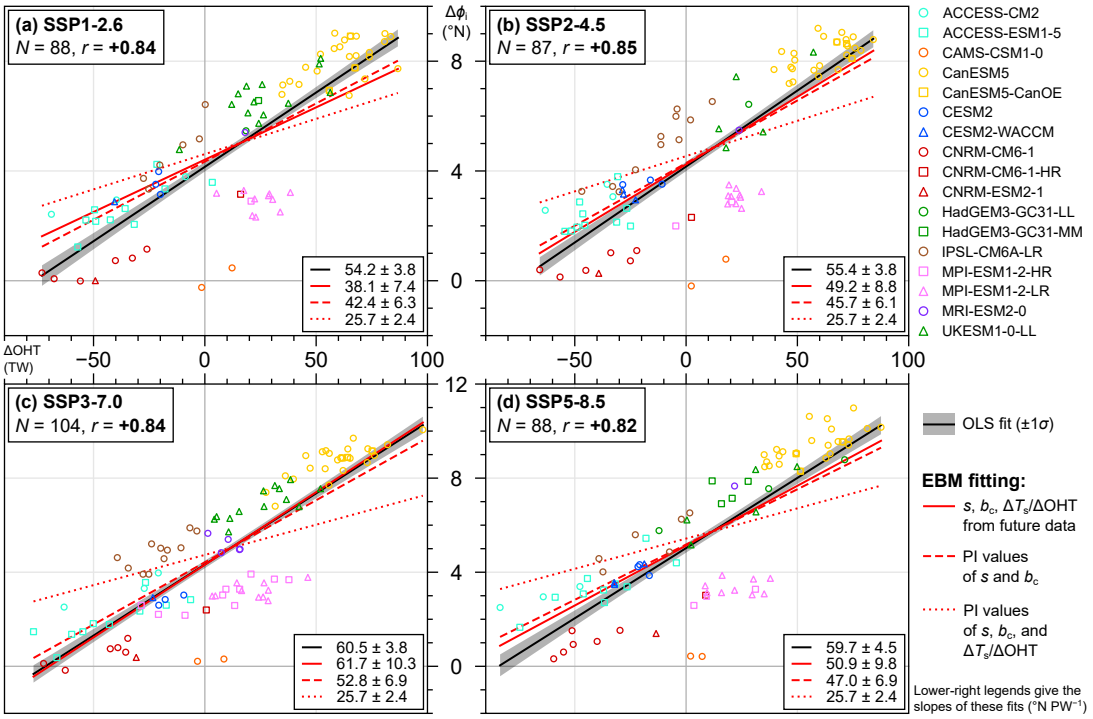

Figure 5.7: Change in poleward OHT (evaluated at $\phi_0 = 65°\text{N}$) and Arctic ϕ_i in the ScenarioMIP future simulations, between the 1975–2000 average and the near-future 2025–2050 average. Each point is an ensemble member of a particular model (upper-right legend outside of axes). Upper-left legends indicate the scenario used, the number N of simulations on the plot, and the correlation r of all points. Lower right legends give the slopes of the various fits described in the lower-right legend outside of the axes: (black) OLS fit to points; (red, solid) EBM fit; (red, dashed) EBM fit but using PI-control values of s and b_c; (red, dotted) EBM fit using purely PI control data. See main text for details of the different EBM fitting procedures.

and T_s are correlated for the majority of future time periods and in all scenarios (Fig. 5.3i,j). Although ΔT_s obviously increases with time, some models show increases in OHT and some show decreases (Fig. 5.5). It could be that ΔOHT responds in the same proportion as ΔT_s such that $\Delta T_\text{s}/\Delta\text{OHT}$ as computed from the PI control can also be taken as a pre-determined constant. If any of s, b_c, or $\Delta T_\text{s}/\Delta\text{OHT}$ can be replaced with the PI value, this reduces the data required to fit the relationship between ΔOHT and $\Delta\phi_\text{i}$ in the future simulations. The values of these terms are shown for each scenario in comparison to the PI-control values in Table 5.2. With the exception of s for SSP1-2.6 and b_c for SSP3-7.0 in the NH, future-derived values of s and b_c are consistent with the PI-derived values

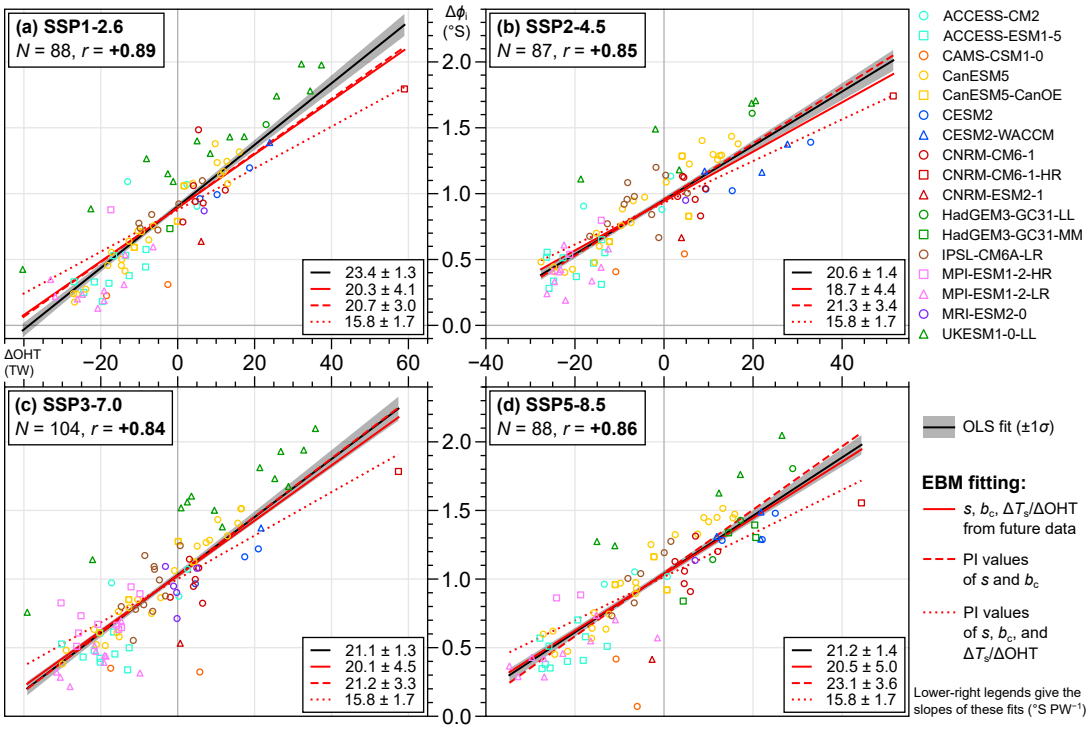

Figure 5.8: As in Fig. 5.7 but for the southern hemisphere.

within error estimates. However, $\Delta T_s/\Delta\text{OHT}$ is about 1.5 times the PI value in all scenarios for the NH and about 30% higher for the SH. Since $\Delta\phi_i/\Delta\text{OHT}$ depends strongly on and increases with $\Delta T_s/\Delta\text{OHT}$, this suggests that the sea ice effective sensitivity to OHT is larger in the future simulations than that arising from natural variability, owing to the disproportionate T_s response compared to that of OHT. In terms of applying Eq. (3.23b) to the future simulations, s and b_c can be taken as constants, verifying the assumptions discussed above in the former case and showing that the rate of BC is not affected by the forcing in the latter. The equation thus reduces to an expression relating changes in OHT, T_s, and ϕ_i, linked by parameters set from the PI-control simulations (cf. Eq. 3.24).

Figures 5.7 and 5.8 plot $\Delta\phi_i$ against ΔOHT (the difference between 1975–2000 and 2025–2050) in the four future scenarios in the NH and SH respectively, with OLS fits across all simulations (black), and the EBM slope predicted by Eq. (3.23b) computed in three ways to show the results of the above discussion

(red). First, the standard 'future' fit where s, b_c, and $\Delta T_s/\Delta\text{OHT}$ are computed from the changes ΔF_{sw}, $\Delta\phi_i$, ΔAHT, ΔOHT, and ΔT_s as appropriate, is shown (solid). Then a 'mixed' fit obtained using PI values of s and b_c but the future data for $\Delta T_s/\Delta\text{OHT}$ (dashed), and finally a 'PI' fit where all three terms are the PI-control values (dotted). The sources of each term in these fits are summarised in Table 5.3. Note that the 'PI' fit is independent of scenario, and since it has now been established that the PI value of $\Delta T_s/\Delta\text{OHT}$ is significantly smaller than the future values, it substantially underestimates the relationship between $\Delta\phi_i$ and ΔOHT in both hemispheres. It is included anyway for comparison of the effective sensitivity of $\Delta\phi_i$ to ΔOHT in the forced response to that arising from natural variability. At this time period, 2025–2050, the forced sensitivity $\Delta\phi_i/\Delta\text{OHT}$ is about a factor of 2 greater than that from internal variability in the NH (from the OLS slopes in Figs. 4.19a and 5.7), and about 30% greater in the SH (Figs. 4.19b and 5.8).

It is remarkable that in all four scenarios there are simulations which have almost no change in sea ice cover ($\Delta\phi_i \sim 0°$) and some which have $\sim 10°$N of sea ice loss in the NH (Fig. 5.7). There are negligible differences in the ranges of ΔOHT and $\Delta\phi_i$ and the OLS slopes are similar in each scenario. The inter-model relationship between ΔOHT and $\Delta\phi_i$ is strong ($r \sim 0.8$), and it is apparent in Fig. 5.7 that the individual-model relationships are less significant (i.e., points for a given model with several ensemble members exhibit significant scatter). Models exhibiting the largest sea ice losses in the low emissions scenario also exhibit the largest sea ice losses in the higher emissions scenarios (and vice versa). Again, larger sea ice losses are associated with larger increases in OHT, and generally Fig. 5.7 suggests that increases (decreases) in OHT enhances (offsets) the rate of sea ice decline. The EBM 'future' and 'mixed' fits capture the relationship between ΔOHT and $\Delta\phi_i$ well in most cases (EBM slope uncertainty estimates are not plotted in Fig. 5.7 but are given in the legends). Similar remarks about

the relation between ΔOHT and $\Delta\phi_\mathrm{i}$ and the lack of scenario differences can be made about the SH (Fig. 5.8). However, in the SH different models tend to overlap, whereas there is more separation of models in the NH. The range of changes in poleward OHT are about half that of the NH, and that of $\Delta\phi_\mathrm{i}$ is about a quarter, so that the multi-model effective sensitivity of sea ice losses to OHT is about half in the SH compared to the NH. This is similar to the result found from internal variability in the PI-control analysis (section 4.3.2).

The fact that the EBM captures the forced response in both hemispheres indicates that underlying physical biases lead to inter-model spread and uncertainty in the projected rates of sea ice decline. This is a combination of internal variability (i.e., as in Fig. 4.19, and shown by the dotted lines in Figs. 5.7 and 5.8) and differences in the forced response across simulations and different models. Inferring from the strong correlations $r\left(\Delta\mathrm{OHT}, \Delta T_\mathrm{s}\right)$ and $r\left(\Delta T_\mathrm{s}, \Delta\phi_\mathrm{i}\right)$ (Fig. 5.3), points lying further to the right in each panel of Figs. 5.7 and 5.8 tend to have larger warming, ΔT_s. This is mostly due to different forced responses (since the future-derived value of $\Delta T_\mathrm{s}/\Delta\mathrm{OHT}$ differs significantly from the PI control value, whereas the other terms, s and b_c, do not). The forced ΔT_s response modifies the effective sensitivities but the difference in NH and SH is still about a factor of 2 as found for the natural variability in section 4.3.2. Consideration of the terms in Eq. (3.23b) (Table 5.2) shows that the explanation for the NH versus SH sensitivities is explained in the same way as was the case for natural variability: s is about twice as large in the SH, such that ϕ_i does not have to retreat as much to generate additional F_sw needed to restore energy balance in the region 65°–90°S compared to that in the NH. In this case, perturbations to the energy balance are caused by both variations in OHT and the forced T_s response.

Since the terms in Eq. (3.23b) are similar in each scenario, the responses $\Delta\phi_\mathrm{i}$ are also similar. Some divergence of the scenarios becomes apparent when the final time period is set further into the future. Figure 5.9 plots the effective

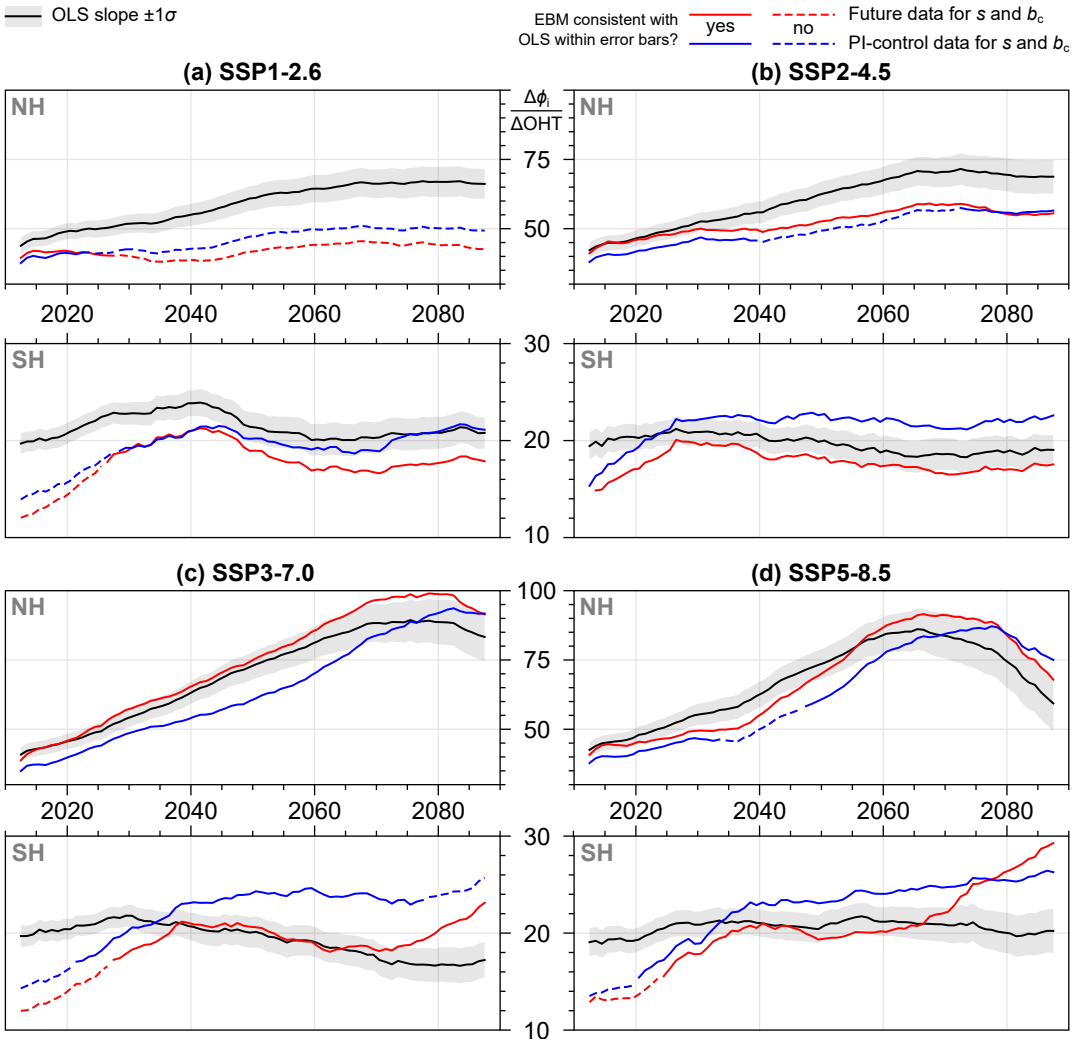

Figure 5.9: Effective sensitivity of sea ice loss to poleward OHT change relative to 1975–2000, $\Delta\phi_\mathrm{i}/\Delta\mathrm{OHT}$ (vertical axes), as a function of time (horizontal axes). This is plotted as the OLS slope (black) with one standard deviation (σ) of the fit (grey shading). The standard 'future' EBM fit is shown by the red lines, and that using the PI-control derived values of s and b_c ('mixed' fit) is shown in blue. Standard deviations of the EBM fits are not shown explicitly, but solid lines indicate where the EBM value agrees with the OLS within error bars, and dashed lines indicate where they do not. Upper (lower) panels in each of (a)–(d) are for the northern (southern) hemisphere. Units of the vertical axes are °N PW^{-1} or °S PW^{-1} as appropriate.

sensitivity of ϕ_i to OHT, as determined from OLS and the 'future' and 'mixed' EBM fitting, as a function of the final time averaging period. In other words, the analysis of Figs. 5.7 and 5.8 is repeated for different future times and the slopes are plotted in Fig. 5.9. The EBM does not well predict the slope in the NH for SSP1-2.6 after 2020, which is likely because the rates of ice decline are

smaller and the reference latitude of 65°N was shown in Fig. 4.19c to not work well in the PI states. The EBM fit using PI-control values of s and b_c captures the OLS sensitivities about as well as the fit using future-derived values of s and b_c. Since the EBM/OLS agreement does not systematically degrade at later times, this suggests that the assumption of using the PI values of B_{up} and β is valid, and that the bulk radiative properties do not substantially change in the future. In SSP3-7.0, the NH sensitivity is captured by the EBM equation for all future time periods in both fitting cases (Fig. 5.9c). In both this scenario and SSP5-8.5, the NH sensitivity starts to decrease around 2070, which is entering the SIF regime and suggests that the effective sensitivity of $\Delta\phi_i$ to ΔOHT decreases. This is qualitatively consistent with the EBM analysis: assuming the mechanisms underlying the future responses are similar to those of natural variability (see section 5.4), the GCM behaviour in the NH can be compared to the EBM K_o sensitivity experiment, in which the effective sensitivity of ϕ_i to OHT reduces considerably in the SIF regime (Table 3.1). Across all scenarios, the SH sensitivity is relatively independent of time compared to the NH where it generally increases before flattening (Fig. 5.9a,b) or decreasing (Fig. 5.9c,d) after about 2070. This is because ΔT_s and ΔOHT increase by roughly the same proportion in the SH.

5.3.2 Comparison of simulated trends to observations

Assessment of simulated multidecadal trends in OHT against the real world is limited due to insufficient temporal range in observations and spatial sparsity of ocean data. However, it is possible to compare recent rates of change of sea ice and surface temperature to the GCM-simulated rates, similar to the study of Rosenblum and Eisenman (2017) who did this for CMIP5 models. As mentioned in section 4.2.3—and based on the EBM analysis presented thus far this has been indirectly verified—OHT plays a role in their finding that models simulating

larger sea ice declines also exhibit larger global warming. To this end, the 'perspective' of the EBM equation is inverted to focus on the relationship between ϕ_i and T_s. Dividing Eq. (3.23a) through by $s\Delta T_\mathrm{s}$ (or multiplying Eq. 3.23b through by $\Delta\mathrm{OHT}/\Delta T_\mathrm{s}$) gives:

$$\frac{\Delta\phi_\mathrm{i}}{\Delta T_\mathrm{s}} = \frac{\beta B_\mathrm{up}}{s\,(1+\beta)} - \frac{1}{sA}\left(1+\frac{b_\mathrm{c}}{1+\beta}\right)\frac{\Delta\mathrm{OHT}}{\Delta T_\mathrm{s}}. \tag{5.1}$$

Here, the 50 yr period 1970–2020 is considered, which is the shortest that can be used in the non-overlapping 25 yr averaging framework (necessary to apply the EBM) and covers the time range of observations. Estimates of the real-world time series of ϕ_i are obtained using the gridded sea ice concentration of the HadISST dataset (Rayner et al., 2003), and applying the ice-edge algorithm as described in section 4.1.2. For surface temperature, HadCRUT4 data (Morice et al., 2012) is used which is averaged over 60°–90°N/°S. Annual means are shown in Fig. 5.10, which also includes sea ice extent for comparison. Linear trends of ϕ_i and T_s over the period 1970–2020 for the NH are then computed using simple OLS regression of the time series. For the SH, the time period is reduced to 1976–2015 to better represent the long-term Antarctic sea ice trend by avoiding the extreme declines around 1973 and 2016 (Fig. 5.10b). Note that the spatial coverage of observation sources over these regions, particularly for T_s, are highly sparse compared to the global coverage; estimates of these rates should thus be taken with caution. The global-mean rate of warming, 0.15°C per decade (Fig. 5.10e), agrees with the value in Rosenblum and Eisenman (2017), with a slight discrepancy because they considered trends over 1979–2013. A high degree of accuracy and/or a comparison with other data sources is not required here, since model spread in the relevant quantities is already much larger than the error bars on observational estimates.

Figure 5.11 plots the changes in ϕ_i between the 1970–1995 and 1995–2020 averages in the combined historical and SSP5-8.5 simulations of the CMIP6 mod-

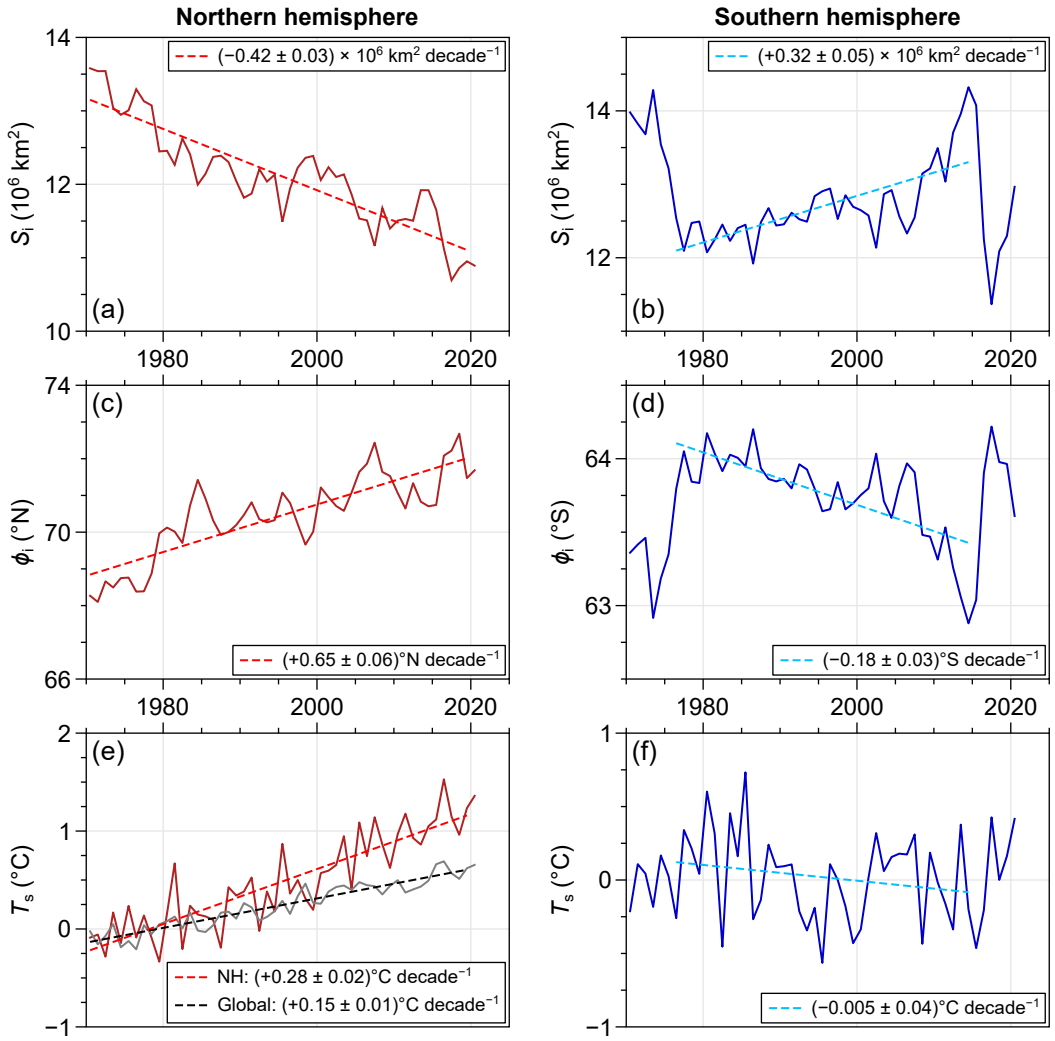

Figure 5.10: Estimates of (a,b) sea ice extent, S_i (c,d) zonal-mean sea ice-edge latitude, ϕ_i, and (e,f) mean surface air temperature, T_s, over recent decades. Diagnostics in (a)–(d) are derived from global sea ice concentration in the HadISST dataset, and (e)–(f) come from HadCRUT4. Surface temperature is averaged over 60°–90°N/°S. In the left panels (NH), linear trends (legends) are fitted over 1970–2020, and in the right panels (SH) they are fitted over 1976–2015. The global-mean surface temperature trend is also shown in (e; black). Uncertainties are standard deviations representing inter-annual variability and do not reflect uncertainties intrinsic to the data.

els, against that of T_s averaged over 60°–90°N/°S. The choice of future scenario is unimportant since only the first 5 yr are needed, for which scenario differences are negligible (e.g., Fig. 1.1). The EBM estimate of the effective sensitivity of ϕ_i to T_s is shown by the magenta lines in Fig. 5.11, computed using Eq. (5.1), and using the 'future' fitting procedure described in the previous section. Spe-

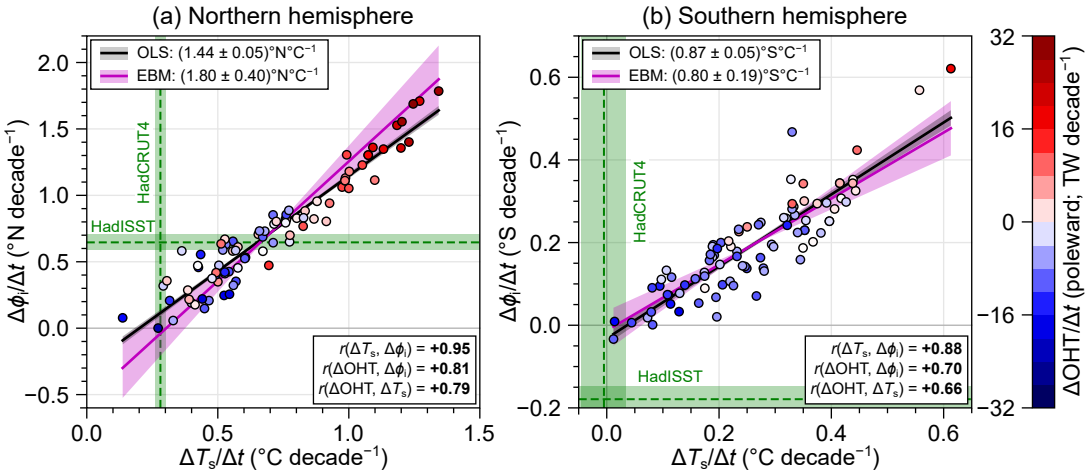

Figure 5.11: (a) Rate of change of NH ice-edge latitude, $\Delta\phi_\mathrm{i}$, plotted against that of surface temperature averaged over 60°–90°N, ΔT_s, in CMIP6 historical and SSP5-8.5 simulations, over the period 1970–2020. Each point is a realisation of a (here, unidentified) model, and rates are computed from the difference in 25 yr means over the periods 1970–1995 and 1995–2020. Colours indicate the corresponding change in poleward OHT across 60°N. Ordinary least squares (OLS) regression lines and the fit of Eq. (5.1) are shown in black and magenta, respectively. Estimates of the observed rates of change derived from the HadCRUT4 and HadISST datasets are indicated in green. (b) As in (a) but for the SH.

cifically, s and b_c are obtained from the changes ΔF_sw, $\Delta\phi_\mathrm{i}$, ΔAHT, and ΔOHT in going from the initial to final 25 yr averages. The OLS slope of $\Delta\mathrm{OHT}/\Delta T_\mathrm{s}$ is used in computing $\Delta\phi_\mathrm{i}/\Delta T_\mathrm{s}$, analogously to fitting Eq. (3.23b) in which the OLS slope of $\Delta T_\mathrm{s}/\Delta\mathrm{OHT}$ is used to compute $\Delta\phi_\mathrm{i}/\Delta\mathrm{OHT}$. To emphasise, these are not independent—indeed, Eqs. (3.23b) and (5.1) are rearrangements of one another—but are two ways of fitting the (effectively) three-dependent-variable relation, Eq. (3.23a). In this case, the third variable hidden in the fitting, ΔOHT, is shown qualitatively on Fig. 5.11 by a colour scale on the points.

The EBM well captures the relationship between the trends in sea ice and surface temperature: the OLS fits overlap the EBM estimates within standard deviations (shading on Fig. 5.11). The multi-model set of trends in Fig. 5.11 are strongly correlated, with $r = 0.95$ in the NH and $r = 0.88$ in the SH. Simulations with larger 1970–2020 declines in sea ice (more positive $\Delta\phi_\mathrm{i}$) are associated with

stronger surface warming (ΔT_s), and the colour coding of points shows again that such simulations also tend to have larger (more positive) increases in OHT into the Arctic/Antarctic regions. Estimates of the observed trends over this time period as described above are indicated by the green dashed lines in Fig. 5.11. Inter-model spread in NH ΔOHT is thus associated with a range in sea ice declines of approximately 0–3 times the observed rate. The result of Rosenblum and Eisenman (2017) is recovered: simulations with sea ice loss rates close to observations do so with substantial positive biases in the rate of (polar) warming. Here, the significance of this finding is improved upon because of the use of polar temperature which is, at least intuitively, more relevant to sea ice than global mean temperature (consistent with the stronger correlation between $\Delta\phi_i$ and ΔT_s compared to those found by Rosenblum and Eisenman, 2017). More generally, the observed rates of $\Delta\phi_i$ and ΔT_s do not coincide with the inter-model relationship in the NH (i.e., observations are offset from the OLS and EBM slopes in Fig. 5.11a). This indicates a fundamental physical bias in models inherited from the previous-generation CMIP5 models. A striking example emphasising this are the simulations which lie closest to the observed rate of warming, which—consistent across models based on the connection of all simulations via the EBM—also have approximately zero Arctic sea ice loss over this period. Some caution should be taken, however, as there is no estimate of the corresponding real-world ΔOHT shown on Fig. 5.11. Also, there is still scatter about the model relationship: variations in ΔT_s (ΔOHT) accounts for about $r^2 = 90\%$ ($r^2 = 66\%$) of variations in $\Delta\phi_i$, so it is not clear whether the observed point $(\Delta T_s, \Delta\phi_i)$ is significantly displaced from models.

In the SH, there is an offset of model trends compared to observations but in the opposite direction to the NH (Fig. 5.11b). Nearly all simulations show Antarctic sea ice declines, and warming of the polar region comparable in magnitude to warming in the NH. Simulations exhibiting reductions in OHT again

have smaller trends in both ϕ_i and T_s and are closer to observations. For the majority of cases, poleward OHT decreases across this period, but Antarctic sea ice retreats anyway. This could indicate that Antarctic sea ice is too sensitive to warming in these models. In both hemispheres, the overall disconnect of models from observations indicates that there is more to the uncertainty in climate projections than spread associated with OHT. This, of course, reflects the limitations of using model output to infer properties of the real world.

5.4 Revisiting the mechanisms

In section 4.2, distinct mechanisms of how OHT affects sea ice were found between the NH and SH, in the context of natural variability arising in the PI-control simulations. This section explores whether these same mechanisms apply in the future simulations—that is, how the changes in OHT drive the inter-model differences in projected sea ice loss as shown in Figs. 5.7 and 5.8. Specifically, do models with larger increases in poleward OHT lead to increased OHTC near the Arctic ice edge and increased higher-latitude AHTC in the NH, but mainly increased OHTC under sea ice in the SH? In the previous section with the EBM analysis, $\Delta T_s/\Delta\text{OHT}$ was found to be slightly larger in the NH than in the SH (Table 5.2). This term is how the different mechanisms manifest in Eq. (3.23b), because the surface temperature increases are larger when a given ΔOHT is mainly released equatorward of the ice edge (sections 3.3.2 and 4.3.1). This provides an initial hint that the same mechanisms could indeed apply to the forced responses. To get a better sense of the mechanisms at play, a similar approach to that in section 4.2 is used: first, the correlations of $\Delta\phi_i$ with ΔOHT and ΔAHT as a function of the latitude at which the latter are evaluated are calculated (similar to section 4.2.1). Then, the relationships of OHTC and AHTC averaged over sea ice (i.e., h_o and h_a) with ϕ_i are considered (similar to section 4.2.3).

5.4.1 Latitude dependence of the correlations

In calculating the correlation between ΔOHT and $\Delta\phi_\mathrm{i}$, there is a choice of future time period and reference latitude ϕ_0 at which OHT is evaluated. Figure 5.3a,b (with $\phi_0 = 65°\mathrm{N}/°\mathrm{S}$) shows that $r\,(\Delta\mathrm{OHT}, \Delta\phi_\mathrm{i})$ remains strong until the end of the 21$^{\mathrm{st}}$ century in the SH, which is also the case in the NH with the exception of SSP5-8.5. The break down of the correlation could be related to a substantial number of simulations becoming SIF. It is not possible to completely ignore the SIF Arctic simulations because many become SIF rapidly, e.g., before 2050 (Figs. 1.2 and 5.14a). To minimise mixing of SIF and non-SIF simulations, the near-future time period 2025–2050 is used in this section, where $r\,(\Delta\mathrm{OHT}, \Delta\phi_\mathrm{i})$ does not change much relative to earlier times for the SSP5-8.5 experiment. With this time period, the sensitivity of $r\,(\Delta\mathrm{OHT}, \Delta\phi_\mathrm{i})$ and $r\,(\Delta\mathrm{AHT}, \Delta\phi_\mathrm{i})$ to ϕ_0 is shown for each experiment in Fig. 5.12, which is analogous to Fig. 4.6 but here represents the correlation across multiple models and ensemble members. The changes in sea ice cover are very similar across the four scenarios, particularly in the SH (Fig. 5.12a). This is partly a consequence of using the near-future time period at which scenario divergence has not fully emerged. The mean changes $\Delta\phi_\mathrm{i}$ are comparable to those arising in internal variability, but note that the correlations plotted in Fig. 5.12b,c are across all model simulations, for which the ranges of $\Delta\phi_\mathrm{i}$ are substantial ($\sim$ 10°N in the NH, and $\sim$ 2°S in the SH, from Figs. 5.7 and 5.8, respectively).

In the NH, $r\,(\Delta\mathrm{OHT}, \Delta\phi_\mathrm{i})$ is consistently strong and significant between 60°–80°N, and peaks in all scenarios with $r \sim 0.95$ around 77°N. This coincides roughly with the mean ϕ_i over 2025–2050, before r decreases for latitudes greater than 80°N. Across roughly the same range of latitudes, $r\,(\Delta\mathrm{AHT}, \Delta\phi_\mathrm{i})$ is negative until about 82°N where it exhibits an abrupt transition to small, insignificant values. This is reminiscent of (the majority of) individual model behaviours shown

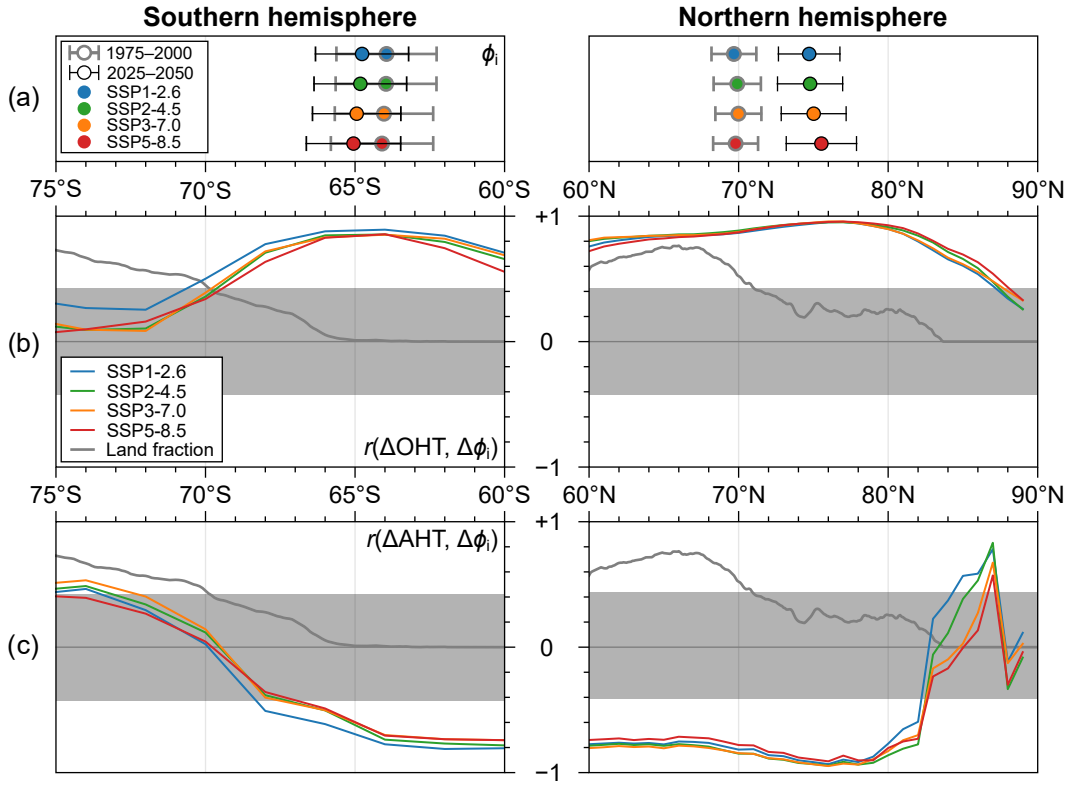

Figure 5.12: (a) Change in ϕ_i between the initial period 1975–2000 (grey) and near-future period 2025–2050 (black) in the four scenarios. Circles indicate multi-model means, and error bars indicate one standard deviation of inter-model spread. (b) Correlation across all model simulations between $\Delta\phi_i$ and the change in OHT between the two time periods, ΔOHT, as a function of the latitude at which OHT is evaluated. (cf. Fig. 4.6a). (c) As in (b) but for the change in AHT between the two time periods, ΔAHT (cf. Fig. 4.6c). Thick dark grey lines in (b)–(c) show the land fraction, and the grey shaded area indicates $|r| < r_{crit}$ based on model means using a t-test at the 95% confidence level.

in Fig. 4.6, which was the first clue to the NH mechanism ultimately found with further analysis throughout section 4.2. However, $r\,(\Delta\text{OHT}, \Delta\phi_i)$ is still significant until about 87°N, by which point the loss of correlation could be attributed to simple geometric effects: the OHT at this latitude is small and too far from ϕ_i to have any influence. Another caveat is that $r\,(\Delta\text{AHT}, \Delta\phi_i)$ is only significantly positive for a small range of latitudes—around 84°–88°N depending on the scenario—whereas the signature of the NH mechanism previously identified is a clear transition from negative to positive correlation occuring roughly across the minimum value of ϕ_i (Fig. 4.6c). Thus, Fig. 5.12 weakly supports the NH mechan-

ism identified in the PI-control simulations being responsible for the relationship between OHT changes and sea ice loss in the NH across models.

The situation in the SH revealed by Fig. 5.12 provides stronger evidence for the same mechanism as identified in the PI-control simulations. The correlation of ΔOHT with $\Delta\phi_i$ in the SH is positive and significant between 60°–70°S. It peaks at around 65°S, coinciding with the mean ϕ_i in all scenarios and is the same latitude at which $r\,(\mathrm{OHT}, \phi_i)$ peaks in the PI-control variability for most models (Fig. 4.6a). The behaviour of $r\,(\Delta\mathrm{AHT}, \Delta\phi_i)$ also partly mimics that of the PI-controls: for lower southern latitudes it is negative, but there is a smooth (compared to the NH) transition to weakly positive correlations poleward of 70°S. However, at these latitudes AHT mostly converges over Antarctica so there are no significant latitude ranges at which $r\,(\Delta\mathrm{AHT}, \Delta\phi_i)$ is positive. This is again reminiscent of the PI control simulations. The SH behaviour thus points towards positive biases in ΔOHT being released under the Antarctic ice pack, as in the natural-variability mechanism, with less caveats compared to the NH.

5.4.2 Heat convergence over sea ice

In section 4.2.3, it was shown that the h_o and h_a diagnostics (OHTC and AHTC, respectively, averaged over sea ice) provide a summary view of the NH and SH mechanisms (Fig. 4.10). Here, these can be used as a different approach to investigating the mechanisms underlying the forced responses. If the same mechanisms do apply, it is expected that in the NH there is no substantial relationship between Δh_o and $\Delta\phi_i$ (because OHT is released ahead of the ice edge, not under it), but a positive relationship between $\Delta\phi_i$ and Δh_a (because ocean heat release increases AHT to higher latitudes). The SH mechanism should manifest as a positive relationship between $\Delta\phi_i$ and Δh_o (because OHT is released under Antarctic sea ice), and a negative relationship between $\Delta\phi_i$ and Δh_a (indicating BC). Figure 5.13

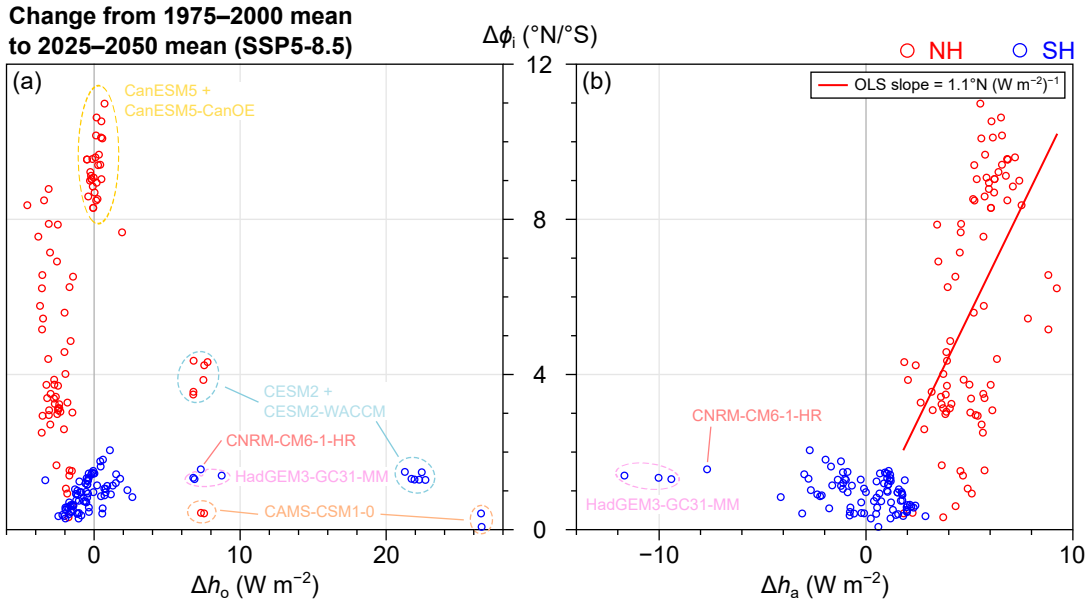

Figure 5.13: Change in ϕ_i plotted against the change in (a) h_o and (b) h_a between the 1975–2000 (historical) average and 2025–2050 (SSP5-8.5) average. Each point is an ensemble member of a particular model. Red circles are for the NH, and blue circles are the SH (cf. Fig. 4.10). In (b), an OLS line is fitted to NH points (see legend).

is essentially the future-simulation version of Fig. 4.10, for the SSP5-8.5 scenario and using the same time-averaging periods 1975–2000 and 2025–2050 as before to compute $\Delta\phi_i$, Δh_o, and Δh_a. Simulations are plotted in red for the NH and blue for the SH for comparison with Fig. 4.10, and the model sources of prominent outliers are annotated.

The distributions of NH and SH points in both panels of Fig. 5.13 broadly resemble the corresponding panels of Fig. 4.10. In the NH, Δh_o does not strongly relate to $\Delta\phi_i$ (Fig. 5.13a). The CAMS-CSM1-0 model is notable for having a relatively substantial increase in $h_o \sim 8$ W m^{-2} but with minimal sea ice loss (despite starting from a substantial Arctic sea ice cover; Fig. 5.1). The CanESM5 model most closely mimics the PI-control behaviour: the distribution of Δh_o for its ensemble members is centred on zero, while $\Delta\phi_i$ increases by several °N. For the remaining models, Δh_o decreases by a few W m^{-2}, independent of $\Delta\phi_i$ [excluding annotated models in Fig. 5.13a, $r\,(\Delta h_o, \Delta\phi_i) = -0.23$]. Figure 5.13b shows that

Δh_a is positive in all simulations for the NH, and there is a weak, but significant, correlation $r\,(\Delta h_a, \Delta\phi_i) = 0.55$. The OLS slope of $\Delta\phi_i/\Delta h_a$ for the NH (Fig. 5.13b) is about twice the corresponding slope in the PI-control simulations (Fig. 4.10b). It is larger here because $\Delta\phi_i$ includes the effect of warming (forced response) in addition to its modulation by OHT (natural variability).

The SH interpretation again generally resembles the PI version, but there are a number of outliers and relatively small changes in sea ice which makes the connection dubious. Figure 5.13a shows that CAMS-CSM1-0 is also unusual in its SH behaviour of h_o: its changes in Antarctic sea ice are among the smallest of all models, despite substantial increases in mean ocean–ice heat fluxes of about 26 W m^{-2}. Further, Fig. 5.8d shows that the corresponding change in OHT for this model is a decrease of around 10 TW, which is also the case if higher southern reference latitudes are used to evaluate OHT. The CAMS-CSM1-0 model also stood out in the SH for the PI analysis, which was attributed to cancelling regions of strong increases and decreases in OHTC [section 4.2.3(b)]. Given its OHT behaviour, the same explanation likely applies here. Similar behaviours of h_o are noted for SH of the CESM2 models and HadGEM3-GC31-MM, although in those cases $\Delta\phi_i$ is more in line with the other models. For the non-annotated models in Fig. 5.13a, there is a significant positive correlation $r\,(\Delta h_o, \Delta\phi_i) = 0.55$. This group of simulations is dominated by CanESM5, but even if this is excluded the correlation is still significant ($r = 0.49$). Since in the SH the overall changes in ϕ_i are comparable in magnitude to that arising from natural variability, it is reasonable to compare the slopes in Figs. 5.13a and 4.10a. Again excluding the annotated models in Fig. 5.13a, the OLS slope of $\Delta\phi_i/\Delta h_o$ in the SH is 0.20°S (W m^{-2})$^{-1}$, which is similar to that found from natural variability [0.16°S (W m^{-2})$^{-1}$; Fig. 4.10a]. There is only a weak negative relationship between Δh_a and $\Delta\phi_i$ in the SH if the annotated models are excluded ($r = -0.34$). Also, h_a increases in roughly half the simula-

tions, for which h_o decreases: $r(\Delta h_o, \Delta h_a) = -0.84$, excluding annotated models, which points to the BC effect manifesting over Antarctic sea ice.

Overall, the plots in Figs. 5.12 and 5.13 are consistent with the same mechanisms identified in the natural variability of $\Delta\phi_i$ applying to the forced response of $\Delta\phi_i$. The outlier models in Fig. 5.13 were also noted as outliers (having larger magnitudes of variability or substantially different effective sensitivities of ϕ_i to OHT) in the PI-control analysis. Ignoring those in Fig. 5.13 improves the comparison with Fig. 4.10. One key difference is that the branching of the two hemispheres is not centred on $\Delta h_o = \Delta h_a = 0$ in Fig. 5.13. This is probably due to the forcing: surface temperature is increasing, which would manifest as an increase in Δh_a in addition to that from natural variability in OHT. Finally, a potential issue with the h_o and h_a diagnostics here is that they are changes following a moving area (the sea ice cover). In this case such area changes are substantial compared to natural variability, particularly in the NH, which could mean that Δh_o and Δh_a signify changing area rather than changes in OHTC and AHTC. However, the reduction in $r(\Delta\text{OHT}, \Delta\phi_i)$ at high latitudes and corresponding abrupt change in $r(\Delta\text{AHT}, \Delta\phi_i)$ shown in Fig. 5.12 suggests this is not the case, i.e., Δh_o and Δh_a still capture meaningful physical responses in the same way as in section 4.2.3.

5.5 The seasonally ice free climate

5.5.1 Timing of the first ice-free summer

If Arctic sea ice continues its declining trend, eventually the summer minimum coverage will vanish. Senftleben et al. (2020) define the timing of a SIF Arctic, t_{SIF}, as the first year of the first 5 yr period for which sea ice extent, S_i, in September, is below a threshold $S_i^\star$. This provides a good indication of the

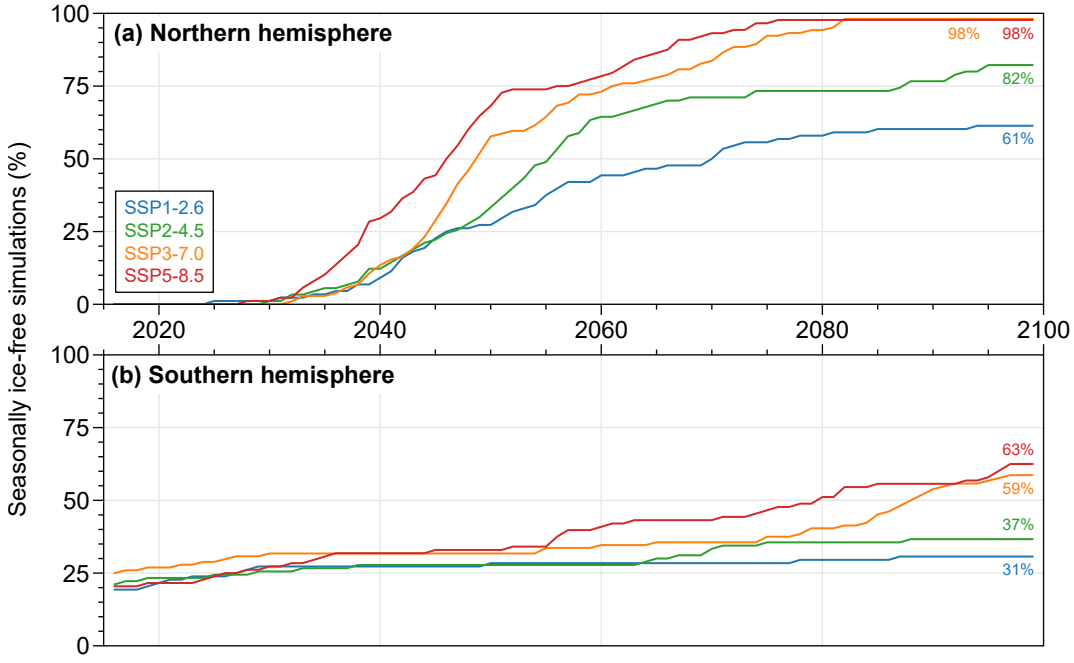

Figure 5.14: Percentage of all simulations which are seasonally ice free in the (a) NH and (b) SH as a function of time in the four future scenarios. Values at the end of the century are labelled on the RHS.

true transition by eliminating any isolated years with September $S_\mathrm{i} < S_\mathrm{i}^\star$. The threshold $S_\mathrm{i}^\star$ is taken as 1×10^6 km^2, which accounts for remnants of thick ice likely to persist along the northern coast of Greenland and in the Canadian archipelago after the central Arctic ocean becomes ice free. It is also roughly the magnitude of internal variability of September sea ice extent (Notz and Stroeve, 2018). Less attention has been given to the loss of summer Antarctic sea ice because over recent decades it has not exhibited the same stark decline as the Arctic (Figs. 1.1 and 5.10a,b). For the sake of comparison with the Arctic, the same threshold condition is applied to the Antarctic sea ice minimum (February). This is used to compute t_SIF in both hemispheres of the CMIP6 future simulations.

Figure 5.14 shows the percentage of simulations which are SIF as a function of time. Initially, in the historical period, all ensemble members of all models have substantial September Arctic sea ice cover (Fig. 5.14a). This model subset suggests that in the two higher-emission scenarios (SSP3-7.0, SSP5-8.5) the Arctic

will be SIF by around 2080. Figure 5.14a emphasises the uncertainty arising from model spread: the range of t_{SIF} is about 2030–2080 in the high-emission scenarios. Note that this is likely an underestimate of the true uncertainty on t_{SIF} from models in general, since this analysis is only considering 17 of the ~ 100 models contributing to CMIP6. In the lower-emission scenarios (SSP1-2.6, SSP2-4.5), not all simulations are SIF by the end of the century. In the SH, models show even less consensus. Around a quarter of simulations are already SIF at the end of the historical period (2015; Fig. 5.14b). Although Antarctic sea ice in the real world has a more pronounced seasonal cycle compared to the Arctic, its minimum extent is $\sim 3 \times 10^6$ km^2 and thus is not SIF based on the 1×10^6 km^2 threshold (Parkinson and Cavalieri, 2012). The relatively slow increase in the number of SIF simulations in the SH suggests that Antarctic sea ice is more resistant to climate change than the Arctic in these models. For example, in the low-emission scenario SSP1-2.6, there is about a 12% increase in the number of SIF simulations in the SH, compared with a 61% increase in the NH. This is also reflected in the future increases in ϕ_{i}: comparing Figs. 5.7 and 5.8, the range of changes in ϕ_{i} in the NH is about 4 times that in the SH. In terms of S_{i}, converting using the factor of 2 difference in $\Delta S_{\mathrm{i}}/\Delta\phi_{\mathrm{i}}$ from Fig. 4.3, the rates of Arctic sea ice loss are still about twice as large as those of the Antarctic.

In section 5.2, it was shown that OHT contributes to inter-model spread in sea ice extent through biases in the initial, mean state (Fig. 5.1) and through relative differences in the rates of change of OHT affecting sea ice loss rates (Fig. 5.3). It might then be expected that t_{SIF} could be related to OHT. Figure 5.15a plots t_{SIF} for the SSP5-8.5 scenario, against OHT at 65°N and averaged over 1975–2000. There is only a weak relationship here when considering simulations collectively, with $r = 0.51$. The sign of r is counterintuitive—larger OHT is (weakly) associated with later t_{SIF}—but this is similar to the situation in Fig. 5.4c. There, the anticorrelation between OHT in 1975–2000 and future

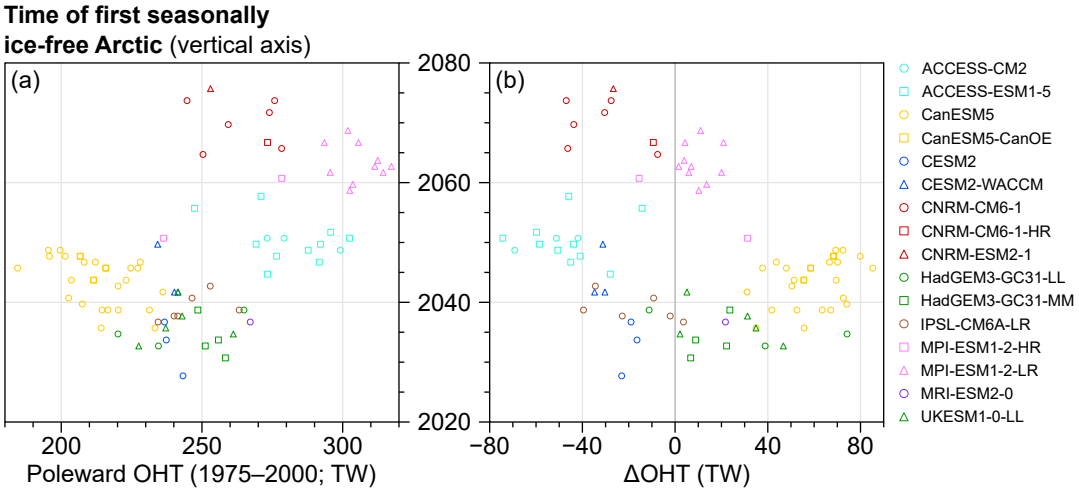

Figure 5.15: Year of the first sea ice-free Arctic summer (t_{SIF}; vertical axes) in CMIP6 SSP5-8.5 simulations, plotted against (a) poleward OHT at averaged over 1975–2000, and (b) the change in OHT at t_{SIF} relative to 1975–2000. In both cases OHT is evaluated at 65°N. CAMS-CSM1-0 is excluded because neither of its ensemble members become SIF by 2100.

ϕ_{i} was attributed to the fact that larger initial OHT is anticorrelated with the future change ΔOHT (Fig. 5.5a). This same effect ultimately prohibits a strong relationship between OHT and t_{SIF}, because t_{SIF} depends on the initial S_{i} (which is correlated with initial OHT; Fig. 5.2a) and the rate of sea ice loss (which is correlated with ΔOHT; Fig. 5.3a). The two effects combine non-trivially and partially cancel each other out, such that there is no strong relationship between either OHT or ΔOHT (Fig. 5.15b) and t_{SIF} across models. Previously it was stated that the effect of ΔOHT was more important, which is consistent with the physically-intuitive negative (albeit weak) correlation $r\left(\Delta\mathrm{OHT}, t_{\mathrm{SIF}}\right) = -0.33$.

The transition to a SIF Southern Ocean is likewise not strongly related to OHT or ΔOHT (Fig. 5.16). The greater separation of models in the SH compared to the NH can be seen in Fig. 5.16a, reflecting the greater role of mean-state biases in OHT (Fig. 5.4b). There is a weak relationship, of the expected sign, with ΔOHT ($r = -0.51$). In sum, Figs. 5.15 and 5.16 show that OHT by itself is not a good predictor of the timing of a SIF climate. This is not a trivial result,

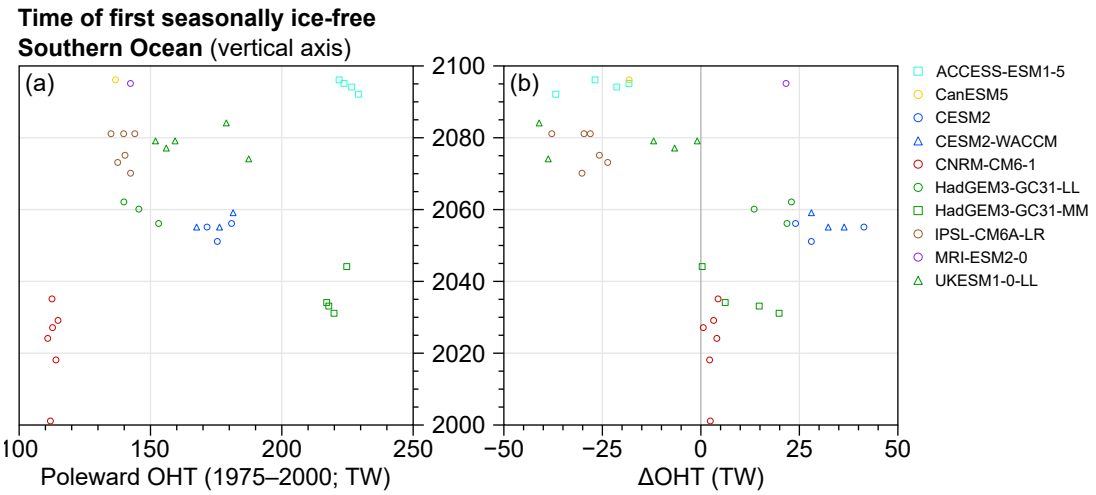

Figure 5.16: As in Fig. 5.15 but for the Southern Ocean. Here, OHT is evaluated at 65°S, and any simulations which are SIF before 2000 or are not SIF by 2100 are excluded.

considering previous findings which clearly show OHT strongly affecting the rate of sea ice loss (sections 5.2–5.3). This occurs because of the conflicting influences of larger initial OHT, which is correlated with larger initial S_i, and greater future increases in OHT, which is correlated with greater rates of ice loss.

It is worth considering other factors that might correlate more strongly with t_SIF. The analysis generating Figs. 5.15 and 5.16 was repeated on the other main diagnostics (AHT, T_s, and S_i) and the correlations with t_SIF are listed in Table 5.4. Most are comparable in strength to those of OHT. In the SH, t_SIF is strongly correlated with the change in T_s and strongly anticorrelated with the change in S_i. However, the direction of these relationships are opposite to intuition: larger decreases in S_i are associated with later onset of SIF conditions. This therefore just reflects that models with initially larger Antarctic sea ice extent have more sea ice to lose before becoming SIF. There may be other factors affecting t_SIF that are not highlighted by this analysis: for example, Screen and Deser (2019) find that an initial negative phase of the interdecadal Pacific oscillation (IPO) leads to a larger rate of sea ice loss, and in turn t_SIF, in a set of simulations of a coupled GCM. This is mediated by increased AHT as the IPO moves to the

Table 5.4: Correlation between the timing of SIF conditions, t_{SIF}, and diagnostics d, across all model simulations. Here, d is averaged over 1975–2000, and Δd is the difference between d averaged over the 25 yr period centred on t_{SIF} and d averaged over 1975–2000 (i.e., as in Figs. 5.15 and 5.16).

d	Northern hemisphere		Southern hemisphere	
	$r\,(d, t_{\mathrm{SIF}})$	$r\,(\Delta d, t_{\mathrm{SIF}})$	$r\,(d, t_{\mathrm{SIF}})$	$r\,(\Delta d, t_{\mathrm{SIF}})$
OHT	+0.51	−0.33	+0.30	−0.51
AHT	−0.15	+0.33	−0.38	+0.20
T_{s}	+0.26	+0.14	−0.38	+0.94
S_{i}	−0.40	+0.01	+0.54	−0.89

positive phase, not necessarily picked up by the AHT diagnostic here which is global. Also, this study considered a single model, whereas the present analysis is attempting to explain the range of t_{SIF} across many models: in the former, the IPO phase accounts for about 7 yr of variation in t_{SIF}, compared to the 50 yr range across multiple models (Fig. 5.15).

5.5.2 Ocean role in the seasonally ice-free Arctic

The Arctic ocean becoming SIF represents a qualitative shift in the nature of the northern high-latitude climate. An obvious effect is the increase in ocean–atmosphere exchanges during the open-ocean part of the seasonal cycle. This was suggested as the main explanation for the roughly equal sensitivities of ϕ_{i} to h_{o} and h_{a} in a SIF climate found in the EBM analysis (section 3.2.3). This section exploits the fact that CanESM5 has a large number of ensemble members (25) in the high-emission scenario SSP5-8.5, all of which become SIF in the NH by 2050 (Fig. 5.17a). This gives a 50 year period (2050–2100) of purely SIF Arctic climate simulation, with 25 data points from a physically consistent source. These are analysed to provide an indication of the role of OHT in this radically different (but plausible future) climate state.

The time series of the key diagnostics in the CanESM5 historical and SSP5-8.5 simulations are shown in Fig. 5.17. The long-term decline in annual-

mean and September S_i is evident from around 1975, consistent with observations, and continues roughly linearly with time (Fig. 5.17a). The first ensemble member becomes SIF in 2036, and all 25 members are SIF in 2048. A slight increase in interannual variability of the September extent can be seen in the few years just before SIF, which is particularly evident in ϕ_i (Fig. 5.17b). For the sea ice diagnostics, the alternative annual mean in which ice-free months are excluded [i.e., average (ii); see section 5.1] are also shown in Fig. 5.17a,b. This leads to larger values of annual-mean S_i, and the rate of decline of average (ii) is smaller than that of average (i). Around 2065 there is also an acceleration in the rate of decline of the second average, most noticeable in S_i, which can be attributed to August and/or October becoming ice free. The average (ii) distorts the view of the trend compared to the standard average (i), but could still offer insight into the interaction of OHT with sea ice.

The full time series of OHT and AHT, each at 65°N, are plotted in Figs. 5.17c and 5.17d, respectively. Over 1975–2050, OHT broadly increases which enhances the rate of ice loss (section 5.3.1). After 2050 (now in the SIF regime), OHT begins to decrease, but the rate of sea ice loss (either average) does not substantially change. This explains the drop in effective sensitivity of the ice edge to OHT at later times (Fig. 5.9d) and suggests OHT exerts less influence on sea ice in the SIF regime. As mentioned in section 5.3.1, this is qualitatively consistent with the EBM sensitivity studies. The long-term changes in AHT roughly mirror those of OHT due to BC. However, after around 2050, AHT does not increase substantially as might be expected from the steady OHT decreases over 2050–2100. An important factor here is the reference latitude at which the heat transports are evaluated, taken as $\phi_0 = 65°\mathrm{N}$ in Fig. 5.17c,d. In the SIF regime, the annual-mean ϕ_i is at least 80°N (Fig. 5.17b). While previously the correlation of OHT with ϕ_i has been shown to be largely independent of ϕ_0 provided $\phi_0 < \phi_\mathrm{i}$ (Figs. 4.6a, right and 5.12b, right), this factor is also considered below.

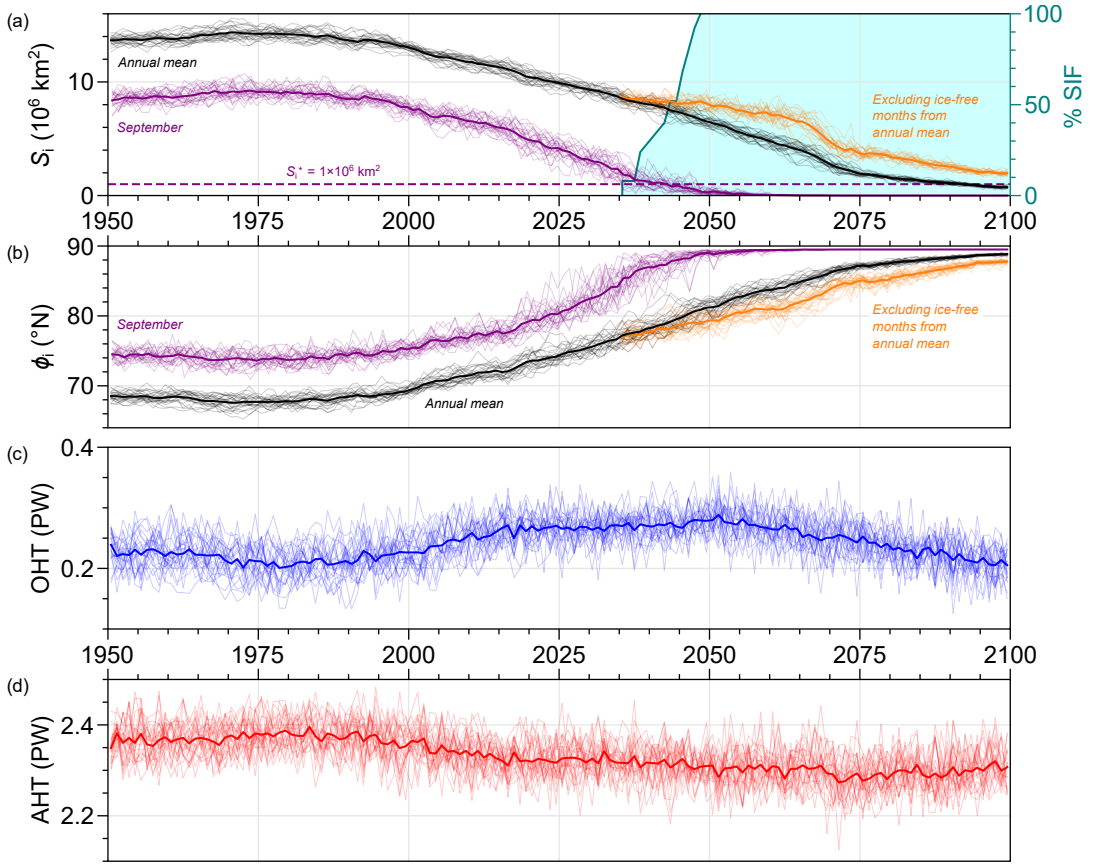

Figure 5.17: Annual-mean time series of (a) sea ice extent, S_i; (b) ice edge latitude, ϕ_i; (c) OHT; and (d) AHT, in CanESM5 historical and SSP5-8.5 simulations. In each case, thick lines denote the mean of all ensemble members (thin lines). For sea ice, the September series are also shown in purple, and the alternative annual averages in which ice-free months are excluded are shown in orange. In (a), the turquoise line and shading indicate the percentage of simulations which are seasonally ice free (SIF; right vertical axis). In (c)–(d), the reference latitude $\phi_0 = 65°$N.

There is no obvious ensemble divergence with time in any of the diagnostics. This suggests that there could be relationships across ensemble members that are valid in both the perennial-ice-cover and SIF regimes. From Fig. 5.17a, an appropriate 50 yr period (i.e., two 25 yr periods) for the perennial regime can be chosen as 1975–2025. For each ensemble member, the differences between the consecutive 25 yr averages of ϕ_i, OHT, and AHT are computed and plotted in Fig. 5.18a,b. This reveals the familiar influence of OHT: simulations with larger ΔOHT (all of which are positive for CanESM5) exhibit larger sea ice losses (Fig. 5.18a). At the same time AHT decreases (Fig. 5.18b), reflecting BC

Table 5.5: Correlation, across ensemble members of CanESM5, between ϕ_i and OHT (columns 'O'), ϕ_i and AHT (columns 'A'), and between OHT and AHT (columns 'BC'), as a function of reference latitude ϕ_0. Values are given for the perennial (1975–2025) and seasonal (2050–2100) regimes. In the latter case, values are given when ϕ_i is annually averaged including ice-free months [average (i)] and excluding ice-free months [average (ii), seasonal*].

ϕ_0	Perennial			Seasonal			Seasonal*	
	O	A	BC	O	A	BC	O	A
65°N	+0.85	−0.65	−0.89	+0.37	−0.51	−0.77	+0.41	−0.49
70°N	+0.86	−0.71	−0.92	+0.42	−0.56	−0.83	+0.44	−0.53
75°N	+0.89	−0.75	−0.93	+0.34	−0.55	−0.83	+0.28	−0.48
80°N	+0.81	−0.21	−0.68	+0.49	−0.79	−0.86	+0.42	−0.73

across ensemble members [$r\,(\Delta\text{OHT}, \Delta\text{AHT}) = -0.89$]. The changes in ϕ_i, OHT, and AHT are also computed for the seasonal regime, 2050–2100, and plotted in Fig. 5.18c,d. Here, statistically significant correlations between changes in OHT and sea ice are evident but the relationship is clearly weaker than in the perennial regime. In this case, OHT decreases in all simulations, but the spread across ensemble members, $\sim$ 30 TW, is about half that of the perennial regime (also the case for $\Delta\phi_i$). The weakened relationship between ΔOHT and $\Delta\phi_i$ is evident regardless of whether ice-free months are included in the average (Fig. 5.18c). There is a slightly stronger anticorrelation between $\Delta\phi_i$ and ΔAHT (Fig. 5.18d), indicating that there is still substantial BC across members in the SIF regime [$r\,(\Delta\text{OHT}, \Delta\text{AHT}) = -0.77$].

As mentioned above, the choice of reference latitude, taken as $\phi_0 = 65$°N in Fig. 5.18, may be inappropriate for the SIF regime where the mean ice edge is much further north (Fig. 5.17a). In Table 5.5, the correlations between $\Delta\phi_i$, ΔOHT, and ΔAHT are listed for several ϕ_0. This shows that correlation between ΔOHT and $\Delta\phi_i$ is about the same strength wherever OHT is evaluated between 65°–80°N. The anticorrelation of $\Delta\phi_i$ with ΔAHT, however, becomes about as strong at $\phi_0 = 80$°N as in the perennial regime (and the signal of BC persists over this range of ϕ_0).

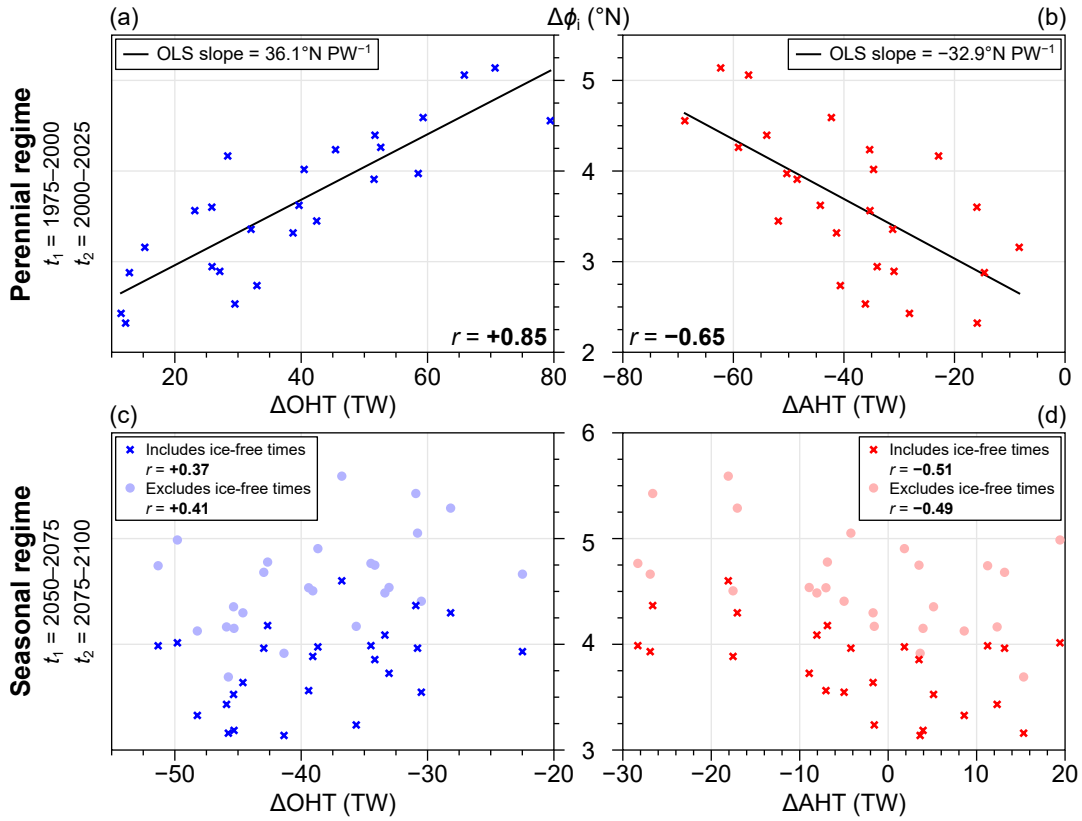

Figure 5.18: Changes in annual-mean ice-edge latitude, $\Delta\phi_i$, between time periods t_1 and t_2 in (a)–(b) perennial and (c)–(d) seasonally ice-free regimes, plotted against the corresponding changes in (a,c) OHT and (b,d) AHT. Each point is an ensemble member of CanESM5, and data comes from the combined historical and SSP5-8.5 simulations. In the seasonal regime, the annual-averages of ϕ_i including (excluding) ice free months are shown by crosses (circles).

This analysis suggests that OHT becomes a less effective driver of sea ice in the SIF regime. Clearly, this conclusion is based off of the behaviour of a single model and only one 50 yr period has been considered. Caution should thus be taken in generalising the results to other models and the real world. While other models become SIF in the Arctic in SSP5-8.5 simulations, CanESM5 is the only model to have a sufficient number of ensemble members (e.g., more than 10) which all become SIF fast enough to create a substantial period of SIF simulation. The effective sensitivity $\Delta\phi_i/\Delta$OHT in the perennial regime (given by the OLS slope in Fig. 5.18a) is comparable to that for the multi-model ensemble (Fig. 5.9d, top, at $t = 2012.5$), which suggests it is consistent with other models in terms of the

sea ice response to OHT changes. It does have the largest initial ensemble-mean Arctic sea ice extent (Fig. 5.1a), but this does not necessarily mean that it is physically inconsistent with other models.

5.6 Discussion

In various ways, this chapter has shown that the relationships between OHT and sea ice identified in the more idealised contexts of chapters 3–4 apply—or, at least, are likely to apply—to future climate projections. On multidecadal timescales, OHT exerts substantial influence on the rates of sea ice loss in both hemispheres, which can be explained from the simple EBM perspective, placing a physical origin on the emergent effective sensitivity of sea ice to OHT. Underlying mechanisms and the difference in sensitivities between hemispheres are similar to those of natural variability occuring in the PI-control simulations. Results are independent of forcing level, although there is evidence that when the Arctic Ocean becomes seasonally ice free under high emissions the importance of OHT is reduced.

In section 5.2, and particularly Fig. 5.1, it was shown that there are significant correlations between the mean states of OHT and sea ice cover in both hemispheres. While this is physically intuitive, it is not trivial that there is a relationship across models at all because different models are constructed independently. The existence of an inter-model Bjerknes compensation (Fig. 5.2g,h) implies that TOA fluxes are similar across models. According to Hourdin et al. (2017), modelling centres tend to prioritise the net TOA flux over other metrics for tuning purposes. This could explain why BC and the other correlations appear across models without taking anomalies. The fact that there is a correlation between sea ice and OHT across models, but not AHT, can then be explained by considering the sensitivities. Model differences in OHT lead to biases in sea

ice. The typical rate of BC is such that the magnitude of AHT variations across models are comparable to those of OHT. But sea ice is more sensitive to OHT than AHT, so that model differences in AHT have relatively little effect on sea ice (about a factor of 2 less important, according to the actual sensitivities estimated in section 3.2). Loosely speaking, for sea ice there is more 'margin for error' with AHT than with OHT.

While it seems clear from this chapter alone that inter-model spread in projections of sea ice are strongly dependent on OHT, quantifying this is not trivial because of the competing effects of mean-state and future-change biases in OHT identified in section 5.2. For example, this manifests in the lack of relationship between the time of onset of SIF conditions and OHT (section 5.5.1). This is a key result, not previously identified, highlighting the challenge of attributing sources of sea ice uncertainty in climate simulations, despite multiple lines of evidence that OHT has a leading-order impact. Crudely, $r^2\left(\Delta\mathrm{OHT}, \Delta\phi_\mathrm{i}\right) \sim 70$–$80\%$ (depending on scenario) of the range in $\Delta\phi_\mathrm{i}$ is explained by model differences in ΔOHT. An estimate of how much of the variance in future sea ice is explained by present-day OHT is found using the lagged correlations in Fig. 5.4, giving a similar percentage. These values give a rough indication of the contribution of OHT to future sea ice uncertainty and do not depend strongly on the underlying forcing strength. This builds on the assertion of Mahlstein and Knutti (2011) that OHT is likely to be a major driver of model uncertainty in sea ice projections, providing some degree of quantification with an underlying physical basis (i.e., the EBM). However, it is important to note these values do not capture the direct effect of OHT (e.g., the impact of OHT via T_s is built into r^2). Natural climate variability leads to multidecadal variability in OHT. For a given scenario, inter-model spread is, in simple terms, the sum of inter-model biases and the natural variabilities of each model (i.e., as represented by spread of ensemble members). Ideally, the former is minimised and the latter are consistent across

models (e.g., Fig. 5.1 shows this is not the case). A better quantification of the real-world multidecadal variability in OHT is needed to understand which models have realistic magnitudes of internal variability, before progress can be made here.

Returning to the caveat noted in section 5.1, how does the use of correlation to identify relationships affect the results of this chapter? In the future simulations, concentrations of atmospheric greenhouse gases are increased, which results in a radiative forcing and thus a transient climate response. Almost all simulations agree that sea ice retreat is part of this response (e.g., Fig. 5.7). Now, it has been shown that the amount of sea ice retreat is strongly correlated with the change in OHT, but also with the change in surface temperature. Although the EBM captures these relationships well (section 5.3), suggesting a real physical link between the diagnostics, there is no evidence either way that OHT or T_s is the 'driving' factor of sea ice loss. Indeed, according to the related analysis of Burgard and Notz (2017), roughly half of CMIP5 models' future sea ice retreat is driven by OHT and half by surface warming. In the PI-control case, no external driving force is present so that only the relation amongst diagnostics is to be determined. Then, with the lagged correlation analysis indicating OHT leading sea ice changes, it is more convincing that the correlation reflects a causal link. The future simulation analysis lacks direct attribution of the effects (ΔOHT, $\Delta\phi_i$, and ΔT_s) back to the cause (rising emissions). While widely understood that rising emissions lead to increased surface temperature and reduced sea ice in the future, the effect on OHT is less known (it increases in roughly half of CMIP6 models and decreases in the other half; Figs. 5.7 and 5.8). This does not affect the conclusion that simulations with smaller increases in OHT have smaller sea ice losses. However, it could be that changes in OHT and the apparent modulating effect on ϕ_i occur for distinct reasons, both tracing back to the 'root cause' of increasing emissions. There are good arguments that this is

not the case—specifically, the indication of the same mechanisms as occurring in the better-understood PI-control case, the fact that the EBM well captures the response, and that the correlations are all of the expected sign (e.g., ΔAHT is negatively correlated with $\Delta\phi_\mathrm{i}$; section 5.2.2). A thorough lagged correlation analysis, such as in Fig. 4.13, might provide more evidence for OHT driving sea ice changes, if all other variables lagged ΔOHT. Despite the advantages this simple methodology has brought, it must be conceded that more detailed, process-focused work is needed to confirm the extent to which the OHT changes directly affect sea ice changes in this context.

It is important to recognise that the changes in sea ice cover (and climate state in general) projected over the 21$^{\mathrm{st}}$ century are substantial. This point is meant in the quantitative sense—which is quite evident from the various figures showing $\Delta\phi_\mathrm{i}$—and the qualitative sense, which is perhaps overlooked in this analysis. In section 5.4, evidence was outlined that the same NH and SH mechanisms could apply to the forced response. Aside from the limitation of correlation analysis discussed above, large losses of sea ice are likely to alter the local oceanography and thus, potentially, the nature of the future relationship between OHT and sea ice. For instance, loss of Arctic sea ice may lead to weakening of the Arctic halocline, providing a new pathway for ocean heat to reach sea ice (see section 1.1.1 and Polyakov et al., 2020). Another aspect is that here, of course, all changes in OHT and ϕ_i correspond to a transient (rather than equilibrium) climate response. Although 25 yr averages are used to emphasise the multidecadal timescale, this could still be insufficient time for the ocean to adjust, such that the true effect on sea ice has not manifested (although the AHT interaction timescale is faster, so this is not affected). The EBM, which assumes a steady-state climate, still captures the CMIP6 model behaviour well. It is possible that the two effects cancel, i.e., the insufficient adjustment time effectively reduces the slope of $\Delta\phi_\mathrm{i}/\Delta$OHT, while the change in underlying mechanism increases it, such that

the EBM gets the right answer but for the wrong underlying assumptions.

There is another important limitation relevant to this chapter: the accuracy of the OHT diagnostic. In section 4.1.2, it was explained that OHT is calculated by integrating the surface flux, F_s, effectively neglecting changes in ocean heat content. This is a valid approximation for the PI-control analysis, but in the future simulations substantial changes in heat storage are inevitable, as has occurred in reality over recent decades (e.g., Zanna et al., 2019). In essence, what has been referred to as 'OHT' is really the net air–sea flux, F_s, but there is no information as to whether this is coming from OHT convergence or from changes in storage (Eq. 1.1). This problem increases with time, thus casting doubt mainly on the interpretation of OHT behaviour in the SIF regime. Although it is unlikely to affect results for the near future (considering that the EBM equation captures the relationship between $\Delta\phi_i$ and ΔOHT; Figs. 5.7 and 5.8), it would be convenient if prepared OHT (and AHT) data were widely available in the CMIP archive for the purposes of multi-model analyses—an issue also raised by Outten et al. (2018).

The difference in behaviour of perennial and seasonal sea ice cover in the Arctic was considered in section 5.5.2, but what about the Southern Ocean? This was not investigated in the same way, primarily because the real-world Antarctic sea ice cover is already close to the SIF regime. Sea ice cannot retreat further than the Antarctic coastline at a maximum of about 78°S, unlike in the Arctic where it can retreat to the north pole. This means that the difference between perennial and SIF regimes is not as dramatic in the SH. It was found—subject to the caveat discussed above—that OHT seems to play less of a role in a SIF Arctic. However, poleward OHT in the SH does affect sea ice over a range of models and time periods, including models which exhibit SIF Antarctic sea ice in their PI-control simulation. The SH behaviour could reflect either the relatively inconsequential difference between perennial and seasonal ice cover there, another

fundamental difference between the hemispheres, or that the caveats associated with OHT render inaccurate conclusions for the SIF Arctic.

5.7 Chapter summary

The results of this chapter are summarised as follows:

1. **Model biases in OHT are associated with spread in present and future sea ice extent:**

   a) Larger initial OHT is associated with smaller initial sea ice extent;

   b) Rates of sea ice loss are strongly positively correlated with changes in OHT;

   c) In the NH, effect (b) is the dominant contribution to future spread, whereas effect (a) is more important in the SH.

2. **Projected rates of sea ice loss are well captured by the EBM Eq. (3.23b) in all scenarios:**

   a) Future increases in poleward OHT tend to enhance the forced rate of sea ice decline (and vice versa);

   b) Some simulations exhibit future decreases in OHT large enough to completely offset sea ice loss due to warming.

3. **Model biases relative to observations can be partly explained by OHT:**

   a) Simulations with rates of recent Arctic sea ice trends comparable to observations do so with significant positive biases in polar surface warming, and such simulations have larger increases in OHT;

b) Modelled Antarctic sea ice trends are only close to realistic when poleward OHT decreases enough to offset the forced response.

4. **The same mechanisms behind the impact of natural variations in OHT on sea ice likely apply to the forced sea ice response.**

5. **In a seasonally ice-free Arctic, the relationship between OHT and sea ice extent becomes weaker:**

   a) OHT is a poor predictor of the timing of a seasonally ice free Arctic;

   b) In a case study of one model, there is a weak relationship between sea ice cover and OHT in the SIF regime;

   c) These specific results should be taken with caution due to caveats associated with OHT diagnosis in the SIF regime and the reliance on a particular model for analysis.

Chapter 6

Conclusions

This thesis has shown that ocean heat transport is a major driver of sea ice changes on multidecadal timescales. The relationship between OHT and sea ice can be explained using simple energy-balance considerations, and manifests in the natural variability and forced response of comprehensive GCM simulations. In turn, this strongly contributes to inter-model spread, uncertainty in future projections, and model biases relative to observations. This chapter provides further discussion of these findings. In section 6.1, the results are summarised in the context of the research questions stated in section 1.4.1. The scope and limitations are discussed in section 6.2, and suggestions for future research directions are given in section 6.3.

6.1 Research questions revisited

1. **What sets the sensitivity of sea ice to OHT?**

   A number of emergent, large-scale climate parameters set the sensitivity of the sea ice-edge latitude to OHT. These are principally atmospheric in origin, and depend on radiative feedbacks, the difference in planetary albedo across the ice edge, the rate of Bjerknes compensation (BC), and

geometric factors relating to land and zonal symmetry (Eq. 3.23b). Sea ice is more sensitive to basal (i.e., oceanic) than surface (i.e., atmospheric) heat transport convergence because the latter is partially lost to space, unlike the former which must be lost to sea ice (Eq. 3.15). The sensitivity also depends on the spatial distribution of the convergence: OHTC concentrated near the ice edge is about twice as effective at reducing sea ice extent than the equivalent convergence uniformly distributed over sea ice. This is because the former case more efficiently eliminates ice and increases surface temperatures. These results were obtained by analysing an idealised energy balance model (EBM) and analogous behaviours arise in comprehensive GCM simulations.

2. **What is the relationship between unforced variability in OHT and sea ice in GCMs?**

   When poleward OHT is anomalously high, sea ice extent is anomalously low. The opposite is true for AHT, which is attributable to BC. These relationships hold in both hemispheres, but hide differences in how Arctic and Antarctic sea ice respond to OHT anomalies. In the NH, OHT mainly converges along the Atlantic sea ice edge rather than under the central ice pack. This efficiently causes the ice edge to retreat, leading to increased AHT into higher latitudes, strong surface warming, and pan-Arctic reductions in ice thickness. In the SH, OHT mainly converges uniformly under Antarctic sea ice, with no direct role of AHT. These behaviours correspond to the two sensitivity experiments of the EBM in which the analogous sea ice behaviours were revealed (K_o for the NH and F_bp for the SH). The relationship within and across models between anomalies in sea ice, OHT, and surface temperature are broadly captured by the EBM Eq. (3.23b). The mechanisms partly explain the difference between NH and SH sensitivities (manifesting in the ΔT_s term in Eq. 3.23b), but here the shortwave and

associated geometric factors (s in Eq. 3.23b) dominate. These results are qualitatively robust across a sample of 20 different coupled GCMs.

3. **To what extent does OHT explain uncertainties in future projections of sea ice?**

   Model biases in OHT contribute to inter-model spread in the mean state and projected rates of sea ice decline. Models exhibiting larger initial sea ice covers tend to have smaller initial poleward OHT. Differences across models in future changes in OHT are in some cases large enough to almost completely offset the effect of global (and polar) warming. The two factors—initial OHT and future OHT change—are anticorrelated, making the attribution of the direct effect of OHT biases non-trivial. A crude approach (using r^2) estimates that around 70–80% of biases in the future sea ice state across models can be explained by differences in OHT. The same underlying mechanisms and explanations of the sea ice effective sensitivity to OHT under natural variability (i.e., as in question 2) apply to the forced responses. These results are independent of future scenario (forcing level). A final, tentative finding is that when the Arctic becomes seasonally ice free, the impact of OHT on sea ice is reduced.

6.2 Discussion

As described in chapter 1, past studies have identified many lines of evidence that the ocean is a key determinant of the sea ice state. The results of this thesis strongly support this, verifying previous findings and generating new insight. The fact that OHT is strongly correlated with the sea ice cover is not entirely surprising considering previous work discussed in section 1.2.3. However, here the analysis of PI-control simulations make this the first study to show that the relationship exists in comprehensive GCMs without forcing—particularly with

sensitivity experiments in which OHT changes are imposed (e.g., Docquier et al., 2021). Since it has also been found here that OHT is strongly related to the future sea ice state this, arguably, increases the significance of such sensitivity studies, by showing their insights are likely relevant to future climate projections. While not without limitations, the EBM is a fresh approach to the problem. For example, although Mahlstein and Knutti (2011) found a strong correlation between OHT and sea ice extent in CMIP3 models, there is yet no explanation for what sets the slope. Here, this result has been extended by verifying it in a larger sample of the latest generation models, examining the dependence on time period and effect of mean state versus rate of change. Furthermore, by applying EBM principles, understanding is gained into why the relationship exists and what sets the slope. That sea ice is intrinsically more sensitive to basal than surface fluxes (Eq. 3.15) has been found before (Thorndike, 1992; Eisenman, 2012); but again, this work extends this result to the heat transports themselves (e.g., in how it manifests in Eq. 3.23a). The emergence of robust, distinct mechanisms between the NH and SH is a novel result. They closely mimic the EBM behaviours, parallel current understanding of the Arctic and Southern Oceans on shorter timescales (section 1.1.1), and are relevant to natural and forced climate variability. This strongly motivates further research into the details underlying the mechanisms (see section 6.3).

This work has important implications for uncertainty in future projections. In general, such uncertainties can be decomposed into contributions from future scenario, model biases, and internal variability. For example, Hawkins and Sutton (2009) find that model uncertainty dominates the overall uncertainty in future global-mean surface temperature projections of CMIP3 models. For near-future sea ice losses, Fig. 1.1 suggests that scenario uncertainty is small until the late 21st century, and Figs. 5.7 and 5.8 suggest that model uncertainty slightly dominates in the NH (consistent with Bonan et al., 2021) while internal variability

dominates in the SH. The strong role of internal variability probably explains why the same inferred mechanisms of natural OHT variability are found to operate in the forced response. Reducing the uncertainty in the forced response could greatly improve the estimation of the future sea ice state, which will involve addressing shortcomings in the ocean components of models. The impact of ocean model differences are known to persist in the latest CMIP6 models—for instance, contributing to spread in simulated AMOC changes (Todd et al., 2020) and in the strength of the Antarctic circumpolar current (Beadling et al., 2020). Since sea ice itself has impacts on the climate (section 1.1.1), addressing such biases could in turn improve other aspects of future climate projections.

In section 1.1.2 it was mentioned that sea ice uncertainties also exist in simulations of distant-past climates, such as the last glacial maximum (LGM) with mid-latitude sea ice coverage. Some results could plausibly apply in these contexts, as previous studies have noted a correspondence between the ocean and sea ice extent in simulations of such states (Ferreira et al., 2011, 2018; Marzocchi and Jansen, 2017). This suggests that better representation of the ocean in models has the potential to improve evaluation of paleoclimate processes by improved confidence in the sea ice state compared to paleoproxy reconstructions. It is not clear whether the qualitative mechanisms are likely to be the same as those found for the pre-industrial, because of differences in the ocean circulation and more extensive sea ice cover (Ferrari et al., 2014). Although the novel EBM developed in this thesis was not designed with such sea ice states in mind, the formulation and equations derived from it only depend on energy conservation principles so should apply anyway (with appropriately re-derived parameter values). Proxy-based estimates place the LGM Antarctic sea ice edge roughly 10°S equatorward of that today (e.g., Crosta, 2009). Using this to (naively) extrapolate from the inter-model trend in Fig. 5.1b suggests that OHT would have to be negative (equatorward in the SH) to enable such sea ice cover. This is inconsistent with

modelling studies finding negligible differences in SH poleward OHT at the LGM relative to pre-industrial (Donohoe et al., 2020). This probably indicates the non-linearity of the OHT–sea ice relationship emerging over the large changes between present day and LGM conditions and the need for a different EBM reference state (rather than a fundamental flaw in applying the EBM in this context). Overall, there are too many unknowns to generalise the results of this thesis to larger sea ice extents such as those existing at the LGM, and further work would be needed to evaluate the relationship between OHT and sea ice in these climates.

According to the EBM analysis, the sensitivity of sea ice to OHT arises due to energetic constraints relating to the TOA fluxes. This does not provide an explanation in terms of fundamentally oceanic processes—indeed, only explicitly atmospheric parameters appear in Eqs. (3.15) and (3.23a). This partly reflects the fact that the ocean in general only affects other components of the climate system by interacting with the atmosphere via air–sea fluxes. It is also the reason that there is no insight here into why the magnitudes of variability differ across GCMs (e.g., the range of OHT anomalies in Fig. 4.9), or why the NH and SH exhibit different mechanisms. This is therefore a limitation of the EBM framework. A comparison can be drawn with the work of Armour et al. (2019), who explain the origin of AHT independently from energetic and dynamic perspectives. Energetically, AHT exists to counteract hemispheric-scale imbalances in the TOA and surface fluxes, explaining the magnitude and distribution of AHT. Dynamically, AHT is the net effect of advection of heat and moisture by atmospheric motions such as the Hadley circulation and transient eddies. These give complementary views of the physics underlying AHT: the energetic perspective does not explain how AHT arises, and the dynamic perspective does not explain why AHT has smooth hemispheric-scale structure (Fig. 1.3b). In the present context, the EBM is obviously the energetic perspective on the sea ice sensitivity to OHT, explaining its magnitude. To complete the picture, a description of the

underlying ocean dynamics determining OHT variations (e.g., from changes in the wind-driven gyres, the AMOC, or the eddy field) is needed. This could also shed light into the factors leading to the different NH and SH mechanisms.

All of the analyses presented in this thesis have focused on the annual-mean sea ice state on multidecadal timescales, because this is of particular importance to future climate projections. However, the onset of seasonally ice-free (SIF) conditions as defined by Senftleben et al. (2020) relies on a 5 yr period of the seasonal-minimum sea ice extent falling below a threshold value, which clearly depends on interannual variability. This raises questions about how strongly OHT influences sea ice at different points of the seasonal cycle and on shorter time scales. Since the present work has generated the required data, it is possible to obtain a preliminary view of how these relationships could appear in summer and winter. Figure 6.1 plots the changes in sea ice, OHT, and surface temperature over recent decades in the same way as Fig. 5.11, but for summer and winter months. This shows that the relationship between all three quantities is weaker in summer than for the annual mean (Fig. 6.1, top). However, for winter, the relationship appears to be about as strong as for the annual mean, and interestingly the offset of the inter-model spread from observations is reduced (increased) in the NH (SH; Fig. 6.1, bottom). This could indicate that different processes occur in summer and winter (but does not affect the interpretation of the annual mean). It is also possible that the better correspondence of the summer Arctic sea ice trends to observations reflects that this is a crucial metric that modelling centres are tuning to. The EBM, by design, only applies to the equilibrium climate state, so cannot explain these trends nor the interannual variability where the system may not have fully adjusted to changes in the ocean state.

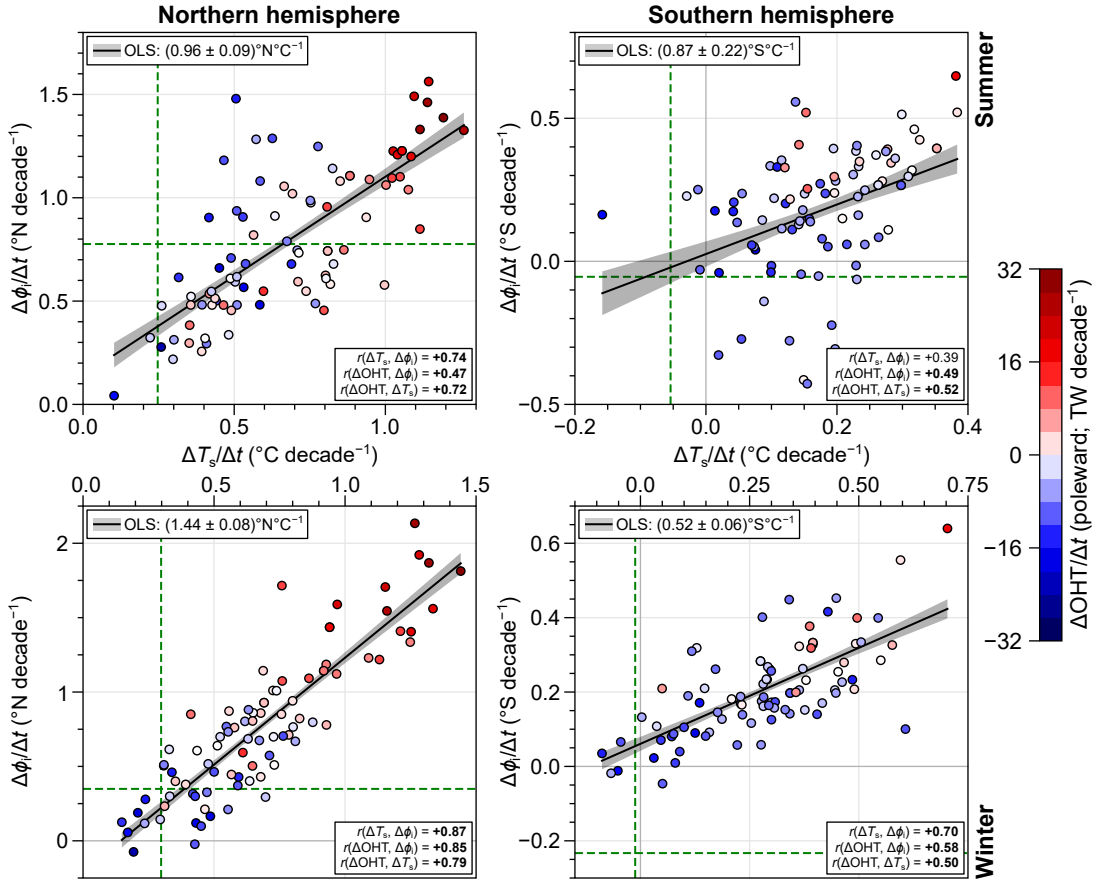

Figure 6.1: As in Fig. 5.11 but for the (top row) summer trend (September in the NH, February in the SH), and (bottom row) winter trend (March in the NH, September in the SH). Again, rates are computed as the difference in means over the periods 1970–1995 and 1995–2020 for the simulations, and as the linear trend over 1970–2000 (NH) and 1976–2015 (SH) for observations. Note that ΔOHT is still a 25 yr average of annual means, while $\Delta\phi_i$ and ΔT_s are 25 yr averages of the relevant monthly means.

6.3 Future research

This work raises several avenues of research that could yield further insight into the nature of the ocean–sea ice relationship and ultimately improve model simulations. Three key areas are suggested here:

1. **Detailed examination of the processes underlying ocean–sea ice interactions.**

   In section 4.2 a clear difference between how OHT anomalies affect sea ice in the NH and SH was identified. These differences are somewhat broad in classification and this work has not provided a complete explanation of why the difference occurs (i.e., the dynamic perspective discussed above). To progress the understanding of the hemispheric differences, a detailed analysis of the oceanic processes is required: for example, what aspects of the ocean circulation are associated with the two OHT pathways in each hemisphere? Specifically, what leads to ocean heat loss ahead of the Arctic ice edge and why does this not occur in the SH? A deeper understanding of these processes is particularly important given the evidence that similar behaviours operate in the projected declines of each hemisphere (section 5.4). This could also help identify causes of model biases in their representation of the ocean state which in turn affect sea ice.

2. **Quantitative analysis to determine the proportion of sea ice uncertainties that can be attributed to OHT biases.**

   This work provides ample evidence that OHT explains a large part of the uncertainty in sea ice simulations, via internal variability and model biases in the mean state and forced response. However, no rigorous quantification of this has been made, and the direct effect of OHT on sea ice is confounded with the effect of surface temperature variations. One approach could be to

consider a single model with a large ensemble (e.g., Kay et al., 2015; Maher et al., 2019). This enables separation of the forced response and internal variability. Similarly, using a combination of coupled atmosphere–ocean and atmosphere-only simulations, the direct effect of OHT on sea ice can be determined (i.e., eliminating purely atmospheric variability in T_s). Such quantification could ultimately settle the question of the role of OHT in sea ice uncertainties, with major implications for modelling efforts.

3. **Analysis of the impact of OHT on sea ice in idealised and/or extended future simulations.**

   Although there is considerable uncertainty on the time of onset (from model spread and the unknown future pathway of emissions and climate change mitigation), it is reasonable to suppose that the loss of summer ice cover is plausible within the coming century. Analysing the SIF climate was limited here, because only one model provided many realisations each with sufficient SIF years. In CMIP6 there are other experiments likely to generate SIF states on longer timescales. Some models provide extensions to the ScenarioMIP future simulations beyond 2100. The idealised abrupt CO_2 quadrupling experiment generates effective radiative forcings comparable to the high-emission SSP3-7.0 and SSP5-8.5 scenarios (i.e., likely to produce a SIF Arctic; Smith et al., 2020). The impact of OHT in such climate states should be evaluated using a more accurate diagnostic for OHT to ensure changes in ocean heat content are not obscuring the results presented in section 5.5. As mentioned in section 5.6, this would be greatly facilitated if the true OHT and AHT diagnostics were readily available in the CMIP data archives. Understanding the future ocean–sea ice relationship in model simulations will become increasingly relevant as the real world moves closer to the SIF state.

6.4 Closing remarks

The changing state of the sea ice cover affects global climate and has direct societal and ecological impacts. In the future, it is likely to remain a prominent metric of climate change and a gauge of model reliability. This thesis brings new insight into the theory underpinning the impact of the ocean and provides tools for the analysis of climate simulations. These have been applied to future projections that are used to inform environmental policy, in which ocean heat transport is identified as a major driver of sea ice changes. Looking forward, identifying and correcting model biases in the ocean state relative to real-world estimates is an essential step towards reducing uncertainties in projections of sea ice.

This page intentionally left blank.

References

Affholder, M., and F. Valiron, 2001: *Descriptive Physical Oceanography*. 1st ed., CRC Press, 370 pp.

Alexeev, V. A., and C. H. Jackson, 2012: Polar amplification: is atmospheric heat transport important? *Clim. Dyn.*, **41**, 533–547, doi:10.1007/s00382-012-1601-z.

Armour, K. C., N. Siler, A. Donohoe, and G. H. Roe, 2019: Meridional atmospheric heat transport constrained by energetics and mediated by large-scale diffusion. *J. Clim.*, **32**, 3655–3680, doi:10.1175/JCLI-D-18-0563.1.

Årthun, M., T. Eldevik, and L. H. Smedsrud, 2019: The role of Atlantic heat transport in future Arctic sea ice loss. *J. Clim.*, **32**, 3327–3341, doi:10.1175/JCLI-D-18-0750.1.

Askenov, Y., E. E. Popova, A. Yool, A. J. G. Nurser, T. D. Williams, L. Bertino, and Coauthors, 2017: On the future navigability of Arctic sea routes: high-resolution projections of the Arctic ocean and sea ice. *Mar. Policy*, **75**, 300–317, doi:10.1016/j.marpol.2015.12.027.

Auclair, G., and L. B. Tremblay, 2018: The role of ocean heat transport in rapid sea ice declines of the Community Earth System Model Large Ensemble. *J. Geophys. Res.*, **123**, 8941–8957, doi:10.1029/2018JC014525.

Aylmer, J. R., 2021: Sea ice-edge latitude diagnostic code. doi:10.5281/zenodo.5494524.

Aylmer, J. R., D. G. Ferreira, and D. L. Feltham, 2020: Impacts of oceanic and atmospheric heat transports on sea ice extent. *J. Clim.*, **33**, 7197–7215, doi:10.1175/JCLI-D-19-0761.1.

Aylmer, J. R., D. G. Ferreira, and D. L. Feltham, 2022: Different mechanisms of Arctic and Antarctic sea ice response to ocean heat transport. *Clim. Dyn.*, doi:10.1007/s00382-021-06131-x.

Beadling, R. L., J. L. Russell, R. J. Stouffer, M. Mazloff, L. D. Talley, P. J. Goodman, and Coauthors, 2020: Representation of Southern Ocean properties across coupled model intercomparison project generations: CMIP3 to CMIP6. *J. Clim.*, **33**, 6555–6581, doi:10.1175/JCLI-D-19-0970.1.

Bi, D., M. Dix, S. Marsland, S. O'Farrell, A. Sullivan, R. Bodman, and Coauthors, 2020: Configuration and spin-up of ACCESS-CM2, the new generation Australian Community Climate and Earth System Simulator Coupled Model. *J. South. Hemisphere Earth Syst. Sci.*, **70**, 225–251, doi:10.1071/ES19040.

Bintanja, R., and F. Selten, 2014: Future increases in Arctic precipitation linked to local evaporation and sea-ice retreat. *Nature*, **509**, 479–482, doi:10.1038/nature13259.

Bitz, C. M., M. M. Holland, E. C. Hunke, and R. E. Moritz, 2005: Maintenance of the sea-ice edge. *J. Clim.*, **18**, 2903–2921, doi:10.1175/JCLI3428.1.

Bitz, C. M., and G. H. Roe, 2004: A mechanism for the high rate of sea ice thinning in the Arctic ocean. *J. Clim.*, **17**, 3623–3632, doi:10.1175/1520-0442(2004)017<3623:AMFTHR>2.0.CO;2.

Bjerknes, J., 1964: Atlantic air–sea interaction. *Adv. Geophys.*, **10**, 1–82, doi:10.1016/S0065-2687(08)60005-9.

Boccaletti, G., R. Ferrari, A. Adcroft, D. G. Ferreira, and J. Marshall, 2005: The vertical structure of ocean heat transport. *Geophys. Res. Lett.*, **32**, L10 603, doi:10.1029/2005GL022474.

Bonan, D. B., F. Lehner, and M. M. Holland, 2021: Partitioning uncertainty in projections of Arctic sea ice. *Environ. Res. Lett.*, **16**, 044 002, doi:10.1088/1748-9326/abe0ec.

Boucher, O., J. Servonnat, A. L. Albright, O. Aumont, Y. Balkanski, V. Bastrikov, and Coauthors, 2020: Presentation and evaluation of the IPSL-CM6A-LR climate model. *J. Adv. Model. Earth Syst.*, **12**, e2019MS002 010, doi:10.1029/2019MS002010.

Bourassa, M. A., S. T. Gille, C. M. Bitz, D. Carlson, I. Cerovecki, C. A. Clayson, and Coauthors, 2013: High-latitude ocean and sea ice surface fluxes: challenges for climate research. *Bull. Am. Meteorol. Soc.*, **94**, 403–423, doi:10.1175/bams-d-11-00244.1.

Bouttes, N., D. Paillard, and D. M. Roche, 2010: Impact of brine-induced stratification on the glacial carbon cycle. *Clim. Past*, **6**, 575–589, doi:10.5194/cp-6-575-2010.

Bracegirdle, T. J., D. B. Stephenson, J. Turner, and T. Phillips, 2015: The importance of sea ice area biases in 21st century multimodel projections of Antarctic temperature and precipitation. *Geophys. Res. Lett.*, **42**, 10 832–10 839, doi:10.1002/2015GL067055.

Budikova, D., 2009: Role of Arctic sea ice in global atmospheric circulation: a review. *Glob. Planet. Change*, **68**, 149–163, doi:10.1016/j.gloplacha.2009.04.001.

Budyko, M. I., 1969: The effect of solar radiation variations on the climate of the Earth. *Tellus*, **21**, 611–619, doi:10.1111/j.2153-3490.1969.tb00466.x.

Budyko, M. I., 1972: The future climate. *Eos Trans. AGU*, **53**, 868–874, doi:10.1029/EO053i010p00868.

Burgard, C., and D. Notz, 2017: Drivers of Arctic Ocean warming in CMIP5 models. *Geophys. Res. Lett.*, **44**, 4263–4271, doi:10.1002/2016GL072342.

Cahalan, R. F., and G. R. North, 1979: A stability theorem for energy-balance climate models. *J. Atmos. Sci*, **36**, 1178–1188, doi:10.1175/1520-0469(1979)036<1178:ASTFEB>2.0.CO;2.

Carmack, E., I. Polyakov, L. Padman, I. Fer, E. Hunke, J. Hutchings, and Coauthors, 2015: Toward quantifying the increasing role of oceanic heat in sea ice loss in the new Arctic. *Bull. Am. Meteorol. Soc.*, **96**, 2079–2105, doi:10.1175/BAMS-D-13-00177.1.

Castruccio, F. S., Y. Ruprich-Robert, S. G. Yeager, G. Danabasoglu, R. Msadek, and T. L. Delworth, 2019: Modulation of Arctic sea ice loss by atmospheric teleconnections from atlantic multidecadal variability. *J. Clim.*, **32**, 1419–1441, doi:10.1175/JCLI-D-18-0307.1.

Christensen, M., and A. E. Nilsson, 2017: Arctic sea ice and the communication of climate change. *Pop. Commun.*, **15**, 249–268, doi:10.1080/15405702.2017.1376064.

Costa, S. M. S., and K. P. Shine, 2012: Outgoing longwave radiation due to directly transmitted surface emission. *J. Atmos. Sci.*, **69**, 1865–1870, doi:10.1175/JAS-D-11-0248.1.

Counillon, F., N. Keenlyside, I. Bethke, Y. Wang, S. Billeau, M. L. Shen, and M. Bentsen, 2016: Flow-dependent assimilation of sea surface temperature in isopycnal coordinates with the Norwegian Climate Prediction Model. *Tellus A*, **68**, 32 437, doi:10.3402/tellusa.v68.32437.

Crosta, X., 2009: Antarctic sea ice history, late quatenary. *Encyclopedia of Paleoclimatology and Ancient Environments*, V. Gornitz, Ed., Springer, Dordrecht, Netherlands, 31–34, doi:10.1007/978-1-4020-4411-3_10.

Crosta, X., J. Etourneau, L. C. Orme, Q. Dalaiden, P. Campagne, D. Swingedouw, and Coauthors, 2021: Multi-decadal trends in Antarctic sea-ice extent driven by ENSO–SAM over the last 2,000 years. *Nat. Geosci.*, **14**, 156–160, doi:10.1038/s41561-021-00697-1.

Dai, A., D. Luo, M. Song, and J. Liu, 2019: Arctic amplification is caused by sea-ice loss under increasing CO_2. *Nat. Commun.*, **10**, 121, doi:10.1038/s41467-018-07954-9.

Danabasoglu, G., J.-F. Lamarque, J. Bacmeister, D. A. Bailey, A. K. DuVivier, J. Edwards, and Coauthors, 2020: The Community Earth System Model Version 2 (CESM2). *J. Adv. Model. Earth Syst.*, **12**, e2019MS001 916, doi:10.1029/2019MS001916.

Day, J. J., J. C. Hargreaves, J. D. Annan, and A. Abe-Ouchi, 2012: Sources of multi-decadal variability in Arctic sea ice extent. *Environ. Res. Lett.*, **7**, 034 011, doi:10.1088/1748-9326/7/3/034011.

Dee, D. P., S. M. Uppala, A. J. Simmons, P. Berrisford, P. Polo, S. Kobayashi, and Coauthors, 2011: The ERA-Interim reanalysis: configuration and performance of the data assimilation system. *Quart. J. Roy. Meteor. Soc.*, **137**, 553–597, doi:10.1002/qj.828.

Ding, Q., A. Scheiger, M. L'Heureux, D. S. Battisti, S. Po-Chedley, N. C. Johnson, and Coauthors, 2017: Influence of high-latitude atmospheric circulation changes on summertime Arctic sea ice. *Nat. Clim. Change*, **7**, 289–295, doi:10.1038/nclimate3241.

Docquier, D., T. Koenigk, R. Fuentes-Franco, M. P. Karami, and Y. Ruprich-Robert, 2021: Impact of ocean heat transport on the Arctic sea-ice decline: a model study with EC-Earth3. *Clim. Dyn.*, **56**, 1407–1432, doi:10.1007/s00382-020-05540-8.

Donohoe, A., K. C. Armour, G. H. Roe, D. S. Battisti, and L. Hahn, 2020: The partitioning of meridional heat transport from the last glacial maximum to CO_2 quadrupling in coupled climate models. *J. Clim.*, **33**, 4141–4165, doi:10.1175/JCLI-D-19-0797.1.

Donohoe, A., and D. S. Battisti, 2011: Atmospheric and surface contributions to planetary albedo. *J. Clim.*, **24**, 4402–4418, doi:10.1175/2011JCLI3946.1.

Draper, N. R., and H. Smith, 1998: *Applied Regression Analysis*. 3rd ed., John Wiley, 736 pp.

Eisenman, I., 2010: Geographic muting of changes in the Arctic sea ice cover. *Geophys. Res. Lett.*, **37**, L16 501, doi:10.1029/2010GL043741.

Eisenman, I., 2012: Factors controlling the bifurcation structure of sea ice retreat. *J. Geophys. Res.*, **117**, doi:10.1029/2011JD016164.

Eisenman, I., N. Untersteiner, and J. S. Wettlaufer, 2007: On the reliability of simulated Arctic sea ice in global climate models. *Geophys. Res. Lett.*, **34**, L10 501, doi:10.1029/2007GL029914.

Eisenman, I., and J. S. Wettlaufer, 2009: Nonlinear threshold behavior during the loss of Arctic sea ice. *Proc. Natl. Acad. Sci.*, **106**, 28–32, doi:10.1073/pnas.0806887106.

England, M., L. Polvani, and L. Sun, 2018: Contrasting the Antarctic and Arctic atmospheric responses to projected sea ice loss in the late twenty-first century. *J. Clim.*, **31**, 6353–6370, doi:10.1175/JCLI-D-17-0666.1.

Eyring, V., S. Bony, G. A. Meehl, C. A. Senior, B. Stevens, R. J. Stouffer, and K. E. Taylor, 2016: Overview of the Coupled Model Intercomparison Project Phase 6 (CMIP6) experimental design and organization. *Geosci. Model Dev.*, **9**, 1937–1958, doi:10.5194/gmd-9-1937-2016.

Ferrari, R., and D. G. Ferreira, 2011: What processes drive the ocean heat transport? *Ocean Model.*, **38**, 171–186, doi:10.1016/j.ocemod.2011.02.013.

Ferrari, R., M. F. Jansen, J. F. Adkins, A. Burke, A. L. Stewart, and A. F. Thompson, 2014: Antarctic sea ice control on ocean circulation in present and glacial climates. *Proc. Natl. Acad. Sci.*, **111**, 8753–8758, doi:10.1073/pnas.1323922111.

Ferreira, D. G., J. Marshal, T. Ito, and D. McGee, 2018: Linking glacial–interglacial states to multiple equilibria of climate. *Geophys. Res. Lett.*, **45**, 9160–9170, doi:10.1029/2018GL077019.

Ferreira, D. G., J. Marshall, C. M. Bitz, S. Solomon, and A. Plumb, 2015: Antarctic ocean and sea ice response to ozone depletion: a two-time-scale problem. *J. Clim.*, **28**, 1206–1226, doi:10.1175/JCLI-D-14-00313.1.

Ferreira, D. G., J. Marshall, and B. E. J. Rose, 2011: Climate determinism revisited: multiple equilibria in a complex climate model. *J. Clim.*, **24**, 992–1012, doi:10.1175/2010JCLI3580.1.

Flocco, D., D. Schroeder, D. L. Feltham, and E. C. Hunke, 2012: Impact of melt ponds on Arctic sea ice simulations from 1990 to 2007. *J. Geophys. Res. Oceans*, **117**, C09 032, doi:10.1029/2012JC008195.

Forget, G., J.-M. Campin, P. Heimbach, C. N. Hill, R. M. Ponte, and C. Wunsch, 2015: ECCO version 4: an integrated framework for non-linear inverse modeling and global ocean state estimation. *Geosci. Model Dev.*, **8**, 3071–3104, doi:10.5194/gmd-8-3071-2015.

Forget, G., and D. G. Ferreira, 2019: Global ocean heat transport dominated by heat export from the tropical Pacific. *Nat. Geosci.*, **12**, 351–354, doi:10.1038/s41561-019-0333-7.

Goosse, H., and V. Zunz, 2014: Decadal trends in Antarctic sea ice extent ultimately controlled by ice–ocean feedback. *Cryosphere*, **8**, 453–470, doi:10.5194/tc-8-453-2014.

Hardy, B. W., and K. H. Jamieson, 2016: Overcoming endpoint bias in climate change communication: the case of Arctic sea ice trends. *Environ. Commun.*, **11**, 205–217, doi:10.1080/17524032.2016.1241814.

Hassell, D., J. M. Gregory, J. Blower, B. N. Lawrence, and K. E. Taylor, 2017: A data model of the Climate and Forecast metadata conventions (CF-1.6) with a software implementation (cf-python v2.1). *Geosci. Model Dev.*, **10**, 4619–4646, doi:10.5194/gmd-10-4619-2017.

Hawkins, E., and R. Sutton, 2009: The potential to narrow uncertainty in regional climate predictions. *Bull. Am. Meteorol. Soc.*, **90**, 1095–1108, doi:10.1175/2009BAMS2607.1.

Held, I. M., and M. J. Suarez, 1974: Simple albedo feedback models of the icecaps. *Tellus*, **26**, 613–629, doi:10.1111/j.2153-3490.1974.tb01641.x.

Heorton, H. D. B. S., N. Radia, and D. L. Feltham, 2017: A model of sea ice formation in leads and polynyas. *J. Clim.*, **47**, 1701–1718, doi:10.1175/JPO-D-16-0224.1.

Ho, J., 2010: The implications of Arctic sea ice decline on shipping. *Mar. Policy*, **34**, 713–715, doi:10.1016/j.marpol.2009.10.009.

Holland, M. M., M. C. Serreze, and J. Stroeve, 2010: The sea ice mass budget of the Arctic and its future change as simulated by coupled climate models. *Clim. Dyn.*, **34**, 185–200, doi:10.1007/s00382-008-0493-4.

Hourdin, F., T. Mauritsen, A. Gettelman, J.-C. Golaz, V. Balaji, Q. Duan, and Coauthors, 2017: The art and science of climate model tuning. *Bull. Am. Meteorol. Soc.*, **98**, 589–602, doi:10.1175/BAMS-D-15-00135.1.

Huang, Y., X. Dong, D. A. Bailey, M. M. Holland, B. Xi, A. K. DuVivier, and Coauthors, 2019: Thicker clouds and accelerated Arctic sea ice decline: the atmosphere–sea ice interactions in spring. *Geophys. Res. Lett.*, **46**, 6980–6989, doi:10.1029/2019GL082791.

Huybers, P., 2016: Daily mean incident solar radiation over the last 3 Myr - data set and MATLAB code. [Accessed August 2019, http://www.people.fas.harvard.edu/~phuybers/Mfiles/Toolbox/inso.m.].

Hwang, Y.-T., and D. M. W. Frierson, 2010: Increasing atmospheric poleward energy transport with global warming. *Geophys. Res. Lett.*, **37**, L24 807, doi:10.1029/2010GL045440.

IPCC, 2021: The Physical Science Basis. Contribution of Working Group I to the Sixth Assessment Report of the Intergovernmental Panel on Climate Change. *Climate Change 2021*, V. Masson-Delmotte, P. Zhai, A. Pirani, S. L. Connors, C. Péan, S. Berger et al., Eds., Cambridge University Press, In press.

Jahn, A., and M. M. Holland, 2013: Implications of Arctic sea ice changes for north Atlantic deep convection and the meridional overturning circulation in CCSM4-CMIP5 simulations. *Geophys. Res. Lett.*, **40**, 1206–1211, doi:10.1002/grl.50183.

Kageyama, M., L. C. Sime, M. Sicard, M.-V. Guarino, A. de Vernal, R. Stein, and Coauthors, 2021: A multi-model CMIP6-PMIP4 study of Arctic sea ice at 127 ka: sea ice data compilation and model differences. *Clim. Past*, **17**, 37–62, doi:10.5194/cp-17-37-2021.

Kapsch, M.-L., R. G. Graversen, and M. Tjernström, 2013: Springtime atmospheric energy transport and the control of Arctic summer sea-ice extent. *Nat. Clim. Change*, **3**, 744–748, doi:10.1038/nclimate1884.

Kay, J. E., C. Deser, A. Phillips, A. Mai, C. Hannay, G. Strand, and Coauthors, 2015: The Community Earth System Model (CESM) Large Ensemble project: a community resource for studying climate change in the presence of internal climate variability. *Bull. Am. Meteorol. Soc.*, **96**, 1333–1349, doi:10.1175/BAMS-D-13-00255.1.

Kay, J. E., and A. Gettelman, 2014: Cloud influence on and response to seasonal Arctic sea ice loss. *J. Geophys. Res. Atmos.*, **114**, D18 204, doi:10.1029/2009JD011773.

Keen, A., E. W. Blockley, D. A. Bailey, J. B. Debernard, M. Bushuk, S. Delhaye, and Coauthors, 2021: An inter-comparison of the mass budget of the Arctic sea ice in CMIP6 models. *Cryosphere*, **15**, 951–982, doi:10.5194/tc-15-951-2021.

Kim, K.-Y., B. D. Hamlington, H. Na, and J. Kim, 2016: Mechanism of seasonal Arctic sea ice evolution and Arctic amplification. *Cryosphere*, **10**, 2191–2202, doi:10.5194/tc-10-2191-2016.

Koenigk, T., and L. Brodeau, 2014: Ocean heat transport into the arctic in the twentieth and twenty-first century in EC-Earth. *Clim. Dyn.*, **42**, 3101–3120, doi:10.1007/s00382-013-1821-x.

Koll, D. D. B., and T. W. Cronin, 2018: Earth's outgoing longwave radiation linear due to H_2O greenhouse effect. *Proc. Natl. Acad. Sci.*, **115**, 10 293–10 298, doi:10.1073/pnas.1809868115.

Kopec, B. G., X. Feng, F. A. Michel, and E. S. Posmentier, 2016: Influence of sea ice on Arctic precipitation. *Proc. Natl. Acad. Sci.*, **113**, 46–51, doi:10.1073/pnas.1504633113.

Kostov, Y., J. Marshall, U. Hausmann, K. C. Armour, D. G. Ferreira, and M. Holland, 2017: Fast and slow responses of southern ocean sea surface temperature to SAM in coupled climate models. *Clim. Dyn.*, **48**, 1595–1609, doi:10.1007/s00382-016-3162-z.

Li, H., A. V. Fedorov, and W. Liu, 2021: AMOC stability and diverging response to Arctic sea ice decline in two climate models. *J. Clim.*, **34**, 5443–5460, doi:10.1175/JCLI-D-20-0572.1.

Liu, C., R. P. Allan, P. Berrisford, M. Mayer, P. Hyder, N. Loeb, and Coauthors, 2015: Combining satellite observations and reanalysis energy transports to estimate global net surface energy fluxes 1985–2012. *J. Geophys. Res.*, **120**, 9374–9389, doi:10.1002/2015JD023264.

Liu, J., M. Song, R. M. Horton, and Y. Hu, 2013: Reducing spread in climate model projections of a September ice-free Arctic. *Proc. Natl. Acad. Sci.*, **110**, 12 571–12 576, doi:10.1073/pnas.1219716110.

Liu, Y., J. Attema, and W. Hazeleger, 2020: Atmosphere–ocean interactions and their footprint on heat transport variability in the northern hemisphere. *J. Clim.*, **33**, 3691–3710, doi:10.1175/JCLI-D-19-0570.1.

Liu, Z., C. He, and F. Lu, 2018: Local and remote responses of atmospheric and oceanic heat transports to climate forcing: compensation versus collaboration. *J. Clim.*, **31**, 6445–6460, doi:10.1175/JCLI-D-17-0675.1.

Liu, Z., H. Yang, C. He, and Y. Zhao, 2016: A theory for Bjerknes compensation: the role of climate feedback. *J. Clim.*, **29**, 191–208, doi:10.1175/JCLI-D-15-0227.1.

Mahajan, S., R. Zhang, and T. L. Delworth, 2011: Impact of the atlantic meridional overturning circulation (AMOC) on Arctic surface air temperature and sea ice variability. *J. Clim.*, **24**, 6573–6581, doi:10.1175/2011JCLI4002.1.

Maher, N., S. Milinski, L. Suarez-Gutierrez, M. Botzet, M. Dobrynin, L. Kornblueh, and Coauthors, 2019: The Max Planck Institute Grand Ensemble: enabling the exploration of climate system variability. *J. Adv. Model. Earth Syst.*, **11**, 2050–2069, doi:10.1029/2019MS001639.

Mahlstein, I., and R. Knutti, 2011: Ocean heat transport as a cause for model uncertainty in projected Arctic warming. *J. Clim.*, **24**, 1451–1460, doi:10.1175/2010JCLI3713.1.

Maksym, T., 2019: Arctic and Antarctic sea ice change: contrasts, commonalities, and causes. *Ann. Rev. Mar. Sci.*, **11**, 187–213, doi:10.1146/annurev-marine-010816-060610.

Marshall, J., and K. Speer, 2012: Closure of the meridional overturning circulation through Southern Ocean upwelling. *Nat. Geosci.*, **5**, 171–180, doi:10.1038/ngeo1391.

Marshall, S., 2012: *The Cryosphere*. 1st ed., Princeton University Press, 288 pp.

Marzocchi, A., and M. F. Jansen, 2017: Connecting Antarctic sea ice to deep-ocean circulation in modern and glacial climate simulations. *Geophys. Res. Lett.*, **44**, 6286–6295, doi:10.1002/2017GL073936.

Massom, R. A., and S. E. Stammerjohn, 2010: Antarctic sea ice change and variability—physical and ecological impacts. *Polar Sci.*, **4**, 149–186, doi:10.1016/j.polar.2010.05.001.

Mauritsen, T., J. Bader, T. Becker, J. Behrens, M. Bittner, R. Brokopf, and Coauthors, 2019: Developments in the MPI-M Earth System Model version 1.2 (MPI-ESM1.2). *J. Adv. Model. Earth Syst.*, **11**, 998–1038, doi:10.1029/2018MS001400.

Mauritsen, T., B. Stevens, E. Roeckner, T. Crueger, M. Esch, M. Giorgetta, and Coauthors, 2012: Tuning the climate of a global model. *J. Adv. Model. Earth Syst.*, **4**, M00A01, doi:10.1029/2012MS000154.

Maykut, G. A., and N. Untersteiner, 1971: Some results from a time-dependent thermodynamic model of sea ice. *J. Geophys. Res.*, **76**, 1550–1575, doi:10.1029/JC076i006p01550.

Meehl, G. A., J. M. Arblaster, C. M. Bitz, C. T. Y. Chung, and H. Teng, 2016: Antarctic sea-ice expansion between 2000 and 2014 driven by tropical Pacific decadal climate variability. *Nat. Geosci.*, **9**, 590–595, doi:10.1038/ngeo2751.

Meehl, G. A., J. M. Arblaster, C. T. Y. Chung, M. M. Holland, A. DuVivier, L. Thompson, and Coauthors, 2019: Sustained ocean changes contributed to sudden Antarctic sea ice retreat in late 2016. *Nat. Commun.*, **10**, 14, doi:10.1038/s41467-018-07865-9.

Melia, N., K. Haines, and E. Hawkins, 2016: Sea ice decline and 21st century trans-Arctic shipping routes. *Geophys. Res. Lett.*, **43**, 9720–9728, doi:10.1002/2016GL069315.

Menary, M. B., T. Kuhlbrodt, J. Ridley, M. B. Andrews, O. B. Dimdore-Miles, J. Deshayes, and Coauthors, 2018: Preindustrial Control Simulations With HadGEM3-GC3.1 for CMIP6. *J. Adv. Model. Earth Syst.*, **10**, 3049–3075, doi:10.1029/2018MS001495.

Miles, M. W., D. V. Divine, T. Furevik, E. Jansen, M. Moros, and A. E. J. Ogilvie, 2013: A signal of persistent Atlantic multidecadal variability in Arctic sea ice. *Geophys. Res. Lett.*, **41**, 463–469, doi:10.1002/2013GL058084.

Morice, C. P., J. J. Kennedy, N. A. Rayner, and P. D. Jones, 2012: Quantifying uncertainties in global and regional temperature change using an ensemble of observational estimates: the HadCRUT4 dataset. *J. Geophys. Res. Atmos.*, **117**, D08 101, doi:10.1029/2011JD017187.

Müller, W. A., J. H. Jungclaus, T. Mauritsen, J. Baehr, M. Bittner, R. Budich, and Coauthors, 2018: A Higher-Resolution Version of the Max Planck Institute Earth System Model (MPI-ESM1.2-HR). *J. Adv. Model. Earth Syst.*, **10**, 1383–1413, doi:10.1029/2017MS001217.

Nijsse, F. J. M. M., P. M. Cox, and M. S. Williamson, 2020: Emergent constraints on transient climate response (TCR) and equilibrium climate sensitivity (ECS) from historical warming in CMIP5 and CMIP6 models. *Earth Syst. Dyn.*, **11**, 737–750, doi:10.5194/esd-11-737-2020.

North, G. R., 1975a: Analytical solution to a simple climate model with diffusive heat transport. *J. Atmos. Sci.*, **32**, 1301–1307, doi:10.1175/1520-0469(1975)032<1301:ASTASC>2.0.CO;2.

North, G. R., 1975b: Theory of energy-balance climate models. *J. Atmos. Sci.*, **32**, 2033–2043, doi:10.1175/1520-0469(1975)032<2033:TOEBCM>2.0.CO;2.

North, G. R., 1981: Energy balance climate models. *Rev. Geophys.*, **19**, 91–121, doi:10.1029/RG019i001p00091.

North, G. R., 1984: The small ice cap instability in diffusive climate models. *J. Atmos. Sci.*, **41**, 3390–3395, doi:10.1175/1520-0469(1984)041<3390:TSICII>2.0.CO;2.

North, G. R., and J. A. Coakley, 1979: Differences between seasonal and mean annual energy balance model calculations of climate and climate sensitivity. *J. Atmos. Sci.*, **36**, 1189–1204, doi:10.1175/1520-0469(1979)036<1189:DBSAMA>2.0.CO;2.

Notz, D., 2015: How well must climate models agree with observations? *Philos. Trans. R. Soc. A*, **373**, 20140 164, doi:10.1098/rsta.2014.0164.

Notz, D., A. Jahn, M. Holland, E. Hunke, F. Massonnet, J. Stroeve, and Coauthors, 2016: The CMIP6 Sea-Ice Model Intercomparison Project (SIMIP): understanding sea ice through climate-model simulations. *Geosci. Model Dev.*, **9**, 3427—3446, doi:10.5194/gmd-9-3427-2016.

Notz, D., and J. Marotzke, 2012: Observations reveal external driver for Arctic sea-ice retreat. *Geophys. Res. Lett.*, **39**, L08 502, doi:10.1029/2012GL051094.

Notz, D., and J. Stroeve, 2016: Observed Arctic sea-ice loss directly follows anthropogenic CO_2 emission. *Science*, **354**, 747–750, doi:10.1126/science.aag2345.

Notz, D., and J. Stroeve, 2018: The trajectory towards a seasonally ice-free Arctic ocean. *Curr. Clim. Change Rep.*, **4**, 407–416, doi:10.1007/s40641-018-0113-2.

Nummelin, A., C. Li, and P. J. Hezel, 2017: Connecting ocean heat transport changes from the midlatitudes to the Arctic Ocean. *Geophys. Res. Lett.*, **44**, 1899–1908, doi:10.1002/2016GL071333.

Olonscheck, D., T. Mauritsen, and D. Notz, 2019: Arctic sea-ice variability is primarily driven by atmospheric temperature fluctuations. *Nat. Geosci.*, **12**, 430–434, doi:10.1038/s41561-019-0363-1.

Olonscheck, D., and D. Notz, 2017: Consistently estimating internal climate variability from climate model simulations. *J. Clim.*, **30**, 9555–9573, doi:10.1175/JCLI-D-16-0428.1.

O'Neill, B. C., C. Tebaldi, D. P. van Vuuren, V. Eyring, P. Friedlingstein, G. Hurtt, and Coauthors, 2016: The Scenario Model Intercomparison Project (ScenarioMIP) for CMIP6. *Geosci. Model Dev.*, **9**, 3461–3482, doi:10.5194/gmd-9-3461-2016.

Otto, A., F. E. L. Otto, O. Boucher, J. Church, G. Hegerl, P. M. Forster, and Coauthors, 2013: Energy budget constraints on climate response. *Nat. Geosci.*, **6**, 415–416, doi:10.1038/ngeo1836.

Outten, S., I. Esau, and O. H. Otterå, 2018: Bjerknes compensation in the CMIP5 climate models. *J. Clim.*, **31**, 8745–8760, doi:10.1175/JCLI-D-18-0058.1.

Parkinson, C. L., 2019: A 40-y record reveals gradual Antarctic sea ice increases followed by decreases at rates far exceeding the rates seen in the Arctic. *Proc. Natl. Acad. Sci.*, **29**, 14 414–14 423, doi:10.1073/pnas.1906556116.

Parkinson, C. L., and D. J. Cavalieri, 2012: Antarctic sea ice variability and trends, 1979–2010. *Cryosphere*, **6**, 871–880, doi:10.5194/tc-6-871-2012.

Polvani, L. M., and K. L. Smith, 2013: Can natural variability explain observed Antarctic sea ice trends? New modeling evidence from CMIP5. *Geophys. Res. Lett.*, **40**, 3195–3199, doi:10.1002/grl.50578.

Polyakov, I. V., T. P. Rippeth, I. Fer, M. B. Alkire, T. M. Baumann, E. C. Carmack, and Coauthors, 2020: Weakening of the cold halocline layer exposes sea ice to oceanic heat in the Eastern Arctic Ocean. *J. Clim.*, **33**, 8107–8123, doi:10.1175/JCLI-D-19-0976.1.

Poulsen, C. J., and R. L. Jacob, 2004: Factors that inhibit snowball Earth simulation. *Paleoceanography*, **19**, PA4021, doi:10.1029/2004PA001056.

Rahmstorf, S., 2006: The thermohaline circulation. *Encyclopedia of Quaternary Science*, S. A. Elias, Ed., 2nd ed., Elsevier, Amsterdam.

Raymond, B., K. Meiners, C. W. Fowler, B. Pasquer, G. D. Williams, and S. Nicol, 2009: Cumulative solar irradiance and potential large-scale sea ice algae distribution off east Antarctica (30°E–150°E). *Polar Biol.*, **32**, 443–452, doi:10.1007/s00300-008-0538-5.

Rayner, N. A., D. E. Parker, E. B. Horton, C. K. Folland, L. V. Alexander, D. P. Rowell, and Coauthors, 2003: Global analyses of sea surface temperature, sea ice, and night marine air temperature since the late nineteenth century. *J. Geophys. Res. Atmos.*, **108**, 4407, doi:10.1029/2002JD002670.

Regehr, E. V., N. J. Lunn, S. C. Amstrup, and I. Stirling, 2010: Effects of earlier sea ice breakup on survival and population size of polar bears in western Hudson Bay. *J. Wildl. Manage.*, **71**, 2673–2683, doi:10.2193/2006-180.

Ridley, J. K., J. A. Lowe, and H. T. Hewitt, 2012: How reversible is sea ice loss? *Cryosphere*, **6**, 193–198, doi:10.5194/tc-6-193-2012.

Ridley, J. K., J. A. Lowe, and D. Simonin, 2008: The demise of Arctic sea ice during stabilisation at high greenhouse gas concentrations. *Clim. Dyn.*, **30**, 333–341, doi:10.1007/s00382-007-0291-4.

Roach, L. A., J. Dörr, C. R. Holmes, F. Massonnet, E. W. Blockley, D. Notz, and Coauthors, 2020: Antarctic sea ice area in CMIP6. *Geophys. Res. Lett.*, **47**, e2019GL086 729, doi:10.1029/2019GL086729.

Roe, G. H., N. Feldl, K. C. Armour, Y.-T. Hwang, and D. M. W. Frierson, 2015: The remote impacts of climate feedbacks on regional climate predictability. *Nat. Geosci.*, **8**, 135–139, doi:10.1038/ngeo2346.

Ronalds, B., E. Barnes, and P. Hassanzadeh, 2018: A barotropic mechanism for the response of jet stream variability to Arctic amplification and sea ice loss. *J. Clim.*, **31**, 7069–7085, doi:10.1175/JCLI-D-17-0778.1.

Rong, X., J. Li, H. Chen, Y. Xin, J. Su, L. Hua, and Coauthors, 2018: The CAMS Climate System Model and a basic evaluation of its climatology and climate variability simulation. *J. Meteorol. Res.*, **32**, 839–861, doi:10.1007/s13351-018-8058-x.

Rose, B. E. J., 2015: Stable "Waterbelt" climates controlled by tropical ocean heat transport: A nonlinear coupled climate mechanism of relevance to Snowball earth. *J. Geophys. Res.*, **120**, 1404–1423, doi:10.1002/2014JD022659.

Rose, B. E. J., and D. G. Ferreira, 2013: Ocean heat transport and water vapor greenhouse in a warm equable climate: a new look at the low gradient paradox. *J. Clim.*, **26**, 2117–2136, doi:10.1175/JCLI-D-11-00547.1.

Rose, B. E. J., and J. Marshall, 2009: Ocean heat transport, sea ice, and multiple climate states: Insights from energy balance models. *J. Atmos. Sci*, **66**, 2828–2843, doi:10.1175/2009JAS3039.1.

Rosenblum, E., and I. Eisenman, 2017: Sea ice trends in climate models only accurate in runs with biased global warming. *J. Clim.*, **30**, 6265–6278, doi:10.1175/JCLI-D-16-0455.1.

Rudels, B., 2012: Arctic Ocean circulation and variability—advection and external forcing encounter constraints and local processes. *Ocean Sci.*, **8**, 261–286, doi:10.5194/os-8-261-2012.

Schweiger, A., R. Lindsay, J. Zhang, M. Steele, H. Stern, and R. Kwok, 2011: Uncertainty in modeled Arctic sea ice volume. *J. Geophys. Res.*, **116**, doi:10.1029/2011JC007084.

Screen, J. A., 2013: Influence of Arctic sea ice on European summer precipitation. *Environ. Res. Lett.*, **8**, 044 015, doi:10.1088/1748-9326/8/4/044015.

Screen, J. A., and C. Deser, 2019: Pacific Ocean variability influences the time of emergence of a seasonally ice-free Arctic Ocean. *Geophys. Res. Lett.*, **46**, 2222–2231, doi:10.1029/2018GL081393.

Screen, J. A., and I. Simmonds, 2010: The central role of diminishing sea ice in recent Arctic temperature amplification. *Nature*, **464**, 1334–1337, doi:10.1038/nature09051.

Séférian, R., P. Nabat, M. Michou, D. Saint-Martin, A. Voldoire, J. Colin, and Coauthors, 2019: Evaluation of CNRM Earth System Model, CNRM-ESM2-1: Role of Earth System Processes in Present-Day and Future Climate. *J. Adv. Model. Earth Syst.*, **11**, 4182–4227, doi:10.1029/2019MS001791.

Sellar, A. A., C. G. Jones, J. P. Mulcahy, Y. Tang, A. Yool, A. Wiltshire, and Coauthors, 2019: UKESM1: Description and Evaluation of the U.K. Earth System Model. *J. Adv. Model. Earth Syst.*, **11**, 4513–4558, doi:10.1029/2019MS001739.

Sellers, W. D., 1969: A global climatic model based on the energy balance of the Earth–atmosphere system. *J. Appl. Meteorol.*, **8**, 392–400, doi:10.1175/1520-0450(1969)008<0392:AGCMBO>2.0.CO;2.

Senftleben, D., A. Lauer, and A. Karpechko, 2020: Constraining uncertainties in CMIP5 projections of September Arctic sea ice extent with observations. *J. Clim.*, **33**, 1487–1503, doi:10.1175/JCLI-D-19-0075.1.

Serreze, M. C., A. P. Barrett, A. G. Slater, R. A. Woodgate, K. Aagaard, R. B. Lammers, and Coauthors, 2006: The large-scale freshwater cycle of the Arctic. *J. Geophys. Res.*, **111**, C11 010, doi:10.1029/2005JC003424.

Serreze, M. C., and W. N. Meier, 2019: The Arctic's sea ice cover: trends, variability, predicatability and comparisons to the Antarctic. *Ann. N. Y. Acad. Sci.*, **1436**, 36–53, doi:10.1111/nyas.13856.

Sévellec, F., A. V. Fedorov, and W. Liu, 2017: Arctic sea-ice decline weakens the Atlantic meridional overturning circulation. *Nat. Clim. Change*, **7**, 604–610, doi:10.1038/nclimate3353.

Siler, N., G. H. Roe, and K. C. Armour, 2018: Insights into the zonal-mean response of the hydrologic cycle to global warming from a diffusive energy balance model. *J. Clim.*, **31**, 7481–7493, doi:10.1175/JCLI-D-18-0081.1.

SIMIP Community, 2020: Arctic sea ice in CMIP6. *Geophys. Res. Lett.*, **47**, e2019GL086 749, doi:10.1029/2019GL086749.

Simpkins, G. R., L. M. Ciasto, D. W. J. Thompson, and M. H. England, 2012: Seasonal relationships between large-scale climate variability and Antarctic sea ice concentration. *J. Clim.*, **25**, 5451–5469, doi:10.1175/JCLI-D-11-00367.1.

Singh, H. A., L. M. Polvani, and P. J. Rasch, 2019: Antarctic sea ice expansion, driven by internal variability, in the presence of increasing atmospheric CO_2. *Geophys. Res. Lett.*, **46**, 14 762–14 771, doi:10.1029/2019GL083758.

Singh, H. A., P. J. Rasch, and B. E. J. Rose, 2017: Increased ocean heat convergence into the high latitudes with CO_2 doubling enhances polar-amplified warming. *Geophys. Res. Lett.*, **44**, 10 583–10 591, doi:10.1002/2017GL074561.

Smith, C. J., R. J. Kramer, G. Myhre, K. Alterskjær, W. Collins, A. Sima, and Coauthors, 2020: Effective radiative forcing and adjustments in CMIP6 models. *Atmos. Chem. Phys.*, **20**, 9591–9618, doi:10.5194/acp-20-9591-2020.

Sun, S., and I. Eisenman, 2021: Observed Antarctic sea ice expansion reproduced in a climate model after correcting biases in sea ice drift velocity. *Nat. Commun.*, **12**, doi:10.1038/s41467-021-21412-z.

Swart, N. C., J. N. S. Cole, V. V. Kharin, M. Lazare, J. F. Scinocca, N. P. Gillett, and Coauthors, 2019: The Candian Earth System Model version 5 (CanESM5.0.3). *Geosci. Model Dev.*, **12**, 4823–4873, doi:10.5194/gmd-12-4823-2019.

Swart, N. C., J. C. Fyfe, E. Hawkins, J. E. Kay, and A. Jahn, 2015: Influence of internal variability on Arctic sea-ice trends. *Nat. Clim. Change*, **5**, 86–89, doi:10.1038/nclimate2483.

Thackeray, C. W., and A. Hall, 2019: An emergent constraint on future Arctic sea ice albedo feedback. *Nat. Clim. Change*, **9**, 972–978, doi:10.1038/s41558-019-0619-1.

Thorndike, A. S., 1992: A toy model linking atmospheric thermal radiation and sea ice growth. *J. Geophys. Res.*, **97**, 9401–9410, doi:10.1029/92JC00695.

Tietsche, S., D. Notz, J. H. Jungclaus, and J. Marotzke, 2011: Recovery mechanisms of Arctic summer sea ice. *Geophys. Res. Lett.*, **38**, L02 707, doi:10.1029/2010GL045698.

Todd, A., L. Zanna, M. Couldrey, J. M. Gregory, Q. Wu, J. A. Church, and Coauthors, 2020: Ocean-only FAFMIP: understanding regional patterns of ocean heat content and dynamic sea level change. *J. Adv. Model. Earth Syst.*, **12**, e2019MS002 027, doi:10.1029/2019MS002027.

Trenberth, K. E., and J. T. Fasullo, 2017: Atlantic meridional heat transports computed from balancing Earth's energy locally. *Geophys. Res. Lett.*, **44**, 1919–1927, doi:10.1002/2016GL072475.

Valero, F. P. J., P. Minnis, S. K. Pope, A. Bucholtz, B. C. Bush, D. R. Doelling, and Coauthors, 2000: Absorption of solar radiation by the atmosphere as determined using satellite, aircraft, and surface data during the atmospheric radiation measurement enhanced shortwave experiment (ARESE). *J. Geophys. Res.*, **105**, 4743–4758, doi:10.1029/1999JD901063.

Vihma, T., 2014: Effects of Arctic sea ice decline on weather and climate: a review. *Surv. Geophys.*, **35**, 1175–1214, doi:10.1007/s10712-014-9284-0.

Voldoire, A., D. Saint-Martin, S. Sénési, B. Decharme, A. Alias, M. Chevallier, and Coauthors, 2019: Evaluation of CMIP6 DECK Experiments With CNRM-CM6-1. *J. Adv. Model. Earth Syst.*, **11**, 2177–2213, doi:10.1029/2019MS001683.

Wagner, T. J. W., and I. Eisenman, 2015: How climate model complexity influences sea ice stability. *J. Clim.*, **28**, 3998–4014, doi:10.1175/JCLI-D-14-00654.1.

Watson, A. J., J. R. Ledwell, M.-J. Messias, B. A. King, N. Mackay, M. P. Meredith, and Coauthors, 2013: Rapid cross-density ocean mixing at mid-depths in the Drake Passage measured by tracer release. *Nature*, **501**, 408–411, doi:10.1038/nature12432.

Wilson, E. A., S. C. Riser, E. C. Campbell, and A. P. S. Wong, 2019: Winter upper-ocean stability and ice–ocean feedbacks in the sea ice-covered Southern Ocean. *J. Phys. Oceanogr.*, **49**, 1099–1117, doi:10.1175/JPO-D-18-0184.1.

Winton, M., 2003: On the climatic impact of ocean circulation. *J. Clim.*, **16**, 2875–2889, doi:10.1175/1520-0442(2003)016<2875:OTCIOO>2.0.CO;2.

Winton, M., 2006: Does the Arctic sea ice have a tipping point? *Geophys. Res. Lett.*, **33**, L23 504, doi:10.1029/2006GL028017.

Yuan, X., 2004: ENSO-related impacts on Antarctic sea ice: a synthesis of phenomenon and mechanisms. *Antarct. Sci.*, **16**, 415–425, doi:10.1017/S0954102004002238.

Yukimoto, S., H. Kawai, T. Koshiro, N. Oshima, K. Yoshida, S. Urakawa, and Coauthors, 2019: The Meteorological Research Institute Earth System Model Version 2.0, MRI-ESM2.0: Description and Basic Evaluation of the Physical Component. *J. Meteorol. Soc. Japan*, **97**, 931–965, doi:10.2151/jmsj.2019-051.

Zanna, L., S. Khatiwala, J. M. Gregory, J. Ison, and P. Heimbach, 2019: Global reconstruction of historical ocean heat transport and storage. *Proc. Natl. Acad. Sci.*, **116**, 1126–1131, doi:10.1073/pnas.1808838115.

Zhang, L., T. L. Delworth, W. Cooke, and X. Yang, 2019: Natural variability of southern ocean convection as a driver of observed climate trends. *Nat. Clim. Change*, **9**, 59–65, doi:10.1038/s41558-018-0350-3.

Zhang, Y., N. Jeevanjee, and S. Fueglistaler, 2020: Linearity of outgoing longwave radiation: from an atmospheric column to global climate models. *Geophys. Res. Lett.*, **47**, e2020GL089 235, doi:10.1029/2020GL089235.

Ziehn, T., M. A. Chamberlain, R. M. Law, A. Lenton, R. W. Bodman, M. Dix, and Coauthors, 2020: The Australian Earth System Model: ACCESS-ESM1.5. *J. South. Hemisphere Earth Syst. Sci.*, **70**, 193–214, doi:10.1071/ES19035.

Zunz, V., H. Goosse, and F. Massonnet, 2012: How does internal variability influence the ability of CMIP5 models to reproduce the recent trend in southern ocean sea ice extent? *Cryosphere*, **7**, 451–468, doi:10.5194/tc-7-451-2013.

Appendices

A CMIP6 atmospheric radiation parameters

Values of the atmospheric radiation parameters, B_{up}, B_{OLR}, and B_{dn}, are derived from CMIP6 model PI-control simulations following the same procedure as described in section 2.3.2 for ERA-Interim data. Here, the relevant fields are restricted to latitudes $\phi_0 \leq \phi \leq 90°\mathrm{N}/°\mathrm{S}$, where ϕ_0 is a fixed reference latitude. This data is first used in section 4.3.1. Tables A.1–A.4 list the results for all 21 models analysed in this thesis (Table 4.1) with $\phi_0 = 65°\mathrm{N}/°\mathrm{S}$ in 5° intervals down to $\phi_0 = 50°\mathrm{N}/°\mathrm{S}$, and Table A.5 uses the global dataset (i.e., $\phi_0 = 0°$). Values derived from ERA-Interim are also included for comparison.

In all cases, there is a choice of reference pressure level, p_0, upon which to take air temperature for the determination of B_{OLR} and B_{dn}. These values are derived with $p_0 = 700$ hPa for the northern hemisphere and $p_0 = 500$ hPa for the southern hemisphere. The tabulated uncertainties are with respect to the temporal variability over the PI-control simulations. The uncertainties in B_{OLR}, B_{dn}, and $\beta = B_{\mathrm{OLR}}/B_{\mathrm{dn}}$ due to the choice of p_0 is comparable to that of the time averaging and, for simplicity, is not included since the uncertainties associated with both sources are small.

Finally, Table A.6 lists the multi-model, PI-control derived values of B_{up}, B_{OLR}, B_{dn}, s, b_{c}, and $\Delta T_{\mathrm{s}}/\Delta\mathrm{OHT}$, with $\phi_0 = 65°\mathrm{N}/°\mathrm{S}$, for various model subsets. This is relevant to the EBM equation fitting in section 5.3 where not all models provide the necessary data to analyse each future scenario (Table 5.1).

Table A.1: Derived values of B_{up}, B_{OLR}, B_{dn}, and $\beta = B_{\mathrm{OLR}}/B_{\mathrm{dn}}$ in the CMIP6 models analysed in this thesis. Here the reference latitude $\phi_0 = 65°\mathrm{N}/°\mathrm{S}$ (i.e., these values are valid for the region between ϕ_0 and the pole). The units of B_{up}, B_{OLR}, and B_{dn} are W m^{-2} °C^{-1}, and β is dimensionless. Uncertainties are with respect to time averaging, except for the multi-model mean which is the standard deviation across models. Uncertainties written as 0.00 are not exactly zero but are < 0.005.

	Northern hemisphere ($\phi_0 = 65°\mathrm{N}$)				Southern hemisphere ($\phi_0 = 65°\mathrm{S}$)			
Model	B_{up}	B_{OLR}	B_{dn}	β	B_{up}	B_{OLR}	B_{dn}	β
ACCESS-CM2	4.90 ± 0.01	3.18 ± 0.02	7.18 ± 0.04	0.44 ± 0.00	4.41 ± 0.02	6.68 ± 0.04	10.57 ± 0.14	0.63 ± 0.01
ACCESS-ESM1-5	4.89 ± 0.01	3.20 ± 0.01	6.54 ± 0.02	0.49 ± 0.00	4.74 ± 0.02	6.40 ± 0.02	8.66 ± 0.07	0.74 ± 0.01
CAMS-CSM1-0	4.97 ± 0.01	3.08 ± 0.01	7.04 ± 0.03	0.44 ± 0.00	5.03 ± 0.02	5.35 ± 0.11	9.00 ± 0.20	0.59 ± 0.03
CanESM5	4.80 ± 0.01	3.09 ± 0.02	6.27 ± 0.03	0.49 ± 0.01	4.71 ± 0.01	6.49 ± 0.03	10.21 ± 0.05	0.64 ± 0.01
CanESM5-CanOE	4.80 ± 0.02	3.08 ± 0.02	6.27 ± 0.02	0.49 ± 0.01	4.72 ± 0.01	6.49 ± 0.04	10.21 ± 0.07	0.63 ± 0.01
CESM2	4.75 ± 0.01	3.29 ± 0.01	7.42 ± 0.03	0.44 ± 0.00	4.67 ± 0.01	6.42 ± 0.03	10.62 ± 0.05	0.60 ± 0.01
CESM2-FV2	4.62 ± 0.01	3.08 ± 0.02	7.58 ± 0.04	0.41 ± 0.00	4.67 ± 0.01	6.64 ± 0.04	11.31 ± 0.09	0.59 ± 0.01
CESM2-WACCM	4.63 ± 0.01	3.00 ± 0.00	7.34 ± 0.03	0.41 ± 0.00	4.64 ± 0.01	6.19 ± 0.05	10.62 ± 0.11	0.58 ± 0.01
CESM2-WACCM-FV2	4.65 ± 0.01	3.02 ± 0.01	7.63 ± 0.02	0.40 ± 0.00	4.68 ± 0.01	6.52 ± 0.03	11.36 ± 0.07	0.57 ± 0.01
CNRM-CM6-1	5.02 ± 0.02	2.85 ± 0.02	6.24 ± 0.03	0.46 ± 0.01	4.56 ± 0.02	6.51 ± 0.03	10.60 ± 0.10	0.61 ± 0.01
CNRM-CM6-1-HR	5.03 ± 0.03	2.80 ± 0.01	6.00 ± 0.02	0.47 ± 0.00	4.78 ± 0.06	6.36 ± 0.03	10.85 ± 0.12	0.59 ± 0.01
CNRM-ESM2-1	5.09 ± 0.04	2.83 ± 0.02	6.23 ± 0.03	0.45 ± 0.01	4.75 ± 0.01	6.46 ± 0.03	10.72 ± 0.06	0.60 ± 0.01
HadGEM3-GC31-LL	4.84 ± 0.01	3.12 ± 0.01	6.98 ± 0.03	0.45 ± 0.00	4.59 ± 0.01	6.87 ± 0.06	11.11 ± 0.12	0.62 ± 0.01
HadGEM3-GC31-MM	4.93 ± 0.02	3.12 ± 0.02	6.88 ± 0.03	0.45 ± 0.01	4.95 ± 0.05	6.74 ± 0.03	11.27 ± 0.10	0.60 ± 0.01
IPSL-CM6A-LR	4.87 ± 0.02	2.93 ± 0.02	7.13 ± 0.02	0.41 ± 0.00	4.28 ± 0.03	6.87 ± 0.03	10.97 ± 0.10	0.63 ± 0.01
MPI-ESM-1-2-HAM	4.90 ± 0.02	3.39 ± 0.01	7.33 ± 0.04	0.46 ± 0.00	5.17 ± 0.01	5.42 ± 0.03	8.44 ± 0.08	0.64 ± 0.01
MPI-ESM1-2-HR	4.91 ± 0.01	2.64 ± 0.01	5.88 ± 0.05	0.45 ± 0.01	4.74 ± 0.01	5.72 ± 0.03	10.03 ± 0.08	0.57 ± 0.01
MPI-ESM1-2-LR	4.78 ± 0.01	2.69 ± 0.01	6.37 ± 0.02	0.42 ± 0.00	4.92 ± 0.01	5.77 ± 0.02	10.36 ± 0.05	0.56 ± 0.00
MRI-ESM2-0	5.24 ± 0.02	2.64 ± 0.01	6.39 ± 0.03	0.41 ± 0.00	5.00 ± 0.01	6.36 ± 0.04	11.31 ± 0.09	0.56 ± 0.01
NorCPM1	4.73 ± 0.01	3.95 ± 0.02	7.81 ± 0.04	0.51 ± 0.01	4.68 ± 0.02	7.79 ± 0.05	9.95 ± 0.10	0.78 ± 0.01
UKESM1-0-LL	4.75 ± 0.02	3.26 ± 0.02	6.96 ± 0.03	0.47 ± 0.00	4.49 ± 0.01	6.80 ± 0.04	10.64 ± 0.10	0.64 ± 0.01
Multi-model mean	4.86 ± 0.15	3.06 ± 0.29	6.83 ± 0.57	0.45 ± 0.03	4.72 ± 0.20	6.42 ± 0.52	10.42 ± 0.81	0.62 ± 0.05
ERA-Interim	4.97 ± 0.03	2.75 ± 0.01	6.34 ± 0.03	0.43 ± 0.00	4.78 ± 0.01	6.48 ± 0.04	10.07 ± 0.11	0.64 ± 0.01

Table A.2: As in Table A.1 but for the reference latitude $\phi_0 = 60°\text{N}/°\text{S}$.

	Northern hemisphere ($\phi_0 = 60°$N)				Southern hemisphere ($\phi_0 = 60°$S)			
Model	B_{up}	B_{OLR}	B_{dn}	β	B_{up}	B_{OLR}	B_{dn}	β
ACCESS-CM2	5.19 ± 0.01	3.11 ± 0.02	7.19 ± 0.03	0.43 ± 0.00	4.72 ± 0.01	6.20 ± 0.03	12.28 ± 0.13	0.50 ± 0.01
ACCESS-ESM1-5	5.28 ± 0.01	3.12 ± 0.01	6.65 ± 0.01	0.47 ± 0.00	5.19 ± 0.01	6.19 ± 0.02	10.77 ± 0.08	0.57 ± 0.01
CAMS-CSM1-0	5.21 ± 0.01	3.04 ± 0.01	7.09 ± 0.03	0.43 ± 0.00	5.08 ± 0.02	5.29 ± 0.12	10.06 ± 0.23	0.53 ± 0.02
CanESM5	5.00 ± 0.01	3.06 ± 0.02	6.30 ± 0.02	0.49 ± 0.00	4.87 ± 0.01	6.23 ± 0.02	11.22 ± 0.05	0.55 ± 0.00
CanESM5-CanOE	5.01 ± 0.02	3.05 ± 0.02	6.30 ± 0.02	0.48 ± 0.00	4.87 ± 0.02	6.22 ± 0.03	11.24 ± 0.08	0.55 ± 0.01
CESM2	5.14 ± 0.02	3.19 ± 0.02	7.39 ± 0.03	0.43 ± 0.00	5.12 ± 0.02	6.14 ± 0.02	12.62 ± 0.06	0.49 ± 0.00
CESM2-FV2	4.92 ± 0.01	3.02 ± 0.02	7.48 ± 0.03	0.40 ± 0.00	5.01 ± 0.01	6.42 ± 0.03	12.97 ± 0.10	0.49 ± 0.01
CESM2-WACCM	5.02 ± 0.01	2.92 ± 0.01	7.27 ± 0.03	0.40 ± 0.00	5.10 ± 0.01	5.93 ± 0.04	12.60 ± 0.11	0.47 ± 0.01
CESM2-WACCM-FV2	4.96 ± 0.01	2.95 ± 0.01	7.52 ± 0.02	0.39 ± 0.00	5.01 ± 0.01	6.31 ± 0.02	13.00 ± 0.07	0.49 ± 0.00
CNRM-CM6-1	5.37 ± 0.03	2.85 ± 0.02	6.30 ± 0.03	0.45 ± 0.01	4.92 ± 0.01	6.27 ± 0.03	12.09 ± 0.10	0.52 ± 0.01
CNRM-CM6-1-HR	5.47 ± 0.03	2.82 ± 0.01	6.06 ± 0.02	0.47 ± 0.00	5.22 ± 0.06	6.06 ± 0.03	12.46 ± 0.10	0.49 ± 0.01
CNRM-ESM2-1	5.43 ± 0.05	2.83 ± 0.02	6.29 ± 0.03	0.45 ± 0.01	5.07 ± 0.01	6.22 ± 0.02	12.14 ± 0.06	0.51 ± 0.00
HadGEM3-GC31-LL	5.16 ± 0.01	3.06 ± 0.01	7.00 ± 0.03	0.44 ± 0.00	4.96 ± 0.01	6.34 ± 0.04	12.91 ± 0.12	0.49 ± 0.01
HadGEM3-GC31-MM	5.28 ± 0.02	3.06 ± 0.02	6.90 ± 0.03	0.44 ± 0.00	5.35 ± 0.03	6.21 ± 0.03	13.08 ± 0.08	0.47 ± 0.00
IPSL-CM6A-LR	5.26 ± 0.02	2.89 ± 0.02	7.16 ± 0.02	0.40 ± 0.00	4.70 ± 0.02	6.34 ± 0.02	13.38 ± 0.10	0.47 ± 0.01
MPI-ESM-1-2-HAM	5.25 ± 0.02	3.27 ± 0.01	7.34 ± 0.04	0.45 ± 0.00	5.35 ± 0.01	5.30 ± 0.03	10.79 ± 0.09	0.49 ± 0.01
MPI-ESM1-2-HR	5.32 ± 0.01	2.59 ± 0.01	5.90 ± 0.04	0.44 ± 0.01	5.13 ± 0.01	5.48 ± 0.01	12.08 ± 0.07	0.45 ± 0.00
MPI-ESM1-2-LR	5.15 ± 0.01	2.62 ± 0.01	6.41 ± 0.02	0.41 ± 0.00	5.18 ± 0.01	5.50 ± 0.01	12.35 ± 0.05	0.45 ± 0.00
MRI-ESM2-0	5.63 ± 0.02	2.61 ± 0.01	6.37 ± 0.02	0.41 ± 0.00	5.40 ± 0.01	6.07 ± 0.03	12.98 ± 0.10	0.47 ± 0.01
NorCPM1	5.02 ± 0.01	3.84 ± 0.02	7.73 ± 0.03	0.50 ± 0.00	5.03 ± 0.03	7.36 ± 0.04	11.76 ± 0.10	0.63 ± 0.01
UKESM1-0-LL	5.07 ± 0.02	3.18 ± 0.02	6.99 ± 0.03	0.46 ± 0.00	4.86 ± 0.01	6.29 ± 0.02	12.52 ± 0.10	0.50 ± 0.01
Multi-model mean	5.20 ± 0.18	3.00 ± 0.26	6.84 ± 0.53	0.44 ± 0.03	5.05 ± 0.19	6.11 ± 0.44	12.16 ± 0.87	0.50 ± 0.04
ERA-Interim	5.38 ± 0.03	2.71 ± 0.01	6.25 ± 0.03	0.43 ± 0.00	5.12 ± 0.02	6.05 ± 0.03	11.79 ± 0.10	0.51 ± 0.01

Table A.3: As in Table A.1 but for the reference latitude $\phi_0 = 55°\text{N}/°\text{S}$.

	Northern hemisphere ($\phi_0 = 55°$N)				Southern hemisphere ($\phi_0 = 55°$S)			
Model	B_{up}	B_{OLR}	B_{dn}	β	B_{up}	B_{OLR}	B_{dn}	β
ACCESS-CM2	5.44 ± 0.01	3.03 ± 0.01	7.16 ± 0.03	0.42 ± 0.00	4.91 ± 0.01	5.62 ± 0.02	12.73 ± 0.10	0.44 ± 0.00
ACCESS-ESM1-5	5.62 ± 0.01	3.04 ± 0.01	6.68 ± 0.02	0.46 ± 0.00	5.42 ± 0.01	5.74 ± 0.01	11.63 ± 0.06	0.49 ± 0.00
CAMS-CSM1-0	5.41 ± 0.01	2.96 ± 0.01	7.07 ± 0.03	0.42 ± 0.00	5.14 ± 0.01	5.03 ± 0.12	10.65 ± 0.25	0.47 ± 0.02
CanESM5	5.29 ± 0.01	2.99 ± 0.02	6.33 ± 0.02	0.47 ± 0.00	5.14 ± 0.01	5.64 ± 0.01	12.19 ± 0.04	0.46 ± 0.00
CanESM5-CanOE	5.30 ± 0.02	2.98 ± 0.02	6.33 ± 0.02	0.47 ± 0.00	5.14 ± 0.01	5.63 ± 0.02	12.20 ± 0.06	0.46 ± 0.00
CESM2	5.54 ± 0.02	3.07 ± 0.02	7.26 ± 0.03	0.42 ± 0.00	5.39 ± 0.01	5.55 ± 0.01	13.11 ± 0.04	0.42 ± 0.00
CESM2-FV2	5.35 ± 0.02	2.94 ± 0.01	7.26 ± 0.03	0.41 ± 0.00	5.29 ± 0.01	5.83 ± 0.01	13.61 ± 0.06	0.43 ± 0.00
CESM2-WACCM	5.42 ± 0.02	2.82 ± 0.01	7.11 ± 0.02	0.40 ± 0.00	5.37 ± 0.01	5.36 ± 0.02	13.08 ± 0.09	0.41 ± 0.00
CESM2-WACCM-FV2	5.39 ± 0.02	2.87 ± 0.01	7.32 ± 0.02	0.39 ± 0.00	5.29 ± 0.01	5.78 ± 0.02	13.66 ± 0.05	0.42 ± 0.00
CNRM-CM6-1	5.67 ± 0.03	2.84 ± 0.02	6.37 ± 0.03	0.45 ± 0.00	5.18 ± 0.01	5.80 ± 0.02	12.62 ± 0.08	0.46 ± 0.00
CNRM-CM6-1-HR	5.77 ± 0.03	2.82 ± 0.01	6.13 ± 0.02	0.46 ± 0.00	5.49 ± 0.03	5.70 ± 0.02	12.87 ± 0.07	0.44 ± 0.00
CNRM-ESM2-1	5.74 ± 0.05	2.83 ± 0.02	6.35 ± 0.03	0.44 ± 0.00	5.27 ± 0.01	5.75 ± 0.02	12.61 ± 0.04	0.46 ± 0.00
HadGEM3-GC31-LL	5.39 ± 0.01	3.00 ± 0.01	6.96 ± 0.03	0.43 ± 0.00	5.16 ± 0.01	5.72 ± 0.02	13.35 ± 0.08	0.43 ± 0.00
HadGEM3-GC31-MM	5.54 ± 0.02	3.00 ± 0.02	6.89 ± 0.04	0.44 ± 0.00	5.49 ± 0.01	5.62 ± 0.02	13.42 ± 0.06	0.42 ± 0.00
IPSL-CM6A-LR	5.55 ± 0.03	2.85 ± 0.02	7.16 ± 0.02	0.40 ± 0.00	5.00 ± 0.02	5.70 ± 0.01	14.38 ± 0.08	0.40 ± 0.00
MPI-ESM-1-2-HAM	5.50 ± 0.02	3.14 ± 0.01	7.27 ± 0.04	0.43 ± 0.00	5.39 ± 0.01	4.96 ± 0.02	11.45 ± 0.07	0.43 ± 0.00
MPI-ESM1-2-HR	5.54 ± 0.01	2.54 ± 0.01	5.91 ± 0.04	0.43 ± 0.00	5.23 ± 0.01	5.12 ± 0.01	12.41 ± 0.05	0.41 ± 0.00
MPI-ESM1-2-LR	5.40 ± 0.01	2.54 ± 0.01	6.40 ± 0.02	0.40 ± 0.00	5.26 ± 0.01	5.04 ± 0.01	12.68 ± 0.04	0.40 ± 0.00
MRI-ESM2-0	5.97 ± 0.02	2.57 ± 0.01	6.36 ± 0.02	0.40 ± 0.00	5.74 ± 0.01	5.58 ± 0.02	13.67 ± 0.08	0.41 ± 0.00
NorCPM1	5.45 ± 0.01	3.65 ± 0.01	7.59 ± 0.03	0.48 ± 0.00	5.36 ± 0.02	6.50 ± 0.03	12.55 ± 0.07	0.52 ± 0.01
UKESM1-0-LL	5.31 ± 0.02	3.10 ± 0.01	6.95 ± 0.03	0.45 ± 0.00	5.10 ± 0.01	5.69 ± 0.01	13.14 ± 0.07	0.43 ± 0.00
Multi-model mean	5.50 ± 0.17	2.93 ± 0.23	6.80 ± 0.46	0.43 ± 0.03	5.27 ± 0.18	5.59 ± 0.33	12.76 ± 0.83	0.44 ± 0.03
ERA-Interim	5.68 ± 0.03	2.66 ± 0.01	6.17 ± 0.02	0.43 ± 0.00	5.33 ± 0.02	5.45 ± 0.03	12.09 ± 0.08	0.45 ± 0.01

Table A.4: As in Table A.1 but for the reference latitude $\phi_0 = 50°\text{N}/°\text{S}$.

	Northern hemisphere ($\phi_0 = 50°$N)				Southern hemisphere ($\phi_0 = 50°$S)			
Model	B_{up}	B_{OLR}	B_{dn}	β	B_{up}	B_{OLR}	B_{dn}	β
ACCESS-CM2	5.67 ± 0.01	2.96 ± 0.01	7.04 ± 0.03	0.42 ± 0.00	5.11 ± 0.18	5.00 ± 0.02	12.22 ± 0.06	0.41 ± 0.00
ACCESS-ESM1-5	5.92 ± 0.01	2.99 ± 0.01	6.61 ± 0.01	0.45 ± 0.00	5.56 ± 0.01	5.16 ± 0.01	11.46 ± 0.04	0.45 ± 0.00
CAMS-CSM1-0	5.57 ± 0.01	2.89 ± 0.01	6.99 ± 0.03	0.41 ± 0.00	5.19 ± 0.01	4.70 ± 0.11	10.51 ± 0.23	0.45 ± 0.02
CanESM5	5.54 ± 0.01	2.91 ± 0.02	6.31 ± 0.02	0.46 ± 0.00	5.32 ± 0.00	4.94 ± 0.01	11.86 ± 0.02	0.42 ± 0.00
CanESM5-CanOE	5.54 ± 0.02	2.90 ± 0.02	6.31 ± 0.02	0.46 ± 0.00	5.33 ± 0.01	4.94 ± 0.01	11.86 ± 0.03	0.42 ± 0.00
CESM2	5.77 ± 0.02	2.97 ± 0.01	7.05 ± 0.03	0.42 ± 0.00	5.48 ± 0.01	4.98 ± 0.01	12.33 ± 0.03	0.40 ± 0.00
CESM2-FV2	5.65 ± 0.02	2.87 ± 0.01	6.95 ± 0.03	0.41 ± 0.00	5.40 ± 0.00	5.12 ± 0.01	12.61 ± 0.04	0.41 ± 0.00
CESM2-WACCM	5.67 ± 0.02	2.74 ± 0.00	6.90 ± 0.02	0.40 ± 0.00	5.45 ± 0.01	4.82 ± 0.01	12.30 ± 0.06	0.39 ± 0.00
CESM2-WACCM-FV2	5.68 ± 0.02	2.79 ± 0.01	7.03 ± 0.02	0.40 ± 0.00	5.40 ± 0.01	5.09 ± 0.01	12.72 ± 0.02	0.40 ± 0.00
CNRM-CM6-1	5.84 ± 0.03	2.81 ± 0.02	6.38 ± 0.03	0.44 ± 0.00	5.27 ± 0.01	5.35 ± 0.01	12.30 ± 0.06	0.44 ± 0.00
CNRM-CM6-1-HR	5.97 ± 0.03	2.80 ± 0.01	6.16 ± 0.02	0.45 ± 0.00	5.63 ± 0.02	5.25 ± 0.01	12.50 ± 0.05	0.42 ± 0.00
CNRM-ESM2-1	5.91 ± 0.05	2.80 ± 0.02	6.37 ± 0.02	0.44 ± 0.00	5.34 ± 0.01	5.30 ± 0.01	12.25 ± 0.04	0.43 ± 0.00
HadGEM3-GC31-LL	5.58 ± 0.01	2.95 ± 0.03	6.85 ± 0.06	0.43 ± 0.01	5.26 ± 0.01	5.09 ± 0.13	12.74 ± 0.21	0.40 ± 0.02
HadGEM3-GC31-MM	5.76 ± 0.03	2.95 ± 0.01	6.79 ± 0.04	0.43 ± 0.00	5.56 ± 0.01	5.02 ± 0.02	12.75 ± 0.05	0.39 ± 0.00
IPSL-CM6A-LR	5.79 ± 0.03	2.80 ± 0.01	7.09 ± 0.02	0.39 ± 0.00	5.18 ± 0.01	5.05 ± 0.01	14.18 ± 0.05	0.36 ± 0.00
MPI-ESM-1-2-HAM	5.64 ± 0.02	3.05 ± 0.01	7.15 ± 0.03	0.43 ± 0.00	5.43 ± 0.01	4.66 ± 0.02	11.29 ± 0.06	0.41 ± 0.00
MPI-ESM1-2-HR	5.73 ± 0.01	2.48 ± 0.01	5.84 ± 0.04	0.42 ± 0.00	5.31 ± 0.01	4.58 ± 0.01	11.71 ± 0.04	0.39 ± 0.00
MPI-ESM1-2-LR	5.55 ± 0.01	2.50 ± 0.01	6.33 ± 0.02	0.39 ± 0.00	5.30 ± 0.01	4.68 ± 0.01	12.29 ± 0.03	0.38 ± 0.00
MRI-ESM2-0	6.18 ± 0.02	2.52 ± 0.01	6.31 ± 0.02	0.40 ± 0.00	5.89 ± 0.01	5.10 ± 0.02	13.29 ± 0.06	0.38 ± 0.00
NorCPM1	5.75 ± 0.01	3.48 ± 0.01	7.36 ± 0.03	0.47 ± 0.00	5.47 ± 0.01	5.55 ± 0.02	11.69 ± 0.05	0.47 ± 0.00
UKESM1-0-LL	5.49 ± 0.02	3.02 ± 0.01	6.83 ± 0.03	0.44 ± 0.00	5.22 ± 0.01	5.04 ± 0.01	12.65 ± 0.04	0.40 ± 0.00
Multi-model mean	5.72 ± 0.17	2.87 ± 0.21	6.70 ± 0.39	0.43 ± 0.02	5.39 ± 0.17	5.02 ± 0.24	12.26 ± 0.73	0.41 ± 0.03
ERA-Interim	5.91 ± 0.03	2.61 ± 0.01	6.04 ± 0.02	0.43 ± 0.00	5.43 ± 0.01	4.81 ± 0.02	11.47 ± 0.07	0.42 ± 0.00

Table A.5: As in Table A.1 but for the reference latitude $\phi_0 = 0°$.

	Northern hemisphere ($\phi_0 = 0°$)				Southern hemisphere ($\phi_0 = 0°$)			
Model	B_{up}	B_{OLR}	B_{dn}	β	B_{up}	B_{OLR}	B_{dn}	β
ACCESS-CM2	7.36 ± 0.01	2.84 ± 0.01	6.03 ± 0.01	0.47 ± 0.00	6.76 ± 0.01	3.23 ± 0.00	6.70 ± 0.00	0.48 ± 0.00
ACCESS-ESM1-5	7.60 ± 0.01	2.90 ± 0.01	6.26 ± 0.01	0.46 ± 0.00	7.15 ± 0.01	3.30 ± 0.00	6.94 ± 0.01	0.48 ± 0.00
CAMS-CSM1-0	7.26 ± 0.01	2.69 ± 0.00	6.27 ± 0.01	0.43 ± 0.00	6.84 ± 0.01	2.95 ± 0.02	6.80 ± 0.04	0.43 ± 0.01
CanESM5	7.32 ± 0.01	2.57 ± 0.01	5.88 ± 0.01	0.44 ± 0.00	6.94 ± 0.01	2.97 ± 0.00	6.66 ± 0.01	0.45 ± 0.00
CanESM5-CanOE	7.33 ± 0.01	2.57 ± 0.01	5.88 ± 0.01	0.44 ± 0.00	6.94 ± 0.01	2.96 ± 0.01	6.65 ± 0.01	0.45 ± 0.00
CESM2	7.61 ± 0.02	2.57 ± 0.00	6.32 ± 0.01	0.41 ± 0.00	7.04 ± 0.01	3.15 ± 0.00	6.93 ± 0.00	0.45 ± 0.00
CESM2-FV2	7.55 ± 0.01	2.61 ± 0.01	6.02 ± 0.01	0.43 ± 0.00	6.90 ± 0.01	3.19 ± 0.01	7.00 ± 0.01	0.46 ± 0.00
CESM2-WACCM	7.53 ± 0.01	2.47 ± 0.01	6.20 ± 0.01	0.40 ± 0.00	7.00 ± 0.01	3.09 ± 0.01	6.92 ± 0.01	0.45 ± 0.00
CESM2-WACCM-FV2	7.50 ± 0.01	2.55 ± 0.00	6.10 ± 0.01	0.42 ± 0.00	6.90 ± 0.00	3.14 ± 0.01	7.01 ± 0.01	0.45 ± 0.00
CNRM-CM6-1	7.40 ± 0.03	2.57 ± 0.01	6.26 ± 0.02	0.41 ± 0.00	6.86 ± 0.01	3.15 ± 0.01	7.23 ± 0.01	0.44 ± 0.00
CNRM-CM6-1-HR	7.49 ± 0.02	2.60 ± 0.01	6.15 ± 0.01	0.42 ± 0.00	7.09 ± 0.01	3.16 ± 0.01	7.25 ± 0.02	0.44 ± 0.00
CNRM-ESM2-1	7.48 ± 0.04	2.57 ± 0.01	6.26 ± 0.02	0.41 ± 0.00	6.92 ± 0.00	3.12 ± 0.01	7.21 ± 0.01	0.43 ± 0.00
HadGEM3-GC31-LL	7.33 ± 0.01	2.77 ± 0.00	6.00 ± 0.01	0.46 ± 0.00	6.88 ± 0.01	3.25 ± 0.00	6.74 ± 0.01	0.48 ± 0.00
HadGEM3-GC31-MM	7.45 ± 0.03	2.76 ± 0.01	6.10 ± 0.01	0.45 ± 0.00	7.10 ± 0.02	3.28 ± 0.00	6.76 ± 0.01	0.48 ± 0.00
IPSL-CM6A-LR	7.56 ± 0.02	2.61 ± 0.01	6.30 ± 0.02	0.42 ± 0.00	6.76 ± 0.01	3.09 ± 0.01	7.38 ± 0.01	0.42 ± 0.00
MPI-ESM-1-2-HAM	7.31 ± 0.01	3.00 ± 0.00	5.94 ± 0.01	0.50 ± 0.00	6.99 ± 0.01	3.20 ± 0.00	6.53 ± 0.01	0.49 ± 0.00
MPI-ESM1-2-HR	7.45 ± 0.02	2.58 ± 0.01	5.54 ± 0.02	0.47 ± 0.00	6.98 ± 0.01	3.03 ± 0.00	6.51 ± 0.00	0.47 ± 0.00
MPI-ESM1-2-LR	7.39 ± 0.01	2.63 ± 0.00	5.60 ± 0.01	0.47 ± 0.00	6.90 ± 0.00	3.02 ± 0.00	6.40 ± 0.00	0.47 ± 0.00
MRI-ESM2-0	7.72 ± 0.01	2.41 ± 0.01	5.83 ± 0.01	0.41 ± 0.00	7.23 ± 0.01	2.99 ± 0.01	6.85 ± 0.01	0.44 ± 0.00
NorCPM1	7.26 ± 0.01	2.64 ± 0.00	6.56 ± 0.01	0.40 ± 0.00	6.85 ± 0.01	3.08 ± 0.00	7.01 ± 0.01	0.44 ± 0.00
UKESM1-0-LL	7.26 ± 0.02	2.76 ± 0.01	6.06 ± 0.01	0.46 ± 0.00	6.84 ± 0.01	3.22 ± 0.00	6.72 ± 0.01	0.48 ± 0.00
Multi-model mean	7.44 ± 0.13	2.65 ± 0.14	6.08 ± 0.24	0.44 ± 0.03	6.95 ± 0.12	3.12 ± 0.10	6.87 ± 0.26	0.46 ± 0.02
ERA-Interim	7.90 ± 0.02	2.40 ± 0.01	5.88 ± 0.01	0.41 ± 0.00	7.22 ± 0.01	3.12 ± 0.01	7.28 ± 0.02	0.43 ± 0.00

Table A.6: Values of B_{OLR}, B_{up}, B_{dn}, s, b_{c}, and $\Delta T_{\mathrm{s}}/\Delta\mathrm{OHT}$ (see Eq. 3.23b), computed from N models' collective PI-control simulations, in various model subsets. The subset labels refer to the experiment for which the set of models provide data for; see Table 5.1. When including CNRM-CM6-1, s cannot be computed because sea ice data was not available for this model's PI-control simulation. Each set is repeated excluding this model. Units of s are W m^{-2} °N^{-1} or °S^{-1}, b_{c} is dimensionless, and of $\Delta T_{\mathrm{s}}/\Delta\mathrm{OHT}$ are °C PW^{-1}.

Model subset	N	B_{up}	B_{OLR}	B_{dn}	β	s	b_{c}	$\Delta T_{\mathrm{s}}/\Delta\mathrm{OHT}$
Northern hemisphere ($\phi_0 = 65$°N)								
All models	21	5.80 ± 0.04	2.62 ± 0.04	7.11 ± 0.13	0.37 ± 0.01	—	-0.89 ± 0.02	22.04 ± 0.76
Excluding CNRM-CM6-1	20	5.77 ± 0.04	2.60 ± 0.04	7.07 ± 0.13	0.37 ± 0.01	0.77 ± 0.02	-0.89 ± 0.02	21.76 ± 0.81
Historical	17	5.84 ± 0.04	2.63 ± 0.04	7.11 ± 0.14	0.37 ± 0.01	—	-0.89 ± 0.02	22.38 ± 0.78
Excluding CNRM-CM6-1	16	5.82 ± 0.04	2.60 ± 0.04	7.06 ± 0.14	0.37 ± 0.01	0.78 ± 0.02	-0.88 ± 0.02	22.14 ± 0.84
SSP2-4.5	16	5.85 ± 0.04	2.64 ± 0.04	7.12 ± 0.14	0.37 ± 0.01	—	-0.89 ± 0.02	22.10 ± 0.78
Excluding CNRM-CM6-1	15	5.83 ± 0.05	2.62 ± 0.05	7.07 ± 0.15	0.37 ± 0.01	0.77 ± 0.02	-0.88 ± 0.02	21.81 ± 0.84
SSP3-7.0	15	5.85 ± 0.04	2.65 ± 0.04	7.16 ± 0.14	0.37 ± 0.01	—	-0.88 ± 0.02	22.39 ± 0.80
Excluding CNRM-CM6-1	14	5.82 ± 0.05	2.62 ± 0.05	7.11 ± 0.15	0.37 ± 0.01	0.78 ± 0.02	-0.88 ± 0.02	22.13 ± 0.86
Southern hemisphere ($\phi_0 = 65$°S)								
All models	21	6.34 ± 0.07	2.58 ± 0.07	6.73 ± 0.20	0.38 ± 0.02	—	-1.23 ± 0.02	17.60 ± 0.61
Excluding CNRM-CM6-1	20	6.34 ± 0.07	2.55 ± 0.07	6.67 ± 0.21	0.38 ± 0.02	1.66 ± 0.04	-1.22 ± 0.02	17.43 ± 0.61
Historical	17	6.40 ± 0.08	2.55 ± 0.07	6.77 ± 0.22	0.38 ± 0.02	—	-1.24 ± 0.03	18.09 ± 0.65
Excluding CNRM-CM6-1	16	6.40 ± 0.08	2.52 ± 0.07	6.71 ± 0.23	0.38 ± 0.02	1.71 ± 0.04	-1.23 ± 0.03	17.91 ± 0.65
SSP2-4.5	16	6.35 ± 0.09	2.52 ± 0.08	6.26 ± 0.24	0.40 ± 0.02	—	-1.23 ± 0.03	16.75 ± 0.68
Excluding CNRM-CM6-1	15	6.35 ± 0.09	2.48 ± 0.08	6.18 ± 0.25	0.40 ± 0.02	1.61 ± 0.04	-1.22 ± 0.03	16.52 ± 0.68
SSP3-7.0	15	6.34 ± 0.09	2.51 ± 0.08	6.19 ± 0.25	0.41 ± 0.02	—	-1.24 ± 0.03	16.78 ± 0.69
Excluding CNRM-CM6-1	14	6.34 ± 0.09	2.47 ± 0.08	6.10 ± 0.25	0.40 ± 0.02	1.62 ± 0.05	-1.23 ± 0.03	16.54 ± 0.69